Universidade do Minho
Escola de Engenharia

Eunice Paula Freitas Cunha

Functionalized graphene for polymer composites

Functionalized graphene for polymer composites
Eunice Paula Freitas Cunha

UMinho | 2016

outubro de 2016

Universidade do Minho
Escola de Engenharia

Eunice Paula Freitas Cunha

Functionalized graphene for polymer composites

Tese de Doutoramento
Ciência e Engenharia de Polímeros e Compósitos

Trabalho efectuado sob a orientação de
Professora Doutora Maria da Conceição de Jesus Rego Paiva
Professora Doutora Maria Fernanda Proença

outubro de 2016

DECLARAÇÃO DE INTEGRIDADE

Declaro ter atuado com integridade na elaboração da presente tese. Confirmo que em todo o trabalho conducente à sua elaboração não recorri à prática de plágio ou a qualquer forma de falsificação de resultados.

Mais declaro que tomei conhecimento integral do Código de Conduta Ética da Universidade do Minho.

Universidade do Minho, 27 de Outubro de 2016

Nome completo: Eunice Paula Freitas Cunha

Assinatura: Eunice Cunha

Acknowledgements

I would like to express my gratitude to everyone that directly or indirectly contributed for the achievement of this thesis.

Firstly, I would like to express my sincere gratitude to my supervisors Dr. Maria da Conceição Paiva and Prof. Maria Fernanda Proença for the continuous support to my PhD study and related research, for their patience, motivation and immense knowledge. Their guidance helped me along the time of research and writing of this thesis. I could not have imagined having better supervisors and mentors for my PhD study.

I also would like to thank Prof. José António Covas, Dr. Loic Hilliou and Dr. Paulo Lopes for their insightful comments and the scientific discussions which motivated me to widen my research from various perspectives.

I would like to express my gratitude to everyone that somehow contributed to my work and pleasant stay in Manchester. I am very grateful to Prof. Robert Young, from The University of Manchester, for accepting me in his group and for all guidance and warm hospitality. Thanks to Cristina Vallés and Zheling Li, for their friendship, valuable advices and availability for helping me. To all my friends that I met in Manchester, Monica Alberto and Rafael Vera many thanks.

I acknowledge Fundação para a Ciência e Tecnologia (FCT) for their financial support through a PhD grant (SFRH/BD/87214/2012).

To my friends that somehow helped me during this long journey. I would like to thank Raquel Santos, Sacha Mould, Paulo Pereira, Daniel Ribeiro, Ana Lima and Igor Lopes for their friendship, stimulating discussions and valuable advices.

Thanks also to academic staff, technicians and researchers of the Department of Polymer Engineering, especially to Mauricio Malheiro.

To all persons and entities that contributed to the work, but are not directly mentioned here, my sincere appreciation.

Finally, I would like to express my eternal gratitude to my family, my mother, my father and my sisters, Daniela and Susana, for their constant love, patience and unconditional support. Without their encouragement, this thesis would not be possible.

Publications

International Journal Publications

D. Moura, S. Caride, M. Sousa, **E. Cunha**, H. Rocha, J. Mano, M. C. Paiva, N. Alves, "High performance free-standing membranes by layer-by-layer assembly of graphene flakes and ribbons with natural polymers" – Accepted for publication in Journal of Materials Chemistry C;

R. Gusmão, **E. Cunha**, M. C. Paiva, D. Geraldo, M. F. Proença, F. Bento, "The role of carbonaceous fragments on the functionalization and electrochemistry of carbon materials" ChemElectroChem, 2016, DOI: 10.1002/celc.201600399;

R.M. Santos, C. Vilaverde**, E. Cunha**, M. C. Paiva, J. A. Covas, "Probing dispersion and re-agglomeration phenomena upon melt-mixing of polymer-functionalized graphite nanoplates", Soft Matter, 12 (2016) 77-86;

E. Cunha, M. C. Paiva, L. Hilliou, J. A. Covas, "Tracking the progression of dispersion of graphite Nanoplates in a polypropylene matrix by melt mixing", Polymer Composites, 2015, DOI: 10.1002/pc.23657;

J. A. Covas**, E. Cunha**, M. C. Paiva, L. Hilliou, "Dispersion of graphite nanoplates during melt mixing", Society of Plastics Engineering, 2015, DOI: 10.2417/spepro.006072, (by invitation from SPE);

E. Cunha, M. F. Proença, F. Costa, A. J. Fernandes, M. Ferro, P. E. Lopes, M. González-Debs, M. Melle-Franco, F. L. Deepak, M. C. Paiva, "Self-Assembled functionalized graphene nanoribbons from carbon nanotubes", Chemistry Open Communications, 4 (2015) 115-119;

E. Cunha, M.F. Proença, G. Pereira, M. J. Fernandes, R. Young, M. Melle-Franco, P. Lopes, M. C. Paiva, "Few-layer graphene in water" – in preparation;

E. Cunha, M. F. Proença, F. Duarte, M. C. Paiva, "Waterborne polyurethane/few-layer graphene nanocomposites" – in preparation;

E. Cunha, M. F. Proença, M. C. Paiva, "Graphene nanoribbons from carbon nanotubes: synthesis and applications" – in preparation.

International Conference Proceedings Books

Oral communications

M. C. Paiva, **E. Cunha**, M. Fernandes, F. Duarte, "Aqueous suspensions of graphite nanoplates and polyurethane for films and coatings", 32nd International Conference of the Polymer Processing Society, Lyon, France, 25-29 June, 2016

M. C. Paiva, **E. Cunha**, O. Voigt, M. Liebscher, F. Simon, J. Pionteck, P. Pötschke, "Melt mixing functionalized nanoplates into PC/SAN blends", 32nd International Conference of the Polymer Processing Society, Lyon, France, 25-29 June, 2016

M.C. Paiva, **E. Cunha**, D. Moura, C. Silva, M. F. Proença, N. Alves, "Multi-layered membranes based on graphene and natural polymers for biomedical applications", European Graphene Forum, Paris, France, 01-03 June, 2016

E. Cunha, M. C. Paiva, M. F. Proença, F. Duarte, "Non-covalent exfoliation of graphite in aqueous suspension for nanocomposite production with waterborne polyurethane", NanoPT2016, Braga, Portugal, 16-19 February, 2016;

E. Cunha, H. Rocha, M. C. Paiva, M. F. Proença, P. Lopes, M. Debs, M. Melle-Franco, F. Deepak, R. Young, L. Hornekaer, "Controlled functionalized graphene nanoribbons produced from carbon nanotubes", Graphene2015, Bilbao, Spain, 10-13 Mars, 2015;

E. Cunha, M. C. Paiva, M. F. Proença, R. Araújo, "Exfoliation of graphite using pyrene and perylene derivatives", NanoPT2015, Porto, Portugal, 11-13 February, 2015;

M. C. Paiva, **E. Cunha**, H. Rocha, M. F. Proença, N. M. Alves, J. F. Mano, M. Melle-Franco, F. L. Deepak, M. Debs, P. E. Lopes, "Graphene nanoribbons and nanoflakes from functionalized carbon precursors", Carbon, Jeju, Korea, 29 June – 4 July, 2014;

M. C. Paiva, R. Araújo, **E. Cunha**, J. Gonçalves, M. Melle-Franco, M. G. Pereira, M. F. Proença, "Simple strategies for stable aqueous suspensions of carbon nanotubes", COMPO2014 Nanocomposites & Biocomposites, Rehovot, Israel, 28 April – 1 May, 2014;

E. Cunha, H. Nunes, L. Hilliou, M. C. Paiva, A. J. Covas, "Dispersion of carbon nanotubes and exfoliated graphite nanoplates in polypropylene", 6th International Conference on Carbon NanoParticle based Composites, Dresden, Germany, 22-25 September 2013;

M. C. Paiva, **E. Cunha**, N.M. Alves, J. F. Mano, M. Melle-Franco, M. F. Proença, F. L. Deepak, J. Rivas, F. Rossier, H. Rocha, "Polymer composites with graphene nanoribbons formed by unzipping of carbon nanotubes", 6th International Conference on Carbon NanoParticle based Composites, Dresden, Germany, 22-25 September 2013;

E. Cunha, M. C. Paiva, M. F. Proença, M. Melle-Franco, F. Costa, A. J. Fernandes, V. Torres, L.M. Almeida, M. A. Ferro, "Graphene Nanoribbons from Carbon Nanotubes", ChemOnTubes, Arcachon, France, 1-5 April 2012;

E. Cunha; E. Oliveira; M. C. Paiva; F. Costa; A. J. Fernandes, "Production of graphene in solution by unzipping of carbon nanotubes", VI International Materials Symposium (XV meeting of SPM – Sociedade Portuguesa de Materiais) Guimarães, Portugal, 18-20 April 2011;

E. Cunha, A. G. Fortes "Preparation of Precursors for the synthesis of Aza-Sugars", Chemical Journeys, University of Minho, Braga, Portugal, 19th March, 2010.

Posters

E. Cunha, F. Duarte, M. F. Proença, M. C. Paiva, "Water few-layer graphene stable suspensions for composite thin films coatings", MRS Fall Meeting & Exhibit, Boston, Massachusetts, USA, 27 November – 2 December, 2016;

E. Cunha, M. F. Proença, R. Young, M. C. Paiva, "Production of Few layer graphene in aqueous suspensions for composite thin films", International Raman Fest: 4th Conference on Advanced Applied Raman Spectroscopy, Berlin, Germany, 19-20 May, 2016.

E. Cunha, F. Duarte, M. F. Proença, M. C. Paiva "Aqueous suspensions of few-layer graphene for composite thin films", Graphene2016, Genoa, Italy, 19-22 April, 2016;

E. Cunha, M. C. Paiva, M. F. Proença, F. Costa, A. J. Fernandes, M. Ferro, P. Lopes, M. Debs, M. Melle-Franco7, F. Deepak, "Production of pyrrolidine – functionalized graphene in solution", Proceedings of Graphene 2014, Toulouse, France, 6-9 May, 2014;

E. Cunha, M. C. Paiva, L. Hilliou, A. J. Covas, "Study of the dispersion of exfoliated graphite nanoplates in polymer melt" NanoPortugal International Conference, Porto, Portugal, 12-14 February 2014;

M. C. Paiva, **E. Cunha**, M. Melle-Franco, M. F. Proença, M. F. Florinda, A. J. Fernandes, "Graphene nanoribbons formed from carbon nanotubes in solution", Carbon, Rio de Janeiro, Brazil, 14-19 July, 2013;

M. C. Paiva, **E. Cunha**, M. F. Proença, R. F. Araújo, F. Costa, A. J. Fernandes, M. A. Ferro, "Formation of Graphene Nanoribbons in Solution", Graphene2012 Conference, Brussels, Belgium, 10-13 April, 2012;

E. Cunha, M. C. Paiva, F. Costa, A. J. Fernandes, Formation of Graphene Nanoribbons in Solution", IV Annual Meeting I3N, Quiaios, Portugal, 9-10 March 2012;

E. Cunha, M. C. Paiva, Carla I. Martins, F. Costa, A. J. Fernandes, Pedro Braquinha, "Formation of Graphene Nanoribbons from Chemically Modified Carbon Nanotubes", III Annual Meeting I3N, Fátima, Portugal, 11 – 12 February 2011;

M.J. Alves, A.Gil Fortes, **E. Cunha**, Vera C. M. Duarte "Stereoselective substitution on (5S,8S)-ethyl-8-tetraacetylglucopyranosyl-1,3-dioxo-2-phenil-2,3,5,8-tetrahydro-1H-[1,2,4]triazolo[1,2,α]pyridazine-5-carboxylate towards the synthesis of azafagomine derivates using C-, O- and S- nucleophiles", 8th International Meeting of the Portuguese Carbohydrate Group, University of Minho, Braga, Portugal, 6 – 10 September, 2009.

Abstract

Along the past decade graphene has emerged as an exciting material revealing potential applications in various fields. The translation of the graphene outstanding properties observed at lab-scale into real-world applications at industrial scale, however, greatly depends on the capacity to produce good quality graphene at large scale. The typical large scale graphene production processes present disadvantages such as high cost, or the formation of graphene with structural defects, or contaminants which are difficult to remove. Recently, interesting approaches to produce graphene were proposed, based on graphite exfoliation in water using amphiphilic molecules such as pyrene derivatives with a polar moiety. Another approach consists in the production of graphene nanoribbons (GNR) by unzipping of carbon nanotubes. These methods allow the production of graphene sheets (GS) and GNR with negligible structural damage, using low boiling point solvents that are easy to remove.

The present work investigated these two graphene production methods. The exfoliation of graphite into GS was achieved by interaction with two different water soluble pyrene derivatives, modified with a carboxylic acid moiety bonded to pyrene through semi-flexible side arms of different lengths. The suspensions produced were formed by approximately 80 % of bi-layer and few-layer graphene. The GNR were produced from pyrrolidine-functionalized carbon nanotubes, through application of ultrasounds in ethanol. Multiwall carbon nanotubes of different diameters, namely with approximately 10 and 110 nm, were covalently functionalized using a simple, solvent free method, and the unzipping was observed to occur in both cases. The unzipping process was assigned to the type of functional groups bonded to the nanotubes. The graphene products were extensively characterized, and tested for polymer composite applications.

Graphene has the potential to improve the mechanical, electrical, thermal and barrier properties of polymer-based nanocomposites. For that purpose graphene, or graphene derivative, has to be homogeneously distributed and dispersed into the polymer matrix, and establish good interfacial adhesion. Solution mixing is a good method to produce homogeneous graphene/polymer nanocomposites, particularly when using water as a solvent. This method is limited to water soluble polymers, however the development of waterborne polymer suspensions is an area of intense research. Waterborne polyurethane

(WPU) is a good example of an eco-friendly synthetic polymer widely used in the coating industry. In this work nanocomposite films were produced incorporating GS formed in aqueous suspension. The composite films presented a large decrease of permeability to water vapor, of the electrical resistivity, and an increase of the mechanical properties.

Melt mixing of reinforcing particles in thermoplastic polymers is probably the most environmentally and economically attractive technique, and a scalable method, for composite production. However, the dispersion of nanoparticles in high viscosity polymer melts is a complex process. Several studies reported in the literature used different mixing equipment (extruders, internal mixers, prototype mixers) to disperse carbon black, carbon nanofibers and carbon nanotubes, in polymer melts. They demonstrated that the nanoparticle dispersion varies with factors such as the intensity and type of hydrodynamic stresses, residence time, and interfacial adhesion. Few studies report the dispersion of graphite-derivatives in polymer melts. In the present work the dispersion in polypropylene of graphite nanoplates, with and without functionalization, was studied using a small-scale prototype mixer designed to generate high extensional flow. The dispersion of the nanoparticles was analyzed along the mixer length, demonstrating the initial agglomerated form of the graphite nanoplates and their dispersion into the original nanoplate size along the melt processing.

Resumo

O grafeno tem sido apresentado como um nano material muito interessante com potenciais aplicações em várias áreas. Contudo, a extrapolação das suas excelentes propriedades, que são observadas à escala laboratorial, para uma escala industrial depende amplamente da capacidade de produção de grafeno em grandes quantidades e com boa qualidade. Os processos que normalmente são utilizados para produção de grafeno em grande quantidade apresentam algumas desvantagens, tais como, elevado custo de produção, a obtenção de grafeno com defeitos estruturais ou com contaminações cuja remoção é difícil. Recentemente foram reportadas abordagens interessantes para a produção de grafeno baseadas na exfoliação da grafite em meio aquoso utilizando moléculas anfifílicas, tais como derivados de pireno com grupos funcionais polares. Outra abordagem consiste na produção de nanofitas de grafeno através da abertura longitudinal de nanotubos de carbono. Estes métodos permitem a produção de folhas de grafeno e nanofitas de grafeno com poucos defeitos estruturais, utilizando solventes com pontos de ebulição baixos que são fáceis de remover.

Neste trabalho foram estudadas estas duas abordagens para a produção de grafeno. A exfoliação da grafite para a formação de folhas de grafeno foi obtida através da interação com dois derivados de pireno solúveis em água, modificados com um grupo funcional ácido carboxílico ligado à molécula de pireno formando cadeias semi-flexíveis com comprimentos diferentes. As suspensões produzidas apresentaram cerca de 80% de grafeno bicamada e grafeno com poucas camadas. As nanofitas de grafeno foram produzidas a partir de nanotubos de carbono funcionalizados com um grupo pirrolidina, através da aplicação de ultrassons em etanol. Os nanotubos de carbono multicamada com diferentes diâmetros, nomeadamente, 10 e 110 nm, foram funcionalizados covalentemente através de uma metodologia simples, sem a utilização de solventes, e a abertura longitudinal dos nanotubos de carbono funcionalizados ocorreu em ambos os casos. O processo de abertura dos nanotubos de carbono funcionalizados foi desencadeado devido ao tipo de grupo funcionais ligados à superfície dos nanotubos. As nanofitas de grafeno bem como o grafeno obtido a partir da exfoliação da grafite foram caracterizados extensivamente e testados para aplicações em compósitos poliméricos.

O grafeno tem potencial para melhorar as propriedades mecânicas, elétricas bem como propriedades de barreira em nanocompósitos poliméricos. Para tal, o grafeno ou

derivados de grafeno têm que estar distribuídos e dispersos homogeneamente na matriz polimérica, e estabelecer uma boa adesão na interface com a matriz.

A mistura em solução é uma boa técnica para a produção de nanocompósitos poliméricos com grafeno de uma forma homogénea, especialmente quando o solvente utilizado é a água. Este método é limitado à utilização de polímeros solúveis em água, contudo o desenvolvimento de polímeros que formam suspensões estáveis em água tem vindo a ser extensamente estudado. O poliuretano de base aquosa representa um bom exemplo de um polímero sintético e ecológico que é amplamente usado da industria dos revestimentos. Neste trabalho foram produzidos filmes nanocompósitos com a incorporação de folhas de grafeno produzidas em suspensão aquosa. Os filmes nanocompósitos apresentaram uma diminuição significativa na permeabilidade ao vapor de água, da resistividade elétrica bem como um melhoramento das propriedades mecânicas.

A mistura de partículas de reforço em polímeros termoplásticos fundidos é provavelmente a técnica mais atrativa do ponto de vista económico e ecológico, e um método que pode ser utilizado para a produção de compósitos poliméricos em escala industrial. Todavia, a dispersão de nanopartículas em polímeros com viscosidade elevada é um processo complexo.

Alguns estudos reportados na literatura usaram diferentes equipamentos de mistura (como por exemplo, extrusoras e misturadores protótipos) para dispersar nanopartículas de carbono, tais como, negro de fumo, nanofibras de carbono e nanotubos de carbono, em polímero fundido. Os estudos demonstraram que a dispersão das nanopartículas varia com fatores como a intensidade e o tipo de tensões hidrodinâmicas, o tempo de residência, e a adesão na interface entre o reforço e a matriz. Poucos estudos reportam a dispersão de derivados de grafite em polímero fundido. Neste trabalho foi estudada a dispersão em polipropileno fundido de nanoplaquetas de grafite, com e sem funcionalização, utilizando um misturador protótipo, que permite o estudo em pequenas quantidades de material, e que foi desenhado para gerar fluxos extensionais elevados. A dispersão das nanopartículas foi analisada ao longo do misturador, demonstrado que os aglomerados de nanoplaquetas de grafite formados evoluíram até às dimensões inicias destas ao longo do processamento em polímero fundido.

Table of contents

Figure index

Table index

Abbreviations

^{13}C NMR	Carbon nuclear magnetic resonance
^{1}H NMR	Proton nuclear magnetic resonance
2D	Two dimensional
A_{av}	Average agglomerate area
Ac_2O	Acetic anhydride
ACN or CH_3CN	Acetonitrile
AEMEA	2-aminoethylmathacrylate hydrochloride
AFM	Atomic force microscopy
AIBN	Azobisisobutyronitrile
ALG	Alginate
APTES	3-aminopropyl triethoxysilane
A_R	Area ratio
BAEMA	2-(tertbutylamino)ethyl methacrylate
C_5F_5N	Pentafluoropyridine
C_6F_5CN	Pentafluorobenzonitrile
C_6F_6	Hexafluorbenzene
C_7F_8	Octafluoro-toluene
CB	Carbon black
CF4	Tetrafluoromethane
CH_3CH_2OH or EtOH	Ethanol
CHI	Chitosan
$ClSO_3H$	Chlorosulfonic acid
CNF	Carbon nanofibers
CNT	Carbon nanotubes
COOH	Carboxylic acid group
$Cu(NO_3)_2.3H_2O$	Copper (II) nitrate trihydrate
$CuSO_4$	Copper (II) sulphate anhydrous
CVD	Chemical vapor deposition
DC	Direct current
DCA	1,3-dipolar cycloaddition
DCC	N,N'-Dicyclohexylcarbodiimide
DCE	1,2 dichloroethane
DCM	Dichloromethane
DEA	Diethanolamine

DMAP	4-Dimethylaminopyridine
DMAPMA	*N*-[3-(dimethylamino)propyl] methacrylamide
DMF -	N,N-Dimethylformamide
DMPA	3,3′-iminobis (*N*,*N*-dimethylpropylamine)
DMSO-d_6	Deuterated dimethyl sulfoxide
DNA	Deoxyribonucleic acid
DP	Pressure drop
EDA -	Ethylenediamine
EDC	1-Ethyl-3-(3-dimethylaminopropyl) carbodiimide
EDS	Energy-dispersive X-ray spectrometry
EG	Expanded graphite
EMI -	Electromagnectic interference
EMIM BF_4	1-ethyl-3-methyl imidazolium tetrafluoroborate
EtOAc	Ethyl acetate
f-CNT	Functionalized carbon nanotubes
FFT	Fast Fourier transform
F-GnP	Functionalized graphite nanoplates
f-GNR	Functionalized graphene nanoribbons
FLG	Few layer graphene
FS	Free standing
FTIR	Fourier transform infrared
FWHM	Full width at a half maximum
GnP	Graphite nanoplates
GNR	Graphene nanoribbons
GO	Graphene oxide
GS	Graphene sheets
H_{12}MDI	Dicyclohexylmethane diisocyanate
H_2O_2	Hydrogen peroxide
H_2SO_4	Sulphuric acid
H_3PO_4	Phosphoric acid
HA	Hyaluronan polymer
HCl	Hydrochloric acid
HDI	Hexamethylene diisocyanate
HDPE	High-density polyethylene
HI	Hydroionic acid
HNO_3	Nitric acid

HOPG	Highly oriented pyrolytic graphite
HRTEM	High resolution transmission electron microscopy
HSQC	Heteronuclear single quantum correlation
IPDI	Isophorone diisocyanate
K_2SO_4	Potassium sulphate
$KMnO_4$	Potassium permanganate
KNO_3	Potassium nitrate
KOH	Potassium hydroxide
LAH	Lithium aluminium hydride
LbL	Layer-by-Layer
LPE	Liquid phase exfoliation
MAEMA	2-(dimethylamino) ethyl methacrylate
MEA	Monothanolamine
MFI	Melt flow index
$MgSO_4$	Magnesium sulphate
MoS_2	Molybdenum disulphide
MPTMS	(3-mercaptopropyl)trimethoxysilane
MWNT	Multiwalled carbon nanotubes
N_2H_4	Hydrazine
N_A	Number of agglomerates
$NaBH_4$	Sodium borohydride
$NaNO_3$	Sodium nitrate
NaOCl	Sodium hypochlorite
NaOH	Sodium hydroxide
N-doped	Nitrogen doped
NH_3	Ammonia
NHS	N-Hydroxysuccinimide
NMP	N-Methyl-2-pyrrolidone
o-CNT	Oxidized carbon nanotubes
o-DCB	*ortho*-dichlorobenzene
o-GNR	Oxidized graphene nanoribbons
OH	Hydroxyl group
$P(H_2O)$	Moisture permeability
PA	Polyamide
PAA	Poly(acrylic acid)
PAHs	Polycyclic aromatic hydrocarbons

PDMAEA	Poly(2-N,N’-(dimethyl amino ethyl acrylate)
PDMS	Polydimethylsiloxane
PEG	Polyethylene glycol
PI	Polyimide
PLA	Polylactic acid
PMMA	Poly(methyl methacrylate
PmPV	- poly(m-phenylenevinylene-co-2,5-dioctoxy-p-phenylenevinylene)
polyPA-*b*-polyPEG-A	Poly(pyrenemethyl acrylate)-*b*-poly[(polyethylene glycol) acrylate]
PP	Polypropylene
PU	Polyurethane
PVA	Polyvinyl alcohol
PVDF	Polyvinylidene fluoride
Py	Pyrene
$Py(OH)_2$ $(SO_3)_2$	6,8-Dihydroxy- 1,3-pyrenedisulfonic acid disodium salt
$Py(SO_3)_4$	1,3,6,8-pyrenetetrasulfonic acid tetrasodium salt
PyBA	1-pyrenebutyric acid
PyBOH	1-pyrenebutanol
PyCA	1-pyrenecarboxylic acid
$PyMeNH_2$	Aminomethylpyrene
$PyNH_2$	1-Aminopyrene
$PyOH(SO_3)_3$	8-Hydroxy-1,3,6-pyrenetrisulfonic acid trisodium salt
PySAH	1-pyrenesulfonic acid hydrate
$PySO_3$	1-pyrenesulfonic acid sodium salt
QCM-D	Quartz crystal microbalance with dissipation monitoring
r-GNR –	Reduced graphene nanoribbons
r-GO	Reduced graphene oxide
rpm	Rotations per minute
SDS	Sodium dodecyl sulphate
SEM	Scanning electron microscopy
SF_6	Sulphur hexafluoride
SiC	Silicon carbide
SiO_2	Silicon dioxide
SLG	Single layer graphene
STEM	Scanning transmission electron microscopy

STM	Scanning tunneling microscope
SWNT	Single walled nanotubes
TEA	Triethylamine
TEM	Transmission electron microscopy
TFA	Trifluoracetic acid
TGA	Thermogravimetric analysis
TLC	Thin-layer chromatography
UHV	Ultra-high vacuum
UV	Ultraviolet
VOCs	Volatile organic solvents
WPU	Waterborne polyurethane
WVT	Water vapor transmission
XPS	X-ray photoelectron spectroscopy
XRD	X-ray diffraction
Zn	Zinc

Symbols

$\dot{\gamma}$	Shear rate
wt.%	Weight percentage
ΔD	Dissipation
Δf	Resonant frequency
ζ	Zeta potential
η -	Viscosity
π	pi
ρ	Density
ω	Phonon
σ	Shear stress

CHAPTER 1. INTRODUCTION

1. INTRODUCTION

This chapter presents the motivation for this PhD thesis and the outline of the work performed in its aim.

1.1. Motivation

Since the isolation of graphene by mechanical exfoliation of graphite in 2004 [1] this material has been the focus of extensive research among the scientific community. The excellent electronic, mechanical, thermal and optical properties of graphene [2] have huge potential applications in various fields such as electronics [3-5], energy storage [6-8], photonics [9, 10], composite materials [11-13], conductive and barrier protection inks and paints [14-17] and sensor technology. [18-20] However, the production of graphene in large scale, with controlled quality and reasonable cost, is still a goal to achieve, and thus continues to be an important research topic.

The large scale graphene production processes are typically based on the conversion of silicon carbide (SiC) to graphene via sublimation of silicon at high temperature, [21, 22] chemical vapor deposition (CVD) growth, [23] oxidation of graphite followed by exfoliation and reduction of the oxidation products [12, 24] and exfoliation of graphite in organic solvents with high surface tension. [25] These methods allow large scale production, however they present disadvantages such as the high cost and the production of graphene with structural defects or contaminants which are difficult to remove.

Recent approaches to produce graphene were proposed, based on graphite exfoliation in water using amphiphilic molecules such as pyrene derivatives with a polar moiety. [26-29] Another approach consists in the production of graphene nanoribbons (GNR) by unzipping of carbon nanotubes. [30-32] These methods allow the production of graphene sheets (GS) and GNR with negligible structural damage, using low boiling point solvents that are easy to remove. The production of GNR is an interesting topic since GNR may present a band gap if the width and the edge configuration of the GNR can be controlled. [33, 34]

Graphene has great potential as a reinforcing phase of polymer-based nanocomposites, having similar mechanical properties to CNT, but superior thermal and electrical properties and larger surface area (**table 1**). [35, 36] However, the production of such polymer nanocomposites requires not only that graphene be produced at a large scale, but

also that it may be incorporated and homogeneously dispersed into polymer matrices, and develop good interfacial adhesion. [11] The method of solution mixing has been used as preparation method for graphene/polymer nanocomposites. [35] This method consists in the direct mixture of graphene suspensions into polymer solutions. The drawback of this technique is the solubilization of the polymer that, in some cases, involves the use of hazardous solvents such as dimethylformamide (DMF), chloroform, dichloromethane (DCM), or toluene. However, the use of "green" solvents such water could override this problem. For that reason, a large effort has been set over the years to develop stable aqueous polymer suspensions, as well as stable suspensions of graphene derivatives in water. Water borne polyurethane (WPU) is a synthetic polymer widely used in the coating industry and has been presented as an eco-friendly alternative since only water is involved during the drying stage. [37]

Melt mixing is an environmentally and economically attractive technique and scalable method for dispersing graphene into polymers. In addition, this process avoids the use of hazardous solvents. [35] However, it does not easily lead to optimal nanoparticle dispersion. [38, 39] Various studies carried out using a variety of mixing equipment (extruders, internal mixers, prototype mixers) for carbon black [40], carbon nanofibers [41], and carbon nanotubes [42, 43], have demonstrated that the intensity and type of hydrodynamic stresses (i.e., shear versus extensional), residence time, and interfacial adhesion play a major part in dispersion. [41, 42, 44] While the dispersion mechanism of carbon nanotubes in polymers is well studied, few studies report the dispersion of graphite-derivatives in polymer melts.

1.2. Thesis outline

This thesis is organized in seven chapters.

Chapter 1 presents the motivation of this work as well as the thesis outline.

Chapter 2 presents an overview of the state of art of the preparation strategies used for the production of graphene, emphasizing the production of graphene in liquid exfoliation and the unzipping of carbon nanotubes. The application of graphene in polymer composites will be also reviewed, namely the incorporation of graphene in polypropylene by melt mixing as well as in waterborne polyurethane by solution mixing.

Chapter 3 addresses the detailed investigation of the unzipping of carbon nanotubes to obtain functionalized (non-oxidized) graphene nanoribbons using a new approach. The

possible application of functionalized graphene nanoribbons, as well graphene nanoribbons produced by oxidation of carbon nanotubes, in the production of nanostructured films using layer-by-layer assembly with natural polymers was studied.

Chapter 4 describes the production of few layer graphene in water using a non-covalent approach. The amphiphilic molecules used for this purpose were synthesized, to produce functionalized pyrene that was used to exfoliate and stabilize few layer graphene in aqueous media.

Chapter 5 comprises the application of the few layer graphene in water suspension on the production of waterborne polyurethane nanocomposite films. The mechanical, electrical as well as the barrier properties were studied.

Chapter 6 describes the dispersion of graphite nanoplates in polypropylene matrix by melt mixing, and presents the study of the dispersion of graphite nanoplates and functionalized graphite nanoplates in the polymer melt, performed on a small-scale prototype mixer. The rheological characterization of the nanocomposites is also presented.

Finally, **Chapter 7** presents the general conclusions regarding the production of graphene and its applications in polymer nanocomposites, and presents considerations for further work.

CHAPTER 2. STATE OF ART

2. STATE OF ART

This chapter presents the state of art of graphene production with emphasis on the unzipping of covalently functionalized carbon nanotubes and exfoliation of graphite through non-covalent interactions with pyrene derivatives. The more relevant characterization techniques will be reviewed. Some potential applications of graphene will also be presented. This chapter will include a final section concerning the production of graphene/polymer nanocomposites

2.1. Graphene Properties

The interest in graphene has been growing exponentially along the past few years due its excellent properties and wide range of possible applications in various scientific fields**.** Graphene is defined as a planar sheet of sp^2 - hybridized carbon atoms in a two - dimensional (2D) honeycomb hexagonal lattice. This material presents a unique band structure in which the conduction band and the valence band just touch each other, forming a zero-band gap material. [33] This characteristic leads to some extraordinary properties such as ultra-high carrier mobility, [2, 45, 46] high thermal conductivity [47, 48] extremely high modulus and tensile strength, [49] and high transparency to incident light over a broad wave length range (97.7% of transmittance). [50] Graphene also exhibits a high surface area which is much greater than that of graphite and even that of carbon nanotubes [51-53]. **Table 1** presents a comparison of some properties of carbon nanotubes and graphene.

Table 1: Comparison of some properties between carbon nanotubes and graphene

	Graphene	**Carbon nanotubes**
Carrier mobility ($cm^2V^{-1}s^{-1}$)	200000 [46]	100000 [54]
Thermal conductivity ($Wm^{-1}K^{-1}$)	3000 - 5000 [48]	3500 [55]
Young's modulus (TPa)	~1 [49]	~1 [55]
Surface area (m^2g^{-1})	2630 [52]	1315 [51]

2.2. Graphene Production

Besides the excellent properties of graphene, its application depends on the ability for the production of this material in large scale, with controlled quality and reasonable cost. Interesting approaches have been reported to produce graphene based on graphite exfoliation as well as on unzipping of carbon nanotubes.

2.2.1. Graphene from graphite exfoliation

The formation of graphene trough exfoliation of graphite has been highly reported along the years. Different methodologies have been applied based in the mechanical exfoliation of graphite, such as the micromechanical exfoliation [1, 56] of highly oriented pyrolytic graphite (HOPG) using scotch tape, and ball milling. During the ball milling process, the moving balls apply their kinetic energy to the graphite, breaking the strong van der Waals interactions between the graphene layers of graphite promoting its exfoliation. [57] **Figure 1** presents a schematic representation of this process. The process can trigger the formation of defects in graphene, since it is necessary the use of active precursors such as melamine, [58] triazine derivatives, [59] ammonia borane [60] and potassium hydroxide (KOH) [61]. Dry ice has also been used to exfoliate graphite through ball milling process. [57, 62]

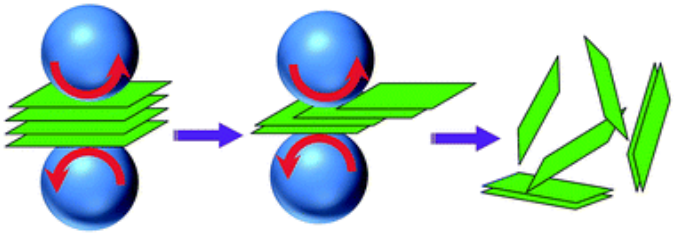

Figure 1: Schematic representation of the ball milling process. [63]

2.2.1.1. Liquid phase exfoliation of graphite

Liquid phase exfoliation (LPE) of graphite is a viable cost effective process which can be easily up-scaled to mass production of graphene. [27] LPE of graphite can be achieved by using polar organic solvents whose interaction energy with graphene is comparable to the van der Waals interactions between of graphene layers. Solvents with a surface tension of about 40 mJ m^{-2}, such *N*-Methyl-2-pyrrolidone (NMP), N,N-Dimethylformamide (DMF) and *ortho*-dichlorobenzene (*o*-DCB) are reported to be ideal for the exfoliation of graphite. [25] Other organic solvents were reported to successfully

exfoliate graphite, namely, some fluorinated solvents [64, 65] such hexafluorbenzene (C_6F_6), octafluoro-toluene (C_7F_8), pentafluorobenzonitrile (C_6F_5CN) and pentafluoropyridine (C_5F_5N) as well as some amine-based solvents, [66] like 3,3′-iminobis (*N*,*N*-dimethylpropylamine) (DMPA), *N*-[3-(dimethylamino)propyl] methacrylamide (DMAPMA), 2-(tertbutylamino)ethyl methacrylate (BAEMA) and 2-(dimethylamino) ethyl methacrylate (MAEMA). The structures of these solvents are presented in the **figure 2.**

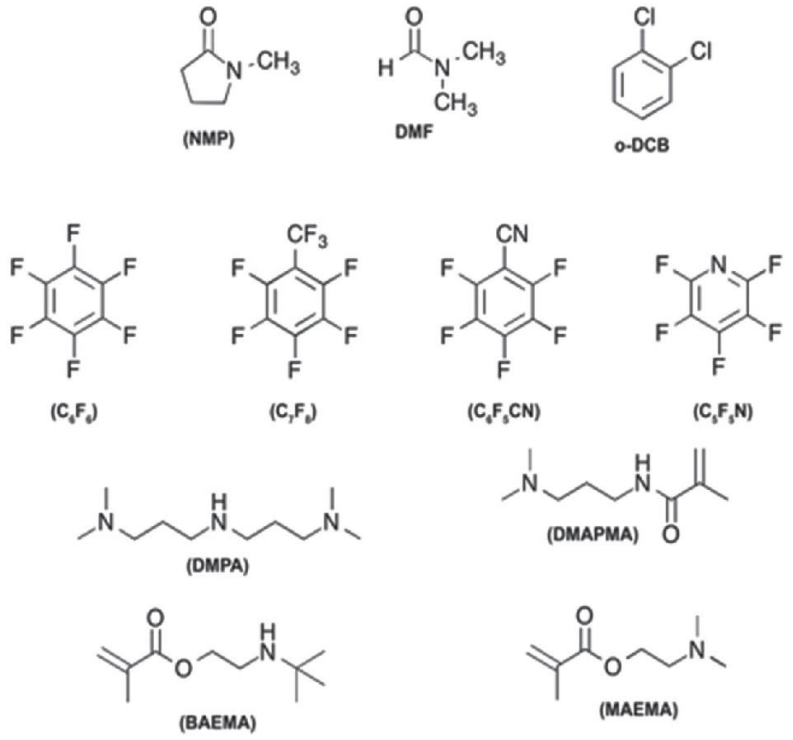

Figure 2: Chemical structure of the organic solvents used in liquid phase exfoliation [67]

The use of large volumes of such organic solvents has negative environmental consequences. Alternative approaches to produce graphene by graphite exfoliation using "green" solvents such as water have been investigated. The covalent functionalization of graphite with functional groups which are soluble in water, namely the oxidation of graphite, has been extensively studied for the production of graphene in aqueous media. [35] Strategies based on the methods developed by Brodie, [68] Staudenmaier, [69] Hummers [70] and modified Hummers methods [71-73] have been widely used to oxidize graphite. These methods require the use of concentrated oxidizing acids and strong oxidants which induces the formation of highly oxidized product. The covalent bonding of oxygen containing functional groups to the graphite surface is essential for the graphene oxide (GO) production and its subsequent dispersion in water. [71, 74, 75] The

downside of this process is that the extensive chemical oxidation disrupts the sp^2 carbon network of the graphite which leads to structural defective graphene oxide sheets with poor electrical conductivity. [35] **Figure 3** shows the structure of the graphene oxide based on solid state ^{13}C NMR (carbon nuclear magnetic resonance) spectroscopy studies. [76, 77]

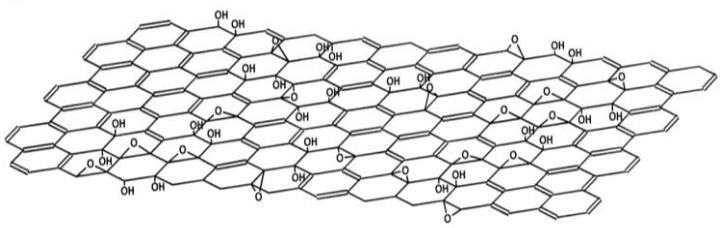

Figure 3: Chemical structure of graphene oxide. [77]

This problem may be partially solved by the reduction of the GO (r-GO) which means the decrease of the oxidation state of the oxygen-containing groups, in order to restore the electrical and thermal conductivity of graphene. However, these processes require the use of toxic and hazardous chemicals or the use of high temperature (up to 1000ºC) and leads to the formation of nanometer size holes on the basal plane. These holes decrease the integrity of the material, thereby significantly altering their physical properties namely the electrical properties. Furthermore, the reduction of GO sheets leads to the loss of their solubility in water and consequently leads to their aggregation and precipitation of the graphene aggregates. [35, 78] Nevertheless, in some applications the use of GO and r-GO can be beneficial as they feature great chemical complexity which allows its use in various scientific areas, such as, catalysis, [79, 80] energy storage [81] and biomedical applications. [82]

The functionalization of graphene with molecules interacting at the non-covalent level has recently gathered a great interest. [67] Polycyclic aromatic hydrocarbons (PAHs) substituted with various side groups have been widely studied for the exfoliation of graphite through non-covalent interactions. Among all PAHs, pyrene derivatives are the most studied compounds. The aromatic structure of the pyrene molecule allows its intercalation and physisorption on the hydrophobic surface of graphene through π-π interactions, while appropriate functional groups attached to the pyrene molecules allows the stabilization of graphene in water. [27, 67, 83]

Compounds such pyrenebutyric acid [84] and pyrene-sulfonic acid salt [85], have been studied for the stabilization of graphene in water. Concentrations of about 10^{-3} mol dm^{-3} of the pyrene derivatives were able to stabilize the graphene in water, although in these studies reduced graphene oxide (r-GO) was initially prepared from graphene oxide (GO) and then stabilized in aqueous media. Liu *et. al*. reported the stabilization of previous produced r-GO [86] in aqueous media using a pyrene-terminated poly(2-N,N'-(dimethyl amino ethyl acrylate) (PDMAEA) which is positively charged, and poly(acrylic acid) (PAA) that has negative charge. [87] The self-assembly of the opposite charged graphene solutions led to the formation of a graphene/polymer composite that showed to be sensitive to pH. **Figure 4** shows a schematic representation of the synthesis of this self-assembled graphene/polymer nanocomposite.

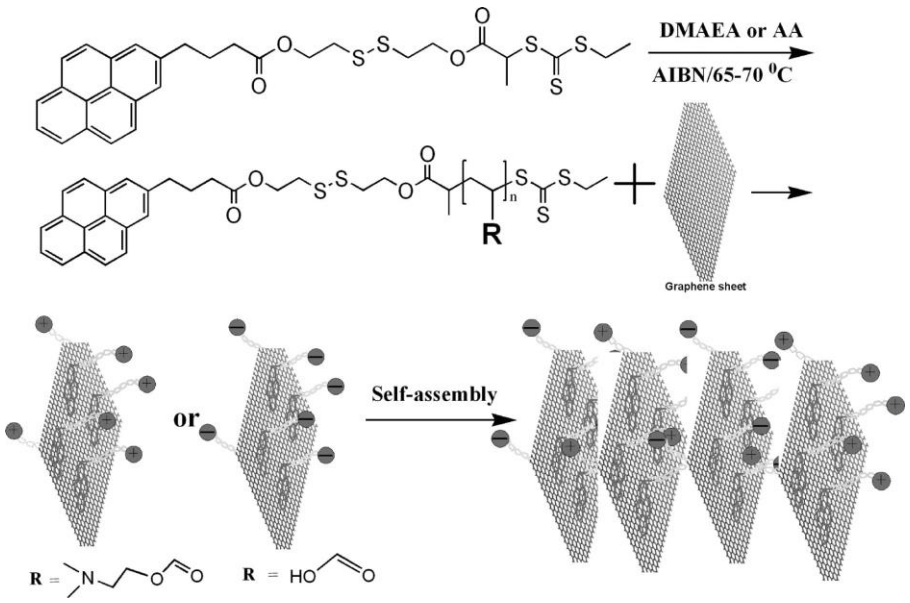

Figure 4: Synthesis of pH sensitive pyrene-polymer composites via π-π stacking interactions for the self-assembly of functionalized graphene into layered structures. [87]

Other approaches based on direct exfoliation of graphite in water have been studied. A pyrene-functionalized amphiphilic block copolymer, poly(pyrenemethyl acrylate)-*b*-poly[(polyethylene glycol) acrylate] (polyPA-*b*-polyPEG-A) produced by Liu *et al.* [88] was used to exfoliate graphite. **Figure 5** present a schematic representation of this exfoliation process. After 6 hours of sonication of 400 mg of the polymer and 10 mg of graphite in 20 mL of water, the yield of exfoliation was 78 %.

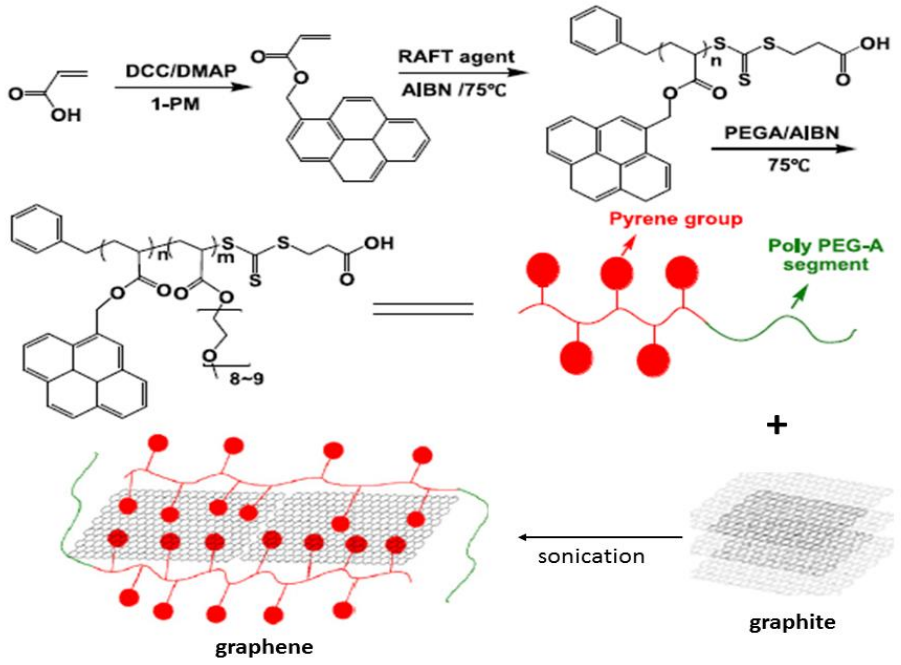

Figure 5: Direct exfoliation of graphite to form graphene using amphiphilic block copolymers with multi-pyrene pendent groups. [88]

Zheng and co-workers [89] reported the exfoliation of graphite into graphene in aqueous media using supercritical carbon dioxide (CO_2) as expanding agent and a pyrene-terminated polyethylene glycol (pyrene-PEG), as stabilizing agent. The process of exfoliation occurred in three steps (**figure 6**). In **step 1** the graphite powder and the polymer were mixed in water. The pyrene-PEG was able to interact with the exposed graphite surface through π-π interactions. However, the limited dangling polymer chains were not sufficient to dislodge the graphene sheets due the strong van der Waals interactions and so, the graphene polymer dispersion was subjected to supercritical CO_2 (**step 2**) which promoted the expansion of the non-covalent functionalized graphite. The out-of-plane dangling chains of the inserted pyrene-PEG increased the distance between adjacent graphene layers and prevented them from re-agglomeration (**step 3**). The yield of graphite exfoliation was 5.1 %.

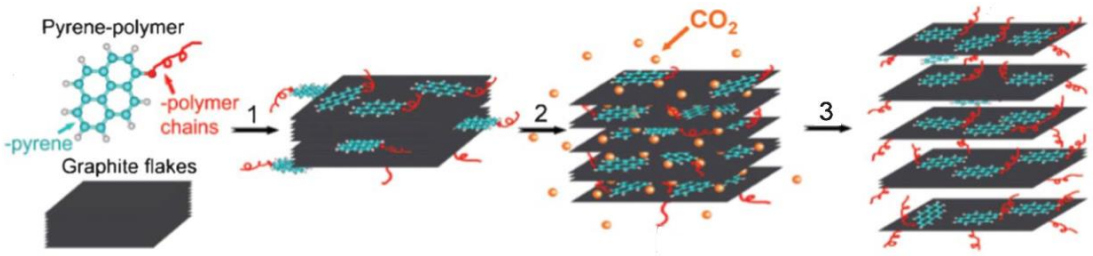

Figure 6: Schematic illustration of the process of pyrene-PEG functionalized graphene sheets using supercritical CO_2. [89]

Also some biocompatible polymers have been functionalized with pyrene moieties to prepare aqueous graphene suspensions for potential use in biomedical applications. [90-92] Zhang *et al.* [90] reported the incorporation of pyrene moieties into hyaluronan natural polymer (py-HA) (**figure 7**) and its use in the exfoliation of graphite in water. The exfoliated py-HA- graphene sheets showed good stability in water and the concentration of graphene in the water suspension was 0.6 mg/mL, 30 % of the initial graphite concentration (2 mg/mL).

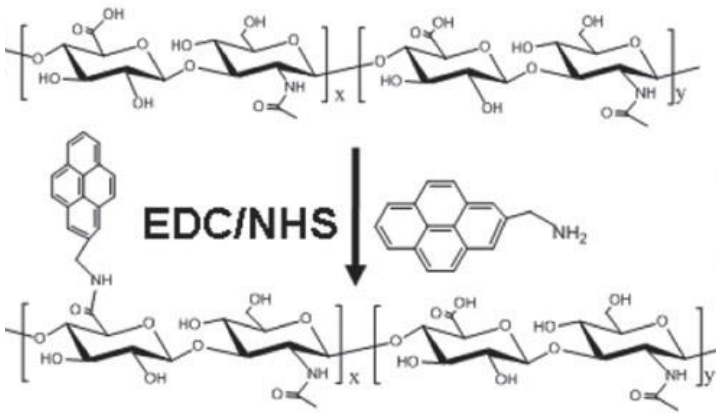

Figure 7: Pyrene-conjugated hyaluronan polymer synthesis [90]

Ihiawakrim *et al.* [91] described the exfoliation of graphite using a biocompatible amphiphilic pyrene based hexahistidine peptide (**figure 8**) which was able to exfoliate, functionalize and stabilize few layer graphene flakes in pure water. The yield of exfoliation of graphite varied from 20 to 60 %, depending of the sonication time and the type of graphite used (expanded graphite or natural graphite).

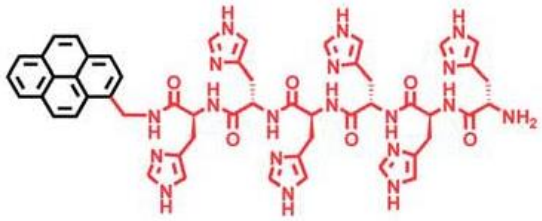

Figure 8: Structure of the amphiphilic pyrene based hexahistidine peptide [91]

Liu and co-workers [92] reported the production of single- and bi-layer graphene by a direct exfoliation from graphite flakes in the presence of pyrene labelled single stranded DNAs (py-ssDNAs) which were synthetized by reacting the 1-pyrenebutyric acid (PyBA) (**figure 9**) with an amino modified DNA. The Py-ssDNA not only enhanced the water solubility and dispersion of graphene but it was also used for specific DNA–DNA hybridization. Pyrene derivatives can be directly used to exfoliate graphite in water

without being functionalized with polymer chains. The process allows the formation of stable water suspensions of graphene and few-layer graphene whose applications in areas such polymer composites, sensors and energy storage have been reported. [93-95] He and co-workers [96] reported the exfoliation of graphite in aqueous dispersion using 1,3,6,8-pyrenetetrasulfonic acid tetrasodium salt ($Py(SO_3)_4$) (**see Figure 9**) and aminomethylpyrene ($PyMeNH_2$), and fabricated transparent conductive films. The concentration of the functionalized pyrenes was 0.4 mg/mL (about 10^{-4} mol dm^{-3}) and the yield of exfoliated graphite was about 50 %. Some remaining aggregates could be found in the final dispersions which would probably decrease the yield taking into account only the formation of single- and few layer graphene. Dong *et al*. [97] reported the use of $Py(SO_3)_4$ for the exfoliation of graphite in water. The concentration of the pyrene derivative in water was between 2 and 4 mg/mL (about 10^{-2} mol dm^{-3}) and the initial concentration of graphite in aqueous media, before the exfoliation process, was 0.2 mg/mL. However, the yield of the exfoliation process was not discussed. Kar and co-workers [94] studied the exfoliation of graphite into stable aqueous suspensions of single- and few- layer graphene using 1-pyrenecarboxylic acid (PyCA) (**figure 9**). The concentration of the pyrene derivative in water was 0.33 mg/mL (10^{-3} mol dm^{-3}) and the initial concentration of the graphite, before the exfoliation process, was 2 mg/mL. The reported yield of exfoliation was 1%. The authors also showed the potential application of this exfoliated graphene in sensitive and selective conductometric sensors as well as in ultracapacitors. A variety of pyrenes were employed by Green and co-workers [93] to test their performance in the exfoliation of graphite. Among all investigated pyrene derivatives, i.e., pyrene (Py), 1-pyrenecarboxylic acid (PyCA), PyBA, 1-pyrenesulfonic acid hydrate (PySAH), 1-Aminopyrene ($PyNH_2$), $PyMeNH_2$, 1-pyrenebutanol (PyBOH), 1-pyrenesulfonic acid sodium salt ($PySO_3$) and ($Py(SO_3)_4$) (**see figure 9**) the $PySO_3$ was found to be the most efficient, yielding graphene dispersion concentration of 1 mg/mL. To quantify the amount of single layer graphene (SLG) and few layer graphene (FLG) in the dispersions, the $PySO_3$ -stabilized graphene samples were characterized by high resolution transmission electron microscopy (HRTEM), which revealed the presence of 2–4 layer thick sheets. Besides the graphene concentration of 1 mg/mL seems to be high, the yield of the exfoliated material was 2%, since the initial concentration of graphite (before the exfoliation process) was 50 mg/mL. In addition, the concentration of the pyrene derivatives in water was 3 mg/mL (about 10^{-3} mol dm^{-3}). Casiraghi *et al.* [26]

reported the exfoliation of graphite in water using the pyrene derivative Py-SO_3. The authors described the production of stable water suspensions of graphene in which about 70 % was identified as few-layer graphene, using a statistical analysis based on Raman spectroscopy. The concentration of the Py-SO_3 in water was 1 mg/mL (10^{-2} mol dm^{-3}) and the yield of exfoliated graphene in water was 2.5 %.

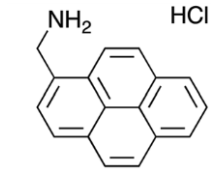

1-aminomethyl pyrene

(Py-$MeNH_2$)

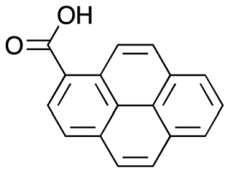

1-pyrenecarboxylic acid

(PyCA)

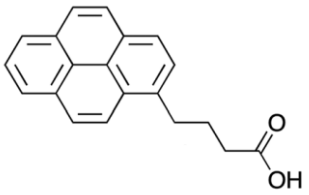

1-pyrenebutyric acid

(PyBA)

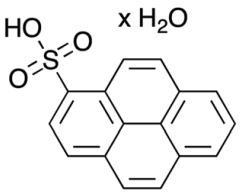

1-pyrenesulfonic acid hydrate

(Py-SAH)

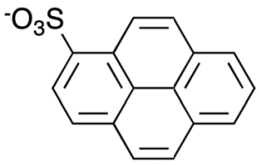

1-pyrenesulfonic acid sodium salt

(Py-SO_3)

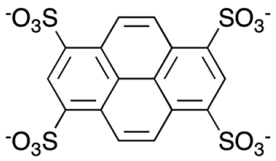

1,3,6,8-pyrenetetrasulfonic tetra acid tetra sodium salt

(Py-$(SO_3)_4$)

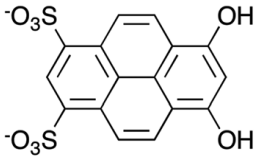

6,8-dihydroxy-1,3-pyrenesulfonic acid disodium salt

(Py-$(OH)_2(SO_3)_2$)

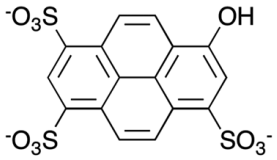

8-hydroxy-1,3,6-pyrenesulfonic acid trisodium salt

(Py-$OH(SO_3)_3$)

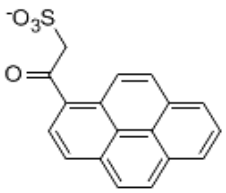

2-Oxo-2-(pyren-1-yl)ethanesufonate, Sodium salt

Figure 9: Molecular structure of pyrene derivatives used to exfoliate graphite

Viinikanoja and co-workers [98] studied water dispersed graphene prepared directly from natural graphite using some pyrene derivatives, namely, $PyMeNH_2$, and the synthetized 2-Oxo-2-(pyren-1-yl)ethanesufonate sodium salt and 1-Methyl-3-[2-oxo-2-(pyren-1-yl)ethyl)]-3H-imidazolium Bromide (according to a procedure described in [99]). The better yield of exfoliation (2.4 %) was obtained for the 2-Oxo-2-(pyren-1-yl)

ethanesulfonate sodium salt (**figure 9**). The concentration of the pyrene derivatives in water was 2 mg/mL (10^{-3} mol dm^{-3}) and the initial concentration of natural graphite in water was 1 mg/mL). Palermo and co-workers [28] investigated the thermodynamics of the exfoliation of graphite. In particular, the authors studied the mechanism of physisorption of various pyrenes on the graphene surface, and successive exfoliation in water. A detailed analysis was performed on pyrenes functionalized with sulfonic groups, in particular, $PySO_3$, 6,8-Dihydroxy- 1,3-pyrenedisulfonic acid disodium salt ($Py(OH)_2(SO_3)_2$), 8-Hydroxy-1,3,6-pyrenetrisulfonic acid trisodium salt ($PyOH(SO_3)_3$), and $Py(SO_3)_4$ were tested. Experimental results collaborated with molecular dynamics simulations, providing evidence for a correlation between molecule-graphene adsorption energy and the amount of dispersed graphene sheets. The results obtained imply that the performance of pyrene-assisted exfoliation is indirectly driven by the molecular dipoles, which are not important *per se*, but since they facilitate the adsorption of pyrenes on graphene sheets, they promote the lateral displacement of the solvent molecules intercalating between the graphene sheets and pyrene molecules.

2.2.2. Unzipping of carbon nanotubes

Graphene is a zero band gap material [2] and thus it is a metallic conductor. An area of graphene research that is showing interest is search for chemical or physical strategies to open an energy band gap in this material, and to change its behavior to semi-conductor. The graphene materials with an energy gap are expected to be formed by controlled oxidation of few layers of graphene, or by fabrication of graphene nanoribbons (GNR). Currently it is difficult to oxidize a few layers of graphene in a controlled way. [35] For GNR the band gap may be achieved by controlling their width and the edge configuration. [33, 34] Carbon nanotubes, which can be viewed as folded graphene sheets or nanoribbons, may be classified in two main types: multiwalled carbon nanotubes (MWNT) and single walled nanotubes (SWNT) **Figure 10** shows the structure of SWNT and MWNT. [100]

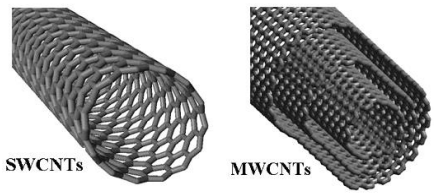

Figure 10: Structure of single walled nanotubes and multiwalled nanotubes [100]

MWNT are composed of a concentric arrangement of graphene cylinders, forming tubes containing from two to several layers and reaching diameters up to 100 nm. SWNT can be visualized by rolling a single graphene sheet into a cylinder. The orientation of the hexagonal lattice with respect to the tube axis defines its chiral vector (**figure 11**), which is denoted by the chiral indices (n, m). The classification of the nanotubes as armchair (n=m) or zigzag (m=0) has its origin from the geometric arrangement of the carbon atoms at the seam of the cylinders. While both these types of tubes possess mirror symmetry, nanotubes with $m \neq n$ are chiral. The latter kind of tubes exists as two enantiomers with right- and left-handed helicity. All armchair SWNT present metallic behavior while zigzag as well as chiral SWNT are semiconductors. [101, 102]

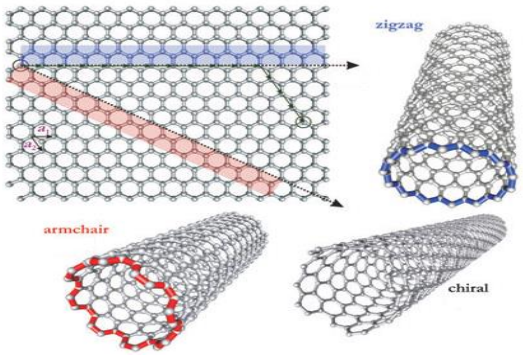

Figure 11: Schematic representation of armchair, zigzag and chiral CNT [101]

Since CNT can be viewed as folded graphene sheets or nanoribbons, it is thus natural to seek the reverse process which is the unzipping of carbon nanotubes to obtain GNR. Many efforts have been made to achieve the synthesis of graphene nanoribbons.

2.2.2.1. Oxidation processes

The oxidation of CNT in the presence of concentrated acids and strong oxidants is a methodology highly used to produce GNR. Tour and his group [103] have studied the unzipping of CNT using the oxidation process. The procedure involves the suspension of CNT in concentrated sulphuric acid (H_2SO_4) followed by treatment with 500 wt.% of potassium permanganate ($KMnO_4$), which is an oxidizing agent. The proposed mechanism for the unzipping comprises the oxidation of the carbon – carbon double bonds in the CNT induced by $KMnO_4$ (**figure 12**). The reduction of the oxygen containing groups was performed using hydrazine (N_2H_4), a reducing agent, as well as thermal treatment, under hydrogen (H_2) to restore the electrical conductivity of the GNR.

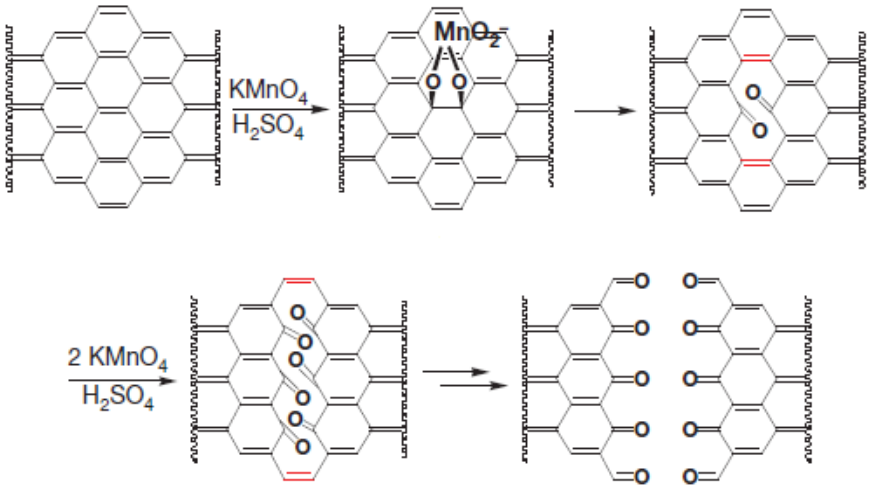

Figure 12: The Proposed chemical mechanism of CNT unzipping [103]

Later, the same group reported [104] that the addition of a weaker acid, such H_3PO_4 (phosphoric acid) or TFA (trifluoracetic acid) to the H_2SO_4 followed by treatment with $KMnO_4$ led to the formation of GNR with fewer defects and/or holes in the basal plane. The proposed mechanism for the effect of the weaker acid was based in the improvement of chemoselectivity by minimizing the oxidation process. After the initial manganite ester (**1 in figure 13**) the vicinal diols **2** that are formed could cleave at the carbon-carbon bond between them, giving the dione **3** and a new hole in the nanoribbon. Destructive oxidation throughout the structure then could occur and lead to the defects and irreversible changes in the basal planes that cannot be repaired with chemical reduction. However, when an acid such H_3PO_4 was present, it protects the vicinal diols by forming cyclic structure **4**, thus preventing or retarding over oxidation to the diones. Moreover, the authors also demonstrated that controlling the amount of $KMnO_4$ could lead to a partially unzipped CNT resulting in a mixture of GNT and GNR. The oxygen groups in GNR can easily react with other compounds, leading to the formation of new functional groups that may find novel applications. The reaction of oxidized GNR (o-GNR) with diazonium salts has been reported to improve the electrical properties of the GNR. [105, 106]

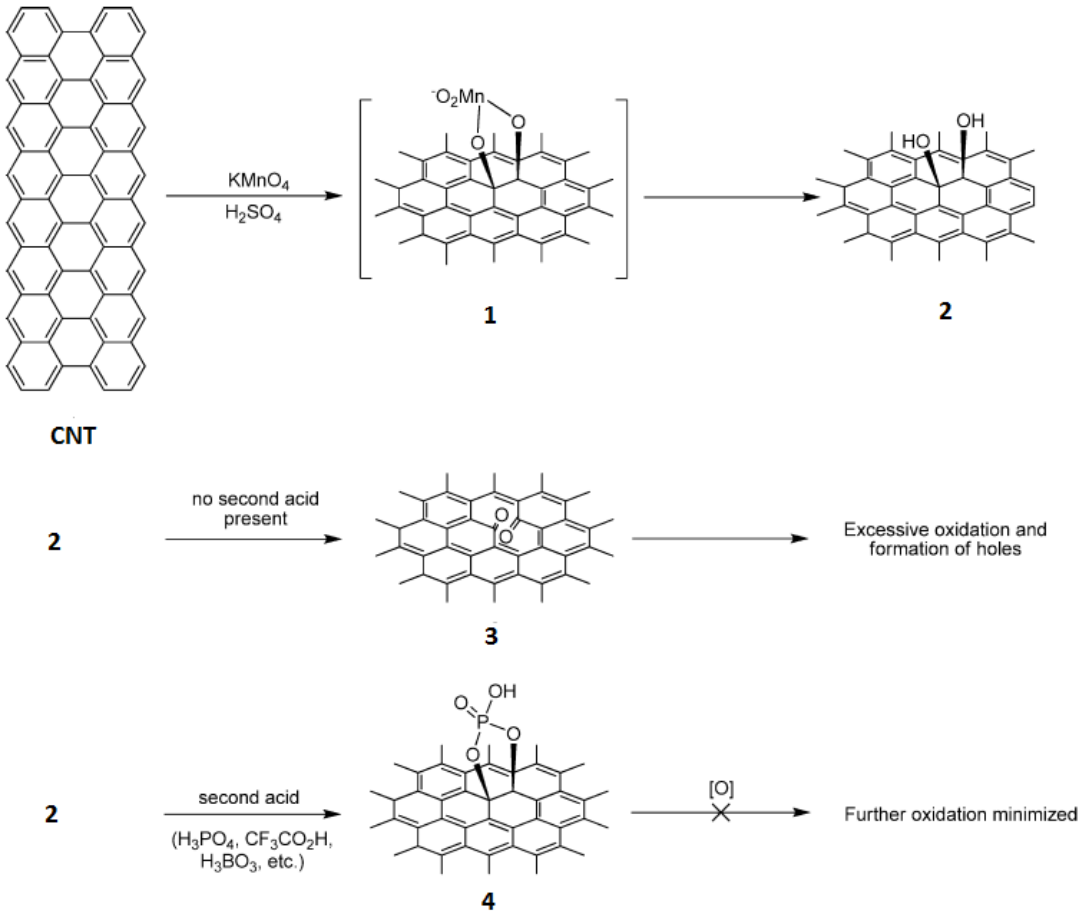

Figure 13: Proposed mechanism for the CNT unzipping when a second weaker acid is used [104]

The oxidative unzipping of CNT also depends on the type of pristine carbon nanotubes used. Castillo-Martinez *et al.* [107] reported that for CVD grown CNT with diameters of 5-15 nm (6-12 walls) and lengths approximately 0.5 µm only partial unzipping of CNT occurred when 500 wt.% of $KMnO_4$ was used, and the total unzipping was attained when 800 – 850 wt.% was used. In the case of CNT with smaller diameter (1-4 walls) and lengths up to 3 mm, 500-700 wt.% of the oxidant agent led to the total longitudinal opening of CNT. The oxidative unzipping of nitrogen-doped (N-doped) CNT has also been studied. [108] The N-doped CNT were previously synthetized by CVD using a benzylamine as carbon/nitrogen source. The presence of nitrogen atoms made the CNT more reactive toward oxidation when compared with undoped CNT. Also the nitrogen content of the unzipped N-doped CNT decreased as a function of the oxidation time, temperature and $KMnO_4$ concentration, controlling this way the concentration of nitrogen within the GNR. Since the N-doped CNT were more reactive, the amount of $KMnO_4$ used varied between 100 - 500 wt.% leading to the total unzipping of CNT. The bamboo structured nitrogen doped CNT was also tested for the oxidative unzipping. [109] The

graphene shells of the bamboo CNT have a "stacked cone" morphology (**figure 14**) and its synthesis has been reported. [110-112]

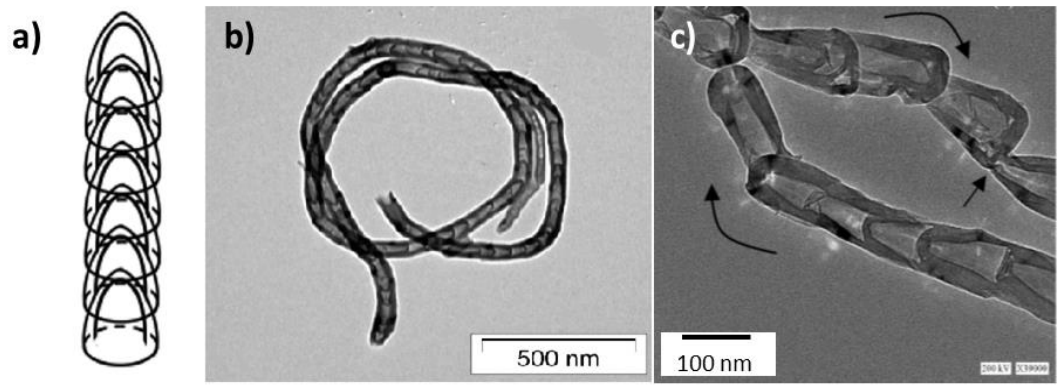

Figure 14: Bamboo carbon nanotubes: a) schematic representation, b) and c) TEM images [110]

The bamboo structured nitrogen doped CNT were unzipped by a chemical oxidation route using potassium permanganate in the presence of trifluoracetic acid or phosphoric acid resulting in the formation of N-doped GNR. The absence of the second weaker acid resulted in the distortion of the bamboo caps and, in these cases, no unzipping occurred. On the basis of the high resolution transmission electron microscopy studies, the authors considered that the bamboo compartments were unzipped via helical or dendritic mechanisms, which are different from the longitudinal unzipping of open channel CNT. [109] The schematic representation of these mechanisms is presented in the **figure 15**.

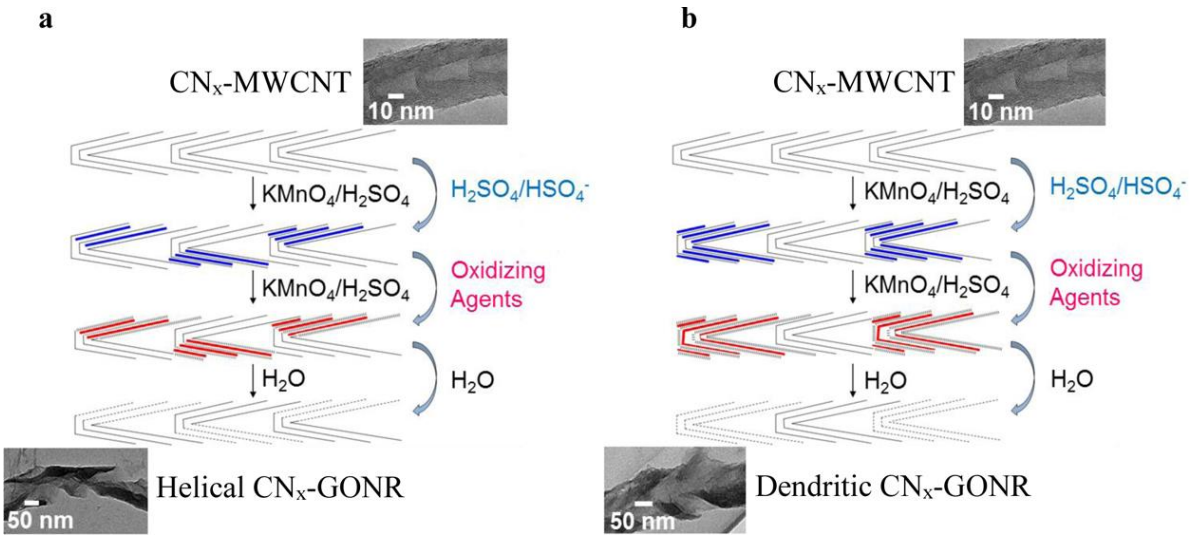

Figure 15: Proposed a) helical and b) dendritic unzipping of bamboo structured nitrogen doped CNT [109]

Other oxidative unzipping processes have been reported in which a mixture of concentrated sulphuric acid and nitric acid (HNO_3) is used. After intercalation of H_2SO_4 and HNO_3 molecules between the coaxial cylinders of the CNT causing its expansion, the

unzipping of the CNTs can occur under sonication [113] or thermal treatment at high temperature. [114]. **Figure 16** represents the proposed mechanism for the unzipping of CNT. The unzipping of these CNT, after the oxidation and intercalation process, can also occur by abrupt heating, where the CNT are frozen in liquid nitrogen and then boiling water is added rising the temperature from *ca.*-200 to 45ºC in a few seconds (5 to 10 s). [115, 116]

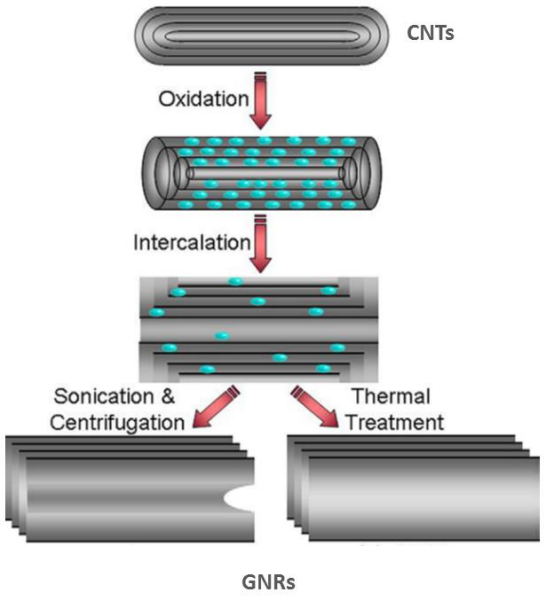

Figure 16: Proposed mechanism for the intercalation of H_2SO_4 and HNO_3 followed by mechanical or thermal unzipping [114]

The Hummer's method [70] and modified Hummer's methods are methodologies frequently applied for the unzipping of CNT. Here, the oxidative unzipping occurs by mixing concentrated H_2SO_4 and sodium nitrate ($NaNO_3$) [117, 118] or potassium nitrate, (KNO_3) [119] followed by treatment with $KMnO_4$. $KMnO_4$ is the most used oxidizing agent, however sodium hypochlorite (NaOCl) has also been studied for the unzipping of CNT previous oxidized using H_2SO_4. [120] Regarding the reduction of the oxygen containing groups of the GNR, hydroionic acid (HI) [121] and lithium aluminium hydride (LAH) [122] have also been used as reducing agents to produce reduced GNR (r-GNR). Gas-phase oxidation has also been studied for the unzipping of CNT. The method is based on the calcination of the CNT in air at 500 ºC which removes impurities and etch/oxidize the CNT at defect sites and ends without oxidizing the side walls. The dispersion in 1,2 dichloroethane (DCE) organic solution of poly(m-phenylenevinylene-co-2,5-dioctoxy-p-phenylenevinylene) (PmPV) followed by sonication promoted the unzipping of the calcinated CNT. [123, 124] Manual grinding [125, 126] of previous oxidized CNT also

showed to be efficient in the unzipping of CNT. The oxidation was performed to obtain CNT with different reactive functionalities of COOH and OH groups by treating them with a mixture of H_2SO_4:HNO_3 [127] and sodium hydroxide (NaOH) [128] respectively. The unzipping occurs in three steps by grinding equal weights of CNT-COOH and CNT-OH. The first step (**figure 17**) is the formation of hydrogen bonds, the second step is the fast proton-transfer that is followed by the third step, the formation of water and carbon dioxide (CO_2) as the products of the exothermic reaction. The released heat can induce the breaking of the carbon-carbon bonds leading to the unzipping. [125]

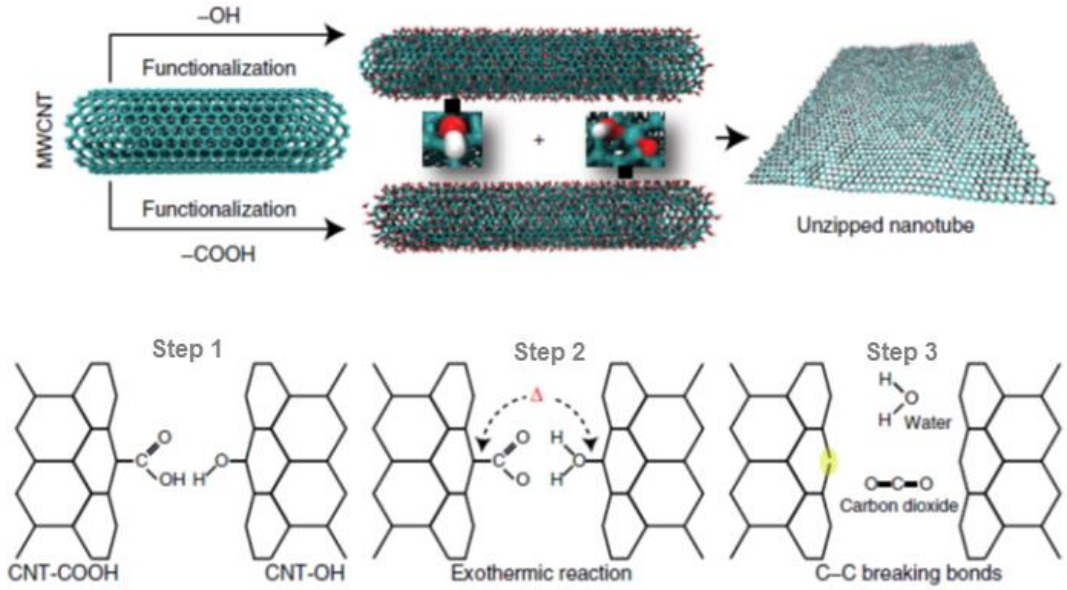

Figure 17: Proposed mechanism for the hydrogen bond-mediated proton transfer unzipping of CNT [125]

The intercalation of oxalic acid followed by the oxidative unzipping of the CNT with H_2SO_4 and $KMnO_4$ was also reported. [129] The oxalic acid was selected owing to its ability to diffuse through the walls of the CNT because it has a molecular length that equals the space between the carbon walls. The intercalation of the oxalic acid among the CNT layers inhibited the destruction of CNT during the unzipping process which enabled potassium permanganate to homogeneously unzip the CNT one by one, until to the interior tube.

2.2.2.2. Intercalation processes

Besides oxidation processes, other methodologies have been studied for the unzipping of CNT to obtain GNR. Cano-Márques *et al.* [130] reported the longitudinal unzipping of

CNT by intercalation of lithium (Li) and ammonia (NH_3) followed by exfoliation with acid treatment using hydrochloric acid (HCl) and abrupt heating at 1000ºC. Also, Tour's group [131] reported the unzipping of CNT by intercalation of potassium vapor (**figure 18a**). The method comprises the exposure of the CNT to hot potassium vapor followed by protonation with ethanol (**figure 18b**). The obtained stacked GNR was then sonicated in chlorosulfonic acid ($ClSO_3H$) to induce the exfoliation of the GNR.

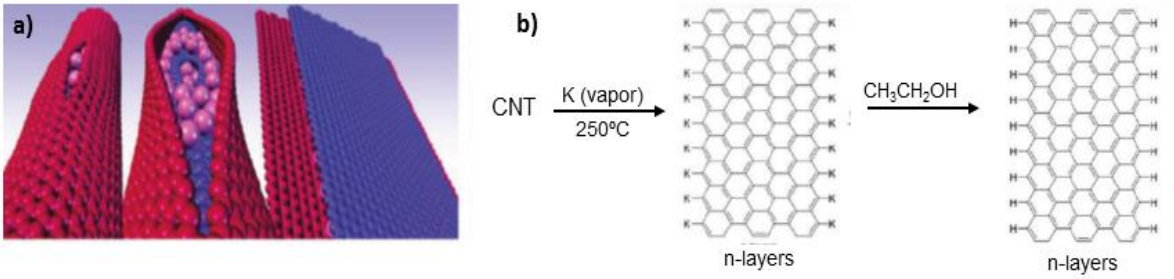

Figure 18: Unzipping of CNT by intercalation of potassium vapour: a) schematic representation, b) protonation of the aryl potassium edges with ethanol. [131]

Later, the same group [132] reported the replacement of the intercalated potassium with haloalkanes by *in situ* functionalization and intercalation with alkyl groups leading to the formation of hexadecyl-, octyl- and butyl-GNR (**figure 19**). Shinde and co-workers [133] reported a hydrothermal approach for the unzipping of CNT. The method involves the use of several counter ions from potassium sulphate (K_2SO_4), potassium nitrate (KNO_3), potassium hydroxide (KOH) and H_2SO_4 in aqueous media, where selective intercalation followed by exfoliation led to the formation of GNR. The sulphate and nitrate ions acted as co-intercalant along with potassium ions resulting into exfoliation of CNT in an effective manner. [133]

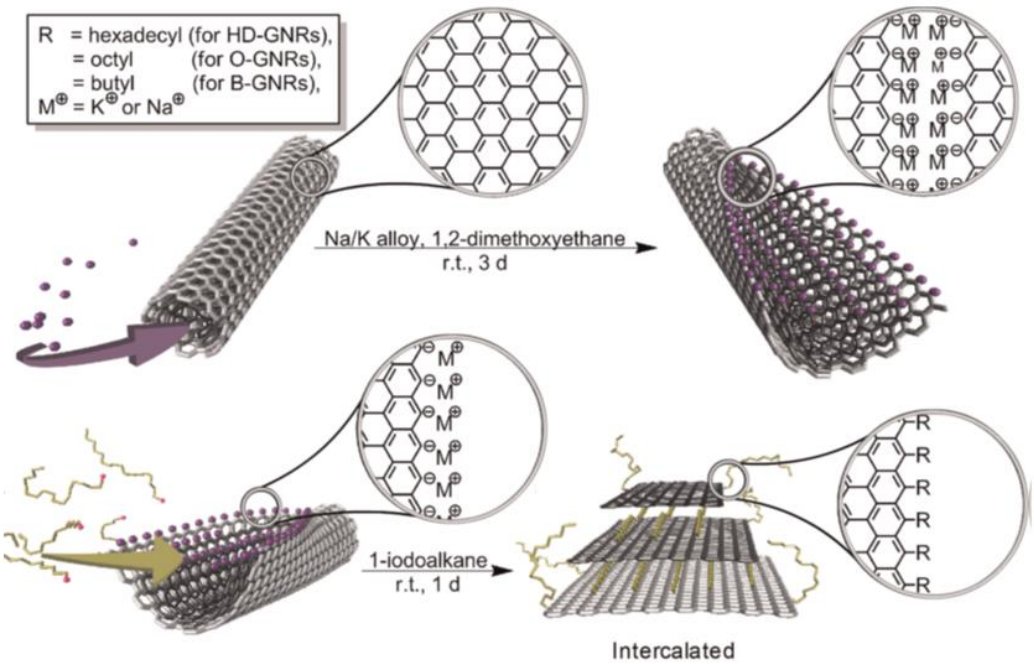

Figure 19: In situ intercalation replacement and selective functionalization of GNR [132]

2.2.2.3. Catalytic processes

Catalytic unzipping of CNT using metal nanoparticles has also been studied to obtain graphene nanoribbons. Terrones's group [134] reported the use of nickel (Ni) and cobalt (Co) to longitudinally unzip CNT (**figure 20**). The process consisted of catalytic hydrogenation of carbon, in which the metal particles "cut" sp^2 hybridized carbon atoms along CNT. [134] Parashar *et al.*[135] also reported the unzipping of CNT using a one-step method that involves the *in situ* grow of Ni nanoparticles that longitudinally cut the CNT walls. Janowska and co-workers [136] reported the catalytic unzipping of CNT in the presence of palladium (Pd) nanoparticles under microwave irradiation, cutting the CNT lengthways.

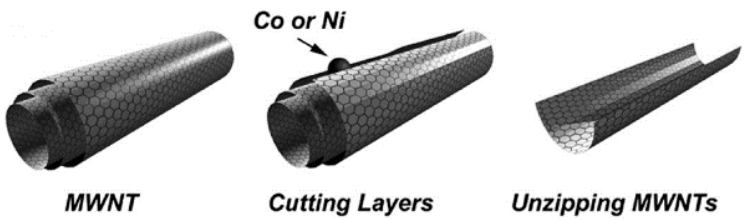

Figure 20: Catalytic unzipping of the CNT using Ni or Co nanoparticles [134]

2.2.2.4. Plasma etching processes

Plasma etching is another methodology described for the unzipping of carbon nanotubes. Jiao *et al.* [137] reported the unzipping of CNT by Argon (Ar) plasma etching of partially embedded CNT in a poly(methyl methacrylate) (PMMA) matrix. The plasma etching applied directly to the CNT (without being embedded in polymer matrix) was also reported by Valentini, [138] where the CNT were treated with tetrafluoromethane (CF_4) plasma etching. As the plasma bombarded the entire CNT, this procedure led to the formation of shorter GNR as well as some unzipped CNT. [138] Nonetheless, the direct plasma etching to the CNT to form GNR by controllable unzipping of the nanotubes has been reported. [139, 140] The process is comprised of two steps, the passivation and the etching. During the passivation, oxygen (O_2), hydrogen (H_2) and sulphur hexafluoride (SF_6) gases were applied under plasma. The etching was achieved by plasma hydrogenation. In the passivation step a thin layer of polymeric carbon-fluorine was formed on the outer layers of the CNT acting as a protective layer in the etching process. [139].

2.2.2.5. Electrochemical processes

The unzipping of CNT by electrochemical processes have also been reported. Pillai's group [141] reported the electrochemical unzipping of CNT at controlled potential, using CNT as working electrode (a glassy carbon electrode modified with CNT). The applied electric field on the CNT electrode in diluted H_2SO_4 initiates the breaking of the sp^2 carbon bonds that continues in the longitudinal direction. The reduction of the oxidized GNR was then performed by applying a negative potential. **Figure 21** shows the schematic representation of the unzipping process. [141]

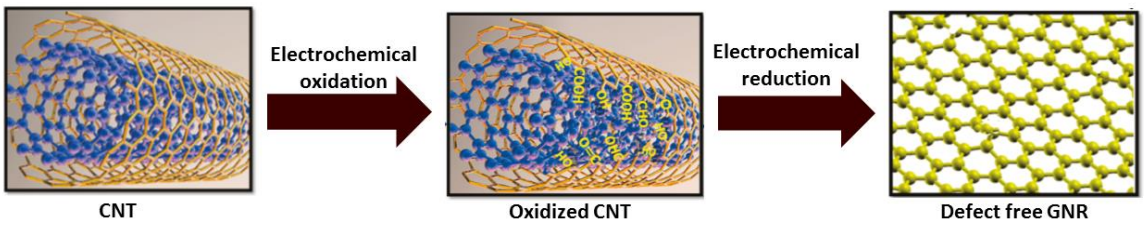

Figure 21: Schematic representation of the electrochemical transformation of GNR from CNT [141]

Latter the same group [142] reported the electrochemical unzipping of CNT using a solid electrolyte that consisted in a sandwich structure containing copper electrodes separated

by a solid polymer electrolyte (Nafion membrane) modified with CNT on both sides. The unzipping occurred by applying a gradient electric field. [142] The group also reported an *in situ* Raman spectroscopy study [143] of the electrochemical unzipping of SWNT, suggesting that the mechanism of unzipping includes the formation of epoxide at the surface of SWNT followed by their successive transformation to graphene nanoribbons. The authors reported that the unzipping of metallic SWNT occurred faster and at lower potential than semiconducting SWNT.

2.2.2.6. Electrical current processes

Electrical current has been also used to unzip carbon nanotubes. Kim and co-workers [144, 145] reported the unzipping of CNT using a high direct current (DC) pulse (about 1500 and 2500 A). The high DC flows through the surface of CNT breaking the sp^2 carbon bonds starting at the tip of CNT and following the current direction. Controlled current induced electrical unzipping of CNT was also reported. [146] The method implies the application of electrical current, under high vacuum, inside a TEM equipment. Using a movable electrode, a CNT was contacted and the unzipping of the outer layer was induced via an applied electrical current through the contact with the CNT. With a proper voltage bias control only part of the CNT outer layer is severed and the GNR is formed. The GNR was then removed from the CNT via sliding between the GNR and the CNT. **Figure 22** shows the proposed mechanism.

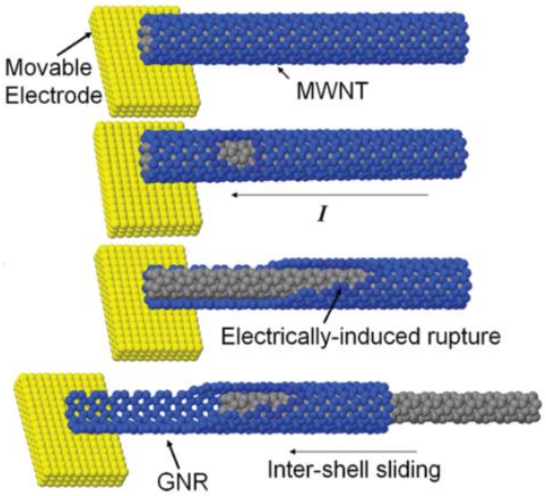

Figure 22: Proposed mechanism for the unzipping of CNT using controlled electrical current [146]

Partially unzipped CNT was also achieved via *in situ* Joule heating inside a TEM equipment. [147] The formation of these partially unzipped CNT was suggested to be

induced by the sequential and spontaneous unzipping of the outmost wall of the CNT under uniformly thermal etching and voltage pulse of 0.2 - 1.0 volts. [147]

2.2.2.7. Other processes

Other methodologies have been reported to obtain graphene nanoribbons by the unzipping of CNT. Controlled unzipping of CNT was reported by Wei *et al.* [148] by sputtering the CNT with zinc (Zn) followed by dissolution in HCl aqueous solution. The SWNT were grown on a silicon/silicon dioxide (SiO_2/Si) substrate, then PMMA was patterned on one side of the SWNT, protecting it from Zn sputtering. After the zinc sputtering, the PMMA was removed by HCl and acetone treatments resulting in a SWNT/GNR intramolecular junction at the interface. **Figure 23** depict this patterned unzipping mechanism.

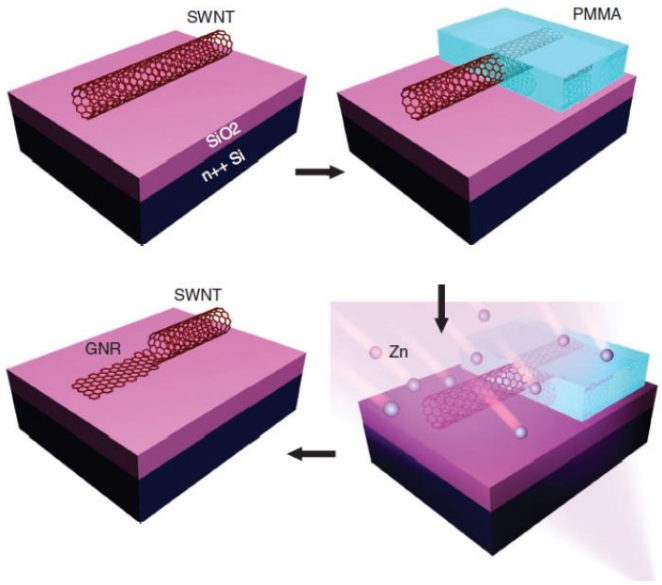

Figure 23: Schematic representation of the patterned unzipping of SWNT for producing SWNT/GNR intramolecular junction. [148]

Hydrogenation reactions have been studied for the unzipping of CNT. Talzin *et al*. [149] reported the unzipping of SWNT by reaction with hydrogen gas. Firstly, the reaction was performed at 400-450 ºC under pressure and H_2 flow. Then the unzipping occurred by hydrogen treatment at higher temperature (550 ºC). Using the microwave irradiation as external energy source, Vadahanambi *et al*. [150] reported the unzipping of CNT in an ionic liquid –assisted splitting method. The authors dispersed the CNT in 1-ethyl-3-

methyl imidazolium tetrafluoroborate (EMIM BF_4) using sonication followed by microwave irradiation to form GNR.

Ozden *et al*. [151] reported the unzipping of CNT using a hypervelocity impact of CNT against a metal target. Through this mechanical impact a large number of defects was produced in CNT as well as rapid atom evaporation resulting in their unzipping. The resulting structures were GNR with various widths (depending on the CNT used) and lengths. The same group [152] later reported the unzipping of carbon nanotubes using a cryo-milling method. The cryo-milling machine was developed by the group and can deform the CNT using a vibrating ball with the weight of 500 g and a frequency of 50 Hz. The deformation rate was calculated to be about 10^8 s^{-1} and to avoid the local melting a constant temperature of 150 K (-123ºC) was maintained throughout by a liquid nitrogen flow. The proposed mechanism for the unzipping was given by experimental and molecular dynamics simulations in which radial and shear loading resulted in the unzipping of CNT**. Figure 24** shows the possible loading conditions in the ball milling experiment.

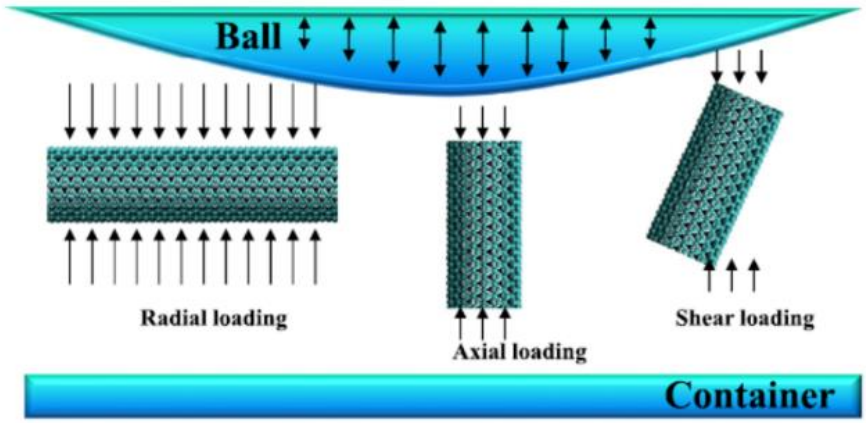

Figure 24: Possible loading conditions in ball milling experiment [152]

Fan and co-workers [153] reported the unzipping of CNT using a microexplosion method. The procedure was based on the filling of CNT with K and then exploding them with water. When the CNT were effectively filled with K, the microexplosion generated by reaction between water and K unzipped the CNT from the weakest point to form GNR. Huang *et al.* [154] reported the unzipping of CNT by a slicing process. The authors prepared perpendicularly aligned CNT/olefin composite films through a conventional slicing technique in which the olefin was infiltrated into a CNT array to produce the composite that was then cut into composite films with thickness varying from about fifty

nanometers to fifty microns. The GNR were produced after the CNT were separated from the polymer matrix by sonication, since the slicing process generated defect at the end of the CNT. The process is illustrated in **figure 25.** The unzipping of flattened carbon nanotubes has been reported, based on the production of flattened CNT which are then unzipped either by oxidation (using H_2SO_4 and $KMnO_4$) [155] or by spontaneous collapse during their grow. [156]

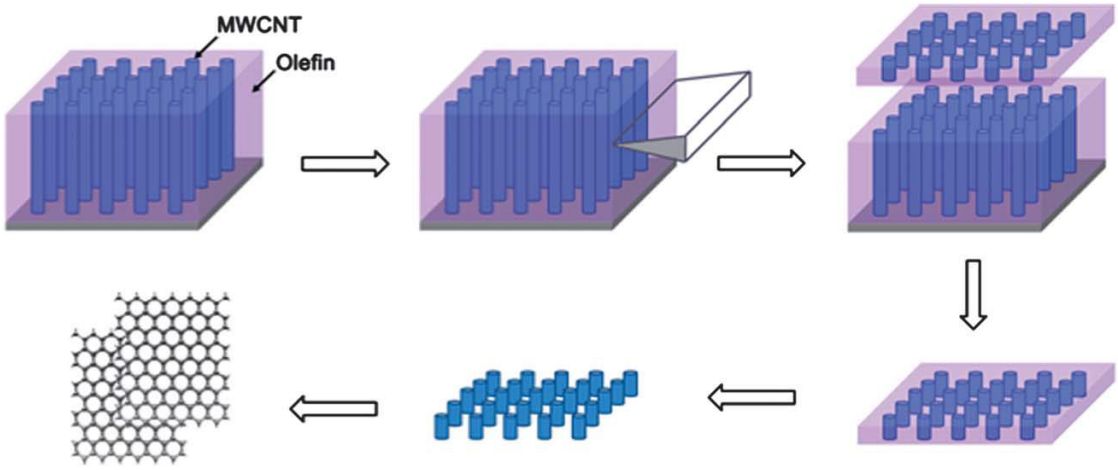

Figure 25: Schematic illustration of the fabrication of GNR by a slicing process [154]

Laser irradiation was also reported to unzip CNT. Kumar *et al.* [157] showed that the irradiation of CNT by an excimer laser with energy of about 200-300 mJ yielded graphene nanoribbons Also, Bang and co-workers [158] reported the unzipping of CNT using pulsed laser irradiation in ethanol with 100 mJ of energy and with a repetition rate and pulse of 30 Hz and 10 ns, respectively.

The formation of graphene nanoribbons by unzipping of carbon nanotubes was achieved on a scanning tunneling microscope (STM) under ultra-high vacuum [159]. The carbon nanotubes were previously functionalized by the 1,3-dipolar cycloaddition (DCA) reaction of azomethine ylides using a one-step and solvent-free approach. [160] The proposed model for the unzipping is based on the perturbation of π-conjugation along the CNT surface induced by the cycloaddition reaction (**figure 26**). The unzipping of the outer layer of the functionalized CNT resulted in a clean and non-oxidized GNR, and the degree of functionalization can be controlled by varying the functionalization conditions. [160]

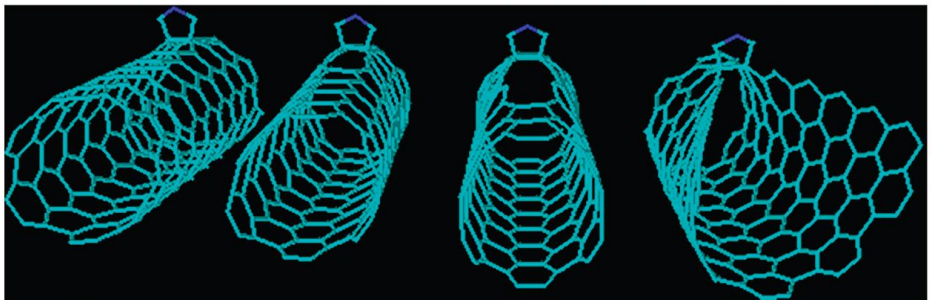

Figure 26: Proposed model for the unzipping of functionalized CNT induced under STM conditions [159]

2.2.2.8. Applications of graphene nanoribbons from carbon nanotubes

The production of GNR by unzipping of CNT has been extensively studied, and their application in various scientific fields has also been the target of extensive research. Applications such as photovoltaic devices, [161] fuel cells, [162-170] supercapacitors, [171-182] radio frequency transmission, [183] optical limiting, [184, 185] lithium-ion batteries, [186-199] electronic devices, [200-207] solar cells, [208-211] tissue engineering, [212] medical imaging, [213, 214] and cancer therapy [215] have been studied for the application of GNR obtained from CNT. Also, textile [216-218] and polymer nanocomposites applications [219-238] have been reported. In fact, GNR obtained from unzipping of carbon nanotubes were used as reinforcement in polymers such polyvinyl alcohol (PVA), [219-221] polyurethane (PU), [222, 223] polydimethylsiloxane (PDMS), [224] polyamide (PA), [225] high-density polyethylene (HDPE), [226] polymethyl methacrylate (PMMA), [227, 228] polyvinylidene fluoride (PVDF), [229] polylactic acid (PLA), [230] polyimide (PI), [231] fluor [232] and silicon [233] elastomers as well as epoxy [234-237] and other thermoset polymers [238] with the aim to improve their mechanical, thermal, electrical and gas barrier properties. Another field of application GNR obtained from CNT is the preparation of sensors. An example is the detection of dopamine [239-245] which has been extensively studied. Dopamine is a neurotransmitter and may be used in the treatment of disorders of the central nervous system, such as Parkinson's disease. Another example is the detection of urea, [246] a biomolecule that is usually monitored in blood analysis, since its early detection can help to preventing various diseases leading to kidney and hepatic failure. The detection of other well-known biomolecules such glucose [247, 248] and cholesterol [249] has also been studied using GNR based sensors. The detection of some contaminants in the environment have also been the target of research. An electrochemical sensor for the

detection of 4-nonyl phenol was investigated. [250] This molecule is an intermediate for the production of polyethoxylate surfactants, however it is also an endocrine disruptor. Moreover, the detection of polycyclic aromatic amines, [251-253] that may be chemical carcinogens, brevetoxin B, [254] which is a toxin that can be detected in seafood, pesticides (carbaryl pesticide), [255] 2,4,6-trinitrotoluene (TNT), [256, 257] used in explosives and that may have harmful effects as toxic and mutagenic substances, have also been reported. Furthermore, graphene nanoribbons obtained from carbon nanotubes has been studied for gene [258, 259] and drug [260, 261] delivery.

Concerning the biomedical applications, cytotoxic studies of the graphene nanoribbons have been performed, however the results are still controversial. While some research works point to the concentration dependence showing viability at low concentrations of o-GNR (below 10 µg/mL), [262-265] others demonstrated that o-GNR could be cytotoxic materials. [266-268] In spite of the great potential of GNR in the biomedical area, the use of these materials in such applications should be carefully considered, its cytotoxicity being still under extensive research.

2.3. Graphene characterization

The characterization of graphene is an essential step for all the graphene research areas, involving measurements based on various microscopy and spectroscopy techniques. Typically, the characterization of graphene involves the determination of the number of layers of stacked graphene in the material as well as the evaluation of its quality in terms of the presence or absence of defects and contaminants. Optical contrast of graphene is a simple method which has been used for the identification of the number of layers. Single layer graphene, bilayer- and few layer graphene (<10 layers), placed on a silicon wafer covered with a 300 nm thick layer of SiO_2, are differentiated using contrast spectra generated from the reflection of light using a white light source. [269] Atomic force microscopy (AFM) is currently used to determine the number of graphene layers stacked within the graphene flakes. The topographic contrast of AFM images allows the determination of the height of the graphene sample. The number of graphene layers may be estimated through the ratio between the total flake height and the graphite interlayer distance. [27, 35, 270] **Figure 27a)** shows an AFM image of single layer graphene. Other useful techniques normally used to characterize graphene are scanning tunneling and

transmission electron microscopies (STM and TEM, respectively). These techniques may provide high resolution images of graphene which allow the morphology study, the structure of graphene and a qualitative analysis of the chemical composition. The STM applies the tunneling current between a sharp metallic tip and a conductive sample. This technique may provide information about the morphology and structure of graphene giving access to the topography of the sample at atomic resolution. STM can be used under ultra-high vacuum, in air and inert atmosphere, at different temperatures ranging from near zero Kelvin to a few hundred of Celsius degrees. [35, 159] This technique requires extremely clean and stable surfaces, and despite that fact STM has been extensively used to image graphene at atomic resolution and to observe its electronic characteristics and its topography. [271, 272] The results greatly depend on the quality of the prepared samples, and the experimental conditions to test them are complex.

Electron microscopy is based on the interaction of the sample with a high-energy electron beam ranging from a few KV to several 100 KV. These interactions may be observed as images of the topography by scanning electron microscopy (SEM) and morphology of the material (TEM). Higher energy beam leads to better resolution, however the operation under high voltage damages the monolayer of graphene. Energy beams of 80 KV and lower have been successfully used to obtain high resolution images of graphene by transmission electron microscopy. [35, 273, 274] Figures **27b)** and **27c)** show TEM and high resolution TEM (HR-TEM) images of graphene.

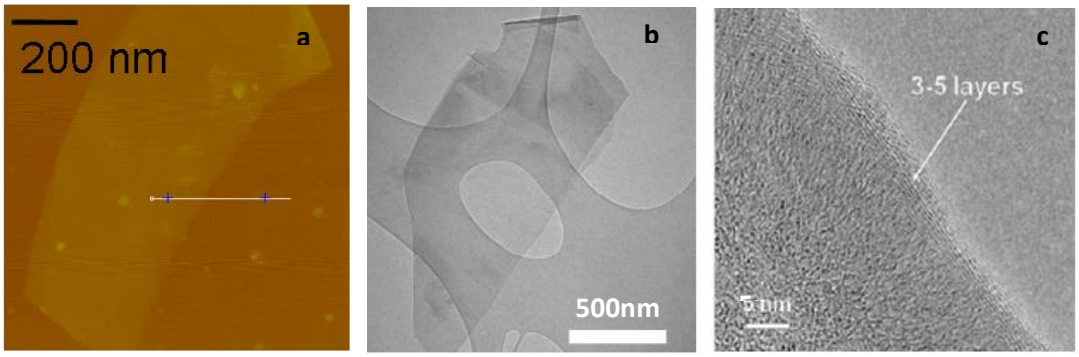

Figure 27: a) AFM image of single layer graphene; b) TEM and c) HR-TEM images of graphene. [25]

Through TEM electron diffraction technique it is possible to observe the typical hexagonal pattern of the graphene structure. [270] In addition, this technique allows distinguishing single- from double- and few- layer by comparing the intensities of the first and the second ring of the diffraction spot. For single layer graphene the intensity of the outer hexagon spot is the same or less than that of the inner one. Conversely, double

layer graphene exhibits higher intensity for the outer hexagon spot. [275] **Figure 28** shows diffraction patterns for single- and double layer graphene as well as their intensity profiles.

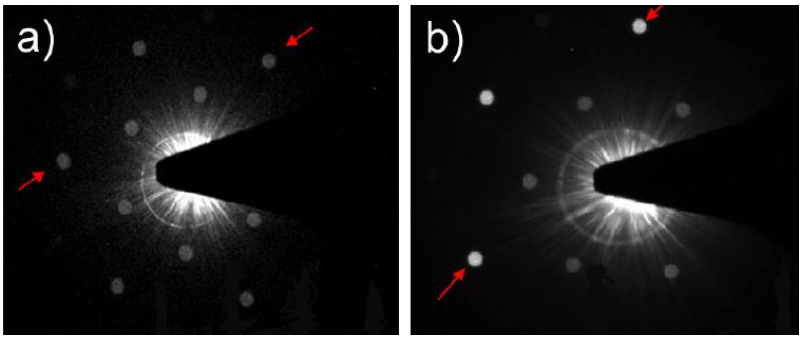

Figure 28: Diffraction patterns of a) single layer and b) double layer graphene

The transmission electron microscopy may also be assisted with energy-dispersive X-ray spectrometry (EDS) which enables a qualitative analysis of the sample identifying its chemical elements. The spectra can be acquired in a short time allowing a rapid evaluation of the specimen.

A quantitative analysis of the chemical elements may be achieved using X-ray photoelectron spectroscopy (XPS). This technique allows the determination of the binding energy of the photoelectrons ejected when the samples are irradiated with X-ray. The binding energy of the inner shell electrons is specific of each element allowing its identification. Furthermore, XPS can also provide information about the chemical functional groups and the electronic structure of the surface molecules based on the "shifts" of the binding energy for each element, measured in eV, induced by its chemical neighborhood. [276, 277]

X-ray diffraction (XRD) may be used to distinguish graphene and graphene derivatives from the original graphite. The pristine graphite exhibits a basal reflection (002) peak at $2\theta = 26.6^{o}$ in the XRD pattern corresponding to a *d* spacing of 0.335 nm. After its oxidation process the interlayer spacing of graphite increases due the presence of functional groups resulting in a shift to lower 2θ of the 002 reflection peak (**figure 29**). Single layer graphene as well as single layer graphene oxide typically exhibit a straight line with no apparent diffraction peak in the XRD pattern indicating that the periodic structure of graphite, due to graphene regular stacking, has been eliminated. [270, 273]

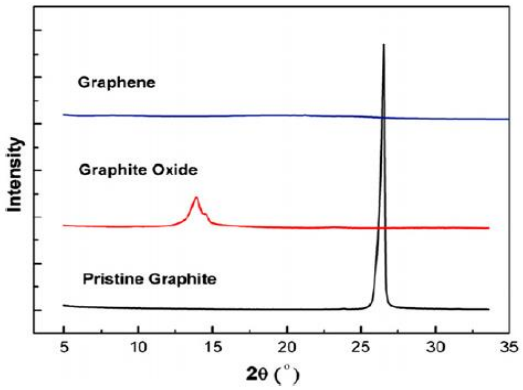

Figure 29: X-ray diffraction patterns of pristine graphite, graphite oxide and graphene [270]

Ultraviolet-visible spectroscopy (UV-Visible) has been used to characterize graphene in suspension. Graphene has a sp^2 structure typical of aromatic compounds which gives a characteristic absorption in the UV-Visible. Typically, graphene and graphene oxide show an absorption peak from 230 to 270 nm. [74, 270, 278, 279] The estimate of the weight concentration, c (g L^{-1}), of graphene may be carried out applying the Lambert-Beer Law (**equation 1**):

$$A=\alpha l c \quad (1)$$

Where A is the measured absorbance, l (m) is the length of the optical path, and α (L g^{-1} m^{-1}) is the absorption coefficient. [27] This technique has been highly used to quantify graphene in suspension. [25, 278, 280] Raman spectroscopy is an important technique for the structural description of carbon-based materials, and is of fundamental importance for the characterization of graphene samples. Raman spectroscopy is based on the inelastic scattering of light which is usually associated to the emission and absorption of phonons. A photon ω_L impinging to a sample causes vibrations of the atoms at their natural vibrational frequencies. When the incident photon loses energy in creating a phonon (emission) the process is designated as Stokes process. Conversely, when the photon gains energy by absorbing a phonon (absorption) the process is designated as anti-Stokes process. Both processes result on the emission of a scattered photon ω_{Sc} (**figure 30**). [281]

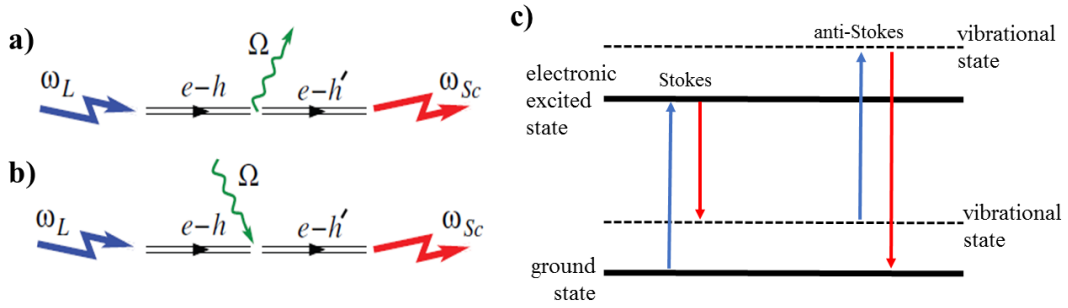

Figure 30: Raman scattering: a) Stokes process; b) anti-Stokes process; and c) Raman scattering resonant conditions [281]

Among all possible phonon modes for sp^2 carbons, only a limited number of phonons are Raman active modes leading to characteristic bands on the Raman spectra, which enables to distinguish differences in the structure of the carbon materials. For a single-layer graphene, which is the fundamental sp^2 carbon material, the Raman spectra present three main characteristic bands. The G band which appears near 1580 cm^{-1} is related to the planar configuration of carbon the sp^2 lattice forming the graphene structure. Due to the strong C-C bonding the G band has a relatively high Raman frequency in comparison to other materials and very small perturbations to the frequency of the G band can be measured. The frequency of the G band is independent of the laser excitation energy (E_{laser}), however it is sensitive to the temperature, strain and doping of the graphene sample. The D band is known as a disorder, or defect band. It represents a ring breathing mode from sp^2 carbon rings, although to be active the ring must be adjacent to a graphene edge or a defect. The D band occurs about 1350 cm^{-1} at 2.41 eV (514 nm) laser excitation energy and is highly dispersive as a function of the E_{laser}. Since the intensity of the D band is directly proportional to the level of defects (or edges) of the sample, the D / G band intensity ratio (I_D / I_G) may provide a sensitive metric for the degree of disorder in the sp^2 carbon structure. Another characteristic band of the graphene Raman spectrum, is the G' or also called 2D band. The 2D band is a second order band and sometimes is referred as an overtone of the D band. However, it is not related to the defects of graphene structure and, as a result, the 2D band is always a strong band in graphene even when the D band is not present. Furthermore, the intensity ratio (I_{2D} / I_G) and the shape of the 2D band may be used to identify the number of stacked graphene layers. [273] In the case of single layer graphene the 2D band is twice the intensity of the G band while in two-layer graphene the G band is stronger than the 2D band. Moreover, the 2D band is shifted to higher frequency in two-layer graphene and has a different shape. As the number of stacked layers is increased the 2D band moves to higher wave number and becomes broader and more asymmetric in shape. In multilayer graphene presenting more than 10 layers the 2D band becomes very similar to that of graphite. [282, 283] **Figure 31** shows the Raman spectra of single-, two- and multilayer graphene.

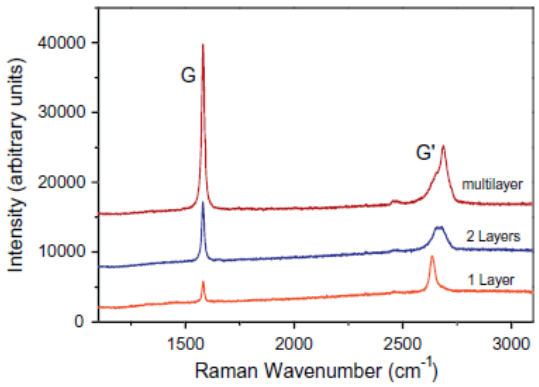

Figure 31: Raman spectra of single-layer, two-layer and multilayer graphene. [273]

Raman spectroscopy technique is useful as an *in situ*, non-contact and non-destructive analysis tool that can be used at room temperature and under ambient operating conditions.

2.4. Graphene polymer nanocomposites

Graphene is a carbon nanomaterial that can potentially improve the properties of polymer-based nanocomposites, as it possesses similar mechanical properties to CNT but superior thermal and electrical conductivity and larger surface area (**table 1**). [35, 36] However, the production of such polymer nanocomposites requires not only that graphene be produced at a large scale, but also that it may be incorporated and homogeneously dispersed into polymer matrices with good interfacial adhesion. [11] These requirements are crucial in order to produce graphene polymer nanocomposites with enhanced mechanical and electrical properties. Concerning the electrical conductivity of the nanocomposites, the concentration of graphene needs to be above the electrical percolation threshold, where a conductive network of graphene is formed. Both conductivity and the percolation threshold may be affected by various factors such as the volume fraction, the orientation and aspect ratio of graphene, its interlayer spacing and the interfacial adhesion with the polymer matrix, its dispersion in the matrix as well as the crystallinity of the matrix. [284] At the nanometer scale, the van der Walls forces between carbon nanoparticles become extremely significant due to their large specific surface area, [285] and so nanoparticles such as graphene or CNT tend to form stable agglomerates. Thus, to achieve uniform dispersion of nanoparticle agglomerates in a polymer matrix, it is necessary to overcome their agglomerate cohesion strength. However, the energy applied to promote their deagglomeration must be carefully

controlled. A low energy input may not induce the breakup of the nanoparticle agglomerates. Conversely, excessive energy input may cause the fragmentation of the primary nanoparticles (the breakage of CNT or the decrease of graphene size, for instance) which may not induce any beneficial effect. [286] **Figure 32** shows a schematic representation of the different stages of the reduction of the particle agglomerate size versus the energy applied to induce agglomerate dispersion.

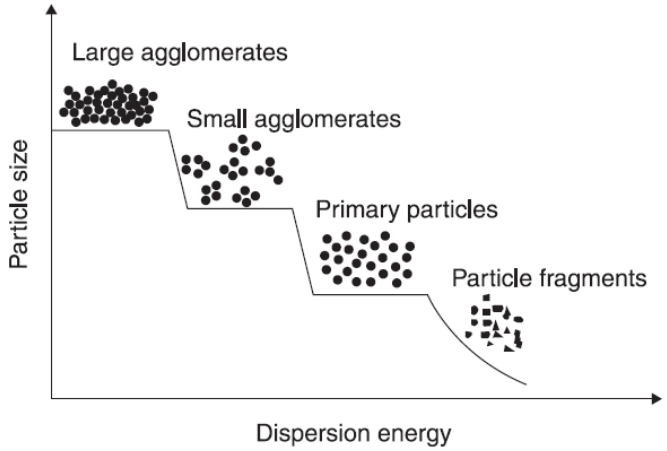

Figure 32: Schematic diagram showing reduction in particle size with the increasing dispersion energy [286]

The fabrication method and processing conditions of the nanocomposites play an important role in the final properties of the nanocomposite, since the energy applied to promote the dispersion of the nanoparticles depend of such parameters. [284] The method of solution mixing and *in situ* polymerization has been used as synthesis strategies for graphene/polymer nanocomposites. In fact, solution mixing is a vastly used technique to fabricate graphene/polymer nanocomposites as the suspension of dispersed graphene can be directly mixed into soluble polymers. The drawback of this technique is the solubilization of the polymer that frequently involves the use of hazardous solvents such as dimethylformamide (DMF), chloroform, dichloromethane (DCM), or toluene. Melt mixing, in contrast, is a most environmentally and economically attractive technique and scalable method for dispersing graphene into polymers. In addition, this process avoids the use of hazardous solvents. [35]

2.4.1. Melt mixing method

The melt mixing technique is frequently used for the preparation of polymer nanocomposites, however it does not easily lead to optimal nanoparticle dispersion. [38] [39] Various studies carried out using a diversity of mixing equipment (extruders, internal mixers, prototype mixers) for carbon black [40], carbon nanofibers [41], and carbon nanotubes, [42, 43] have demonstrated that the intensity and type of hydrodynamic stresses (i.e., shear versus extensional), residence time, and interfacial adhesion play a major part in dispersion. [41, 42, 44] The pioneering work of Taylor [287] and Grace, [288] followed by several other studies, [289-291] showed the importance of extensional flow on the elongation and the break-up of the agglomerates of nanoparticles in polymers and its effectiveness compared with shear flow. [292, 293]

In the specific case of the dispersion of carbon nanotubes Pötschke *et al.* [43, 44, 285] performed several experiments to study their mechanism of dispersion into polymer melts. During the dispersion stage, the size reduction of the large agglomerates was attributed to two main mechanisms, namely rupture and erosion of the CNT agglomerates. The rupture mechanism consists in the rapid breakage of the large CNT agglomerates into smaller ones, while in the erosion mechanism the individual CNT located at the agglomerate surface are slowly eroded into the bulk polymer melt by the polymer wetting action. **Figure 33** present a schematic representation of these mechanisms.

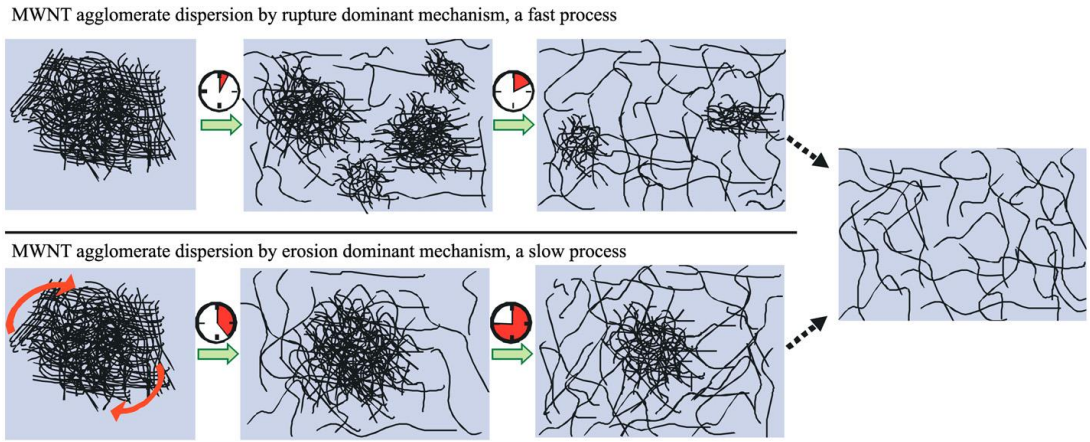

Figure 33: Schematic descriptions of CNT agglomerate dispersion mechanism. [43]

These studies led to a proposed model to estimate the contribution of rupture and erosion mechanisms during the CNT agglomerate dispersion. At low mixing speeds, it was observed that both mechanisms contributed to dispersion, whereas rupture dominated with increasing mixing speed. [43]

Covas *et al.* [41, 42] studied the mechanism of dispersion of CNT in polypropylene (PP) matrix using extensional flow. They developed a prototype small scale mixer, inspired by the concept developed by Nguyen et al. [294]. The mixing device created repetitive converging–diverging flow sequences along its length generating a strong extensional flow component, while precisely controlling flow rate and temperature. In addition, the device allowed to collect samples at various axial locations along the mixer for further characterization. **Figure 34** shows the schematic representation of the mixer device.

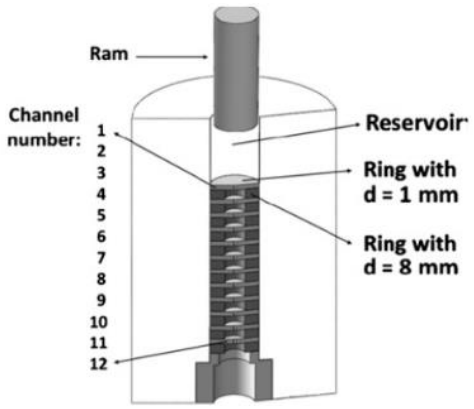

Figure 34: Schematic representation of the prototype small-scale mixer [41]

The studies performed showed that the application of converging-diverging flow improved the dispersion of the nanoparticle agglomerates producing smaller agglomerates and dispersing a larger fraction of the individual CNT when compared with twin screw extrusion. [41] The same authors studied the influence of the chemical functionalization of the CNT and carbon nanofibers (CNF) on their dispersion in PP matrix. [41, 295] The functionalization route lead to bonding of PP grafted with maleic anhydride on pyrrolidine functionalized CNT PP improving the dispersion of both CNT and CNF in the PP matrix. While the dispersion mechanism of carbon nanotubes in polymers is well studied, for graphite and graphene it is far from being well understood. However, the incorporation of graphene and graphite based materials into PP may convey interesting properties to the composite. [296, 297] **Table 2** presents mechanical and electrical properties reported in the literature for graphene or graphite related materials in polypropylene matrix, produced by melt mixing.

Table 2: Mechanical and electrical properties of PP composites with graphene or graphite related materials

Graphene/graphite type (Supplier)	Equivalent diameter (µm)	Treatment	Tensile modulus ratio[1]	Electrical percolation threshold (wt.%) [2]	Highest conductivity (S cm^{-1})	Ref.
GnP (XG Sciences Inc., USA)	5 15 25	Used as received	1.09 (8wt.%) 1.08 (8wt.%) 0.94 (8wt.%)	-	-	[298]
GnP (UCAR International Inc.)	1 15	Used as received	-	15	10^{-3} (55wt.%)	[284]
Natural graphite flake (grade 3061, Sigma Aldrich)	500	Thermal expansion	2.12 (10wt.%)	1 – 3	10^{-7} (3wt.%)	[299]
GnP (XG Sciences Inc., USA)	5 10	Used as received	2.3 (22wt.%) 1.9 (22wt.%)	13 9	10^{-3} (18wt.%)	[300]
Graphite (Alfa Aesar Co., Ltd.)	45	r-GO	1.74 (1wt.%)	1 - 2	10^{-6} (5wt.%)	[301]
Grafite (Merck)	50	r-GO	-	11	10^{-3} (22wt.%)	[302]
Graphite (Sigma Aldrich)	20	r-GO	2.0 (3wt.%)	-	-	[303]
GnP (Asbury Carbon)	2	Used as received	1.5 (5wt.%)	1 – 3	10^{-3} (10wt.%)	[304]
GnP (XG Sciences Inc., USA)	1 15	Used as received	-	18 - 20	10^{-3} (55wt.%) 10^{-2} (55wt.%)	[305]
GnP (Angstron Materials Inc.)	40-50	Used as received	-	8 - 10	10^{-4} (15wt.%)	[306]
GnP (XG Sciences Inc., USA)	5	Used as received	1.5 (10wt.%)	5	10^{-4} (20wt.%)	[307]
GnP (Nanjing Kefu nano-Tech Co. Ltd.) (Suzhou Hengqiu Graphene Tech. Co. Ltd.) (Nanjing Jichang Kefu Nano-Tech Co. Ltd.)	<10 0.5-20 10-50	Used as received	2.2 (0.5wt.%) 1.9 (0.5wt.%) 1.5 (0.5wt.%)	-	-	[308]
Graphene nanosheets (Enerage Inc., Taiwan)	-	Used as received	2.5 (20wt.%)	5	10^{-3} (20wt.%)	[309]
Natural graphite (grade 2369, from Graphexel Ltd.)	-	Electrochemical exfoliation 5µm (eq. diameter) 20µm	 1.1 (20wt.%) 1.9 (20wt.%)	-	-	[310]
Graphite (grade KFL, Graphite Kropfmuhl GmbH)	100	r-GO	-	2 - 5	10^{-6} (7.5wt.%)	[311]
GnP (XG Sciences Inc., USA)	5	As received r-GO	1.2 (3wt.%) 1.2 (3wt.%)	-	10^{-10} (3wt.%) 10^{-9}(3wt.%)	[312]
EG (SGL Technologies GmbH)	-	Used as received	-	6 - 8	10^{-5} (20wt.%)	[313]
GnP (XG Sciences Inc., USA)	25	Used as received	-	5 - 10	10^{-4} (40wt.%)	[314]

[1] Ratio between the tensile modulus of the composite and the polymer (PP)

[2] When loading was reported in volume percent, the density of bulk graphite (2.2 g cm^{-3}) was used to convert to a weight percent loading

Graphite nanoplates (GnP), a thin form of graphite flakes with thickness ranging from that of graphene to approximately 100 nm, have recently attracted attention as an economically viable alternative for the development of functional and structural nanocomposites. [315] Normally these materials are obtained by expansion process, using heat or microwave irradiation, resulting in GnP or expanded graphite (EG) with an interlayer spacing higher than that of graphite (0.335 nm).[38, 305, 316] The incorporation of graphene and graphite related materials in PP matrix have been studied showing to improve the final properties of the composite, namely the mechanical and electrical properties. However, even when using the same type of nanoparticles and composite processing technique, the properties of the corresponding composites may vary considerably depending on the process parameters.

2.4.2. Solution mixing

Solution mixing, as mentioned before, presents the disadvantages of the large volume of volatile organic solvents (VOCs) that is released to the atmosphere during the drying stage that leads to composite consolidation, causing pollution problems. However, the use of "green" solvents such water could override this problem. For that reason, a large effort has been set over the last years to develop stable aqueous polymer suspensions, as well as stable suspensions of graphene derivatives in water.

Polyurethane (PU) is a versatile polymeric material which has been extensively used as paints, adhesives and coatings in a wide variety of applications in the field of construction, textiles, foot wear, furniture, packaging, electronics, automotive and aerospace, among others. [222, 317-323] The methods for the production of PU can be differentiated by the process of preparation: solvent free, in solution (using organic solvents) and in water. [317] The latter is denominated as waterborne polyurethane (WPU) and has been presented as an eco-friendly alternative to other solvent-borne PU since only water is involved during the drying stage. The basic components of WPU are similar to those which are known from solvent-borne polyurethanes. Mainly they are diisocyanates (containing two –NCO groups per molecule), polyols (containing a plurality of hydroxyl -OH groups), amines, catalyst and aditives. [37] The addition polymerization reaction of diisocyanates and polyols leads to the formation of polyurethane (**figure 35**).

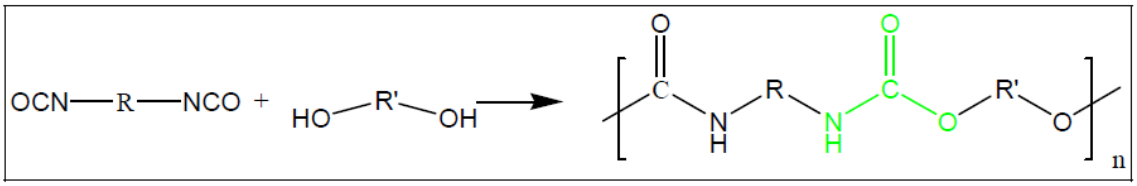

Figure 35: Reaction of diisocyanate and polyol to form polyurethane

Predominantly, aliphatic diisocyanates like the linear hexamethylene diisocyanate (HDI) and cycloaliphatic dicyclohexylmethane diisocyanate (H_{12}MDI) and isophorone diisocyanate (IPDI) are used. The structure of these compounds is presented in **figure 36**. Concerning the polyols, a wide range can be found and the variation of its molecular weight, structure and functionality are critical for the performance of the final product.

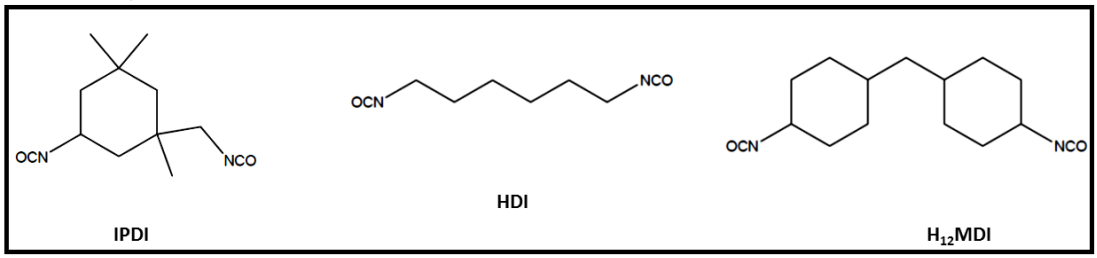

Figure 36: Chemical structures of IPDI, HDI and H_{12}MDI

The waterborne polyurethane is obtained by the modification of the polyurethane chains with hydrophilic groups which allows the dispersion and stabilization of PU in water. [37] Various processes have been developed for the preparation of WPU. In all of these processes, a medium molecular weight polymer (the prepolymer) is formed by the reaction of suitable diols or polyols (usually macrodiols such as polyethers or polyesters) with a molar excess of diisocyanates or polyisocyanates in the presence of an internal emulsifier. The emulsifier is a diol with hydrophilic groups that can be designated as anionic, cationic and non-ionic depending on their ionic non-ionic nature and they will be responsible for the stabilization of the WPU chains in water. Depending on the emulsifier used the resulting WPU can be designated as anionic, cationic and non-ionic WPU. [317] The most common produced WPU are anionic which normally has carboxylic acid groups or sulfonic acid groups in the polymer chains. The cationic groups frequently used to produce cationic WPU are quaternary ammonium salts while the non-ionic group commonly used for the production of non-ionic WPU is [poly(ethylene oxide)]. [37, 324] **Figure 37** illustrates examples of those WPU structures.

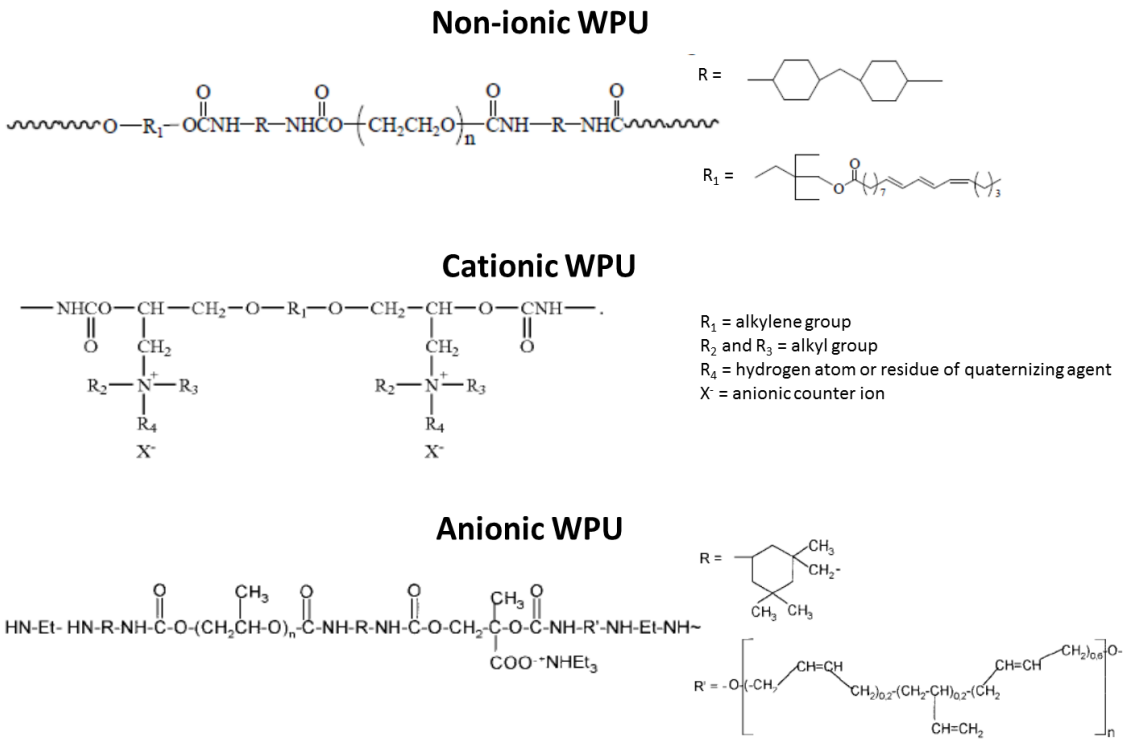

Figure 37: Examples of WPU polymer structures: Non-ionic WPU (from ref. [325]); cationic (from ref. [326]) and anionic WPU (from ref. [327]).

WPU typically presents excellent elasticity, abrasion resistance and flexibility. [37, 317, 324, 328] Some of the properties of WPU such as water resistance, thermostability and mechanical properties are inferior to those of solvent-borne PU. The incorporation of carbon based reinforcing materials in the WPU matrix has been used to improve the mechanical, thermal, electrical and barrier properties of the composites, relative to WPU. Carbon Black (CB) has been studied as reinforcement in WPU matrix to improve mechanical and water resistance of the nanocomposite, regarding its application as functional coatings on leather and textiles. [329]. CNT have been incorporated to improve the properties of WPU nanocomposite films. Oxidation [330-334] and functionalization of CNT with ethylenediamine (EDA) [335] and isophorone diisocyanate (IPDI) [336] has been performed as strategy to improve the dispersion of CNT in the WPU matrix and consequently enhance the final properties of the composites like the mechanical and electrical properties as well as the water resistance. The applications of WPU/CNT composites films as actuators [337], sensors [338], electromagnetic interference shielding (EMI) [339, 340] devices as well as textile [341, 342] and antistatic [343] coatings have been studied.

Reduced graphene oxide (r-GO) has also been highly used to improve the properties of the WPU nanocomposites. Ding *et al*. [344] reported the incorporation of thermally reduced graphene oxide into WPU matrix that demonstrated to improve the thermal and electrical properties of the nanocomposite, showing a percolation threshold between 1 and 2 wt.%. Yousefi and co-workers described [345] the *in situ* production and reduction of GO/WPU nanocomposites. The resulting nanocomposite films showed very good conductivity with a percolation threshold of about 0.2 wt.%. Later the same group [346] reported the application of those r-GO/WPU nanocomposites as water vapor barrier, resulting in an enhancement of 73 % of the barrier effect for 3 wt.% of r-GO incorporation. Li *et al*. [347] also reported the *in situ* reduction of the GO during its mixture with WPU. The resulting nanocomposites showed good electrical properties achieving to 10^{-3} S cm^{-1} of conductivity at 10 wt.% of r-GO incorporation. The oxygen barrier properties were tested showing an improvement of barrier effect of 92 % for the same content of r-GO. Anjanaputa and co-workers [348, 349] reported the improvement of electrical and mechanical properties of the thermally reduced GO/WPU nanocomposites. The group studied the *in situ* incorporation of the r-GO (during the synthesis of the WPU) versus the physical mixing concluding that the former promoted larger improvement of the final properties of the nanocomposites. GnP was also reported to improve the mechanical, thermal and the electrical properties of WPU nanocomposites, showing a percolation threshold of 1 wt.%. [350, 351] The functionalization of graphene may induce a better interaction with the polymer matrix. As so, the graphene oxide has also been studied for the improvement of the physical properties of WPU nanocomposites. Kim *et al.* [352] reported the incorporation of GO into a silanized WPU. The GO/WPU nanocomposites were synthesized from polycaprolactone diol, isophore diisocyanate, dimethylol butanoic acid and (3-aminopropyl) triethoxysilane with GO as a multifunctional crosslink as well as reinforcement. The covalently incorporated GO into the silanized WPU highly improved the mechanical properties of the nanocomposite. Furthermore, the oxygen groups of GO may also be used for chemical reactions with other compounds [353]. Li *et al.* [354] reported the *in situ* functionalization of GO with IPDI during the WPU synthesis. The resulted nanocomposite showed a good dispersion of the functionalzed GO with enhanced mechanical and thermal properties as well as improved water resistance. Following a similar approach, Lou and co-workers [355, 356] showed that the IPDI functionalized GO improved the thermal, mechanical and electrical

properties of the WPU nanocomposite, describing an enhancement of three orders of magnitude for the electrical conductivity (from 10^{-12} to 10^{-9} S cm^{-1}) with the incorporation of 2.5 wt.% of IPDI-GO. The functionalization of the GO with a titanate coupling agent was also reported. [357] The incorporation of 0.4 wt.% of these functionalized GO into WPU matrix led to an improvement of the corrosion of a steel surface. Wang *et al.* [358] reported the incorporation of GO functionalized with 3-aminopropyl triethoxysilane (APTES) in WPU by physical mixing. The resulting nanocomposites showed better mechanical properties with an enhancement of 50 % of the Young's modulus and 56 % of the tensile strength for 1.0 wt.% of APTES-GO incorporation. Using the same functionalization approach, Lei et al. [359] described the *in situ* incorporation of APTES-GO in WPU matrix. The mechanical properties of the resulting nanocomposites improved, showing an enhancement of the 279 % of the Young's modulus, although the tensile strength improvement was only 10 %, for the same amount of APTES-GO incorporation (1.0 wt.%). Pan and co-workers [360] reported the functionalization of GO with different hydramines, namely monothanolamine (MEA), diethanolamine (DEA) and triethylamine (TEA), which are weaker reducing agents when compared with hydrazine. The reaction of the GO with these compounds induced some reduction of the oxygen containing groups of the graphene but also some surface modification. The incorporation of these functionalized GO in WPU matrix resulted in nanocomposites with enhanced mechanical properties, showing an improvement of the tensile strength of 49 %, 36 % for MEA-GO and DEA-GO, respectively, and a decrease of 21 % for TEA-GO (for 1.0 wt.% of incorporation). In addition, the non-covalent functionalization of r-GO with surfactants, namely the sodium dodecyl sulphate (SDS), was reported to produce WPU nanocomposites with improved mechanical and electrical properties. The incorporation of 4.0 wt.% of these functionalized r-GO led to an enhancement of 100 % of the Young's modulus and an electrical conductivity of 10^{-6} S cm^{-1}. The combination of GO and carbon nanotubes was also studied for the improvement of WPU nanocomposites performance. The ratio of 1:1 (GO:CNT) showed to improve the tensile strength by 25 % when compared with the same amount of only GO in WPU nanocomposite. [361] Some of the WPU nanocomposites properties described above are presented in the **table 3**. The applications of graphene (r-GO, GO or functionalized GO) / WPU composites as EMI shielding devices, [355, 362, 363] and textile [364], anticorrosive [357, 365, 366] and flame retardant [367] coatings have been studied.

Table 3: Mechanical and electrical properties of CNT and graphene in WPU matrix

Carbon based material	Tensile modulus ratio[(1)]	Electrical percolation threshold (wt.%) [(2)]	Highest conductivity (S cm^{-1})	Permeability decrease (%)	Ref.
Oxidized CNT	-	0.24	10^{-6} (0.4wt.%)	-	[330]
Oxidized CNT	1.2 (1.5wt.%)	0.5 - 1.0	10^{-4} (1.5wt.%)	-	[332]
Oxidized CNT	-	0.98	10^{1} (20.0wt.%)	-	[333]
EDA functionalized CNT	1.7 (4.0wt.%)	-	-	-	[335]
IPDI functionalized CNT	2.7 (3.0wt.%)	0.3	10^{-1} (3.5wt.%)	-	[336]
CNT and surfactant (aromatic modified polyethyleneglycol)	-	4.8	10^{2} (76.2wt.%)	-	[339]
Oxidized CNT	2.2 (2.0wt.%)	-	-	-	[341]
Oxidized CNT	1.2 (1.5wt.%)	0.5 – 1.0	10^{-3} (1.5wt.%)	-	[343]
GnP	2.4 (2.0wt.%)	1.0	10^{-7} (2.0wt.%)	-	[351]
r-GO	2.0 (4.0wt%)	1.0 – 2.0	10^{-6} (4.0wt.%)	-	[368]
r-GO	1.1 (6.0wt.%)	1.0 – 2.0	10^{-4} (6.0wt.%)	-	[348]
GO	7.2 (1.0wt.%)	-	-	-	[352]
r-GO	21.2 (3.0wt.%)	-	-	73 (3.0wt.%) water vapor	[346]
r-GO	-	-	10^{-3} (10wt.%)	92 (10.0wt.%) oxygen	[347]
r-GO		1.0 – 2.0	10^{-4} (6.0wt.%)	-	[344]
IPDI functionalized-GO	-	-	10^{-9} (2.5wt.%)	-	[355]
APTES functionalized r-GO	7.2 (0.5wt.%)	-	-	-	[359]
r-GO AEMEA[(3)] functionalized-GO	-	1.0	10^{-2} (11.0wt.%) 10^{-1} (11.0wt.%)	-	[362]
MPTMS[(4)] functionalized-GO	-	1.5 – 2.0	10^{-7} (2.5wt.%)	-	[355]

[(1)] Ratio between the tensile modulus of the composite and the pristine polypropylene

[(2)] When loading was reported in volume percent, the density of bulk graphite (2.2 g cm^{-3}) was used to convert to a weight percent loading

[(3)] 2-aminoethylmathacrylate hydrochloride monomer

[(4)] (3-mercaptopropyl)trimethoxysilane

CHAPTER 3. GRAPHENE NANORIBBONS FROM CARBON NANOTUBES

This chapter is based on the article:

Cunha E., Proença M., Costa F., Fernandes A., Ferro M., Lopes P., González-Debs M., Melle-Franco M., Deepak F., Paiva M., "Self-assembled functionalized graphene nanoribbons from carbon nanotubes", *Chemistry Open Communications*, 4 (2015) 115-119.

And part of the articles:

Rocha H., Cunha E., Costa R., Alves N., Mano J., Melle-Franco M., Hornekaer L., Young R., Paiva M., "Functionalized graphene nanoribbons: properties and film applications" – In preparation

Moura D., Caridade S., Sousa M., Cunha E., Rocha H., Mano J. Paiva M., Alves N., "High performance free-standing membranes by layer-by-layer assembly of graphene flakes and ribbons with natural polymers" – Accepted for publication in Journal of Materials Chemistry C.

3. GRAPHENE NANORIBBONS FROM CARBON NANOTUBES

3.1. Introduction

The unzipping of carbon nanotubes to obtain graphene nanoribbons have been extensively studied (see section 2.2.2. in chapter 2). The outstanding properties of the GNR make these materials interesting for application in a wide range of scientific fields, including electronic, sensors and biomedical applications (section 2.2.2.8., chapter 2).

Implants and biodevices such as bone fixation devices or scaffolds for regenerating cardiac tissue, may lead to severe immunological reactions in the host body, and therefore reduce the performance of the implant/device. [369-372] In this context, natural polymers are promising materials to overcome such issues due to their inherent biodegradability and biocompatibility, however, they lack mechanical and electrical properties. [373, 374] These properties may be improved by the preparation a nanocomposite material, combining synergies of natural polymers with a reinforcing material like graphene or graphene nanoribbons. Chitosan (CHI) is a natural-derived polysaccharide obtained from the N-deacetylation of chitin which can be extracted from the exoskeleton of insects and crustaceans, and is an interesting polymer for biomedical applications. This natural polymer has a nontoxic, antibacterial, antifungal, mucoadhesive, haemostatic and biocompatible behavior. [375, 376] Alginate (ALG) is another abundant low cost natural polymer derived from brown algae, also used in the biomedical area. This natural polysaccharide is hydrophilic, biocompatible and non-immunogenic, with the ability to absorb 200 to 300 times more water than its own weight. [377, 378] This is another interesting property of these polymers, that make them widely explored for biomedical purposes. [376, 378]

Layer-by-Layer (LbL) assembly has emerged as a simple and environmentally friendly technique to obtain materials with a nanometer or micrometer scale control of the size, morphology and molecular structure. This method is based in the sequential adsorption of oppositely charged macromolecules (polycations and polyanions) on a substrate surface, via electrostatic forces, hydrophobic interactions, hydrogen bonds, van der Waals forces, charge transfer interactions or covalent bonds. Depending on the substrate, different structures may result, including free-standing membranes (FS). [379, 380]

In this work a method was developed to produce functionalized (non-oxidized) graphene nanoribbons from carbon nanotubes. Inspired by the observation of the unzipping of

functionalized CNT under ultra-high vacuum scanning tunneling microscopy (UHV STM), [159] where the type of functionalization played a key role in the unzipping process [381], an alternative method to produce GNR in solution was developed and presented. The CNT were functionalized by the 1,3-dipolar cycloaddition reaction of azomethine ylides, and their surface chemistry characterization was described elsewhere. [160] The unzipping of the functionalized outer layer was achieved in ethanol solution, producing stable suspensions of functionalized GNR (f-GNR). The stacking of the f-GNR, obtained from large and small diameter functionalized CNT upon solvent evaporation, generated stacks with a large interlayer spacing required to accommodate the functional groups at the GNR surface, as confirmed by molecular modelling.

The unzipping of carbon nanotubes through oxidation route has been widely used, leading the production of oxidized GNR (o-GNR) in high concentration (see section 2.2.2. in chapter 2). In this work o-GNR was also produced using a modified Hummer's method. Both f-GNR and o-GNR were used to study the formation of LBL membranes with natural polymers. The build-up of multi layered membranes with chitosan and o-GNR (CHI/o-GNR) as well as chitosan and f-GNR-alginate (CHI/f-GNR-ALG) was investigated *in situ* by quartz crystal microbalance with dissipation monitoring (QCM-D). The QCM-D studies showed that these materials could be used to prepare free-standing membranes by LBL technique, which might be potentially used in different biomedical applications, such tissue engineering and drug delivery.

3.2. Experimental

3.2.1. Preparation of functionalized graphene nanoribbons

Two types of CNT were investigated, NC7000 from Nanocyl® and MWNT SA from Sigma-Aldrich (catalog reference 659258), both produced by Chemical Vapor Deposition (CVD). NC7000 has a diameter of 7-10 nm and MWNT SA has a diameter of 110-170 nm. The CNT were functionalized by the 1,3-dipolar cycloaddition reaction of azomethine ylides using a one-pot functionalization procedure described elsewhere [160] leading to the formation of pyrrolidine-type groups bonded to the CNT surface. The functionalization was carried out at 250 ºC during 5 hours.

The unzipping of the f-CNT was performed using an Ultrasonic processor UP100H from Hielscher, equipped with a sonotrode MS2. CNT suspensions were prepared by mixing 5 mg of functionalized CNT in 8 mL of ethanol. A blank test was conducted using 5 mg of

pristine CNT in 8 mL of ethanol. Ultrasound energy was applied to the suspensions during 15 minutes at maximum power. The suspensions were centrifuged to separate the unzipped CNT, and the GNR supernatant solutions were collected.

3.2.2. Preparation of oxidized graphene nanoribbons

o-GNR were synthetized by a modified Hummers' method. Briefly, 4 g of CNT NC7000 were added to 500 mL of H_2SO_4 and stirred for 4 h. Secondly, in an ice bath, 32 g of $KMnO_4$ were slowly added to the previous mixture and kept stirring for 2 h. The mixture was then heated up to 60 ºC and stirred overnight. After that 300 mL of distilled water was added, followed by 30 mL of hydrogen peroxide (H_2O_2). All steps were performed with the solution placed in an ice-bath. Afterwards, the solution was distributed into 50 mL tubes and centrifuged under 3500 rpm in a Labofuge 400 (Heraeus Instruments, USA) for 15 min and the supernatant was discarded. The precipitate was washed with distilled water for a total of 3 cycles. The resulting precipitate was then collected, followed by the addition of 250 mL of HCl, and it was left stirring for 15 min. The mixture was again centrifuged and washed for 3 cycles. After the centrifugation procedure, the supernatant was discarded and distilled water was added to the solid part and then filtered with a nylon membrane filter (Whatman, UK). The solid was dried for 48 h at 100 ºC and finally milled. At this stage, the resultant powder consists mostly of oxidized carbon nanotubes (o-CNT). In order to achieve extensive exfoliation, o-CNT were dispersed in distilled water and submitted to 4 h ultrasound treatment in the ultrasonic bath, where exfoliation of o-CNT occurred. The final suspensions had a concentration of 0.25 mg/mL and the pH was adjusted to a basic value of 8.

3.2.3. Graphene nanoribbons characterization

The solutions of f-GNR and o-GNR were analyzed by UV-visible spectroscopy on a Shimadzu UV-240 1 PC, using 10 mm path length quartz cells. The thermogravimetric analysis (TGA) analysis was performed on a Modulated TGA Q500 from TA Instruments. The samples were heated at 10 ºC/min under a constant flow of N_2. The Fourier transform infrared (FTIR) spectra were collected in transmission mode using a *Jasco 4100* spectrophotometer.

The micro Raman analysis was performed on a LabRAM HR Evolution Raman spectrometer (Horiba Scientific, Japan) using a laser excitation wavelength at 532 nm. The results treatment was performed by LabSpec6 *software.*

TEM of the f- GNR obtained from functionalized MWNT SA (GNR MWNT SA) was performed on an Energy Filtered 200kV Transmission Electron Microscope HR-(EF)TEM - JEOL 2200FS. TEM analysis of the GNR obtained from functionalized NC7000 (GNR NC7000) was carried out on a Titan ChemiSTEM 80-200 kV probe Cs corrected microscope. Low-magnification TEM and high-resolution TEM (HRTEM) images were acquired with a GATAN ULTRASCAN 1000 P camera controlled with a Digital Micrograph software integrated in the microscope's user interface. The samples were prepared by adding a drop of the GNR solution onto a lacey carbon Cu grid (300 mesh, Ted Pella) and allowing it to dry under vacuum.

X-rays diffraction experiments were performed on a PANalytical X´Pert PRO XRD System using the Cu Kα1 wavelength of 0.15406 nm from a copper X-ray tube operated at 45 kV and 40 mA. A PIXcel-3D detector was used, and the scan range was from 4 to 40 ° in 2θ. The GNR samples were deposited on glass lamellae by solvent evaporation.

The unzipping process produced functionalized GNRs with widths equal or larger than 35 nm for the GNR NC7000 and 350 nm for the GNR MWNT SA. For this reason, a model of functionalized graphene (**see Scheme 1**), as opposite to finite GNR, was chosen. Graphene layers and their intermolecular interactions were modelled with the MM3 force field that has been found to give accurate intermolecular structures. [382] All the calculations were performed with the TINKER molecular mechanics suite [383] using three dimensional periodic boundary conditions. [384] The shape and dimensions of unit cells containing five functionalized graphene layers with different concentrations of functional groups were systematically obtained by energy minimization.

The stability of the o-GNR and f-GNR solutions was assessed with a Zetasizer Nano-Zs equipment (Malvern Instruments, UK), and at least three zeta potential measurements were performed for each sample. The results presented are the average of these measurements.

3.2.4. Quartz crystal microbalance with dissipation monitoring (QCM-D)

The build-up of the multilayered membranes was followed *in situ* by quartz crystal microbalance with dissipation monitoring (QCM-D; Q-Sense). The resonant frequency (Δf) and dissipation (ΔD) variations were recorded as function of time in the QCM-D. The QCM-D experiments started with alternating deposition of CHI and o-GNR, or, GHI

and f-GNR-ALG. Fresh solutions were deposited for 6 min and a washing step with distilled water for 4 min at a flow rate of 50 µL/min. A temperature of 25 ºC was used for all measurements and the experiments were performed in triplicate. Two different multilayer membranes were obtained, (CHI/o-GNR) and (CHI/f-GNR-ALG)

The results obtained for the multilayer films prepared on the QCM-D were modeled in the QTools *software* using a Voigt based model, which allowed to estimate the shear modulus and thickness of the films, using the flowing equations:

$$\Delta f \approx -\frac{1}{2\pi\rho_0 h_0}\left\{\frac{\eta_S}{\delta_S} + h_L\rho_L\omega - 2h_L\left(\frac{\eta_S}{\delta_S}\right)^2\frac{\rho_L\omega^2}{\mu_L^2+\omega^2\eta_L^2}\right\} \quad (2)$$

$$\Delta D \approx -\frac{1}{\pi f\rho_0 h_0}\left\{\frac{\eta_S}{\delta_S} + 2h_L\left(\frac{\eta_S}{\delta_S}\right)^2\frac{\rho_L\omega}{\mu_L^2+\omega^2\eta_L^2}\right\} \quad (3)$$

where Δf is the resonant frequency variation, ΔD is the dissipation variation, ω is the angular frequency of the oscillation, ρ_0 and h_0 the density and thickness of the crystal, respectively, η_S the solution viscosity, δ_S the viscous penetration depth of the shear wave in the solution, given by (η_S/ρ_S), ρ_S the solution density, and h_L, η_L, μ_L and ρ_L the thickness, viscosity, elastic shear modulus and density of the adsorbed layer, respectively. [385, 386]

3.3. Results and Discussion

3.3.1. Production and characterization of the functionalised graphene nanoribbons

The functionalization reaction of the pristine CNT (NC7000 and MWNT SA) is expected to bond mainly pyrrolidine-type groups at the CNT surface (**Figure 38, compound 1**), although some functional groups may retain the protective group *R* of the amino acid used in the functionalization reaction (*R*=$COOCH_2C_6H_5$, in **Figure 38, compound 2**), as discussed in [160].

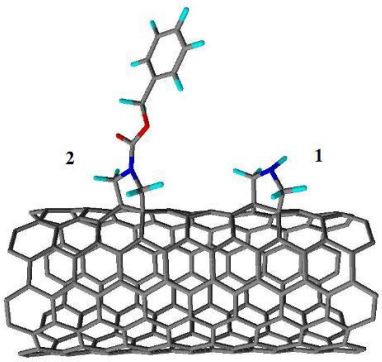

Figure 38: CNT functionalization products (N- dark blue; O- red; H- light blue).

The thermogravimetric analysis (TGA) of the pristine and functionalized CNT (**figure 39**) presented a weight loss of about 14% and 17% for the f-NC7000 and f-MWNT SA respectively. The thermal decomposition was observed above 350 ºC. The TGA of the functionalized GNR was obtained by first subjecting the GNR sample to an isothermal stage at 150 ºC for 1 h, to eliminate remaining ethanol, and then heating from 150 ºC to 700 ºC at 10 ºC/min, under a constant flow of N_2. The weight loss of the GNR at 600 ºC was approximately 76 % for GNR NC7000 and 69 % for GNR MWNT SA. Thermal degradation of the GNR starts at approximately 250 ºC (lower than the corresponding f-CNT), and proceeds up to 500 ºC that may correspond to the degradation of the pyrrolidine functional groups bonded to the GNR (degradation temperature similar to that observed for the corresponding functionalized CNT). It should be noticed that while the CNT contain one functionalized graphene layer (the outer layer), the stacked GNR are expected to have all layers functionalized. Another difference to notice is the presence of edges in the GNR, that are almost absent in the f-CNTs. These edges may be decorated with different functional groups (see reference [74]), and may also present some oxidation level.

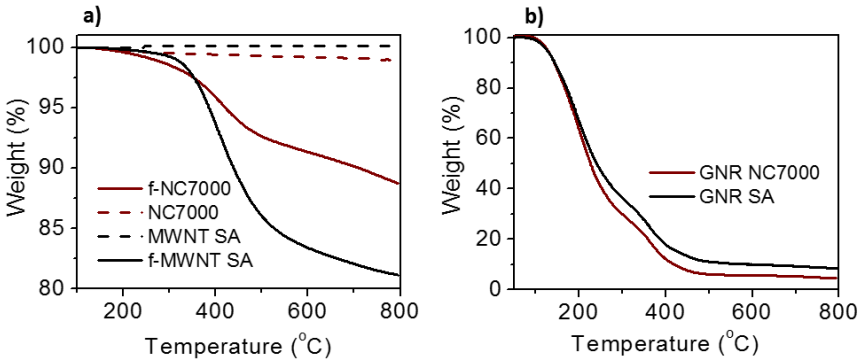

Figure 39: TGA curves of a) functionalized and non-functionalized carbon nanotubes; b) functionalized graphene nanoribbons.

Equal volumes of ethanolic solutions of GNR MWNT SA and GNR NC7000 with similar concentration were deposited on NaCl crystal windows and dried at 150 ºC during 4 hours in an oven. The Fourier transform infrared (FTIR) spectrum (**figure 40**) of the GNR NC7000 present a broad peak centered near 3300 cm^{-1}that may be related to O–H stretching mode. The small peaks located at 3030-3060 cm^{-1} may be associated to aromatic C-H stretching, possibly from edge terminations of the GNR. The peaks near 2920 cm^{-1} and 2850 cm^{-1} correspond to aliphatic C–H stretching vibrations and may be due to CH_2 in the pyrrolidine groups. The peak at 1715 cm^{-1} corresponds to the C=O stretching vibration, presenting two well defined shoulders towards lower wavenumbers, indicating the presence of carboxylic groups and other carbonyl forms (quinone, for example) bonded to the GNR, possibly due to original oxidation of the CNT surface, and to some degree of oxidation during unzipping of the CNT. The spectrum of GNR MWNT SA shows a similar pattern compared to the NC7000 spectrum, although presenting lower intensity, and lower background transmission, that may result from the higher number of layers stacking observed in GNR MWNT SA. Thus, FTIR shows that both GNR types present a similar chemistry

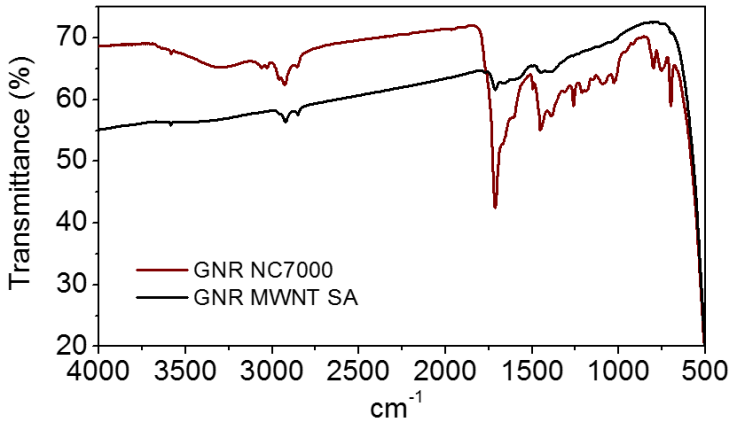

Figure 40: FTIR spectra of graphene nanoribbons

The UV-visible absorption spectra obtained for the GNR solutions are presented in **Figure 41**. The spectra of the solutions of GNR NC7000 and GNR MWNT SA show two shoulders, at approximately 250 nm and 300 nm, similar to the spectra of graphene oxide nanosheets reported elsewhere. [278, 283] These signals were considered indicative of the presence of graphene nanoribbons in solution. The spectra obtained for the blank tests (GNR NC7000 pristine and GNR MWNT SA pristine, **Figure 41**) reveal an absorption spectrum similar to that of the solvent near λ = 230 nm indicating that the sonication

process does not induce the unzipping of the pristine CNTs, or the formation of a detectable amount GNR.

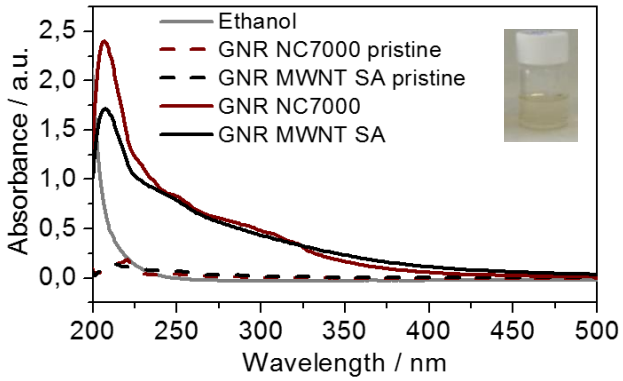

Figure 41: UV-visible spectra of GNR solutions produced from pristine and functionalized NC7000 and MWNT SA, in ethanol. The insert shows a picture of the solution of GNR NC7000 in ethanol.

The weight absorptivity of the GNR in solution was measured by UV-visible spectroscopy at 250 nm, and the values determined were (1600 ± 200) $L.g^{-1}m^{-1}$ for the GNR from f-NC7000 (GNR NC7000) and (2000 ± 100) $L.g^{-1}m^{-1}$ for the GNR from f-MWNT SA (GNR MWNT SA). These results are in the same range of values reported in the literature for graphene solutions. [278, 280] GNR concentrations of 50 and 40 $mg.L^{-1}$ were measured for the solutions obtained by ultrasonication of the f-NC7000 and f-MWNT SA in ethanol, respectively.

GNR were deposited from solution on Si wafers, as well as samples of NC7000 and MWNT SA and analyzed by Raman spectroscopy. The acquired Raman data was typical of sp^2 hybridized carbon, as illustrated in **Figure 42** for all the systems studied. For the carbon nanotubes, the G and D bands appear as prominent features compared to a weaker 2D band. Notably, the spectrum of MWNT SA shows intense G and 2D bands and a smaller D band indicating that these large diameter nanotubes have lower defect contents. [387] The spectra obtained for GNR shows a sharp intense symmetric G band and an asymmetric and blue shifted 2D band, typical of the formation of few-layer GNR. This result is compatible with the stacking of the GNR deposited by solvent evaporation. [283]

Transmission electron microscopy (TEM) images of samples obtained from concentrated ethanol solutions showed the presence of films that likely arise from GNR agglomeration during solvent evaporation. The films from GNR NC7000 samples form smaller domains **(Figure 43a)** compared to those from GNR MWNT SA samples **(Figure 43d).**

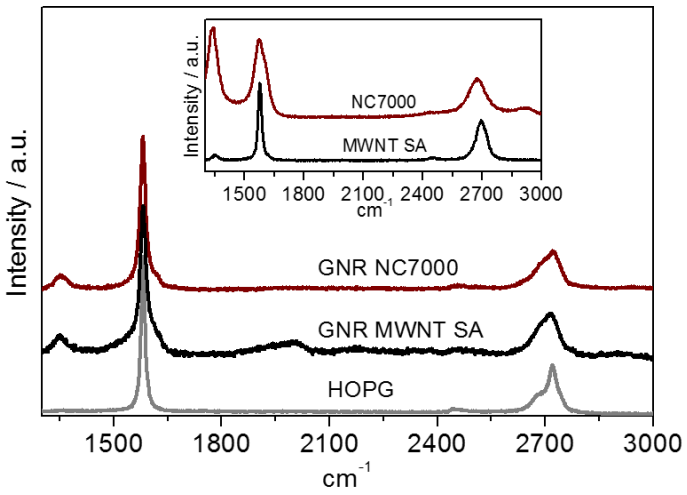

Figure 42: Raman spectra of the CNT (insert) and of the GNR deposited on Si from ethanol solutions. HOPG spectrum is included for comparison

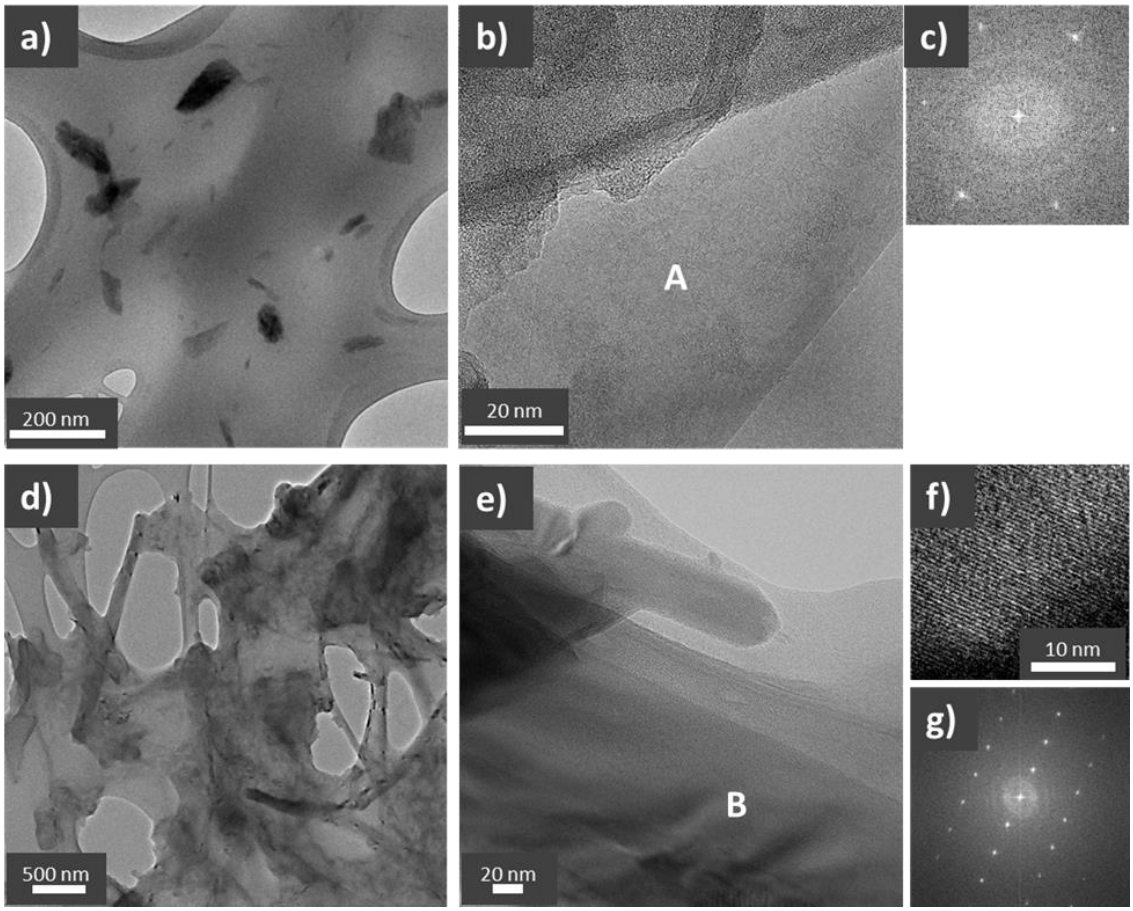

Figure 43: TEM micrographs of GNR formed in ethanol by unzipping of NC7000 (a; b) and MWNT SA (d; e); FFT calculated on the area A, for GNR NC7000, and B for GNR MWNT SA are shown in c) and g), respectively; magnification of the area B in micrograph e) showing the regular pattern (f)

Images from GNR NC7000 were obtained on an 80 kV high resolution TEM, and showed areas with few layers of graphene, such as represented in **Figure 43b**. Fast Fourier transforms (FFT) obtained at the spot marked with A, shown in **Figure 43c**, revealed hexagonal patterns typical of graphene. GNR MWNT SA present larger ribbons and their stacks were robust enough to be imaged on a 200 kV TEM **(Figure 43d and 43e).** The TEM image of **Figure 43e** shows the presence of large stacks of GNR that hamper the observation of the 110 graphene plane. Magnification of the image at the spot marked with **B** illustrates the GNR stacking through the regularly spaced parallel lines **(Figure 43f).** The FFT pattern obtained at the spot B, shown in **Figure 43g**, provides a measure of the interlayer spacing of approximately 0.49 nm. The micrographs also show remaining CNT fragments entangled in the GNR formed.

X-rays diffraction of the GNR NC7000 and GNR MWNT SA was performed on samples deposited on glass slides by solvent evaporation. The X-ray intensity profiles for both GNR NC7000 and GNR MWNT SA exhibited a single peak at 31.68 ° (2θ). This peak is not present on the starting functionalized CNT material **(Figure 44).** The peak obtained for the GNR MWNT SA is sharper than the peak of the GNR NC7000. The average thickness of the crystallites (perpendicular to the crystallographic planes) estimated using the Scherrer equation, was calculated to be 0.81 nm and 2.49 nm for GNR NC7000 and GNR MWNT SA, respectively.

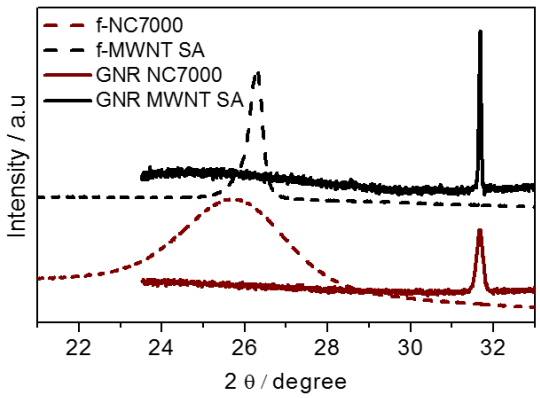

Figure 44: X-ray intensity profiles of the GNR NC7000 and GNR MWNT SA deposited on glass lamella from ethanol solutions (full lines), and of the corresponding f-CNT starting material (dotted lines).

Molecular models were applied to study the effect of the functionalization degree in the interlayer distance, **Figure 45**. Interestingly, very similar distances were found for the highest functionalization densities, namely: 0.54 to 0.51 nm for 8 to 72 graphene layer

carbon atoms per functional group. In contrast, lowering the concentration reduces abruptly the interlayer distance to 0.41 nm for 98 carbon atoms per functional group. This is due to the fact that, at lower densities, the graphene sheets are able to flex to accommodate the functional groups decreasing more efficiently the interlayer density. By further reducing the functional group concentration the graphite spacing is asymptotically approached. At the experimental functional group concentration of 1 group per 50 graphene carbon atoms, an interlayer distance of 0.51 nm is obtained, see **Scheme 1**.

Considering the structure found with molecular modelling (**Scheme 1**), the X-ray diffraction peak observed can be assigned to the 002 set of crystallographic planes considering the c dimension of the unit cell defined as the graphene-to-graphene interlayer distance. From the X-ray data this distance is calculated to be 0.56 nm which is close to the estimated values from molecular modeling, 0.51 nm, and to the value of 0.49 nm measured from TEM micrographs. The average number of graphene layers in these self-assembled stackings, calculated from the X-ray crystallite thickness, is 2-3 for GNR NC7000 and 5-6 for GNR MWNT SA.

It should be remarked that the GNR deposited by solvent evaporation remain soluble, that is, addition of ethanol to the deposited GNR leads to their complete re-solubilization. This phenomenon is probably associated with the larger separation between graphene sheets that allow solvent molecules to readily enter the interlayer void space **(see Scheme 1)** facilitating the exfoliation.

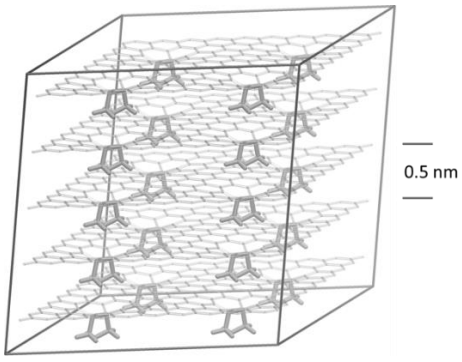

Scheme 1: Computer model of functionalized graphene (one functional group per 50 graphene carbon atoms).

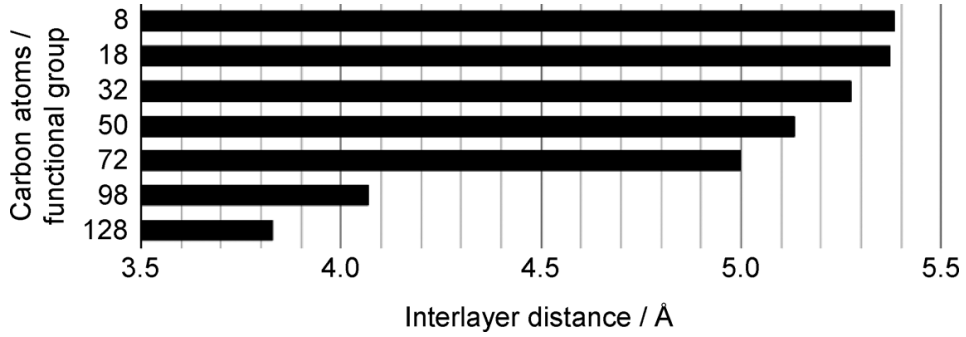

Figure 45: Average interlayer distance (Angstrom) versus functional group concentration (number of graphene carbon atoms per functional group).

3.3.2. Production and characterization of oxidized graphene nanoribbons

The oxidation process by the modified Hummers' method was evaluated on o-CNT (o-NC7000) powders. **Figure 46 a)**, shows that the thermal degradation of o-NC7000 occurs in three steps. A continuous slow degradation was verified until approximately 490 ºC. The weight loss increases at a faster rate in the range of 490 ºC to 590 ºC. These values are in agreement with the results shown by Chen *et al.* [388]. In accordance with the authors, the stability of the slope along the degradation process reveals a high purity of the material. Above 590 ºC, the o-NC7000 degradation decreases slowly, originating a residual weight loss of ≈5%, that may be assigned to metal or metal oxide present in the CNT before the thermal degradation [388]. Below 150 ºC the weight loss may be attributed to the evaporation of strongly adsorbed water. Above this temperature the thermal degradation of the oxygen-containing functional groups (-OH, -COC-, -CO, -COOH, etc) takes place, producing mainly CO and CO_2, leading to a thermal degradation of 39.7%. The residual weigh observed above 800 ºC is mostly constituted by sp^2 carbon. [35, 388, 389]

Raman spectroscopy is a useful technique for graphene-based materials characterization. **Figure 46 b)** reveals three major peaks for the CNT NC7000 pristine (NC7000). The first, near 1350 cm^{-1} (D band), is due to the presence of disorder in the sp^2 carbon lattice of graphene atoms; the second peak at 1580 cm^{-1} (G band) is assigned to the E_{2g} phonon mode of graphite, and results from the in-plane bond-stretching motion of the ordered sp^2 bonded carbon atoms; and the peak at 2700 cm^{-1} (2D band) has almost the double frequency of the D band and results from the second order Raman scattering. Typically, this last peak can be used to determine the number of stacked layers (<10 layers) in few-layer graphene, by the shape, width and position of the peaks. [281, 283, 390] The o-GNR

are characterized by broader D and G bands compared to the NC7000 pristine. The o-GNR show a decrease of I_D/I_G (0.84) compared to NC7000 pristine (1.38). The ratio between these peaks has been used as a method to predict the disorders caused by chemical covalent modification, ripples, edges and charged impurities [391]. In particular, it was reported that the D peak reveals a weak intensity for edges in a zigzag conformation and a stronger intensity if an armchair edge is formed [391]. The behavior observed for the NC7000 pristine may be explained by the high concentration of defects in the pristine form caused mostly by the production technique. As explained previously, the low D peak intensity present on the oxide state may suggest a zigzag edge conformation. The 2D band of o-GNR spectrum show a large decrease in the intensity after oxidation. This is indicative of a significant loss of regular hexagonal sp^2 carbon lattice after the oxidation procedure. Besides, it reveals that the oxidized graphene nanoribbons lost their carrier mobility, as suggested by Zhu *et al.* [391].

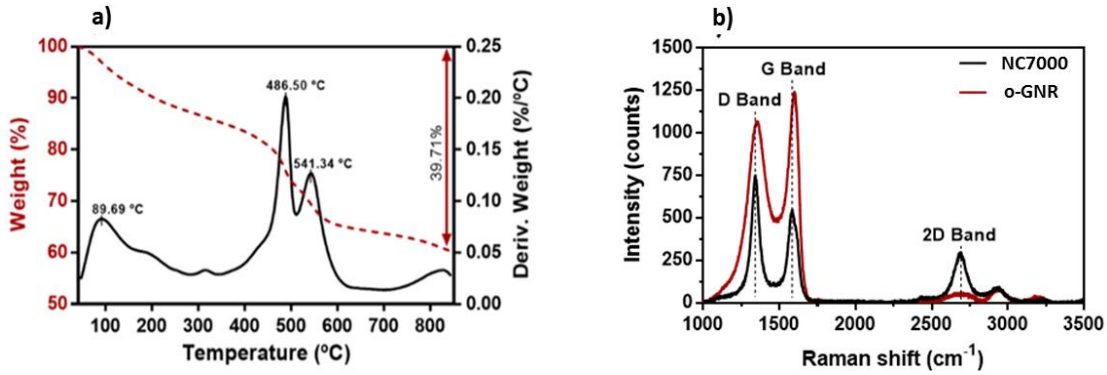

Figure 46: (a) TGA thermogram of o-NC7000, under a heating rate of 10 °C/min; (b) Raman spectra obtained at 532 nm for o-NC7000 and pristine NC7000.

The UV-visible spectra of o-GNR in **Figure 47 a)** shows an absorption band at 247 nm. The UV-visible spectra may be attributed to π→π* and n→π* electronic transitions of the conjugated bonds. The obtained values are in agreement with those reported in literature. [74, 103, 278] FTIR analysis was carried out to characterize the chemistry of the functional groups on the oxidized materials. The resulting spectrum is presented in **Figure 47 b)**. The peak at 1708 cm^{-1} for o-GNR is related with the C=O stretching vibration of carboxyl and carbonyl groups that may originate in ketone [392]. Also, o-GNR present a peak at 1583 cm^{-1} corresponding to the sp^2 C=C stretching vibrations, and therefore this peak is associated with the non-oxidized graphene domains [393]. The peak present at approximately 1420 cm^{-1} may be assigned to the deformation vibrations of C-

OH groups [393]. The peaks observed in the range between 1226-1110 cm^{-1} may be assigned to stretching vibrations of C-O in alkoxy or epoxy groups [394]. Regarding the wide peak observed near 3403 cm^{-1}, it is associated to the O-H stretching vibration and may be due to the presence of intercalated water [395]

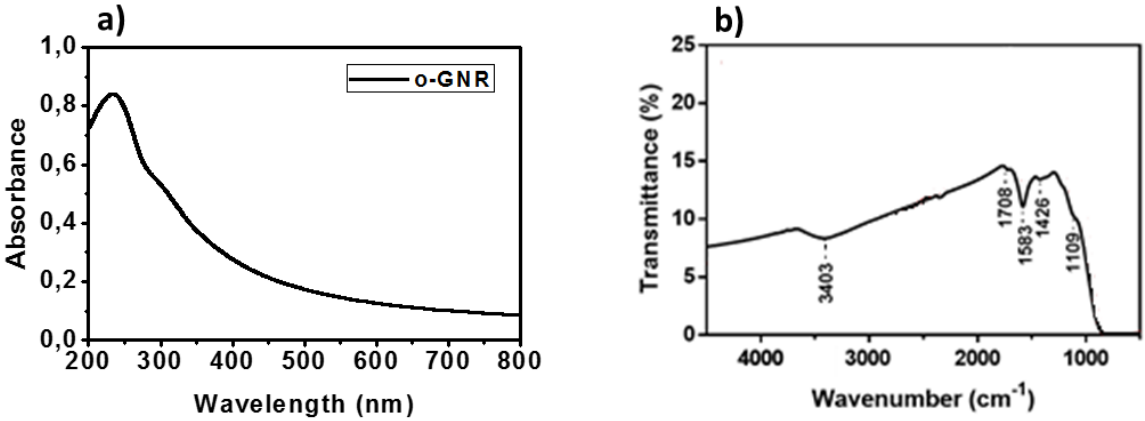

Figure 47: (a) UV-visible spectra of o-GNR (black line) and o-GF (red line) aqueous solution at a concentration of 0.25 mg/mL. (b) FTIR spectra of dried o-GNR (black line) and o-GF (red line).

3.3.3. Layer-by-Layer assembly of graphene nanoribbons and natural polymers: Quartz crystal microbalance with dissipation monitoring (QCM-D)

The stability of the colloidal suspensions of GNR (o-GNR and f-GNR) was characterized by zeta potential (ζ) measurements. o-GNR presents a zeta value of -37±8 mV. According to the literature these ζ values are indicative that o-GNR is capable to form stable suspensions in water, mainly due to the electrostatic repulsion between the particles, provided by the negative charge, which is caused by the ionization of the carboxylic acid and phenolic groups under basic pH conditions. [73, 396] Since the f-GNR (GNR NC7000) solutions are characterized by a low ζ (+2.1 ± 1.3 mV) that does not favor electrostatic interactions with polyelectrolytes required for LbL deposition, a solution of f-GNR and ALG (f-GNR/ALG) was prepared. ALG is a polyanion at pH>3 [385], and may be conjugated with CHT under acidic conditions. [385, 397] A solution of f-GNR-ALG in 25 % ethanol /75 % distilled water was prepared, and its ζ was found to be suitable for LbL deposition (-21.8 ± 0.8 mV). CHT presents a positive ζ of around +13 mV at pH 5.5.

To demonstrate the possibility of assembling multilayers to form membranes using particular of the of CHI/f-GNR-ALG and CHI/o-GNR layers QCM-D technique was

used. This technique is capable of measuring the frequency and dissipation variations in real time. A frequency decrease is the indication of the adsorption of the polyelectolyte and thus demonstrates the possible construction of the multilayer film. The dissipation factor is useful to investigate the viscoelastic properties of the built multilayer film. [398] As shown in **Figure 48**, the decrease of Δf/υ indicates that after either CHI or o-GNR or f-GNR-ALG deposition the polyelectrolyte adsorbs to the crystal surface.

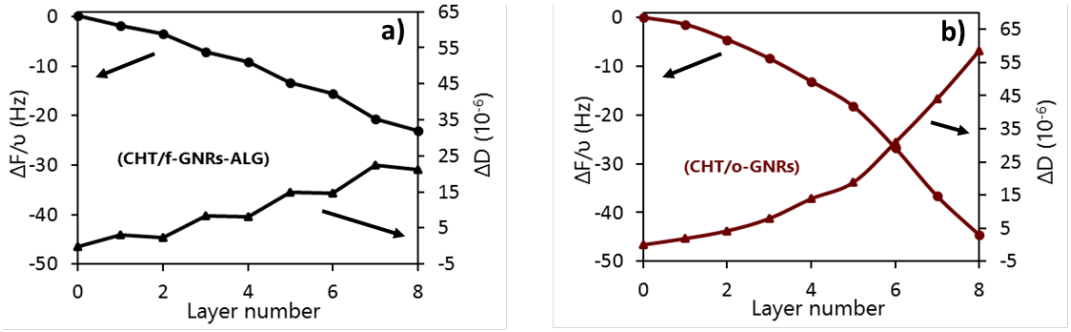

Figure 48: QCM-D results showing the build-up of the (a) CHI/f-GNRs-ALG and (b) CHI/o-GNR membranes as function of the layer number. The normalized frequency (Δf) is represented by circles, and the dissipation (ΔD) by the triangles.

Comparing both formulations, it is clearly observed that the membranes containing o-GNR show the highest frequency decrease and at the same time higher Δ*D*, which in fact indicates that the o-GNR containing membranes may present higher shear modulus. In order to verify this hypothesis, the QCM-D data were modelled using a Voigt based model. **Figure 49** shows the final shear modulus and thickness of the multilayer films produced. As hypothesized, the multilayer film containing o-GNR presented higher shear modulus (318 KPa). The CHI/f-GNR-ALG also presented a high shear modulus (250 KPa) when compared with the control CHI/ALG multilayer film (80 KPa), indicating that f-GNR may also improve the mechanical properties of these films. The thickness of the multilayer films containing GNR (o-GNR or f-GNR) tend to decrease when compared to the CHI/ALG flms. While the CHI/ALG films showed a final thickness (after 8 layers) of 75 nm, the CHI/ o-GNR and CHI/ f-GNR-ALG multilayer films presented a thickness of 65 and 31 nm, respectively (after 8 layers). The decrease of the thickness of the composite fims (containing o-GNR or f-GNR) may arise from their strong interaction with the natural polymer, since these GNR are functionalized, and may result in a denser structure of the composite film, enhancing the mechanical properties. [399] Also, the incorporation of the GNR, which is a rigid material, may affect the adsorption of the CHI leading to a decrease of the amount of adsorbed material and consequently a decrease in the thickness of the composite film. Similar results were obtained by *Guzmán et al*. [400] in where the adsorption of cationic polysaccharide polymers onto negatively charged

substrates was limited by the rigidity of the chains, leading to a decrease of the number of adsorbed chains. Nevertheless, both membrane formulations (CHI/ o-GNR and CHI/ f-GNR-ALG) showed that the sequential deposition process was successfully achieved and it presented a stable and reproducible behavior with the possibility to obtain thicker free-standing membranes.

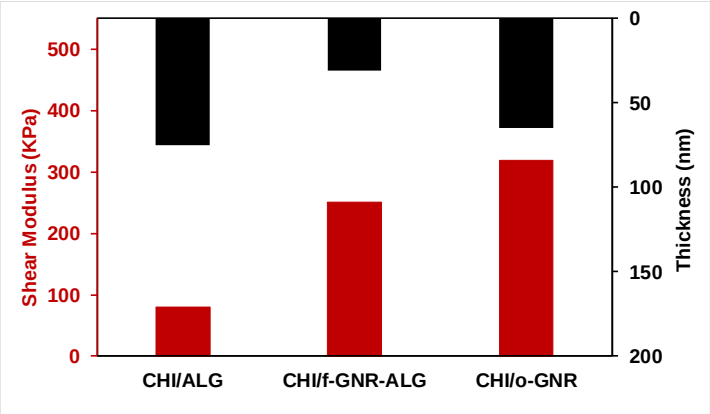

Figure 49: final shear modulus and thickness of the multilayer films produced

3.4. Conclusions

In summary, self-assembled f-GNR stacks were observed and characterized by TEM, X-ray diffraction and Raman. The f-GNR were successfully produced in solution by unzipping of functionalized CNT of different diameters. The CNT were functionalized with pyrrolidine-type groups, originating pyrrolidine-functionalized GNR. Raman spectroscopy evidenced the sp^2 character of the f-GNR. TEM illustrated the formation of larger GNR from CNT with larger diameter, and a tendency of the deposited GNR to form regular stacks with an interlayer distance of approximately 0.5 nm. The formation of regular stacks was confirmed by X-ray diffraction, calculating the stack length as 2-3 f-GNR layers when formed from NC7000, and 5-6 f-GNR layers when formed from MWNT SA. Computer models estimated interlayer distances of similar magnitude and showed that the interlayer distances depend on the concentration of functional groups. o-GNR were successfully produced by oxidation of CNT. The assembly of the multilayered membranes of CHI/f-GNR-ALG and CHI/o-GNR layers was studied by QCM-D technique. Both membrane formulations showed that the sequential deposition process was successfully achieved and it presented a stable and reproducible behavior with the possibility to obtain thicker free-standing membranes with improved mechanical properties.

3.5. Supporting information

Electron microscopy of the carbon nanotubes was performed on a 200 kV Transmission Electron Microscope HR-(EF)TEM - JEOL 2200FS. **Figure 50** shows the TEM images of the multi-wall carbon nanotubes used in this study, illustrating the differences in diameter.

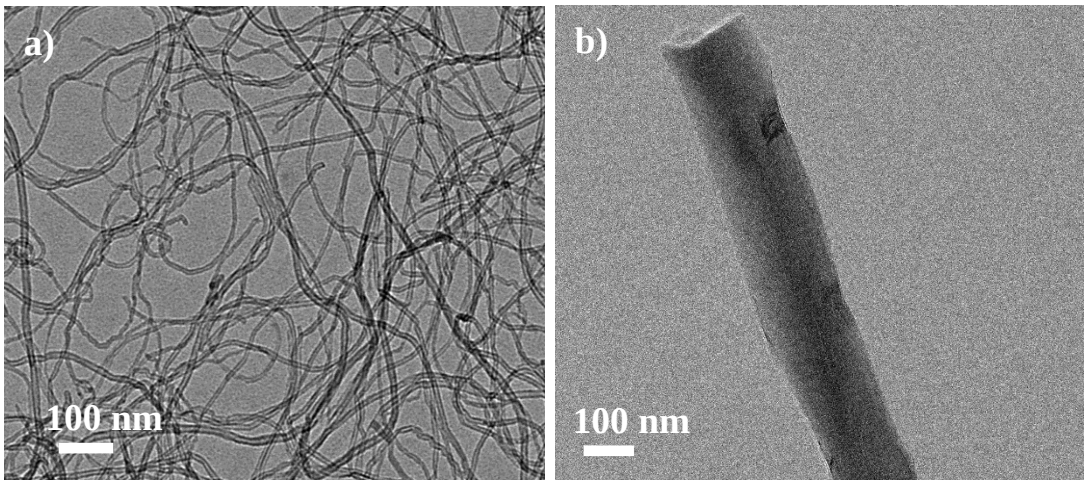

Figure 50 TEM images of a) pristine CNT NC7000 and b) Pristine CNT SA

CHAPTER 4. FEW-LAYER GRAPHENE IN WATER

This chapter is based on the article:

E. Cunha, M.F. Proença, G. Pereira, M. J. Fernandes, R. Young, M. Melle-Franco, P. Lopes, M. C. Paiva, "Few-layer graphene in water" – in preparation;

4. FEW LAYER GRAPHENE IN WATER

4.1. Introduction

Along last decade, graphene has emerged as an exciting material revealing potential applications in various fields. [35, 401, 402] However, the extrapolation of these outstanding properties observed at lab-scale into large-scale industrial applications is limited by the lack of effective methods for graphene production. Liquid phase exfoliation (LPE) of graphite is a potentially viable cost effective process, which can be easily up-scaled to mass-production of graphene and few layer graphene (see section 2.2.1. in chapter 2). Typically, LPE processes occur in organic solvents, although its use in large volumes has negative environmental consequences. Water is a "green" solvent that could overcome this problem. However, it has a high surface tension (72 mJ m^{-2}) which limits its interaction with graphite and graphene, and the ability to form stable suspensions. In fact, solvents with surface tension of near 40 mJ m^{-2} [403] are reported to be ideal for the exfoliation of graphite into graphene [25]. Moreover, due the hydrophobic nature of graphene sheets they tend to re-aggregate in aqueous dispersions. However, the performance of water for LPE of graphite can be largely increased with the aid of amphiphilic molecules that strongly interact with water and with graphene simultaneously. These molecules help the dispersion of graphite flakes and graphene, preventing their aggregation. Polycyclic aromatic hydrocarbons such as pyrene derivatives have been studied for the exfoliation and stabilization of graphene and few layer graphene in water (see section 2.2.1. in chapter 2). The adsorption of pyrene derivative molecules onto the graphene surface occurs via π-π interactions between the planar π-conjugated surfaces while appropriate functional groups attached to the pyrene molecules, which are soluble in water, allows their stabilization in aqueous media. Normally, the pyrene derives reported in the literature, which are used for the exfoliation and stabilization of graphene in water are commercially available. However, the high cost of these compounds may be a limitation for their use. In this chapter, the synthesis of two pyrene derivatives through a simple and low cost functionalization methodology is presented, using as starting compound the pyrene molecule itself. This synthesis methodology lead to a high yield of the final compounds, and can potentially be scaled-up for large scale production. These two pyrene derivatives were soluble in water and they were tested for the exfoliation and stabilization of two different types of graphite nanoplates (GnP) [315] in aqueous media, at low pyrene concentration ($5x10^{-5}$ mol dm^{-}

^{3}). The procedure allowed the stabilization in water of about 90 % of the initial amount of the GnP in which up to 60 % were found to be few layer graphene (< 10 layers). The very low concentration of pyrene derivatives used in this work (to our knowledge, the lowest reported in the literature) to exfoliate graphite in water opens perspectives to an efficient process to obtain few layer graphene.

4.2. Experimental

4.2.1. Materials

Two grades of GnP were purchased from XG Siences, grade C (GnPC) and grade H5 (GnPH5). GnPC has, according to the manufacturer, a size distribution ranging from very small (100 nm) to relatively large flakes (1-2 µm), an average thickness of approximately 2 nm and a typical average surface area of 750 m^2/g, while GnPH5 has a nominal equivalent diameter of 5 µm, thickness of 15 nm, and an average surface area of 60 - 80 m^2/g. Copper (II) nitrate trihydrate ($Cu(NO_3)_2.3H_2O$), anhydrous copper (II) sulphate ($CuSO_4$) and potassium hydroxide pellets (KOH) were purchased from Sigma Aldrich. Maleic anhydride 99 % pellets and pyrene 98 % were purchased from Acros Organics. 4-nitrobenzaldehyde was purchased from Merck. Acetic anhydride (Ac_2O) and sodium borohydride ($NaBH_4$) were purchased from VWR chemicals. Ethyl acetate (EtOAc), petroleum ether 40-60 ºC, ethanol absolute (EtOH) and acetonitrile (ACN) were purchased from Fisher Scientific. Anhydrous magnesium sulphate ($MgSO_4$), dicholoromethane (CH_2Cl_2) and diethyl ether were purchased from Panreac. Deuterated dimethyl sulfoxide (DMSO-d_6, 99.80 %) was purchased from Euriso-top.

The detailed information about the synthesis of the pyrene derivatives is presented in the supporting information.

4.2.2. Preparation and characterization of the exfoliated graphite suspension

The pyrene derivatives were dissolved in distilled water at a concentration of $5x10^{-5}$ mol dm^{-3}, adjusting the pH to 7 by addition of potassium hydroxide (KOH). GnP suspensions were prepared by mixing approximately 5.0 mg of GnP in 10 mL of each pyrene derivative solution using an Ultrasonic processor UP100H from Hielscher, equipped with a sonotrode MS2. Ultrasound energy was applied to the suspensions during 1 h at maximum power. The suspensions were centrifuged (8000 rpm, 1 h) to remove larger

aggregates and the supernatant was collected. These stable suspensions were analyzed by UV-visible spectroscopy on a Shimadzu UV-240 1 PC, using quartz cells with 10 mm pathlength. The concentration was determined using Lambert Beer's Law and the extinction coefficient for these materials was calculated using a procedure reported elsewhere. [25]

The suspensions were sprayed on a glass slide using a XL2000 Airbrush with a 0.4 mm nozzle and analyzed by Raman spectroscopy. Raman spectra were obtained on a Horiba LabRAM HR Evolution confocal microscope using a laser excitation of 532 nm (2.33 eV). A 100x objective lens was used to focus the laser onto the sample. For each sample, 60 spectra were collected and analyzed using the LabSpec 6 software. Lorentzian functions were used to fit the spectra characteristic peaks

Transmission electron microscopy (TEM) samples were prepared by deposition of liquid suspensions of exfoliated GnP samples on 400 mesh carbon coated copper grids (Electron Microscopy Sciences, CF400-Cu) and dried using a heat plate. A voltage of 200 kV was used to image the samples on a CM200 Philips, Holland. The samples were also analyzed by scanning transmission electron microscopy (STEM) using a NanoSEM FEI Nova 200 microscope. The powder samples obtained from solvent evaporation of the same liquid suspensions of exfoliated GnP samples as well as the pristine GnP were analyzed by scanning electron microscopy (SEM) using the same equipment. The thermogravimetric analysis of these powder samples was performed on a Modulated TGA Q500 from TA Instruments. The samples were heated at 10 ºC/min under a constant flow of N_2. The pristine graphite was also analyzed for comparison.

4.3. Results and Discussion

The exfoliation of graphite to generate stable aqueous suspensions of graphene required the preparation of a molecule combining a core unit that would allow an effective $\pi-\pi$ interaction with the graphene layer and a functional group exhibiting a strong affinity for the water molecule. The approach that was used involved the combination of a pyrene ring with a carboxylic acid moiety. The distance between these polar and non-polar groups was adjusted through semi-flexible side arms of different length (structures **2a** and **2b** in **scheme 2**)

4.3.1. Synthesis of pyrene derivative

The water-soluble pyrene derivatives were prepared from pyrene, where the amino substituent was incorporated by nitration (compound **1**) using copper nitrate [404] followed by reduction with sodium borohydride (compound **2**). The 1-aminopyrene **2** was directly combined with maleic anhydride generating a carboxylic acid 3-carbons away from the pyrene core (compound **2a**). Compound **2** was also further reacted with p-nitrobenzaldehyde leading to the imine **3**. Reduction of **3** allowed the transformation of the water-labile imine into a stable secondary amine and the simultaneous evolution of the nitro group to the primary amine (compound **4**). Finally, reaction with maleic anhydride generated the same end-group with the carboxylic acid function further separated from the pyrene ring by a benzyl group (compound **2b**). The sample used in the exfoliation studies was obtained by a one-pot reaction from imine **3**, where the reaction mixture containing amine **4** was directly reacted with maleic anhydride. The product was identified by ^{1}H NMR as a mixture of **2a** and **2b** in a 1:2 ratio.

These two pyrene rings decorated with side-arms of different length ended by a carboxylic acid function and their precursors were fully characterized by FTIR spectroscopy and by ^{1}H and ^{13}C NMR analysis (including bidimensional techniques of HMBC and HMQC).

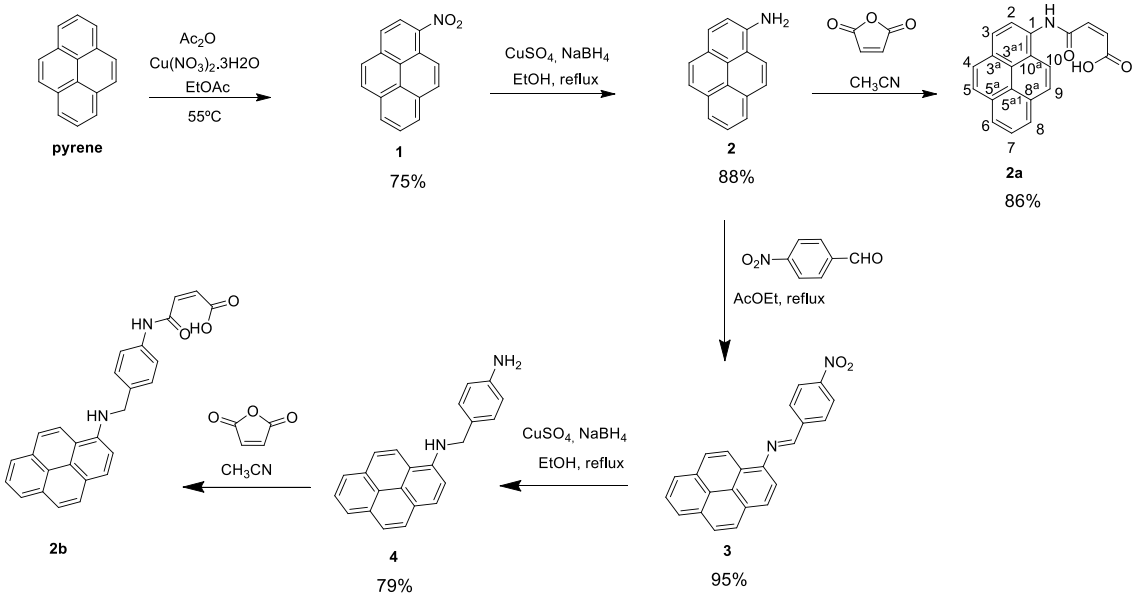

Scheme 2: Schematic representation of the pyrene derivatives synthesis

The spectra are available as supporting information (**Figures 60, 62, 64, 66 and 68**). The structure of compound **2a** was confirmed by the presence of the amide and the carboxylic

acid protons at δ 10.84 and 13.26 ppm, respectively in the ^{1}H NMR spectrum. The *cis* configuration of the exocyclic alkene was supported by the coupling constant between both protons of this functional group (J=12.1 Hz) typical for this isomer. [405] The two carbonyl groups were visible in the ^{13}C NMR spectrum at δ 164.46 ppm (for the amide) and δ 166.84 ppm (for the carboxylic acid). Compound **2b** shows a more elaborate side chain where it is also possible to identify the amide and carboxylic acid protons, by ^{1}H NMR, as singlets at δ 10.39 ppm and at δ 13.08 ppm (broad signal). The methylene group that appears at δ 4.64 ppm in the ^{1}H NMR spectrum, together with the AB pattern of the neighbouring aromatic ring (two doublets at δ 7.42 and 7.56 ppm) confirm the presence of the benzyl group. The *cis* configuration of the alkene was maintained, as evidence by the coupling constant that remains in the typical range for this isomer (J=12.4 Hz). [405] In the ^{13}C NMR spectrum, the signals at δ 163.08 and 166.78 ppm were assigned to the carbonyl groups. The FT-IR spectra are also presented as supporting information (**Figures 59, 61, 63, 65, 67 and 69**). Compounds **1** and **3** present the two characteristic bands of the nitro groups at 1506 and 1331 cm^{-1} and at 1511 and 1338 cm^{-1} respectively, corresponding to the $–NO_2$ asymmetric and symmetric stretching vibrations. After reduction to **2** and **4** respectively, the characteristic symmetric and asymmetric stretching vibrations of the primary amino group can be seen at 3445 and 3379 cm^{-1} (for **2**) and at 3436 and 3376 cm^{-1} (for **4**). Reaction of **2** and **4** with maleic anhydride leads to the final products **2a** and **2b** showing the characteristic intense bands for the stretching vibration of the carbonyl groups at 1711 and 1703 cm^{-1} respectively.

4.3.2. Exfoliation of graphite

The final compounds **2a** and **2b** were tested for their ability to exfoliate the GnP grade H5 (GnPH5) and grade C (GnPC) in water and stabilize the few layer graphene (FLG) formed. Aqueous solutions of these synthesized compounds were prepared at very low concentration ($5x10^{-5}$ mol dm^{-3}). GnPH5 and GnPC were added to the **2a** and **2b** solutions and their exfoliation was carried out by application of ultrasounds. The dispersions were centrifuged and the supernatant was collected analyzed. The same procedure was applied to GnPH5 and GnPC in distilled water without the pyrene derivatives (blank tests). **Figure 51** shows the UV-Visible spectra of these dispersions and their comparison with the initial pyrene derivatives solutions.

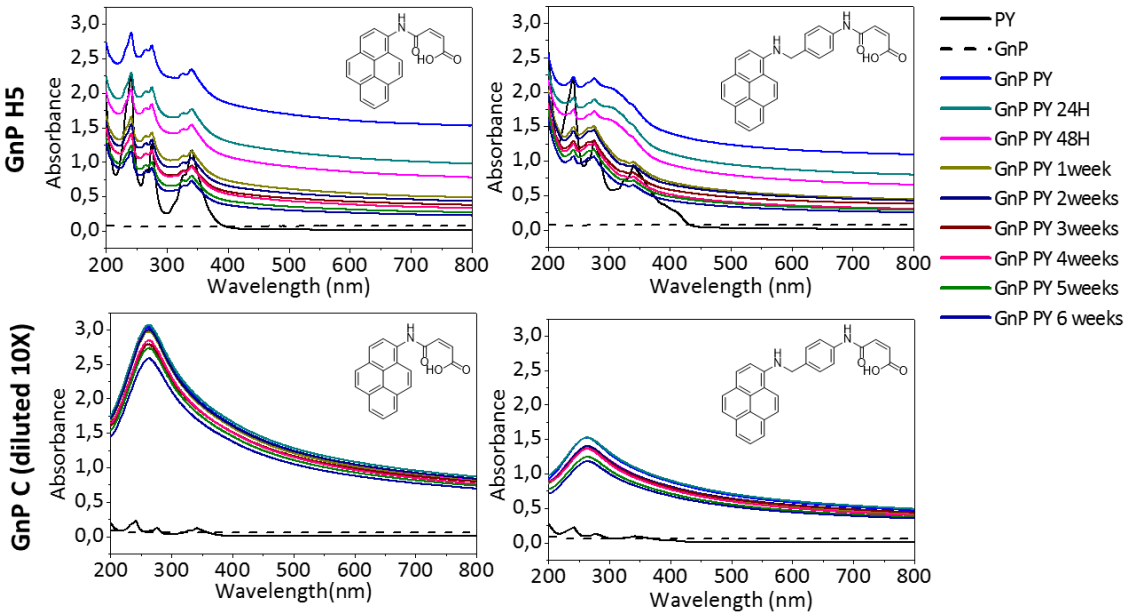

Figure 51: UV-visible spectra of the stable dispersions of exfoliated graphite and the comparison with the initial pyrene derivatives solutions

The initial solutions of the pyrene derivatives show the characteristic peaks between 200 and 600 nm. [98] In general, compared to the absorption of the initial pyrene derivatives solutions, the baseline absorption of all exfoliated GnP dispersions (GnP PY) absorbs over the whole wavelength range, as it was expected for graphene dispersions. [73, 94] Furthermore, the absorption of the GnP PY dispersions showed to be stable along the time even after 6 weeks. For the GnPH5 PY dispersions the original peaks of the pyrene derivatives remain visible, although broader and with lower intensity. This is the fingerprint of the π-π interactions between these functionalized aromatic compounds and exfoliated graphite. [98] This observation was also reported for single walled carbon nanotubes dispersed in water/pyrene-derivative solutions. [406] For the GnPC PY, the suspensions obtained after centrifugation were highly concentrated, resulting in the saturation of the absorption peaks. The spectra presented in the **figure 51** were obtained for the diluted suspensions (10x dilution), producing an absorption peak with a similar shape as the absorption peaks reported for graphene and graphene oxide in solution. [71, 98, 407] Moreover, the original peaks of the pyrene derivatives are not visible probably due the high concentration of GnPC in suspension. The absorption observed for the blank tests (dashed lines) showed very low intensity in the whole wavelength range indicating that the pyrene derivatives play an important role in the stabilization of these GnP in water. The extinction coefficient of the exfoliated GnP in water was measured from UV-visible spectra, at 660 nm, yielding the values of 2100 ± 100 $Lg^{-1}m^{-1}$ for GnPH5 and 2200

± 100 $Lg^{-1}m^{-1}$ for GnPC. These results are in the same range as other values reported in the literature [25, 98] Based on the extinction coefficient values obtained, the estimated concentration of GnP in suspension along the time varies as represented in **(figure 52**).

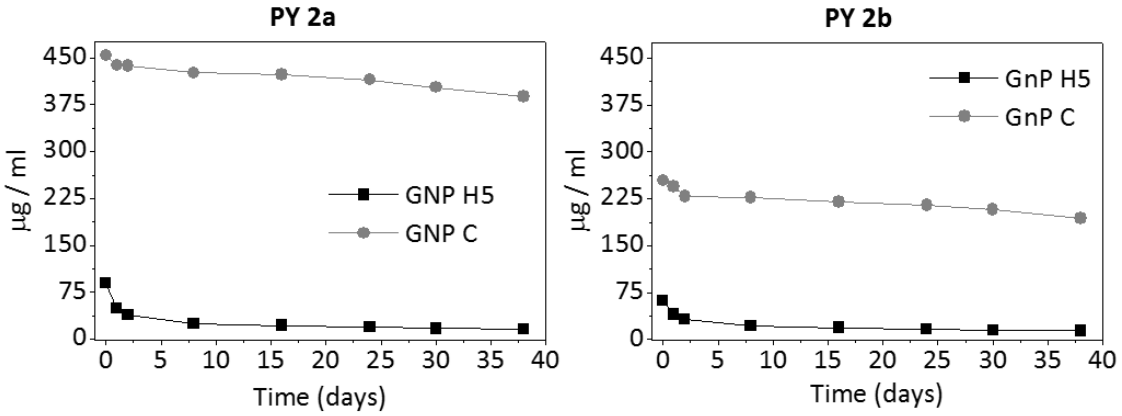

Figure 52: concentration of GnPH5 and GnPC in water.

Immediately after the suspensions were prepared the concentration of GnPH5 using the pyrene derivative **2a** and **2b** was 90 µg/mL (18%) and 62 µg/mL (13%), respectively. For GnPC the concentration in suspension using the same pyrene compounds was 454 µg/mL (90 %) and 254 µg/mL (51 %), respectively. The % yield of GnP in suspension was calculated taking into account the initial concentration of GnP prior to exfoliation (approximately 500 µg/mL). The GnPC has a higher yield of nanoparticles in aqueous suspension probably due to their smaller dimensions, compared to GnPH5, that facilitate the exfoliation process. Furthermore, the GnPC atomic concentration of oxygen is approximately 7 %, while for GnP H5 it is lower than 1 %, according to the producer. Thus, GnPC present a higher oxidation degree compared to GnP H5, a fact that may also influence its dispersibility in water. However, it should be noted that in the absence of the pyrene derivatives the GnP C *per se* is not stable in aqueous dispersion, as was demonstrated by the UV-visible analysis (blank tests, **figure 51**).

In any case the yield of 13 % and 18 % obtained for the GnPH5 suspensions is quite relevant when compared with the values reported in the literature for similar systems showing yields from 1.0 to 2.5 %. [26, 93, 94, 98]

Figure 53 shows the thermogravimetric curves of the pristine and exfoliated GnP as well as the pyrene derivatives. Both compounds **2a** and **2b** show a residue that remains at 800 °C with a total weight loss at this temperature of 76 ± 2% for pyrene **2a** and 63 ± 1% for pyrene **2b.** Considering the boiling point of pyrene to be approximately 400 °C, this

residue indicates that the functionalized pyrenes can combine during heating under nitrogen, forming heavier molecules that remain stable at 800 °C. The TGA curve of pristine GnPH5 is characteristic of a thermally stable material, with a weight loss of 3,5 % at 800 °C. At the same temperature, the weight loss of the exfoliated GnPH5 using **2a** and **2b** compounds is 20 ± 1% and 25 ± 2%, respectively, and these weight losses are related with the decomposition of the pyrene derivative molecules adsorbed on the GnP surface. The weight loss of pristine GnPC at 800 ºC is 7.5 %, larger than that observed for GnPH5, possibly due to the larger content of oxygen containing groups of the former. The GnPC exfoliated using both pyrene derivatives presented a weight loss at 800 ºC of 27 ± 4 % for compound **2a** and 18 ± 2% for compound **2b**, values that are similar to those observed for GnPH5 in spite of the much larger surface area of GnPC.

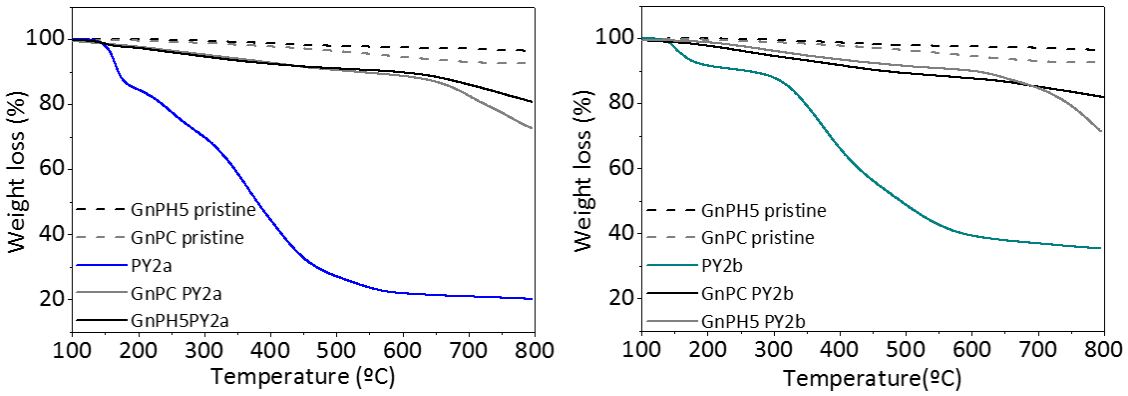

Figure 53: TGA curves of the pristine and the exfoliated GnP

The weight of PY**2a** and PY**2b** adsorbed at the surface of each GnP was estimated by a simple mass balance, considering the TGA residual weights at 800 ºC. The results, expressed in terms of the weight of PY (in mg) adsorbed on the GnP (per mg of pristine material) are as follows: GnPH5 adsorbed 0.29 mg/mg of PY2a and 0.61 mg/mg of PY2b, while GnPC adsorbed 0.38 mg/mg of PY2a and 0.23 mg/mg of PY2b.

Raman spectroscopy is an important tool for the characterization of graphene samples. For a single-layer graphene, which represents the fundamental sp^2 carbon hexagonal lattice, the Raman spectrum presents three main characteristic bands, associated to the G, D and G' (or 2D) modes. The G mode, observed near 1580 cm^{-1}, has E_{2g} symmetry, and reflects the in-plane bond stretching motion of pairs of C sp^2 atoms, [390] relating to the planar configuration of the sp^2 bonded carbon typical of the graphene structure. Due to the strong C-C bonding in graphene the G band is observed at a relatively high Raman frequency in comparison to other materials, and very small perturbations to the frequency

of the G band can be measured. The frequency of the G band is independent of the laser excitation energy (E_{laser}), however it is sensitive to the temperature, strain and doping of the graphene sample. The D mode, observed near 1350 cm^{-1} at 2.41 eV (514nm) laser excitation energy, is a breathing mode of A_{1g} symmetry, forbidden in perfect graphene, becoming active in the presence of disorder. Its presence indicates the existence of a hexagonal sp^2 carbon network disturbed by chemical bonding that reduces the hexagonal network symmetry, such as observed adjacent to a graphene edge or a defect. Thus, the D band is known as a disorder mode, or defect band The D mode is highly dispersive as a function of the E_{laser}. The 2D mode is the second order of the D mode, sometimes referred as an overtone of the D band. However, it is not related to the defects of graphene structure and thus the 2D band is always strong in graphene even when the D band is absent. Furthermore, the shape and the position of the 2D band can be used to identify the number of graphene layers. [273] In the case of the single layer graphene the 2D band is twice the intensity of the G band. Also, this band may be fitted with a single Lorentzian function with a full width at a half maximum (FWHM) near 24 cm^{-1}. Bilayer graphene typically displays a G band with higher intensity compared to the 2D band. The fitting of the 2D band in bilayer graphene requires four characteristic Lorentzian functions, each with a FWHM of ~24 cm^{-1}. Moreover, the 2D band is shifted to higher frequency in bilayer graphene and has a different shape. As the number of layers increases the 2D band moves to higher wave number and becomes broader and more asymmetric in shape. Its deconvolution becomes more complex, and for few-layer graphene (less than 10 layers) it may be fitted with three Lorentzian functions with a FWHM higher than 24cm^{-1} each. For more than 10 layers the 2D band becomes very similar to that of graphite, that can be deconvoluted in two Lorentzian functions. [282, 283].

Figure 54 shows the Raman spectra of pristine GnP and non-covalently exfoliated GnP using the pyrene derivatives **2a** and **2b**.

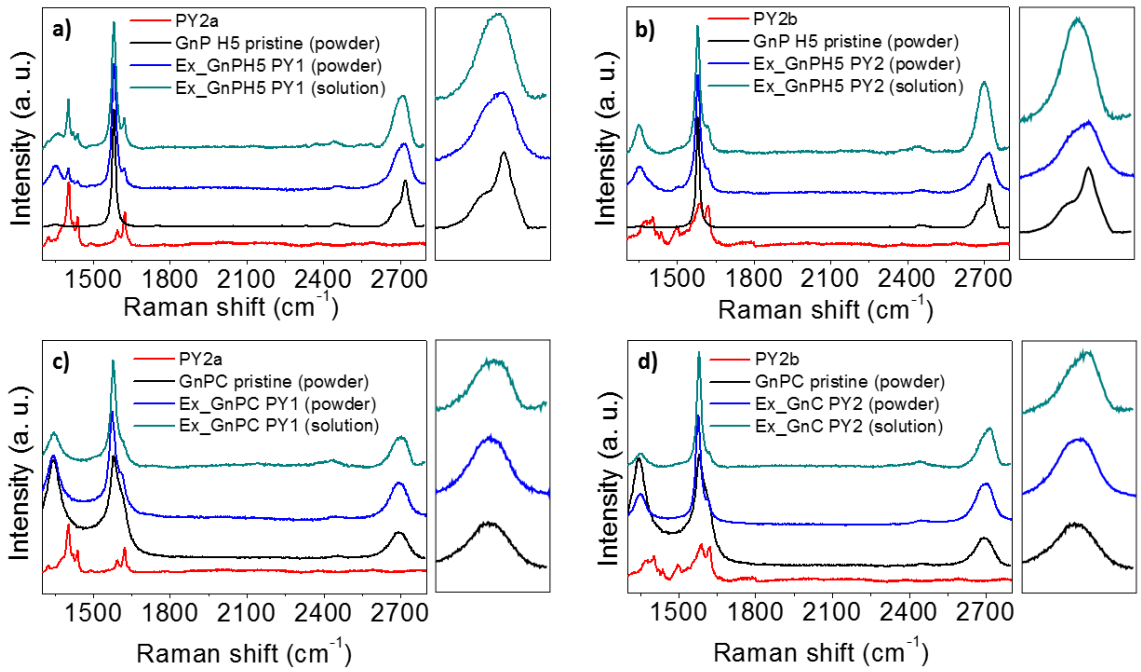

Figure 54: Raman spectra of pristine graphite and non-covalently exfoliated graphite using the different pyrene derivatives.

The Raman spectrum of the pristine GnPH5 has the typical shape of graphitic materials. The D band, at 1350 cm^{-1} is almost inexistent compared to the G band (at 1581 cm^{-1}) which indicates the good structural quality of the pristine graphite. The 2D band position of the pristine GnPH5 occurs at 2722 cm^{-1}. After the exfoliation process with pyrene derivatives **2a** and **2b** in solution (**figure 54a and 54b**) the Raman spectra obtained for the materials deposited on a glass slide showed the presence of FLG and higher exfoliation products such as bilayer graphene. The bilayer graphene presents a symmetric 2D band centered at 2702 cm^{-1} that may be deconvoluted using four Lorentzian functions (**figure 55b**). The D band of the exfoliated material presents higher intensity than the pristine GnPH5 flakes and this fact can be related with the presence of the pyrene derivatives on the surface of the exfoliated GnP. [97] Also, the characteristic peaks of the pyrene derivatives can be observed in these spectra. The Raman spectra of the exfoliated GnPH5 in powder from, obtained from solvent evaporation of the stable suspensions (after the exfoliation process), showed a more symmetric 2D band compared to the pristine GnPH5, centered near 2712 cm^{-1}. This 2D band can be fitted with three Lorentzian functions (**figure 55b**), which is consistent with the presence of few-layer graphene. **Figures 54c and 54d** show the Raman spectra of the pristine and exfoliated GnPC, obtained using the pyrene derivatives **2a** and **2b**. The spectra of the pristine GnPC shows a prominent D band near 1350 cm^{-1}, with a slightly higher intensity than the G

band (at 1581 cm^{-1}) which may be related to the smaller flake size, and thus higher edge-to-basal plane ratio, as well as to a higher initial oxidation, in agreement with the TGA analysis. The 2D band position occurs near 2692 cm^{-1} showing high symmetry, although with lower intensity compared to the G band. After the exfoliation process, the D band has a lower intensity relative to the G band, which may result from the selective adsorption of the more graphitic (less oxidized) flakes by the pyrene derivatives. The less "defective" GnPC may adsorb higher amounts of pyrene, and thus are more stable in aqueous suspension. A statistical analysis of the GnPC spectra shows the presence of 2D bands similar to those of the pristine material, but also typical of FLG, for the exfoliated GnPC. [282].

A statistical analysis of the flakes formed was reported by Schlierf *et al*. [28] that studied the exfoliation of graphite in water using pyrene derivatives with different functional groups. The distribution in sheet thickness and the presence of monolayers were measured by a statistic analysis of the 2D band performed on 60 to 70 different flakes for each pyrene derivative used. Also, Jang and co-workers [408] performed a statistical analysis and studied the deconvolution of the 2D band of about 105 different sample spots to identify mono layer and few layer graphene. The authors reported the exfoliation of graphite using the 1-pyrene sulfonic acid sodium salt by in situ supercritical fluid ethanol exfoliation. In the present work, a statistical analysis of the graphene flake structure was performed by collecting the Raman spectra of sixty different flakes across each sample (GnPH5 PY2a, GnPH5 PY2b, GnPC PY2a and GnPC2b). After the exfoliation procedure, the spectra of bilayer and FLG were identified. **Figure 55a** shows the yield of bilayer, FLG, and pristine flakes after the exfoliation process, for all samples.

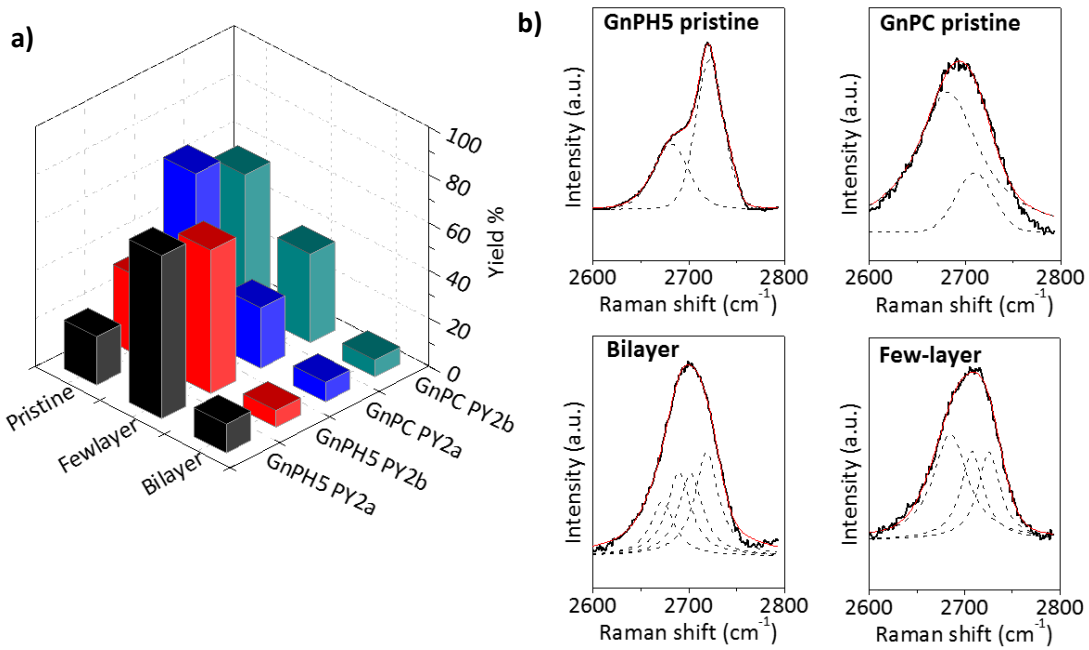

Figure 55: a) Yield of exfoliation process for the GnPH5 and GnPC; b) Lorentzian features of the deconvoluted 2D band of the pristine materials, bilayer and few layer graphene.

The spectra identified as "pristine" quantifies the fraction of non-exfoliated material. It should be noted that the pristine GnP C is an expanded graphite already formed by thin flakes, as demonstrated by its Raman spectrum. The FLG and bilayer graphene spectra were identified based on the position of the 2D band and its deconvolution. Typically, the 2D band of bilayer graphene occurred at 2702 cm^{-1}, presenting a symmetric shape that could be deconvoluted using four Lorentizan functions with a FWHM of about 24 cm^{-1}, shown in **figure 55b**. For FLG the 2D band position occurred between 2706 cm^{-1} and 2712 cm^{-1}, with a more asymmetric shape compared to bilayer graphene, and deconvoluted using three Lorentizan functions (**figure 55b**). The analysis demonstrated that the pyrene derivative **2a** led to 12 % of bilayer graphene, 68 % of FLG and 20 % of non-exfoliated GnPH5, while for GnPC it led to 8 % of bilayer, 25 % FLG and 67 % of the pristine material. The pyrene derivative **2b** led to 7 % of bilayer graphene, 60 % of FLG and 33 % of non-exfoliated GnPH5, while for GnPC it led to 7 % of bilayer graphene, 37 % of FLG and 56 % of the pristine material. The results are summarized in **figure 55a**, showing that the pyrene derivative **2a** was more effective for the exfoliation of GnPH5 leading to the formation of overall 80 % of bi- and few-layer. Schlierf *et al.* [28] reported a similar result for the exfoliation of graphite using a mono substituted pyrene derivative (1-pyrene sulfonic acid). The authors obtained a yield of exfoliation of 86% (a total of single- to few-layer), however using a higher concentration of pyrene

derivative ($3.3x10^{-4}$ mol dm^{-3}) and longer sonication time (5 to 35 hours) compared to the conditions used in this work.

In the case of the GnPC, PY **2b** led to the formation of a higher amount of bi- and few-layer graphene, however, being the pristine GnPC an exfoliated material, the formation of few layer graphene may result from some stacking of layers, although it is still less than 10 layers.

Figure 56 shows SEM and STEM images of the pristine GnPH5 as well as the exfoliated GnPH5. The SEM images show GnPH5 flakes that appear thinner after exfoliation. STEM images also show thin flakes of GnPH5 treated with both pyrene derivatives.

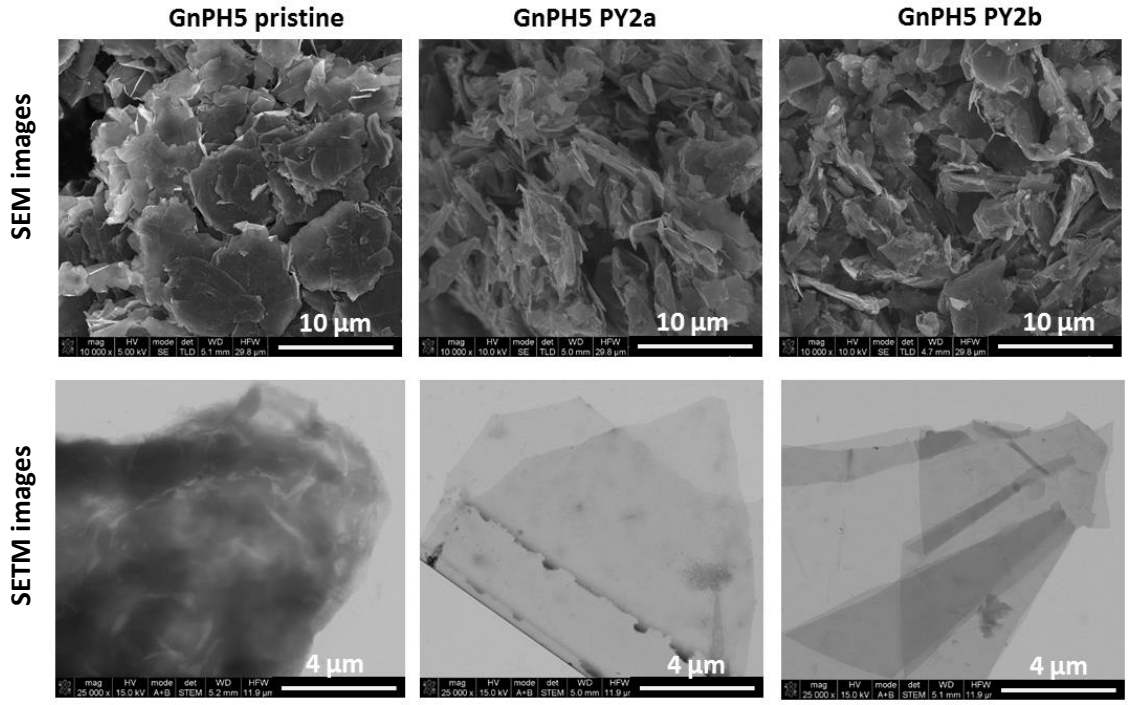

Figure 56: SEM and STEM images of the pristine and exfoliated GnPH5

Figure 57 shows SEM and STEM of the pristine and exfoliated GnPC. The GnPC flakes are small and agglomerated, and may be dispersed forming suspensions in water.

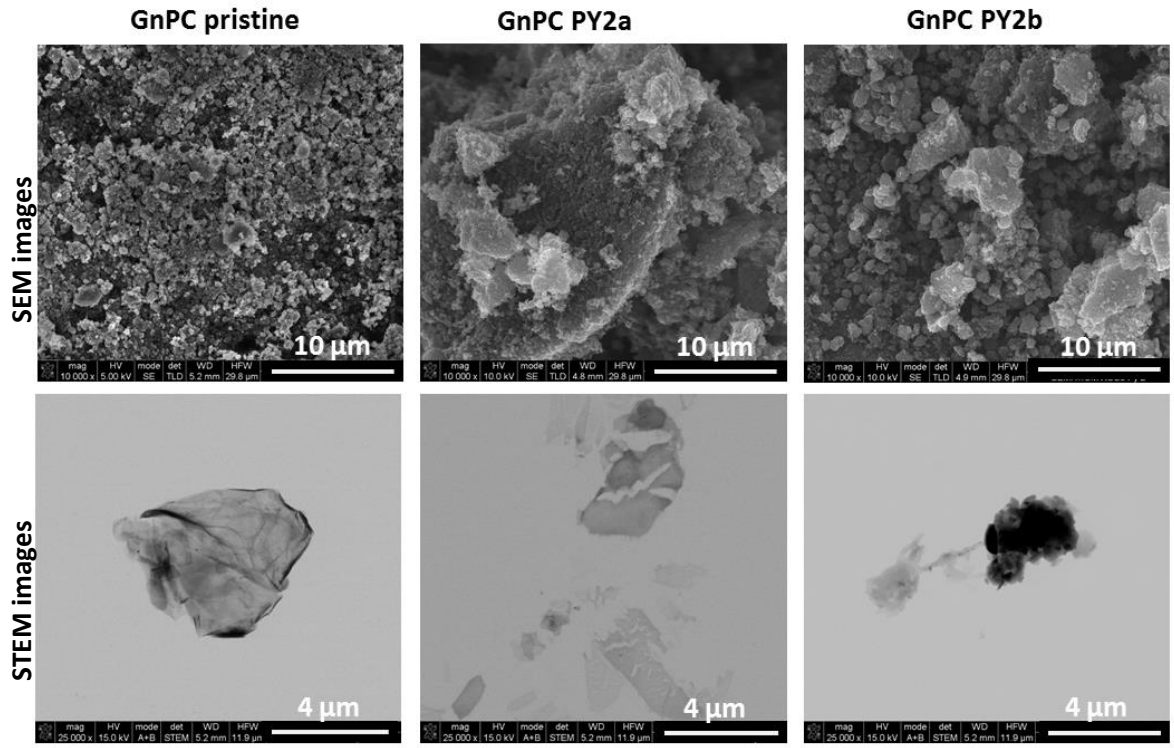

Figure 57: SEM and STEM images of the pristine and exfoliated GnPC

The GnP suspensions obtained using the pyrene derivative **2a** were analysed by TEM (**figure 58**). The images revealed the formation of few layer graphene and the electron diffraction of the amplified TEM image showed the typical hexagonal pattern of graphitic materials.

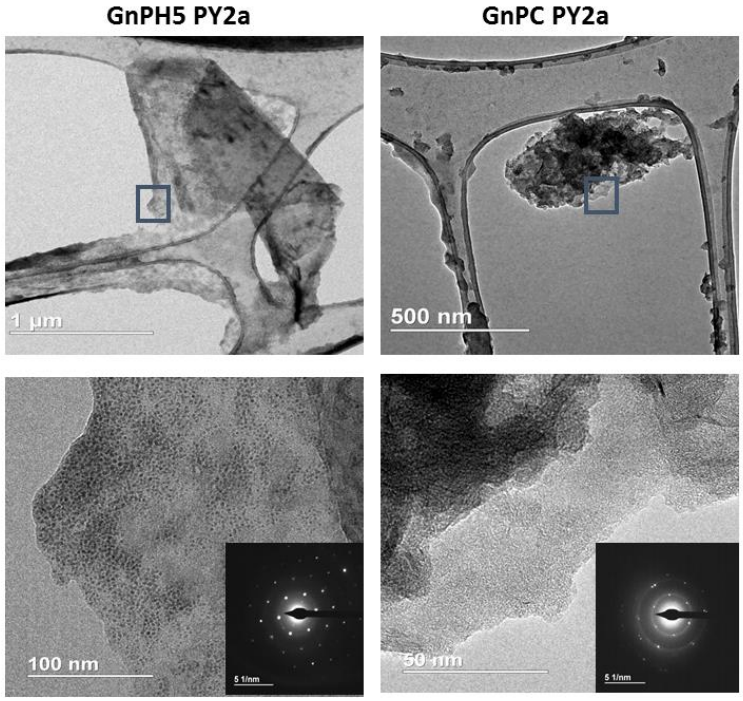

Figure 58: TEM image a) and amplified TEM image b) of exfoliated graphite using pyrene derivative 1;

4.4. Conclusions

In summary, two pyrene derivatives were synthetized (PY **2a** and PY **2b**) through a simple and low cost functionalization methodology which lead to a high yield of the final compounds, and can potentially be scaled-up for large scale production. These two pyrene derivatives were soluble in water and they were tested for the exfoliation and stabilization of two different types of graphite nanoplates (GnP) in aqueous media. The pyrene derivative **2a** showed to be more effective in the exfoliation process leading to a formation of 80% of a total of bi- and few-layer graphene for GnPH5. The few layer graphene was also confirmed by STEM images. The very low concentration of pyrene derivatives used in this work (to our knowledge, the lowest reported in the literature) to exfoliate graphite in water opens perspectives to an efficient process to obtain few layer graphene.

4.5. Supporting information

Synthesis of the pyrene derivatives

The NMR spectra were recorded on a Varian Unity Plus ($_1$H: 300MHz, ^{13}C: 75MHz) or on a Bruker Advance III 400 (^{1}H: 400Mz, ^{13}C 100 Mz) including the ^{1}H – ^{13}C correlation spectra (HSQC). Deuterated DMSO-d_6 was used as solvent. The chemical shifts are

expressed in δ (ppm) and the coupling constants, *J*, are reported in hertz (Hz). The peak patterns are indicated as follows: s, singlet; d, doublet; t, triplet; m, multiplet; q, quartet and br, broad. Fourier Transform Infra-red spectra were recorded on a Spectrum 100 Perkin-Elemer apparatus in transmission mode using NaCl pellets.

1-Nitropyrene (1) was prepared according to a reported procedure. [404] Briefly, $Cu(NO_3)_2.3H_2O$, (6.20 g, 27.70 mmol) was added to a mixture of pyrene (4.00 g, 19.80 mmol) and acetic anhydride (5.20 mL, 55.40 mmol) in ethyl acetate (50 mL). The mixture was stirred at 55ºC for 20 h and a thick yellow precipitate formed. The reaction mixture was cooled to room temperature and the inorganic materials were filtered off. The crude product obtained by removal of the solvent in the rotary evaporator was purified by column chromatography using a silica gel column (3.20 cm x 19.00 cm, 10 -60% CH_2Cl_2/ petroleum ether) to give the pure product (3.70 g; 75 %). The FTIR spectrum is presented in **figure 59.**

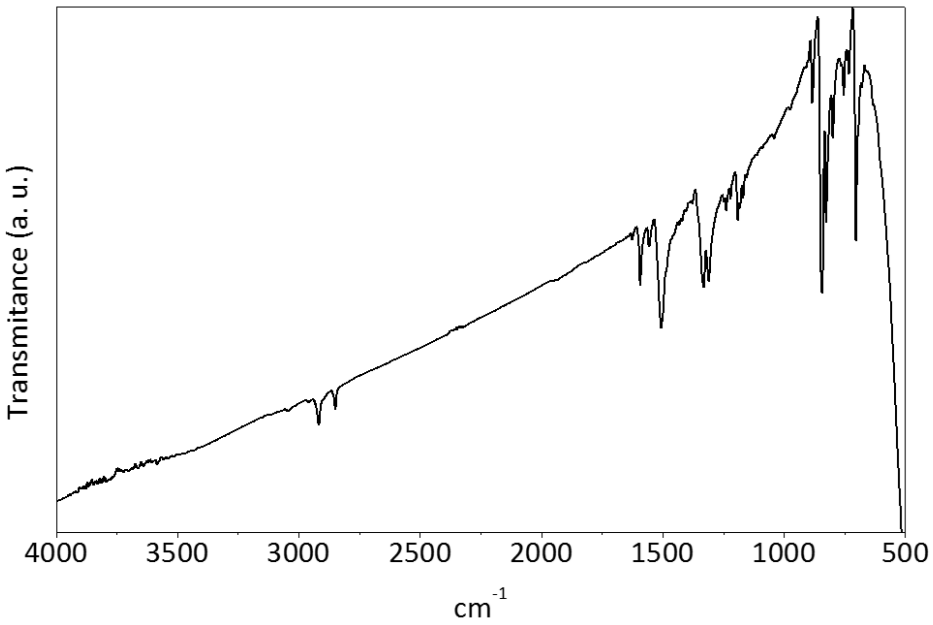

Figure 59: FTIR spectra of the 1-Nitropyrene (1)

1-Aminopyrene (2): 1-Nitropyrene (**1**) (13.50 mmol, 3.30 g) was dissolved in ethanol (200 mL), the mixture was cooled in an ice bath, and copper (II) sulfate (32.40 mmol, 5.20 g) was added. After stirring for 10 min, sodium borohydride (67.50 mmol, 3.80 g) was added slowly during 15 min. The mixture was refluxed overnight, cooled to room temperature and the solvent was removed in the rotary evaporator. The reaction mixture was dissolved in dichloromethane (100 mL) and water (100 mL) was added. The aqueous layer was extracted with dichloromethane (3 x 30 mL), and the organic layers were washed with brine (2 x 30 mL) and dried with $MgSO_4$. Removal of the solvent in the rotary evaporator gave compound **2** (2.40 g, 82 %). ^{1}H NMR (400 MHz, DMSO-d_6): δ (ppm) 6.32 (s, 2H, -NH2), 7.40 (d, *J* = 8.3 Hz, 1H, H2), 7.71 (d, *J* = 8.8 Hz, 1H,H5), 7.86 (t, *J* = 7.7 Hz, 1H, H7), 7.88 (d, *J* = 8.8 Hz, 1H, H4), 7.92 (d, *J* = 9.3 Hz, 1H, H10), 7.97 (d, *J* = 8.4 Hz, 1H, H2), 7.98 (d, 1H, H6), 7.99 (d, 1H, H8), 8.29 (d, J = 9.2 Hz, 1H, H9). ^{13}C NMR (100 Mz, DMSO-d_6): δ (ppm) 113.13 (C2), 114.72 (C3^a), 121.39 (C10^a), 121.76

(C5), 122.13 (C9), 122.37 (C6), 122.91 (C8), 124.14 (C10), 125.14 ($C3^{a1}$), 125.70 ($C5^{a1}$), 125.85 (C7), 126.52 (C3), 127.70 (C4), 131.67 ($C8^{a}$), 132.02 ($C5^{a}$), 144.36 (C1).
The NMR spectra is presented in **figure 60**.

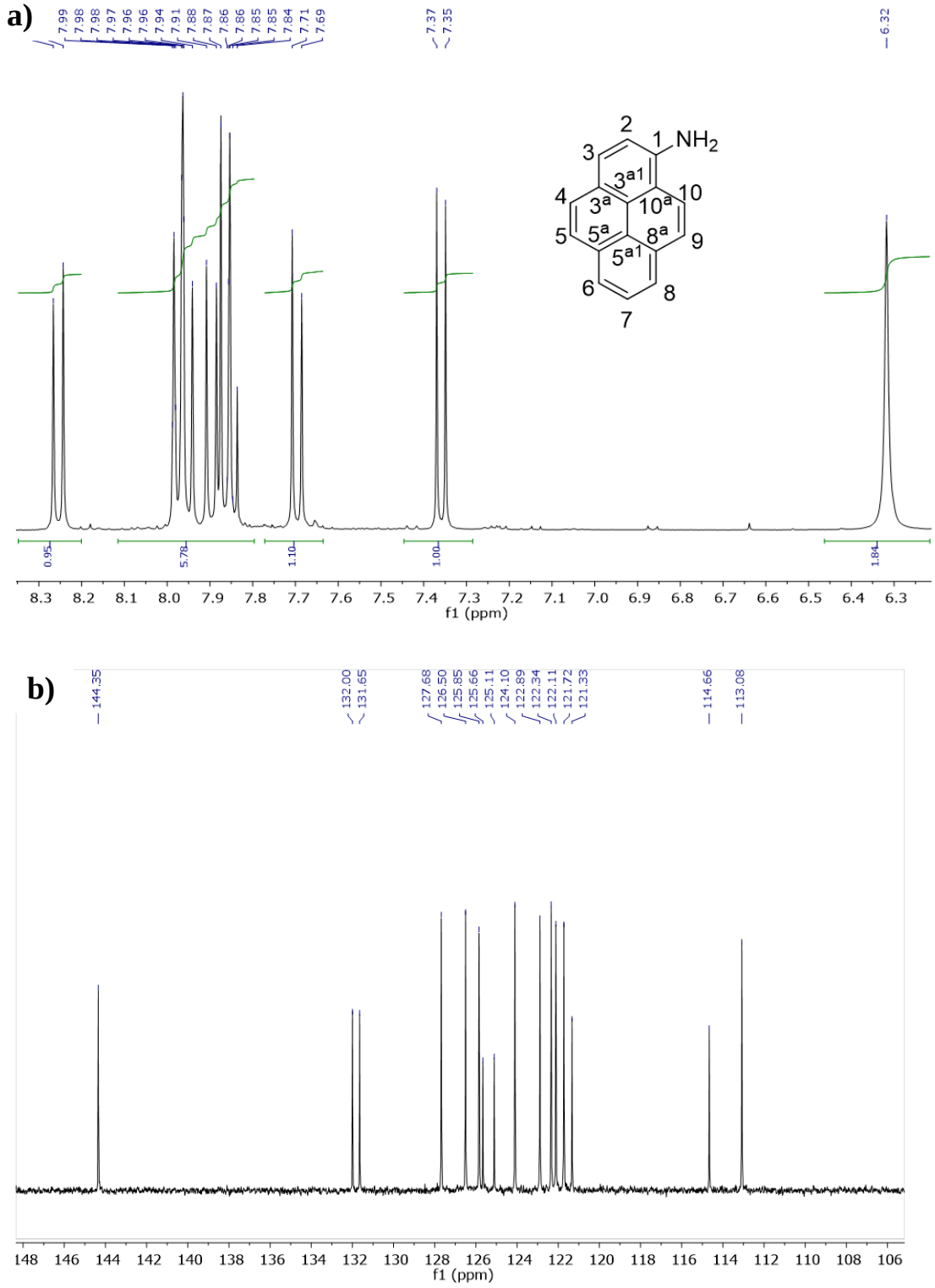

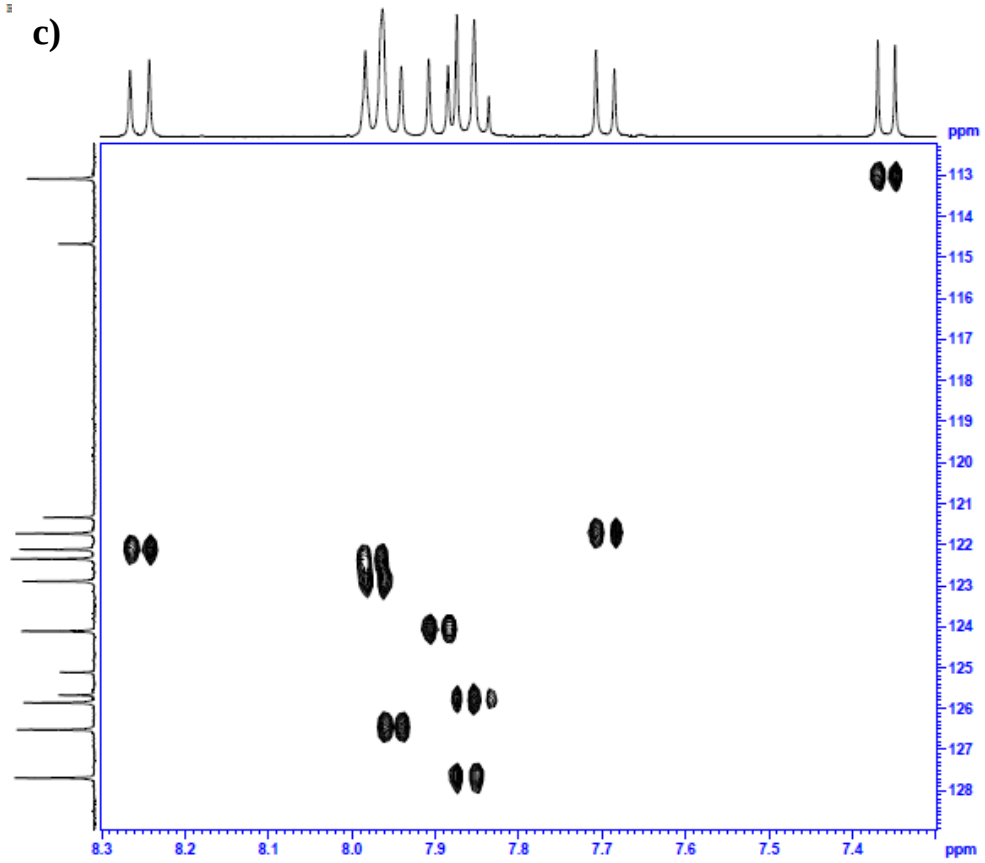

Figure 60: NMR spectra of 1-Aminopyrene (2): a) ^{1}HNMR; b) ^{13}C NMR; and c) 2D HSQC (Heteronuclear Single Quantum Correlation).

The FTIR spectra is presented in **figure 61**.

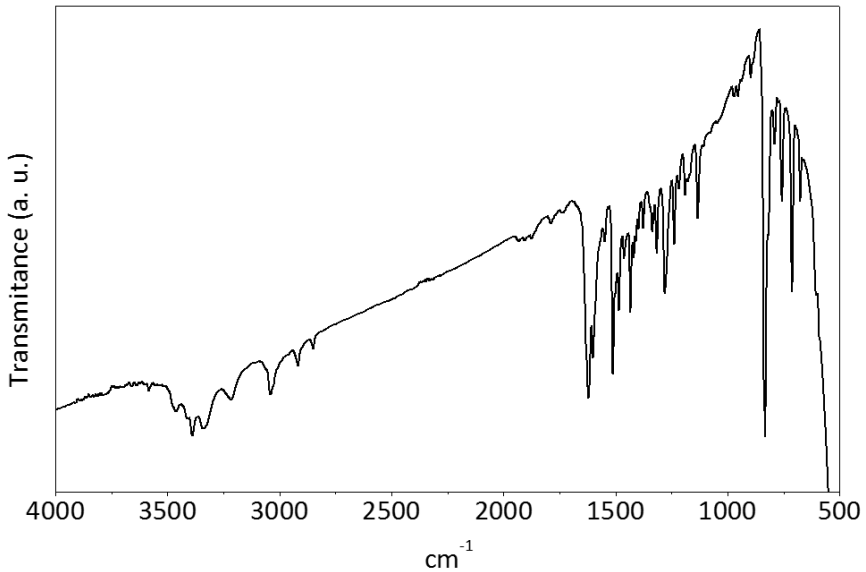

Figure 61: FTIR spectra of the 1-Aminopyrene (2)

(Z)-4-oxo-4-(pyren-1-ylamino)but-2-enoic acid (2a): Maleic anhydride (16.60 mmol, 1.60 g) was added to a solution of 1-aminopyrene (11.10 mmol, 2.40 g) in acetonitrile (200 mL) and the mixture was stirred at room temperature. The reaction was followed by TLC (20% ethyl acetate/petroleum ether) and after 4 hours the precipitate was filtered. Compound **2a** (3.00 g, 86 %) was obtained as a yellow solid. ^{1}H NMR (400MHz, DMSO-d_6): δ (ppm) 6.43 (d, 1 H, *J* = 12.4 Hz, CH), 6.77 (d, 1 H, *J* = 12.4 Hz, CH), 8.08 (t, 1 H, *J* = 7.6 Hz, H7), 8.13-8.18 (m, 2 H, H5 and H10), 8.22 (d, 1 H, *J* = 9.2 Hz, H4), 8.29-8.34 (m, 4 H, H2, H3, H6 and H8), 8.41 (d, 1 H, *J* = 9.2 Hz, H9), 10.84 (s, 1 H, NH), 13.27 (s broad, 1 H COOH). ^{13}C NMR (100 Mz, DMSO-d_6): δ (ppm) 122.45 (C9), 123.19 (C2), 123.84 (C3a), 124.04 (C3a1), 124.36 (C5a1), 124.98 (C3), 125.05 (C6 or C8), 125.34 (C6 or C8), 126.47 (C7), 126.79 (C5 and C10), 128.54 (C10a), 130.49 (C8a), 130.83 (C5a), 130.85 (CH), 131.10 (C1), 164.53 (COOH), 167.05 (C=O).
The NMR spectra is presented in **figure 62.**

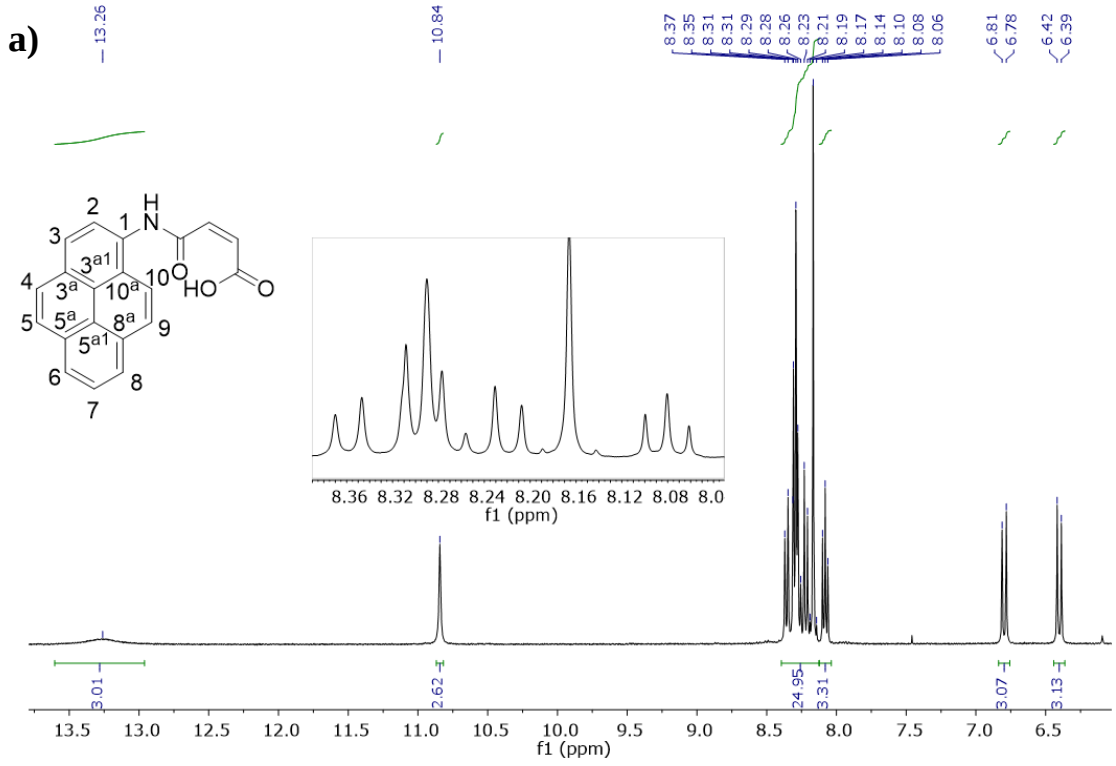

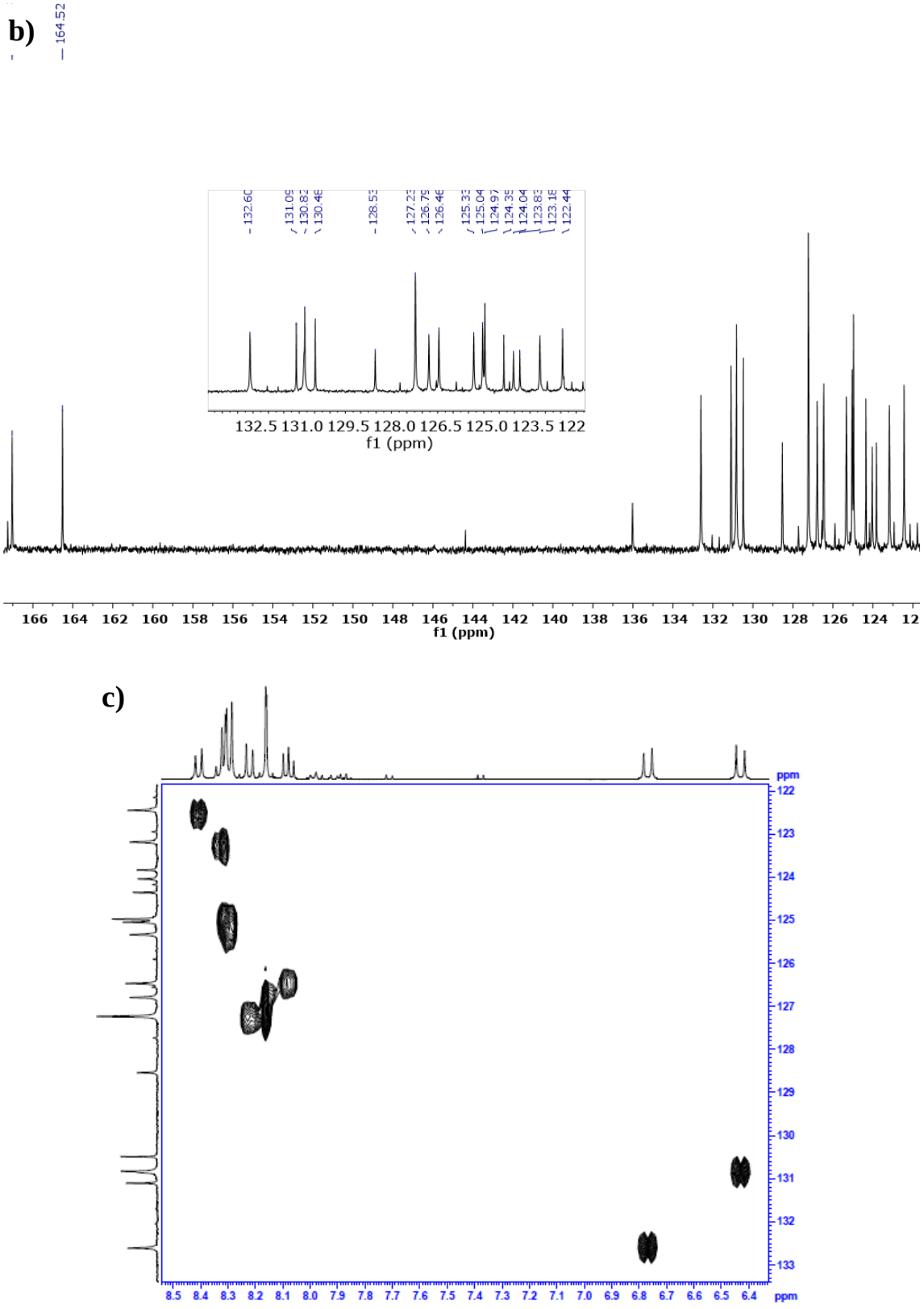

Figure 62: NMR spectra of (Z)-4-oxo-4-(pyren-1-ylamino)but-2-enoic acid (2a): a) ^{1}HNMR; b) ^{13}C NMR; and c) 2D HSQC (Heteronuclear Single Quantum Correlation).

The FTIR spectrum is presented in **figure 63.**

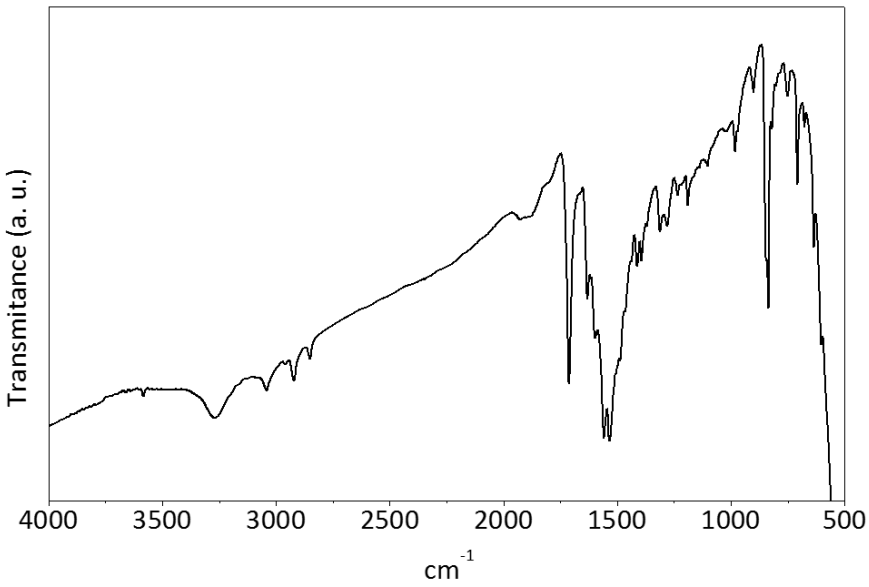

Figure 63: FTIR spectra of the (Z)-4-oxo-4-(pyren-1-ylamino)but-2-enoic acid (2a)

(E)-N-(4-nitrobenzylidene)pyren-1-amine (3): 4-Nitrobenzaldehyde (1.38 mmol, 0.21 g) was added to a solution of 1-aminopyrene (1.38 mmol, 0.30 g) in ethyl acetate (20 mL) and the mixture was stirred at 85ºC. The reaction was followed by TLC (20% ethyl acetate/petroleum ether). When all the reagents were consumed the solvent was removed in the rotary evaporator. Recrystallization with diethyl ether gave compound **3** (0.45 g, 93 %) as a brown solid.^{1}H NMR (400MHz, DMSO-d_6): δ (ppm) 8.04 (d, 1 H, *J*= 8.0 Hz, C2-H py), 8.07 (t, 1 H, *J* = 7.6 Hz, H7 py), 8.13-8.19 (m, 2 H, H5 and H6 py), 8.23 (d, 1 H, *J* = 9.2 Hz, H9 py), 8.27-8.30 (dd, 2 H, *J* = 7.6 Hz, H6 and H8 py), 8.32-8.38 (m, 5 H, CH Ph and H3 py), 8.69 (d, 1 H, *J* = 9.2 Hz, H10 py), 9.07 (s, 1 H, CH). ^{13}C NMR (100 Mz, DMSO-d_6): δ (ppm) 115.70 (C2 py), 125.79 (C10 py), 123.92 (C5^{a1} py), 124.05 (CH Ph), 124.40 (C3^{a1} py), 125.35 (C8 py), 125.45 (C6 py), 125.48 (C10a py), 125.85 (C3 py), 126.58 (C7 py), 127.14 (C4 or C5 py), 127.28 (C4 or C5 py), 127.47 (C9 py), 129.80 (CH Ph), 129.89 (C3a py), 130.81 (C8a py), 130.98 (C5a py), 141.80 (C Ph), 143.60 (C1 py), 148.82 (C Ph), 159.23 (CH).
The NMR spectra is presented in **figure 64.**

a)

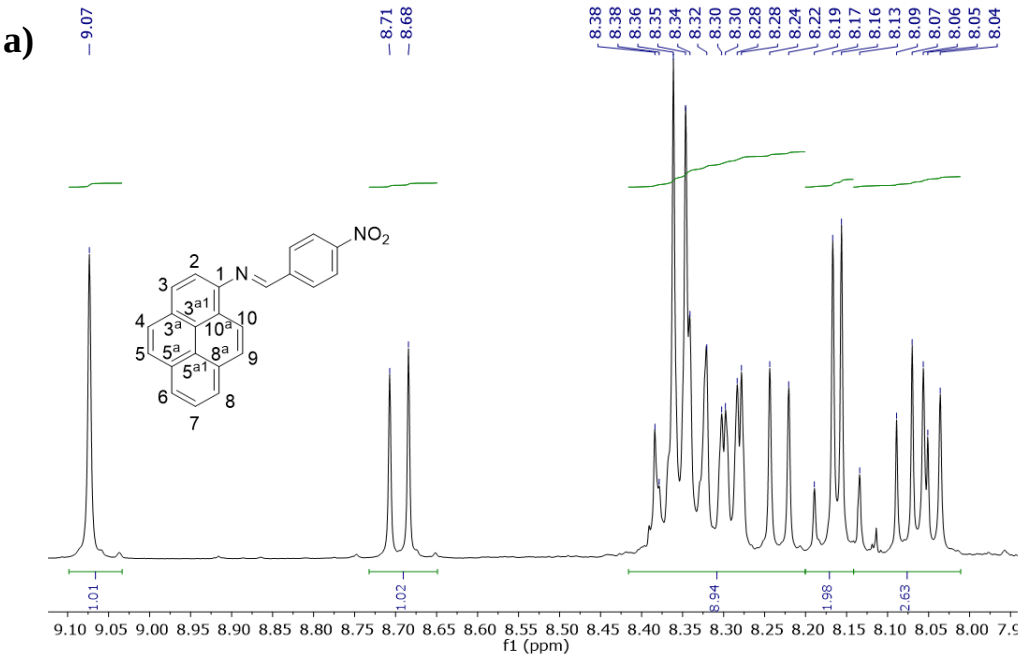
9.07
8.71
8.68
8.38
8.38
8.36
8.35
8.34
8.32
8.30
8.30
8.28
8.28
8.24
8.22
8.19
8.17
8.16
8.13
8.09
8.07
8.06
8.05
8.04
NO2
1.01
1.02
8.94
1.98
2.63
f1 (ppm)

b)

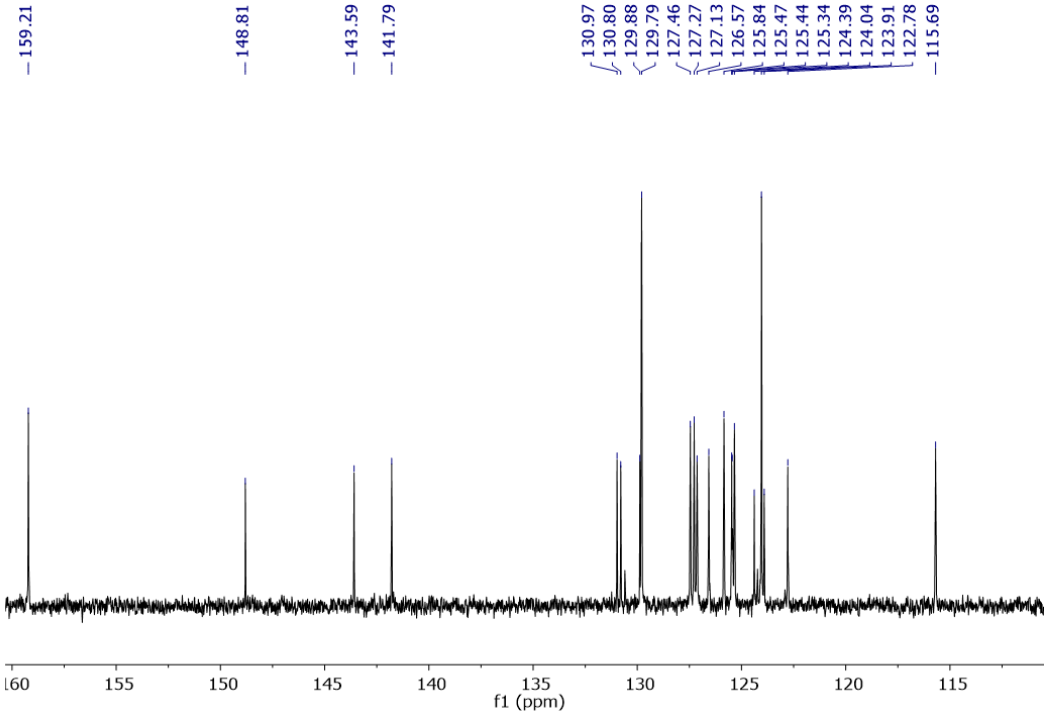
159.21
148.81
143.59
141.79
130.97
130.80
129.88
129.79
127.46
127.27
127.13
126.57
125.84
125.47
125.44
125.34
124.39
124.04
123.91
122.78
115.69
f1 (ppm)

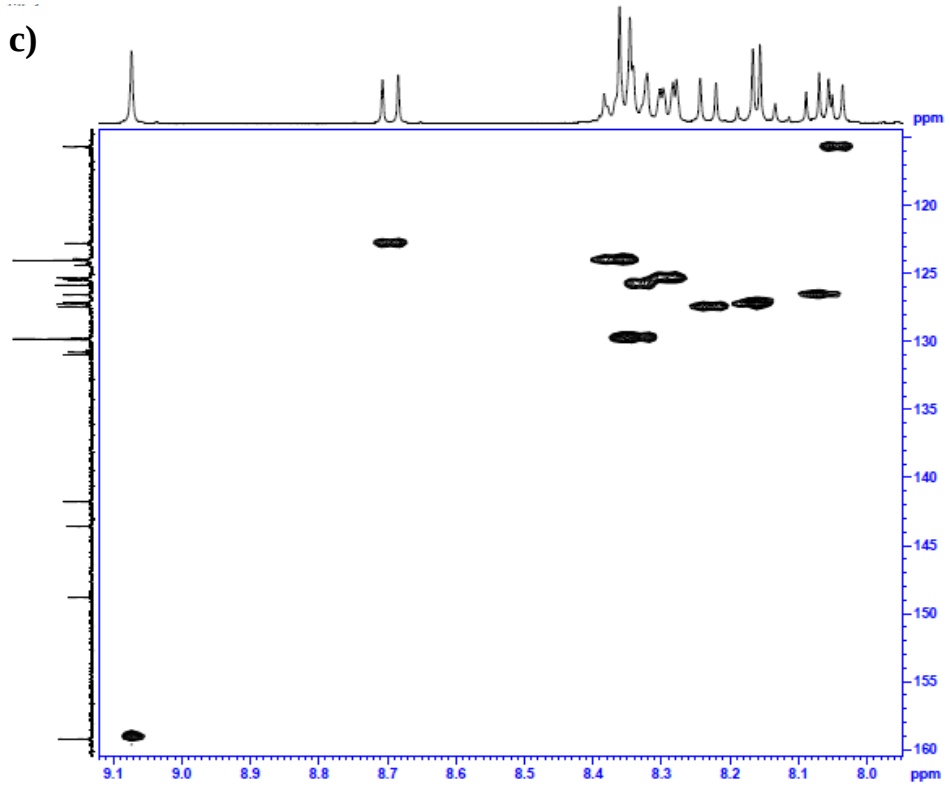

Figure 64: NMR spectra of (E)-N-(4-nitrobenzylidene)pyren-1-amine (3): a) ^{1}HNMR; b) ^{13}C NMR; and c) 2D HSQC (Heteronuclear Single Quantum Correlation).

The FTIR spectrum is presented in **figure 65.**

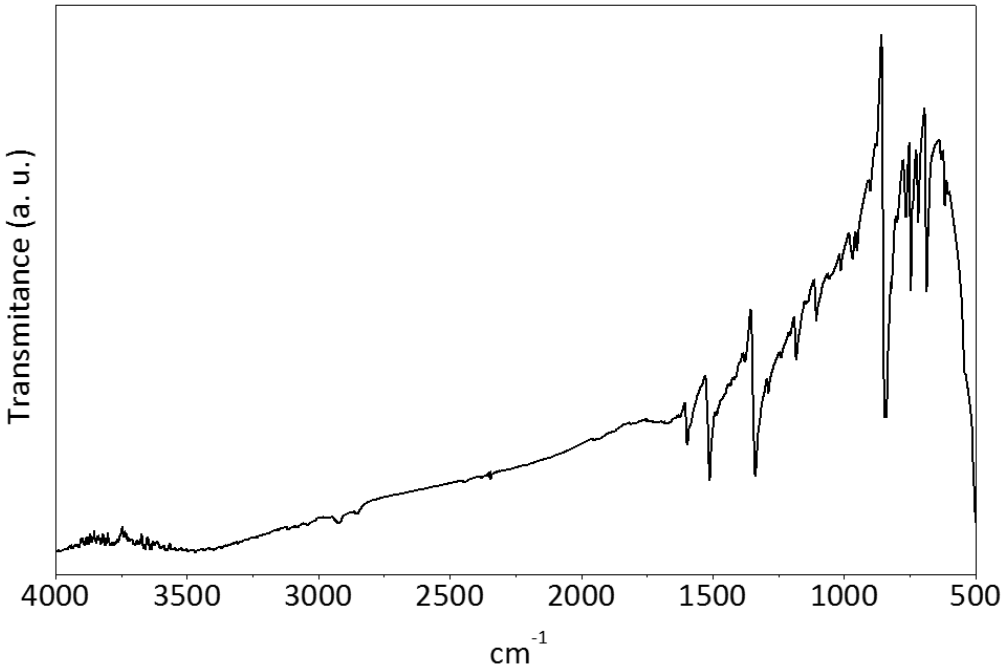

Figure 65: FTIR spectra of the (E)-N-(4-nitrobenzylidene)pyren-1-amine (3)

N-(4-aminobenzyl)pyren-1-amine (4): Compound **3** (1.0 mmol, 0.35 g) was dissolved in ethanol (10 mL), the mixture was cooled in an ice bath, and copper (II) sulfate (2.4 mmol, 0.38 g) was added. After stirring for 10 min, sodium borohydride (5.00 mmol, 0.19 g) was added slowly during 15 min. The mixture was refluxed overnight and cooled to room temperature. The solvent was removed in the rotary evaporator. The reaction mixture was dissolved in dichloromethane (50 mL) and water (100 mL) was added. The aqueous layer was extracted with dichloromethane (3 x 30 mL), and the organic layers were washed with brine (2 x 30 mL) and dried with $MgSO_4$. Removal of the solvent in the rotary evaporator gave compound **4** (0.24 g, 73%) as a brown solid. ^{1}H NMR (400MHz, DMSO-d_6): δ (ppm) 4.48 (d, 2 H, *J* = 5.6 Hz, CH_2), 4.89 (s broad, 2 H, NH_2), 6.51 (d, 2 H, *J* = 8.4 Hz, CH-Ph), 7.12 (d, 2 H, *J* = 8.4 Hz, CH-Ph), 7.20 (d, 1 H, *J* = 8.8 Hz, H2 py), 7.30 (t, 1 H, *J* = 5.6 Hz, NH), 7.68 (d, 1 H, *J* = 9.2 Hz, H9 py), 7.83 (d, 1 H, *J* = 8.8 Hz, H3 py), 7.86 (t, 1 H, *J* = 7.6 Hz, H7 py), 7.92-8.01 (m, 4 H, H5, H6, H8 and H10 py), 8.42 (d, 1 H, *J* = 9.2 Hz, H4 py). ^{13}C NMR (100 Mz, DMSO-d_6): δ (ppm) 46.18 (CH_2), 109.00 (C2 py), 113.95 (2CH Ph), 115.95 (C10a), 121.07 (C3a), 121.44 (C4 py), 121.95 (C9 py), 122.54 (C8 py), 123.02 (C6 py), 124.53 (C10 py), 125.12 (C8a py), 125.49 (C5a py), 125.97 (C7 py), 126.56 (C5 py), 126.51 (C Ph), 127.76 (C3 py), 127.83 (2CH Ph), 131.53 (C5a1 py), 132.08 (C3a1 py), 143.52 (C1 py), 147.40 (C Ph).
The NMR spectra is presented in **figure 66.**

a)

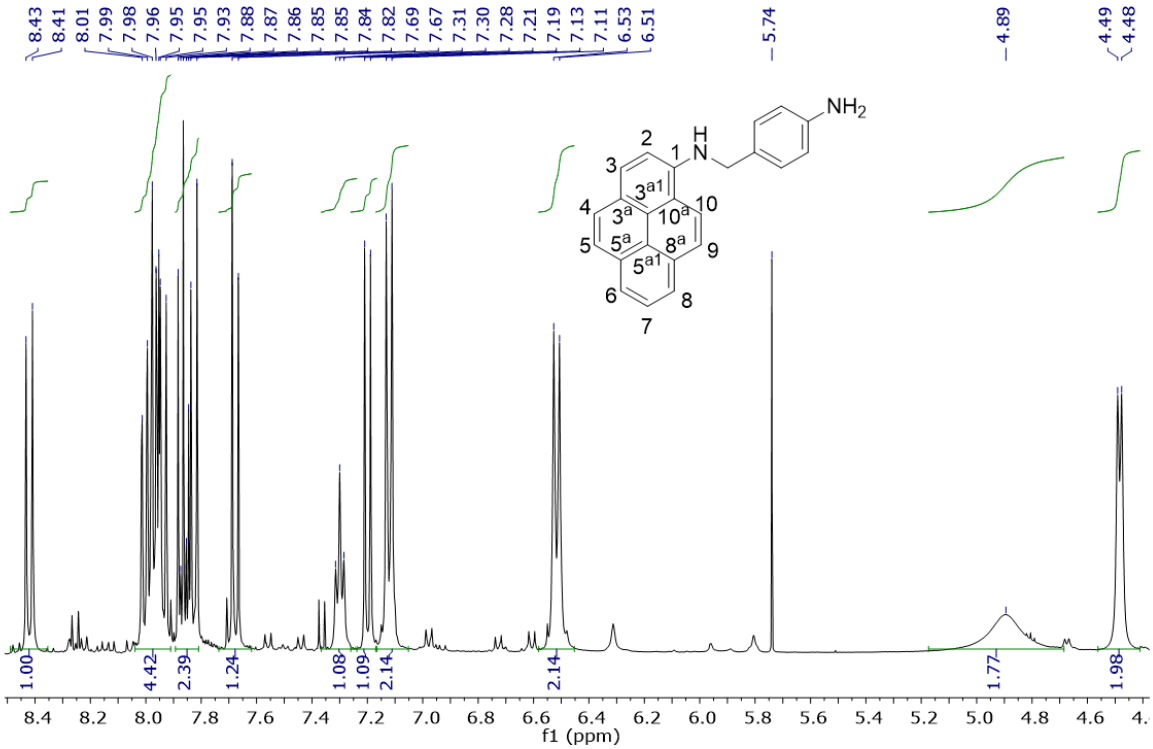

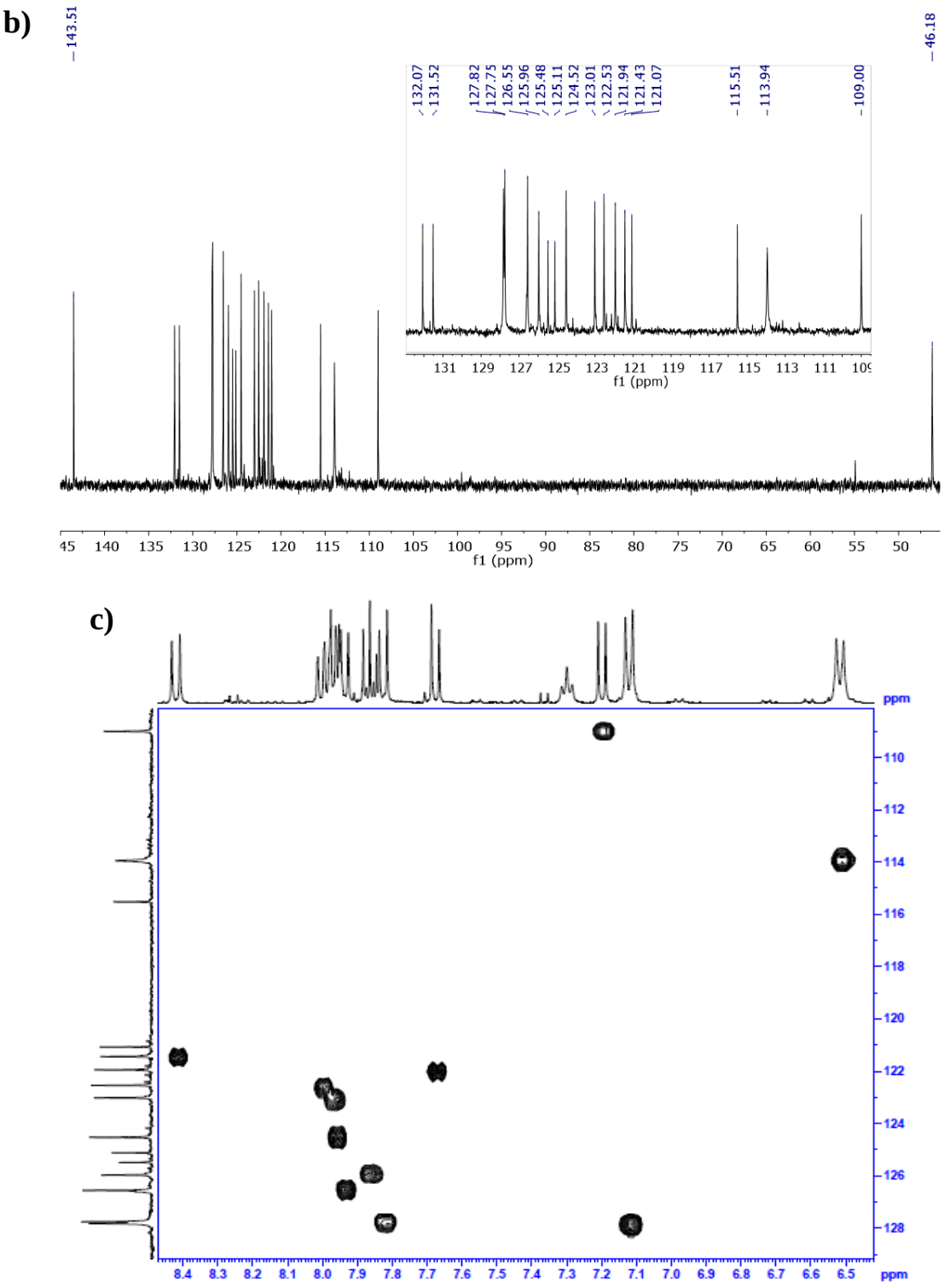

Figure 66: NMR spectra of N-(4-aminobenzyl)pyren-1-amine (4): a) ^{1}HNMR; b) ^{13}C NMR; and c) 2D HSQC (Heteronuclear Single Quantum Correlation).

The FTIR spectra is presented in **figure 67.**

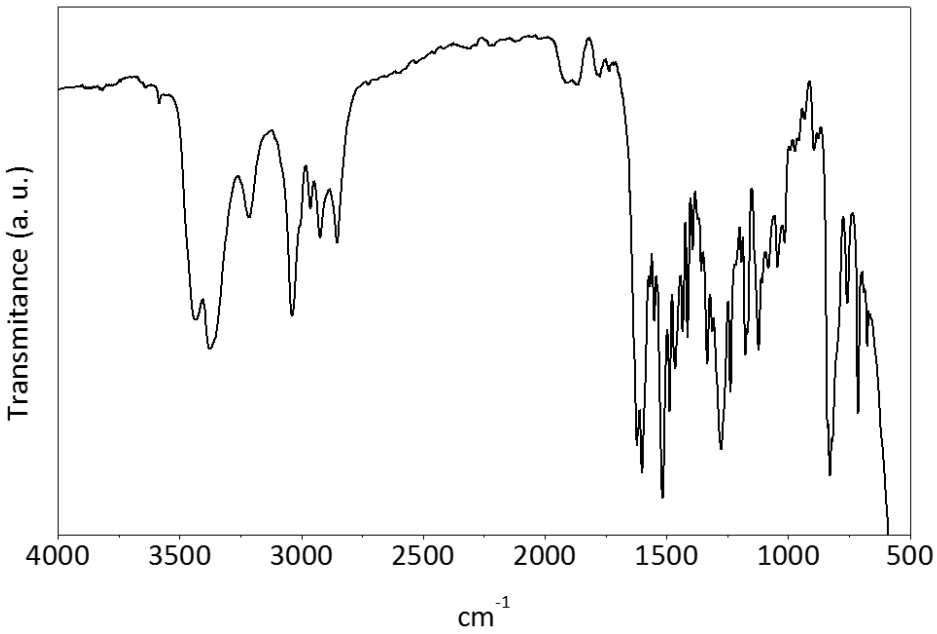

Figure 67: FTIR spectra of the N-(4-aminobenzyl)pyren-1-amine (4)

(Z) 4-oxo-4-((4-((pyren-1-ylamino)methyl)phenyl)amino)but-2-enoic acid (2b): Maleic anhydride(1.8 mmol, 180.0 mg) was added to a solution of compound 4 (1.50 mmol, 0.48 g) in acetonitrile (20 mL) and the reaction was stirred at room temperature. The reaction was followed by TLC (20% ethyl acetate/petroleum ether) and after 4 hours the precipitate was filtered. The compound obtained (0.56 g) was a mixture of compound **2a** and **2b** in a 1:2 ratio.^{1}H NMR (400MHz, DMSO-d_6): δ (ppm) 4.64 (s, 2 H, CH_2), 6.28 (d, 1 H, *J* = 12.0 Hz, CH), 6.41 (d, 1 H, *J* = 12.4 Hz, CH **2a**), 6.45 (d, 1 H, *J* = 12.4 Hz, CH), 6.81 (d, 1 H, *J* = 12.0 Hz, CH **2a**), 7.16 (d, 1 H, *J* = 8.4 Hz, H-Ph), 7.42 (d, 2 H, *J* = 8.4 Hz, H-Ph), 7.57 (d, 2 H, *J* = 8.8 Hz, H-Ph), 7.69 (d, 1 H, *J* = 8.8 Hz, H-Ph), 7.83 (d, 1 H, *J* = 8.8 Hz, H-py), 7.88 (t, 1 H, *J* = 7.6 Hz, H-py), 7.94 (d, 1 H, *J* = 8.4 Hz, H-py), 7.98-8.04 (m, 3 H, H-py), 8.08 (t, 1 H, *J* = 7.6 Hz, H-py **2a**), 8.16 (s, 2 H, NH and H-py **2a**), 8.22 (d, 1 H, *J* = 9.2 Hz, H-py **2a**), 8.28-8.30 (m, 3 H, H-py **2a**), 8.37 (d, 1 H, *J* = 9.2 Hz, H-py **2a**), 8.45 (d, 1 H, *J* = 9.2 Hz, H-py **2a**), 10.38 (s, 1 H, NH), 10.85 (s, 1 H, NH **2a**), 13.04 (s broad, 1 H, COOH **2a** and **2b**). ^{13}C NMR (100 Mz, DMSO-d_6): δ (ppm) 46.02 (CH_2), 108.88 (CH Ph), 115.61 (C), 119.55 (CH Ph), 119.67 (CH Ph), 121.25 (C), 121.36 (CH py), 122.09 (CH Ph), 122.42 (CH py **2a**), 122.62 (C-H Py), 123.09 (C-H py), 123.33 (C-H py **2a**), 123.78 (C **2a**), 124.15 (C **2a**), 124.31 (C **2a**), 124.65 (C-H py), 124.93 (C-H py **2a**), 125.03 (C), 125.05 (CH py **2a**), 125.34 (C-H py **2a**), 125.44 (C), 125.97 (C-H py), 126.45 (C-H py **2a**), 126.52 (C-H py **2a**), 126.83 (C-H py **2a**), 127.20 (C-H py), 127.35 (C-H Ph), 127.69 (C-H py **2a**), 128.61 (C **2a**), 130.03 (C-H **2a**), 130.44 (C),130.60 (C-H), 130.78 (C **2a**), 130.87 (C **2a**), 131.46 (C), 131.54 (C-H), 132.74 (C-H **2a**), 135.54 (C), 137.08 (C), 143.17 (C), 163.08 (C=O), 164.46 (C=O **2a**), 166.77 (COOH), 166.83 (COOH **2a**).
The NMR spectra is presented in **figure 68**.

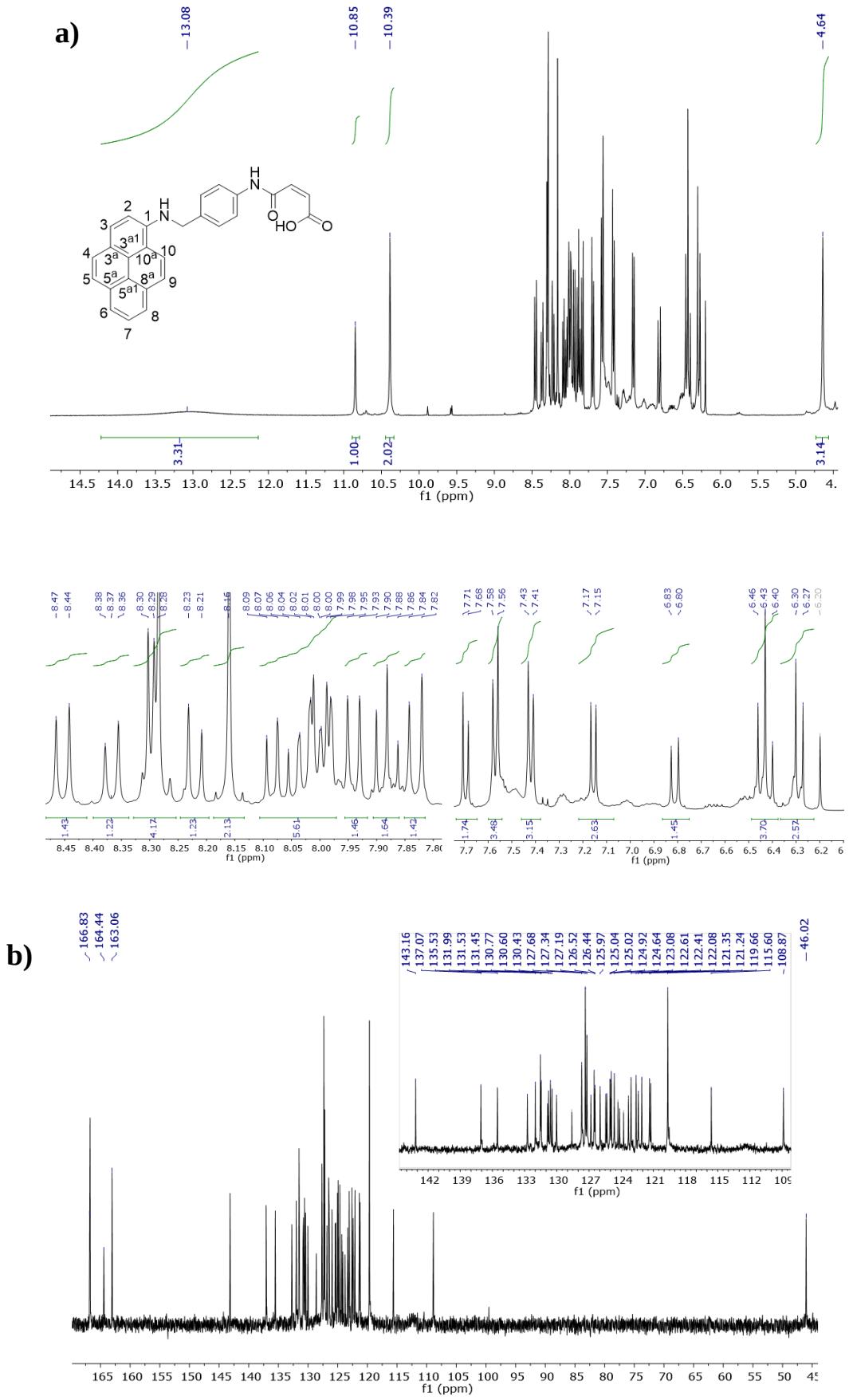

Figure 68: NMR spectra of (Z) 4-oxo-4-((4-((pyren-1-ylamino)methyl)phenyl)amino)but-2-enoic acid (2b): a) ^{1}HNMR; b) ^{13}C NMR;

The FTIR spectra is presented in **figure 69**.

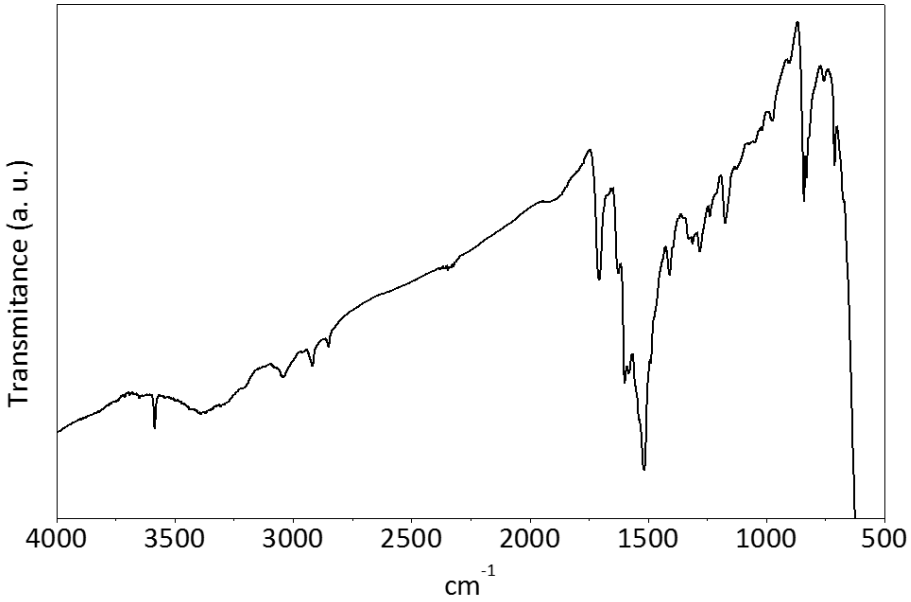

Figure 69: FTIR spectra of the 4-oxo-4-((4-((pyren-1-ylamino)methyl)phenyl)amino)but-2-enoic acid (2b)

CHAPTER 5. WPU/FEW LAYER GRAPHENE NANOCOMPOSITE FILMS

This chapter is based in the article:

E. Cunha, M. F. Proença, F. Duarte, M. C. Paiva, “Waterborne polyurethane/few-layer graphene nanocomposites” – in preparation;

5. WPU/ FEW LAYER GRAPHENE NANOCOMPOSITE FILMS

5.1. Introduction

In the last decade graphene has emerged as an exciting material revealing potential applications in various fields including in the polymer nanomaterials science. [35] Recently, the production of graphene based on graphite exfoliation through non-covalent interactions with pyrene derivatives was reported (see section 2.2.1.1. in chapter 2). [93] [28] This approach was used for the exfoliation and stabilization of graphene in water, leading to the production of few- and single- layer graphene without structural damage. The suspension of graphene in water allows its easy mixture with water-soluble polymers and with polymers that form stable suspensions in water. Waterborne polyurethane (WPU) is a synthetic polymer used as high quality surface coating, providing an eco-friendly process without emission of volatile organic compounds (VOCs). The potential applications of graphene/WPU thin films in antistatic coatings, electromagnetic shielding and corrosion-resistant coatings have been reported. (see section 2.4.2. in chapter 2).

In this work we prepared FLG/WPU, CNT/WPU and FLG/CNT/WPU nanocomposites and evaluated the mechanical, electrical and barrier properties of the nanocomposite films. The production of FLG was performed by non-covalent exfoliation of three different types of pristine graphite and graphite nanoplates in aqueous media using the pyrene derivative 2a (chapter 4). The stable aqueous suspensions were constituted by more than 70 % of FLG and bi-layer graphene, and produced WPU composites with improved mechanical properties compared to the corresponding pristine graphite composites. The composite barrier properties increased by approximately 40 % relative to pure polymer films, for composites with 0.5 wt.% content of FLG. The electrical conductivity of the FLG/CNT/WPU is highly improved, showing an increase of 6 orders of magnitude when compared with WPU film, and 3 orders of magnitude when compared with the FLG/WPU composite, for 0.5 wt.% of reinforcement.

5.2. Experimental

5.2.1. Materials

Graphite and graphite nanoplates were obtained from three different suppliers: XGSciences, USA (grade GnP C); Nacional de Grafite, Brasil (grade Micrograf HC11); Graphexel Ltd., UK (graphexel grade 2369). The nomenclature adopted in this work is GnP C, Micrograf and Graphexel, respectively. Multiwalled carbon nanotubes (CNT), grade NC7000, were supplied by Nanoyl SA, Belgium. Waterborne polyurethane, grade

ICO-THANE 10, was purchased from I-Coats N. V., Belgium. The pyrene derivative was synthetized according the procedure described in chapter 4.

5.2.2. Preparation and characterization of few layer graphene suspensions

The preparation of the few layer graphene and their suspensions was carried out as described previously in section 4.2.2. of chapter 4.

5.2.3. Preparation and characterization of the WPU composites films

Water suspensions of FLG obtained from GnPC, Micrograf, Graphexel as well as CNT were dispersed in WPU at loadings of 0.025, 0.05, 0.1 and 0.5 wt.%, using an Ultrasonic processor UP100H from Hielscher, equipped with a sonotrode MS7D during 1H. The mixtures were then cast onto a polypropylene plate mould and dried at ambient conditions for 48 h. The dried films (typically about 50 µm thick) were cured at 80 ºC for 6 h in a convection oven. Composite films were also prepared with the pristine graphite-based materials and WPU for comparison purposes, using the same procedure. Hybrid composite films FLG/CNT/WPU with 0.5 wt.% overall content (0.25 wt.% FLG and 0.25 wt.% CNT) were also produced.

The mechanical property measurements were performed on a universal testing machine Instron 4505 at a crosshead speed of 25 mm/min, according to ASTM D 882. The values quoted were the average of 10 specimens tested. Thermogravimetric analysis was performed on a Modulated TGA Q500 from TA Instruments. The samples were heated at 10 ºC/min under a constant flow of N_2(g). The Raman spectra and the Raman mapping of the composite films were acquired on a Horiba LabRAM HR Evolution confocal microscope using a laser excitation of 532 nm. The measurements of volume resistivity were carried out on a picoammeter Kethley 6487 with Kethley electrodes 8009. Three nanocomposite films were prepared and analyzed for each composition. At least 3 measurements were acquired for each sample. For each applied voltage the corresponding current value was the average of 100 measurements. The water vapor transmission (WVT) tests were performed using the desiccant method according to the standard of ASTM E96-66. Scanning electron microscopy (SEM) of the cryo-fractured composite films was performed on a NanoSEM FEI Nova 200 microscope after platinum coating.

5.3. Results and Discussion

5.3.1. Few layer graphene suspensions

The synthetized pyrene derivative (Py2a described in chapter 4), represented in **figure 70**, was used to test the exfoliation of the three different pristine graphite and graphite nanoplates in water.

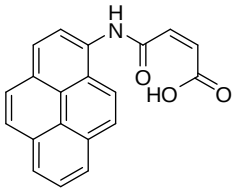

Figure 70: Pyrene derivative used in the exfoliation process.

The pristine graphite-based materials purchased from different suppliers present different morphologies in terms of particle size (or equivalent diameter), as shown in the **figure 71.** GnPC morphology and oxygen content was described previously in section 4.2.1. of chapter 4. Micrograf is an expanded graphite with equivalent diameter between 3 and 60 µm and Graphexel is a natural crystalline graphite with a large equivalent diameter of approximately 180 µm.

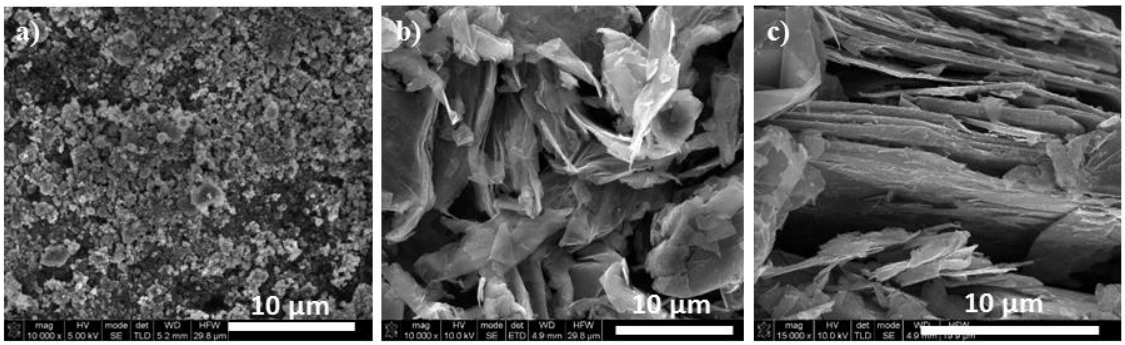

Figure 71: Scanning electron microscopy of the pristine graphite and graphite nanoplates: a) GnP C, b) Micrograf, c) Graphexel

The thermogravimetric analysis of the pristine GnPC (**figure 72**) presents a weight loss of about 7.5 % at 800 ºC, a large value compared to the weight loss observed for Micrograf and Graphexel. This larger weight loss results from the thermal degradation of the oxygen containing groups of GnPC. The weight loss at 800ºC for Micrograf and Graphexel are 0.7 % and 1.7 %, respectively.

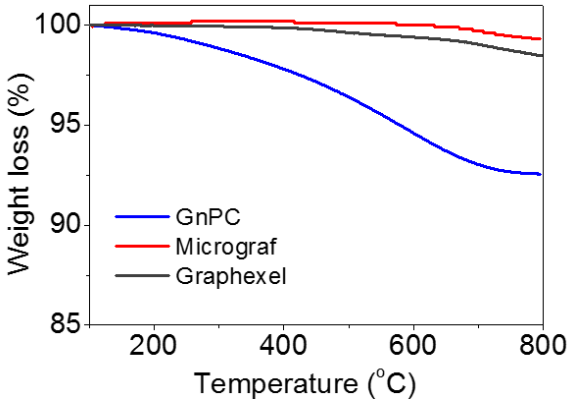

Figure 72: Thermogravimetric analysis of the pristine GnPC, Micrograf and Graphexel

The GnPC, Micrograf and Graphexel were added to Py aqueous solution ($5x10^{-5}$ mol dm^{-3}) and the exfoliation of the pristine materials was carried out by ultrasound application. The dispersions were then centrifuged to remove large aggregates and the supernatant was collected, resulting in stable aqueous suspensions of few layer graphene. The FLG suspensions were analyzed by UV-visible spectroscopy and their stability along the storage time was studied (**figure 73**). The Py solution shows the typical absorption peaks between 200 and 600 nm. [98]. The FLG suspension spectra show an absorption over the whole wavelength range as it was expected for the graphene dispersions. [73, 94] Moreover, the suspensions demonstrated good stability along the time. The aqueous suspensions of FLG produced from GnPC and Micrograf (figure **73a and 73b**) were diluted 10x and 2x, respectively, to perform the UV-visible analysis. The spectra of these stable FLG suspensions showed an absorption peak at about 265 nm typical of graphene and graphene oxide suspensions. [71, 98, 407] Graphexel FLG suspensions still present some of the Py peaks, although at very low intensity. This effect was reported to be due the π-π interactions between pyrene derivatives and exfoliated graphite [98]

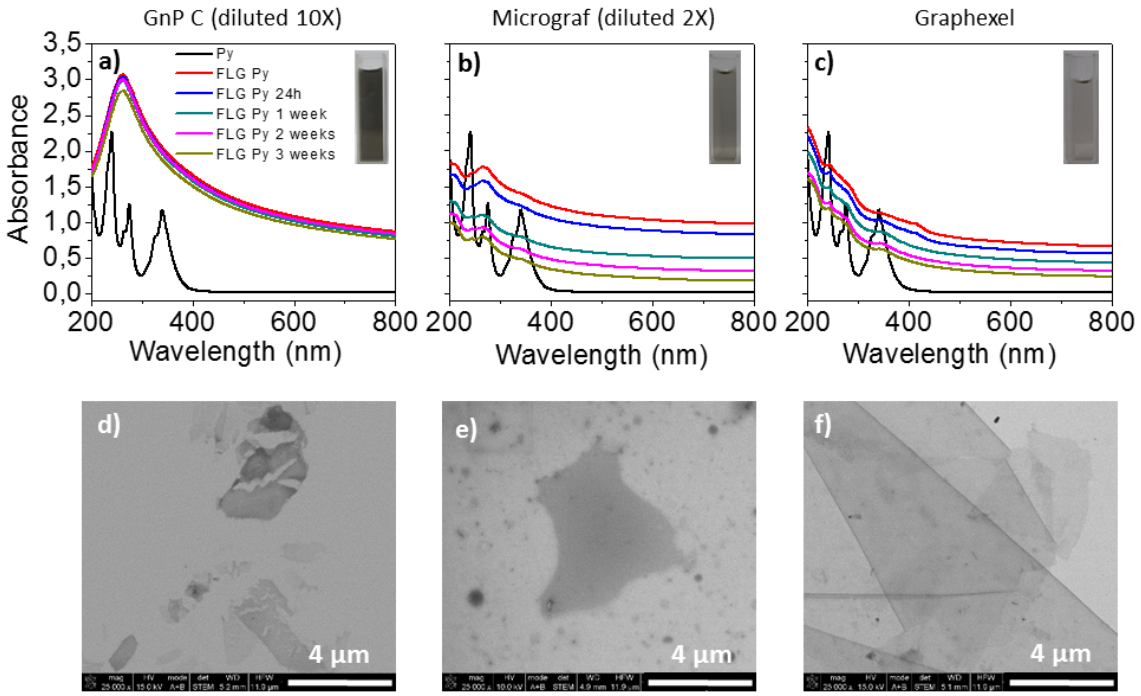

Figure 73: UV-visible spectra of the few layer graphene suspensions: a) GnPC, b) Micrograf, c) Graphexel; and their scanning transmission electron microscopy images d), e) and f), respectively.

The STEM images of the FLG formed in Py aqueous suspension (**figure 73d, 73e and 73f**) show the formation of thin flakes with sizes within the reported initial equivalent diameter of the pristine materials. The concentration of these FLG suspensions was calculated using the extinction coefficient values obtained in previous work, (chapter 4) and it is shown in **figure 74**. The yield of exfoliation was calculated relative to the initial concentration of the graphite-based material, which was 500 µg/ml. The concentration of FLG obtained from GnPC was 450 µg/ml, representing 90 % of the initial concentration of the pristine material. The concentration of FLG from Micrograf was 91 µg/ml (18 % yield) and from Graphexel it was 31 µg/ml (6 % yield).

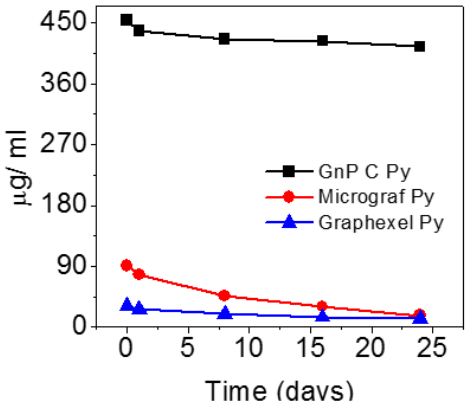

Figure 74: Concentration of FLG suspensions along the shelf time

The higher yield of FLG in aqueous suspension was obtained with GnPC probably due to their smaller flake dimensions and thickness in the pristine material. Additionally, the pristine GnPC is an expanded material with some residual oxidation, which may be an advantage for the exfoliation and stabilization in water. Micrograf, also obtained from an expansion process but having a larger equivalent diameter than GnPC, presents a yield of 18 % in aqueous suspension. The pristine Micrograf presents a negligible weight loss at 800ºC indicating a stable graphene structure with few functional groups attached to its surface. Graphexel is distinct from the other two materials as it is a natural graphite (not expanded) with large equivalent flake diameter and thickness, and thus its expected yield of exfoliation in water was very low. In this context, the yield of 6 % of FLG produced from Graphexel in water is quite relevant, when compared with other results reported in the literature. [94, 98]

The Raman spectrum of the pristine Graphexel (**figure 75 c**) presents the typical shape of graphite. The G band is observed at 1581 cm^{-1} and the D band, which normally is observed at about 1350 cm^{-1}, is barely identified indicating the good structural quality of the pristine graphite. The 2D band position occurs at 2722 cm^{-1}, presenting the typical asymmetric shape that can be fitted using two Lorentzian functions (**figure 76a**). After the exfoliation process with the pyrene derivative, the Raman spectra obtained for the Graphexel water suspension deposited on a glass slide showed the presence of FLG and higher exfoliation products such as bilayer graphene. The bilayer graphene presents a symmetric 2D band centered at 2702 cm^{-1} that may be deconvoluted using four Lorentzian functions (**figure 76c**). The D band of the exfoliated material presents higher intensity than the pristine Graphexel flakes and this fact can be related with the presence of the pyrene derivatives on the surface of the exfoliated material. [97] Also, the characteristic peaks of the pyrene derivatives can be observed in these spectra.

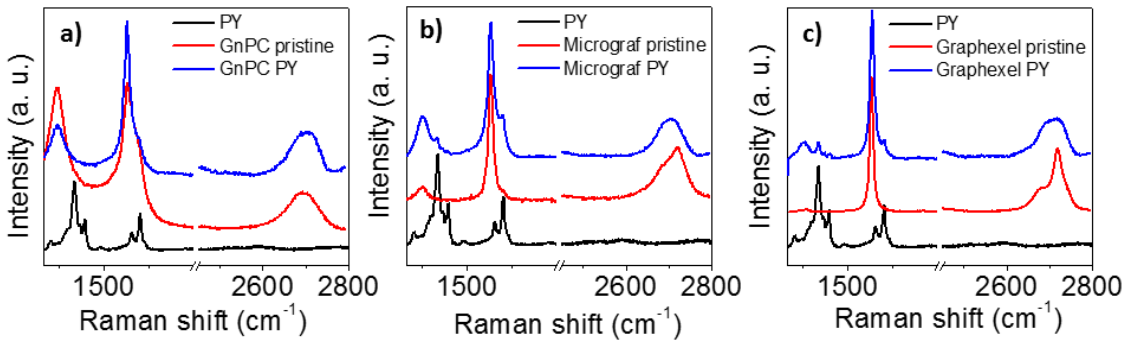

Figure 75: Raman spectra of the pristine and FLG: a) GnPC, b) Micrograf, c) Graphexel

Similarly to the observations reported for the FLG obtained from Graphexel, the exfoliated Micrograf in suspension also presented a Raman spectrum typical of bi-layer graphene (**figure 75 b**). The pristine Micrograf material presents a more symmetric 2D band compared to the pristine Graphexel, which may be due to its previous expansion procedure. The Raman spectra of the pristine and exfoliated GnPC is presented in the **figure 75c**, showing a prominent D band near 1350 cm^{-1} with a slightly higher intensity than the G band (at 1581 cm^{-1}) which may be related to the smaller flake size, and thus higher edge-to-basal plane ratio, as well as to the initial oxygen content. The 2D band position occurs near 2692 cm^{-1} showing high symmetry, although with lower intensity compared to the G band. The large downshift of the 2D band of the pristine GnPC relative to the other pristine graphites indicates that this material is already formed by thin flakes itself. After the exfoliation process the D band presents a lower intensity relative to the G band, indicating the selective adsorption of Py on the less oxidized flakes. The less "defective" GnPC may adsorb a higher amount of pyrene, and thus are more stable in aqueous suspension. Furthermore, the 2D band position is upshifted and similar to the 2D band of FLG produced from Micrograf and Graphexel.

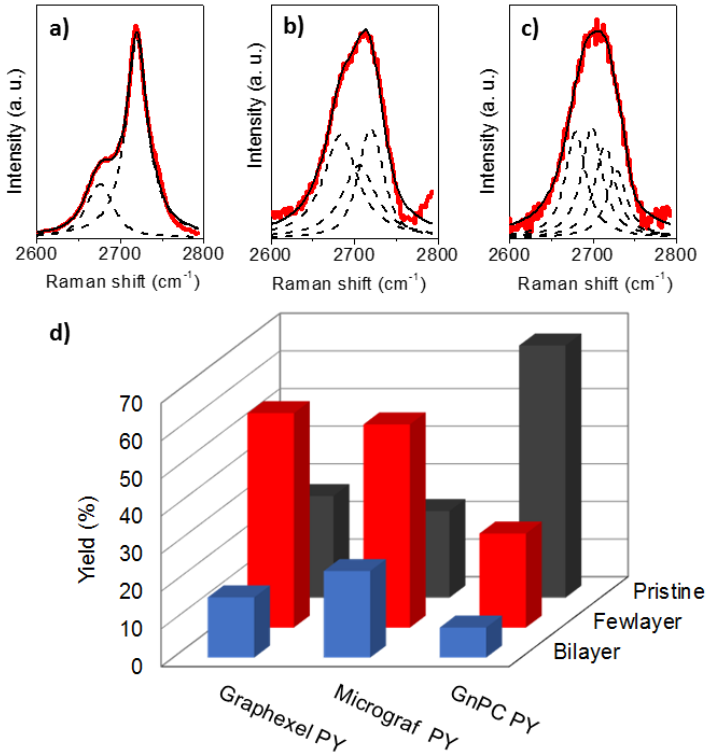

Figure 76: Lorentzians features of the deconvoluted 2D band: a) pristine graphite, b) few layer graphene and c) bi-layer graphene; d) Yield of few layer and bi-layer graphene in the exfoliated GnPC, Micrograf and Graphexel suspensions.

After the exfoliation procedure, the spectra of bilayer and FLG were identified. A representative analysis of the graphene flake structure was performed by collecting the Raman spectra of sixty different flakes across each sample, as described in chapter 4. **Figure 76d** shows the results obtained for the yield of bilayer, FLG, and pristine flakes after the exfoliation process, for all samples. The spectra identified as "pristine" quantifies the fraction of the spectra which are similar to the pristine material. The FLG and bilayer graphene spectra were identified based on the position of the 2D band and its deconvolution. Typically, the 2D band of bilayer graphene occurred at 2702 cm^{-1}, presenting a symmetric shape that could be deconvoluted using four Lorentizan functions with a FWHM of about 24 cm^{-1}, shown in **figure 76c**. For FLG the 2D band position occurred between 2706 cm^{-1} and 2712 cm^{-1}, it is less symmetric compared to bilayer graphene, and may be deconvoluted using three Lorentizan functions (**figure 76b**). [281] The analysis demonstrated that the Graphexel water suspensions presented 16 % of bi-layer graphene, 57 % of FLG and 27 % of non-exfoliated material. The Micrograf suspensions contained 23 % of bi-layer graphene, 54 % of FLG and 23 % pristine material. Finally, the GnPC aqueous suspensions presented 8 % of bi-layer graphene, 25 % of FLG and 67 % of pristine material. In the latter case, the pristine material is itself considerably exfoliated, as discussed in chapter 4. The total amount of few-layer graphene (corresponding to the sum of bi- and FLG) for Graphexel and Micrograf water suspension was 73 % and 77 %, respectively. These values are in agreement with the results reported by Schlierf *et al.* [28] , that performed a similar analysis, concluding that 86 % of exfoliated material (corresponding to the overall single- to few-layer graphene) was obtained by exfoliation of graphite in water using 1-pyrene sulfonic acid. However, both concentration of pyrene derivative ($3.3x10^{-4}$ mol dm^{-3}) and the sonication time (5 to 35 hours) were higher than those used in this work.

5.3.2. Few layer graphene/ waterborne polyurethane composite films

The GnPC, Micrograf as well as Graphexel FLG suspensions were mixed with waterborne polyurethane. Thin films of WPU/FLG at low loading level, from 0.025 wt.% to 0.5 wt.%, were prepared and the production of WPU films using the pristine graphitic materials was also performed for comparison. The mechanical properties of all produced WPU composite films were tested and the results are depicted in the **figure 77**. In general, the mechanical properties are enhanced with the incorporation of the pristine graphite and

graphite nanoplates as well as the FLG (obtained from GnPC, Micrograf and Graphexel). The Young's modulus, yield strength and tensile strength increased with increasing content of the reinforcement for the pristine material and for FLG.

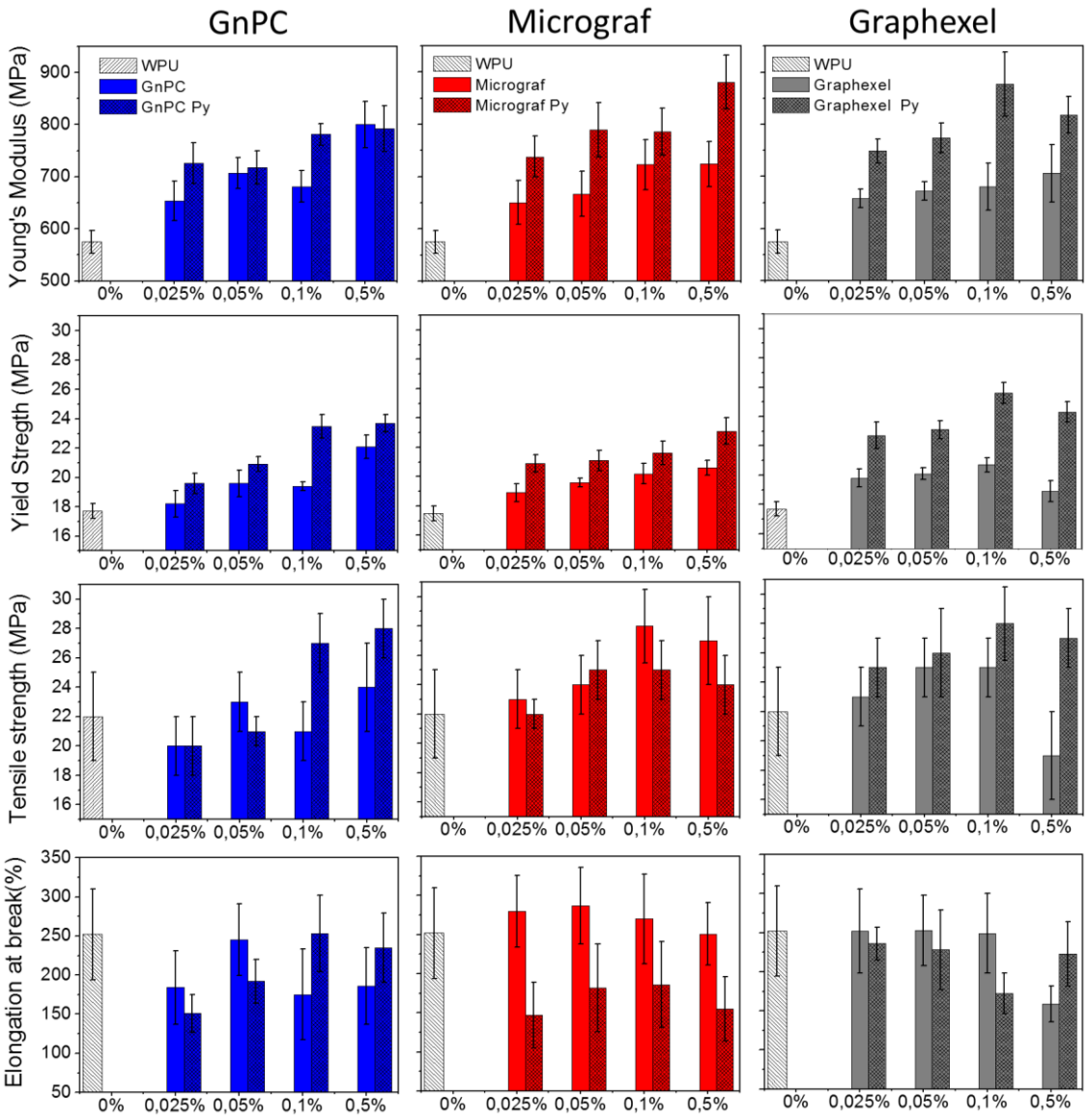

Figure 77: Variation of the Young's modulus, yield strength, tensile strength and elongation at break of the WPU composite films with the increase of the pristine material and FLG content

Micrograf and Graphexel tend to reach their maximum mechanical properties already at 0.1 wt. of FLG loading. The elongation at break tends to slightly decrease for all composite films, however it is always above 150 %.

Table 4 compares the mechanical properties of the WPU composite films produced in this work, namely the Young's modulus, with results reported in the literature.

Table 4: Young's Modulus increase/ decrease of waterborne polyurethane reinforced with graphene/ graphite related materials

WPU composite films reinforcement	Young's Modulus increase/ decrease (%)	Ref.
Graphene nanoplates (GnP) (0.5wt.%)	-48%	[350]
r-GO (0.5wt.%)	-42%	[348]
GO (0.5wt.%)	330	[352]
f-graphene with APTES[(1)] (0.5wt.%)	620	[359]
r-GO + SDS [(2)] (1.0wt%)	4	[368]
GnPC (0.5wt.%)	39	This work
GnPC Py (0.5wt.%)	38	This work
Micrograf (0.5wt.%)	26	This work
Micrograf Py (0.5wt.%)	41	This work
Graphexel (0.5wt.%)	23	This work
Graphexel Py (0.5wt.%)	42	This work

[(1)] (3-aminopropyl)triethoxysilane

[(2)] sodium dodecyl sulphate

While for non-functionalized GnP [350] and r-GO [348] incorporated in WPU matrix (0.5wt.%) the reported Young's modulus values decreased 48 % and 42 %, respectively, for covalent functionalized graphene such as GO [352] the improvement of the Young's modulus can achieve to 330 % (for 0.5 wt.% of incorporation). Also, the *in situ* incorporation of functionalized graphene with (3-aminopropyl)triethoxysilane (APTES), during the WPU synthesis, led to an improvement of the Young's modulus of 620 %. [359]. Thus, covalent functionalization of graphene may be a viable alternative to obtain good mechanical properties of WPU, however the disruption the sp^2 carbon network of the graphene leads to structural defective graphene sheets with poor electrical properties [35], which was not reported in the examples given in table 4. Conversely, non-functionalized r-GO with sodium dodecyl sulphate (SDS) led an improvement of 4 % of the Young's modulus, for the incorporation of 1.0 wt.% of r-GO. [368] In the present work, the FLG obtained by non-covalent functionalization with the pyrene derivative led to better results, inducing an enhancement of 38 to 42 % of the Young's modulus, for the loading of 0.5 wt.%. Furthermore, the incorporation of the pristine graphitic materials (GnPC, Micrograf or Graphexel) improved the Young's modulus in the range of 23 – 39

%, which are interesting results compared with non-functionalized graphene related materials reported in the literature, for the same loading (0.5 wt.%). [348, 350]

The mechanical properties are closely related with the interfacial adhesion between reinforcement and polymer matrix. **Figure 78** shows SEM images of the composite films with 0.5 wt.%. The images showed a good interfacial adhesion between the graphite-based reinforcement and the WPU matrix, in agreement with the mechanical characterization. The larger agglomerates were observed for the pristine Graphexel composites, as illustrated in the SEM images, affecting the its mechanical properties when compared with the pristine GnPC and Micrograf however, there is still an enhancement relative to WPU film.

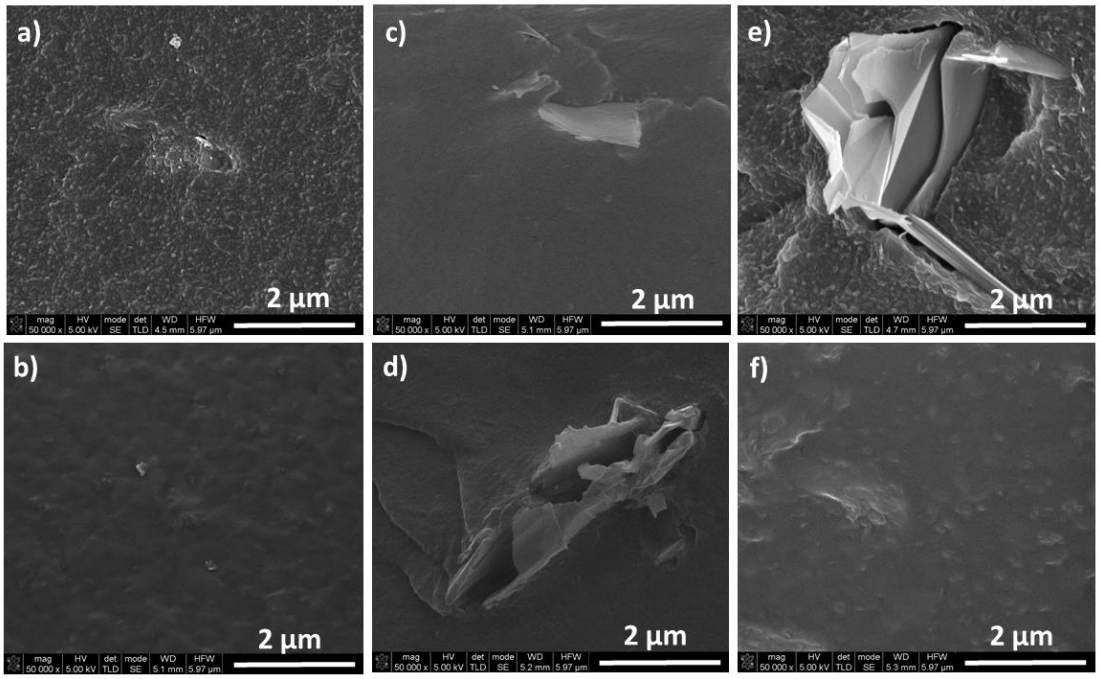

Figure 78: SEM images of the pristine and few-layer graphene: a) and b) GnPC, c) and d) Micrograf, e) and f) Graphexel composite films at 0.5wt.% of content.

The Raman spectra of the WPU composite films with 0.5 wt.% and its comparison with the pristine graphite-based materials, as well as the WPU itself, is presented in the **figure 79**. The D and G bands of the Raman spectra of GnPC, Micrograf and Graphexel, when incorporated into the WPU matrix, is very similar with the spectra of the pristine materials. Also, the WPU film presents a characteristic band between 1400 and 1500 cm^{-1} quite distinct from the typical bands of the graphite nanoplates, which allows its easy identification in the composite films. In fact, in the WPU composite films both signals (WPU and graphitic materials) are identified, which enables the construction of a Raman

map of the distribution of FLG on a previously selected area of the composite films. The same area (25 x 25 µm) was used for the analysis of each sample: a Raman spectrum was acquired at each 0.5 µm, and for each spectrum the area of the WPU band (from 1400 and 1500 cm^{-1}) and the G band of the graphite nanoplates (from 1550 to 1650 cm^{-1}) were measured. The map was built based on the calculated ratio of the area of the WPU band to the area of the G band of the graphite material ($A_{WPU\ band}$ /$A_{G\ band}$). In the Raman mapping image (**figure 79**) the green spots corresponds to large value of the ratio, corresponding to the detection of mostly WPU, while the black spots correspond to a ratio near zero.

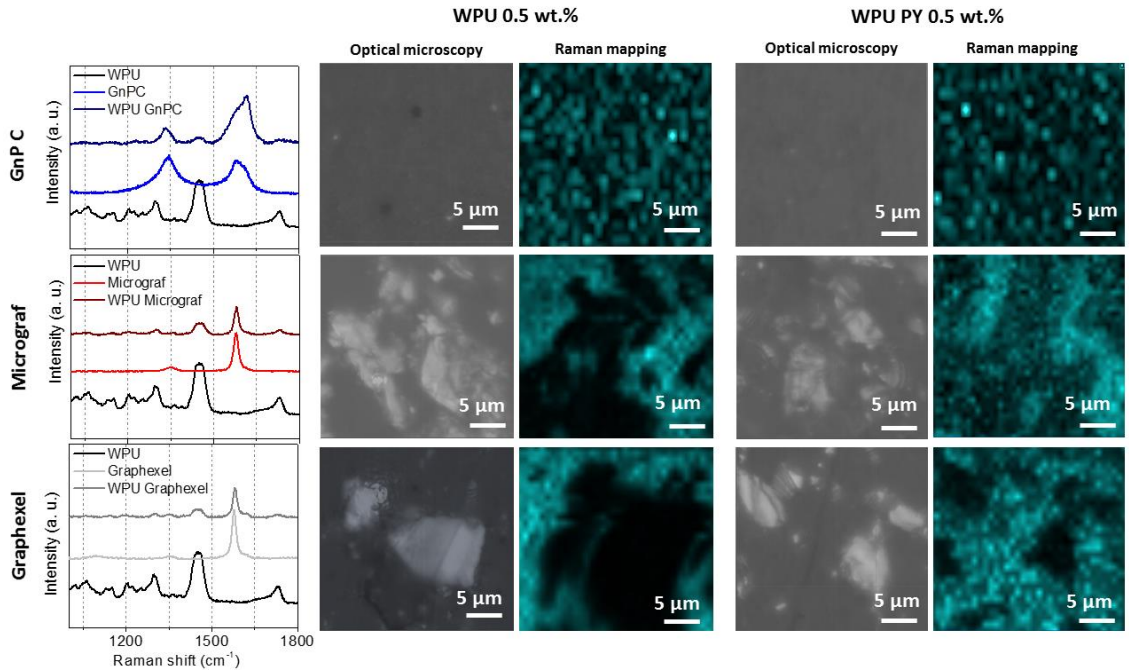

Figure 79: Raman spectra and optical microscopy image of the selected area for the Raman mapping analysis of the WPU composite films (0.5wt.%)

The optical microscopy images of the GnPC composite (WPU 0.5 wt.%) and FLG obtained from GnPC (WPU PY 0.5 wt.%), presented in the **figure 79**, showed to be very uniform and the GnPC particles are difficult to detect. However, when the Raman mapping is performed, a good dispersion of GnPC in the WPU matrix is identified. For all the analyzed areas of these composite films no significant differences are observed for the distribution of GnPC WPU and FLG GnPC WPU. Both showed a good distribution, and this may be related with the similar mechanical properties of both composite films. For Micrograf and Graphexel composites, the dispersion seems to improve when FLG is used. This may be in agreement with the significant enhancement of the mechanical

properties of FLG Micrograf and Graphexel composites when compared with the pristine Micrograf or Graphexel composites. The thermogravimetric analysis results obtained for the same samples is presented in the **figure 80**. The designation of WPU GnPC corresponds to the pristine GnPC WPU composite film and the identification of WPU GnPC PY corresponds to the GnPC FLG WPU composites, since the FLG was obtained by non-covalent exfoliation process using the pyrene derivative (PY). Similar designations are used for the Micrograf and Graphexel WPU composites.

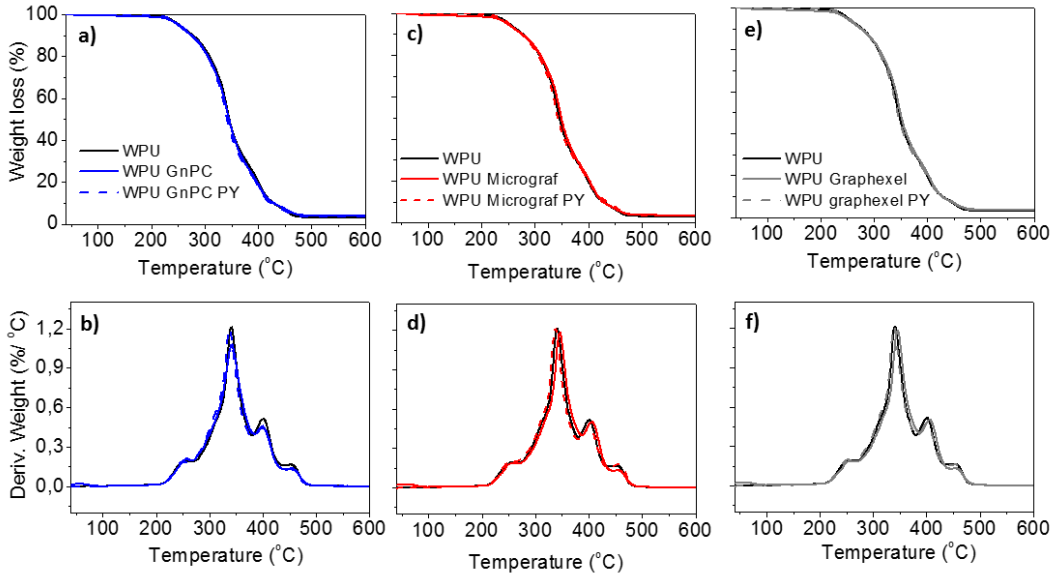

Figure 80: Thermogravimetric analysis of the: a) and b) GnPC, c) and d) Micrograf and e) and f) Graphexel WPU composites, at 0.5 wt.% and its comparison with WPU and FLG WPU films.

The results showed that the incorporation of the pristine graphitic material as well as FLG did not affect the thermal properties of the WPU films, since the weight loss as well as the derivative weight loss curves of the composite films are very similar to the WPU film.

A property of particular practical importance and interest in the present study was the moisture permeability or water vapor transmission (WVT), which is a measure of the rate at which water vapor passes through a polymer film. The WVT rate was calculated according to the specifications of ASTM E96:

$$WVT = G/tA = (G/t)/A \quad (4)$$

where G is the weight change, t is the testing time and A is the test area (dish mouth area). The moisture permeance was calculated from the known WVT rate using the following equation:

$$\text{Permeance} = WTV/\Delta P = WTV/S(R_1 - R_2) \quad (5)$$

where ΔP = vapor pressure difference (in mmHg ($1.333x10^2$ Pa)); S = saturation vapor pressure at test temperature; R_1 = 90% and R_2 = 0%, relative humidity values inside the test chamber and dish, respectively. The saturation water vapor pressure at 38 ºC was considered as S = 49.692 mmHg. The coefficient of moisture permeability, $P(H_2O)$, was calculated as follows:

$$P(H_2O) = \text{Permeance} \times \text{Thickness} \quad (6)$$

Where Thickness corresponds to the thickness of the WPU films. The results of $P(H_2O)$ for the WPU and WPU composites at 0.5 wt.% loading (GnP and FLG GnP, Micrograf and FLG Micrograf, Graphexel and FLG Graphexel) are presented in **figure 81**.

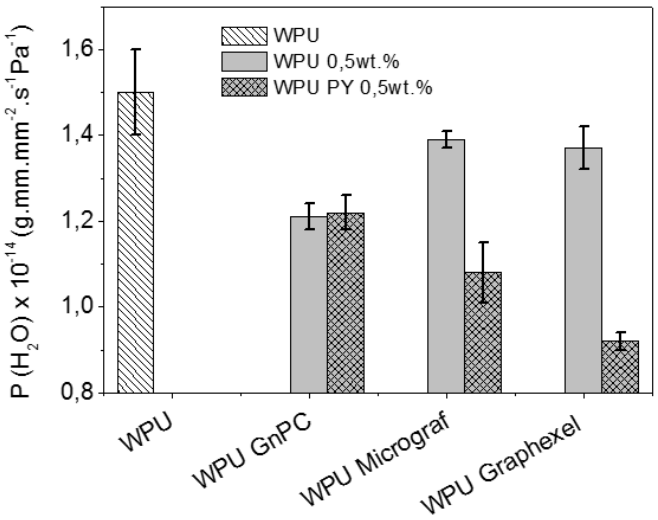

Figure 81: Coefficient of moisture permeability of the WPU composite films with 0.5wt.% of content.

The incorporation of the graphite-based materials (pristine and FLG) reduced the $P(H_2O)$. For GnPC no significant difference is observed between the films with pristine GnPC and FLG GnPC, presenting a decrease of 20 % of $P(H_2O)$ relative to WPU, in both cases. This difference is more accentuated for Micrograf and Graphexel materials. A decrease of about 10 % is observed for both pristine Micrograf and Graphexel, but this percentage is higher for FLG Micrograf (29 %) and FLG Graphexel (40 %). The effectiveness of the FLG WPU composites as moisture barrier was clearly demonstrated, showing to be more effective than the pristine graphitic materials. Furthermore, the FLG WPU composite films prepared in this work presented a superior performance when compared with values reported in the literature, namely for GO/WPU 0.5 wt.% composite, that showed a

decrease of 25 % of P (H_2O) [346] and 2D layered material molybdenum disulfide (MoS_2)/ WPU 0.5 wt.% composite in which P(H_2O) decreased 6 %. [409].

The electrical properties of the composite films were analyzed. Typically, the conductivity of the GnPC and Micrograf composite films (for pristine and FLG materials) were found to be very similar, showing an increase of about two orders of magnitude when compared with the WPU itself. The pristine Graphexel WPU composites demonstrated an increase only about one order of magnitude, although the FLG Graphexel WPU composite improved the electrical conductivity value by 3 orders of magnitude. These results are presented in the **figure 82**. Despite all conductivity values are in the range of the insulating materials, these results showed that the electrical properties are enhanced with the incorporation of the graphite-based materials. Moreover, 0.5 wt.% of incorporation is a low content for the improvement of electrical properties, since the percolation threshold for graphene WPU composite is typically above 1.0 wt.% [351, 362, 363] Carbon nanotubes typically present a lower percolation threshold that, in the case of CNT WPU composite films, was reported to be above 0.2 wt.%. [330, 336] Possible synergetic effects of mixing graphene and CNT to form WPU composites were also studied, since this approach has the potential to improve the mechanical, thermal and electrical properties of the composite films. [361] Taking this as motivation we prepared FLG / CNT / WPU composite films and the mechanical, electrical and barrier properties were studied.

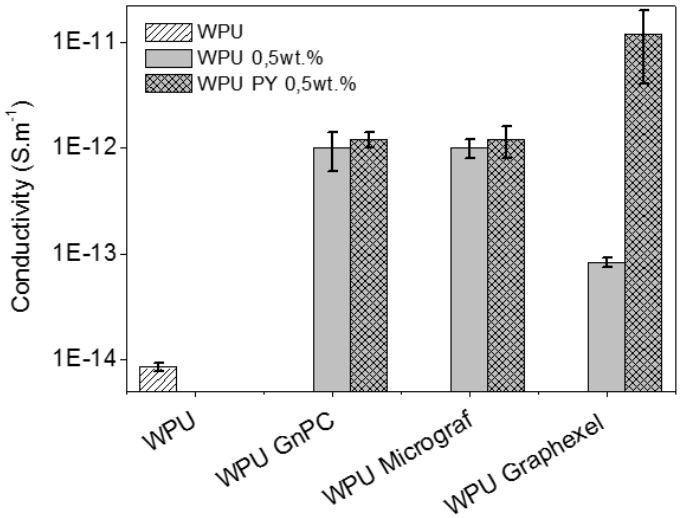

Figure 82: Conductivity of the WPU composite films with 0.5wt.% of content.

The results obtained showed that the FLG Graphexel WPU composite presented better mechanical, electrical and barrier properties. For that reason this graphite-based material

was selected to prepare FLG Graphexel / CNT / WPU films, with the total incorporation of 0.5 wt.%, in which 0.25 wt.% was FLG Graphexel and 0.25 wt.% was CNT. Also, CNT WPU 0.5 wt.% composite films were produced to evaluate the synergistic effect of mixing FLG and CNT. **Table 5** shows the comparison of the mechanical, electrical and barrier properties of all 0.5 wt.% WPU composites produced. As depicted in this table, the mechanical and barrier properties are not significantly changed when CNT are mixed with the FLG. However, the electrical conductivity shows an increase of 6 orders of magnitude relative to WPU film, and 3 orders of magnitude when compared with the Graphexel FLG WPU composite. Despite the electrical conductivity of CNT WPU composite is in the same order of magnitude (10^{-8} Sm^{-1}), there is a clear synergistic effect of the FLG and CNT, since only 0.25 wt.% of CNT content was added in the FLG/CNT/WPU composite, and the composite with Graphexel FLG WPU presents lower conductivity.

Table 5: Mechanical, electrical and barrier properties of the WPU composite films at 0.5wt.% loading.

WPU films 0.5wt.%	Young's Modulus (MPa)	Yield strength (MPa)	Tensile strength (MPa)	Elongation at break (%)	Conductivity (Sm^{-1})	WVT decrease (%)
WPU	575±22	17.7±0.5	22±3	252±58	$(8.5\pm0.8)\times10^{-15}$	0
WPU/GnPC	800±22	22.1±0.8	24±3	186±49	$(1.0\pm0.4)\times10^{-12}$	20
WPU/GnPC Py	792±44	23.7±0.6	29±2	235±58	$(1.2\pm0.2)\times10^{-12}$	20
WPU/Micrograf	724±43	20.6±0.5	27±3	251±40	$(1.0\pm0.4)\times10^{-12}$	9
WPU/Micrograf Py	811±52	23.1±0.9	24±2	155±41	$(1.2\pm0.4)\times10^{-11}$	29
WPU/Graphexel	706±55	18.9±0.7	19±3	159±23	$(8.3\pm0.8)\times10^{-14}$	10
WPU/Graphexel Py	818±35	24.3±0.7	27±2	223±41	$(1.2\pm0.8)\times10^{-11}$	40
WPU/Graphexel/CNT Py	812±20	24.4±0.7	24±2	179±41	$(5.1\pm0.7)\times10^{-8}$	39
WPU/CNT Py	843±55	23.1±0.9	22±1	113±38	$(3.8\pm0.9)\times10^{-8}$	35

5.4. Conclusions

In summary, aqueous FLG suspensions were produced from different graphite and graphite nanoplate materials using a pyrene derivative. The water suspensions showed to be stable along the storage time. The as-prepared suspensions were formed by up to 70% of FLG (considering from bi- to few- layer graphene) as identified by Raman

spectroscopy. The formation of FLG was imaged by STEM analysis. Composites were produced with GnPC, Micrograf or Graphexel and WPU as matrix, as well as FLG GnPC, FLG Micrograf or FLG Graphexel/WPU. The composites presented improved mechanical properties as the reinforcement content was increased up to 0.5 wt.%. For 0.5 wt.% of incorporation the FLG/WPU composites showed higher mechanical properties compared with the pristine graphite or graphite nanoplates/WPU composites. The electrical conductivity and barrier properties of FLG Graphexel/WPU composites presented higher performance, showing and increase of 3 orders of magnitude in electrical conductivity and 40 % of P(H_2O) decrease, respectively, demonstrating the importance of flake size for these properties. The mechanical and barrier properties are not significantly changed when CNT are mixed with the FLG Graphexel. However, the electrical conductivity is highly improved, showing an increase of 6 order of magnitude when compared with WPU film, and 3 orders of magnitude when compared with the FLG Graphexel/WPU composite. Despite the electrical conductivity of CNT/WPU composite is in the same order of magnitude (10^{-8} Sm^{-1}), there is a clear synergistic effect of the FLG and CNT, since only 0.25 wt.% of CNT was added in the hybrid FLG/CNT/WPU composite.

CHAPTER 6. DISPERSION OF GRAPHITE NANOPLATES IN A POLYPROPYLENE MATRIX

This chapter is based on the article:

E. Cunha, M. C. Paiva, L. Hilliou, J. A. Covas, "Tracking the progression of dispersion of graphite Nanoplates in a polypropylene matrix by melt mixing", Polymer Composites, 2015, DOI: 10.1002/pc.23657;

J. A. Covas**, E. Cunha**, M. C. Paiva, L. Hilliou, "Dispersion of graphite nanoplates during melt mixing", Society of Plastics Engineering, 2015, DOI: 10.2417/spepro.006072, (by invitation from SPE).

6. DISPERSION OF GRAPHITE NANOPLATES IN A POLYPROPYLENE MATRIX

6.1. Introduction

Exfoliated graphite in the form of thin flakes with a large surface area and nanometric thickness may be considered a 2D nanomaterial. These graphite nanoplates [315] (GnP) tend to agglomerate due to Van der Waals interactions, similar to other graphitic carbon nanoparticles such as nanotubes or fullerenes. Since GnP exhibit similar mechanical and electrical properties to carbon nanotubes (CNT) and may present larger surface area, [38, 296] they have great potential to be used in polymer nanocomposites for structural and functional applications. [13, 38, 39, 296, 297] However, in most practical situations, maximum performance is expected when the GnP agglomerates are dispersed into their primary 2D particles (or even further exfoliated into smaller thinner particles) in the polymer matrix and have good interfacial adhesion [296]. While the problem of interfacial bonding with the polymer may be solved by tailored chemical functionalization of the graphite surface, [410-412] the dispersion of these particle agglomerates in polymers is complex. The technique adopted to produce the nanocomposites may largely affect the dispersion of the agglomerated GnP into their individual flakes. Solution blending and in situ polymerization associated to sonication can achieve good dispersion, but involve the use of solvents. [13, 39] Melt compounding is economically attractive and successfully used in industry to prepare polymer blends and composites but, so far, has not always been able to achieve optimal nanoparticle dispersion. [13, 38] Previous studies carried out using a variety of mixing equipment (extruders, internal mixers, prototype mixers) for carbon black [40], carbon nanofibers [41], and carbon nanotubes [42, 43] have demonstrated that the intensity and type of hydrodynamic stresses (i.e., shear versus extensional), residence time, and interfacial adhesion play a major part in dispersion. [41, 42, 44, 413] However, while the dispersion mechanism of carbon black and carbon nanotubes in polymers is well studied, for GnP it is far from being well understood.

This work reports the dispersion of GnP in polypropylene by melt mixing using a small-scale continuous prototype mixer. The focus is to study the progression of the dispersion of GnP, a process that is not well understood. Composites were prepared with 2 and 4 wt.% of GnP, as-produced and functionalized by grafting polypropylene modified with maleic anhydride to the GnP surface. The processability of the composites was similar to that of polypropylene, as assessed by capillary rheometry. The nanoparticle dispersion

was analyzed by optical microscopy. The progression of the number of agglomerates and their size, for pristine and functionalized nanoparticles, was observed along the mixer. The final agglomerate dimensions were found to be similar for pristine and functionalized GnP, and indicated that agglomerate dispersion progressed toward individual nanoparticles. The interface improvement of functionalized GnP with polypropylene was observed by scanning electron microscopy.

6.2. Experimental

6.2.1. Materials

Polypropylene ICORENE PP CO14RM from ICO polymers, with a density of 0.900 g/cm^3 and an MFI of 13 g/ 10 min (190 ºC/2.16 kg) was selected as matrix. Polypropylene grafted with maleic anhydride (PP-g-MA), containing 8–10 wt.% of maleic anhydride, with an MFI of 28 g/10 min (2.16 kg/155ºC) and density of 0.934 g/cm^3 was purchased from Sigma Aldrich. The GnP was a commercial grade from XG Sciences Inc., designated by the producer as "graphene nanoplatelets," xGnP ® - grade H, with nominal equivalent diameter of 5–25 µm, thickness of 15 nm, and an average surface area of 60–80 m^2/g. According to the recommended nomenclature [315], flakes formed by more than 10 stacked graphene layers (corresponding to flake thickness in the range 3–4 nm considering the interlayer spacing of graphite) should not be designated as "graphene". The nominal thickness of xGnP ® - grade H is approximately 15 nm, thus the designation "graphite nanoplates" (GnP) will be used here, according to Ref. [315], which indicates the following reference names: graphite "nanoplates," "nanosheets," or "nanoflakes". The GnP were functionalized by the 1,3-dipolar cycloaddition reaction of azomethine ylides as described elsewhere [160], by heating GnP with the reagents at 250 ºC during 3h, resulting in GnP with covalently bonded pyrrolidine-type groups. Then, reaction of these groups with maleic anhydride grafted in PP was carried out under the conditions described in Ref. [295], leading to the covalent modification of the GnP surface with PP-g-MA, yielding PP-functionalized GnP (F-GnP).

6.2.2. Composite Preparation

Polypropylene with 2 or 4 wt.% of GnP or F-GnP in powder form were premixed and melt mixed at 200ºC at various rates, using a prototype small-scale continuous mixer [41] [42]. Simultaneously, a continuous filament is extruded. As illustrated in **Fig. 83**, the mixer consists of a vertical stack of circular rings having the same external diameter, but with alternate inner diameters of 1 and 8 mm. This assemblage sits at the bottom of the barrel of a ROSAND RH10 capillary rheometer; the velocity of the descending ram defines the flow rate, the set temperature being also precisely controlled. Consequently, the melt is subjected to repetitive 8:1 and 1:8 converging/diverging flows, which create a strong extensional component near to the longitudinal symmetry axis [292]. Since the pioneering work of Grace for liquid suspensions [288], it is well recognized that extensional flows are much more efficient for dispersion purposes than pure shear flows. A pressure transducer (Dynisco PT420A; 0–3000 psi) was flush mounted at the entrance of the mixer and connected to a Dynisco 1390 strain gage indicator with analog retransmission output accuracy span of 0.2 %. In turn, the indicator was connected to a DAQPad6020E data acquisition system from National Instruments and driven by custom written LabViewTM routines. The latter perform on-the-fly oversampling of the acquired data, which results in a significant improvement of sensitivity of the pressure transducer [414]. After each run, the stack of rings was quickly removed from the rheometer and the material present inside the rings with larger inner diameter was collected, quenched in water, and retained for subsequent characterization. Since each pair of rings with distinct inner diameters yields one material sample, the latter is identified relative to its creator pair (e.g., sample 2 relates to material collected from the second pair of rings). The experiments were performed using 2–8 stacked pairs of rings and the average shear rates at the small (capillary) channels varied between 200 and 3500 s^{-1}.

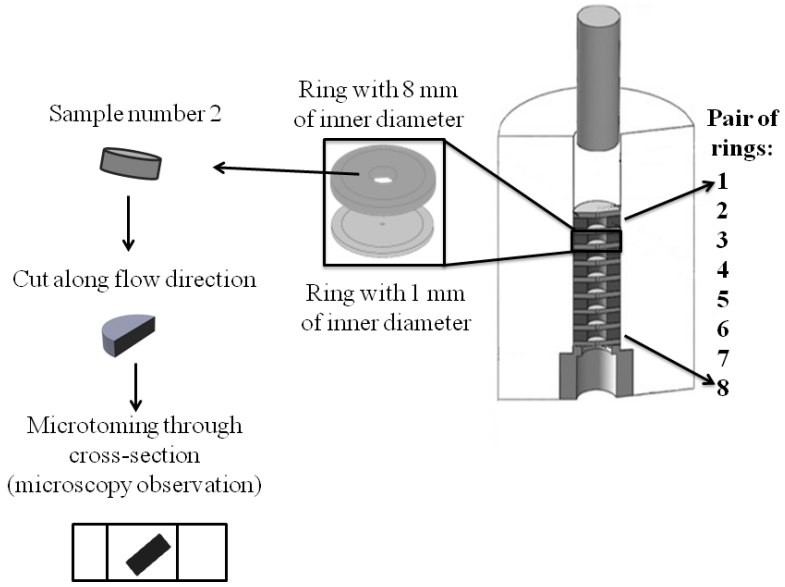

Figure 83: Schematic representation of the prototype small-scale continuous mixer and of the samples collected for optical microscopy observation

PP was characterized by capillary rheometry to obtain the viscosity at high shear rates (typically 10^2–10^4 s^{-1}). PP in powder form was fed into the reservoirs of the dual bore (equipped with 2 capillary dies with 1mm diameter and lengths of 2 and 8 mm to allow online Bagley corrections) Rosand RH10 capillary rheometer, pre heated to 200ºC. After 10 min at 200ºC to attain thermal equilibrium, the step ramps of piston velocities (from small to large) were performed and the steady pressure drop reading was recorded for each velocity.

6.2.3. Composite Characterization

The dispersion of GnP and F-GnP in the PP matrix at various axial locations of the mixer was analyzed by optical microscopy, using a BH2 Olympus optical transmission microscope coupled to a LEICA DFC 280 digital camera. Sections of 5 μm thickness were cut longitudinally through the thickness of the samples collected, using a Leitz 1401 microtome, as schematically presented in **Fig. 83**. Image J software was used to measure the number of GnP or F-GnP agglomerates and their area. Twenty images were captured per sample, meaning that approximately 3000 agglomerates were analysed per collected sample. The initial size of the GnP and F-GnP powders was measured by optical microscopy, using the following procedure: approximately 5 ppm of each powder was mixed manually with epoxy resin, spread on a glass slide and cured at room temperature for 48 h. Four samples were prepared for each powder mixture and 100 images were

captured as described above, thus enabling the analysis of approximately 800 agglomerates per type of GnP. Scanning electron microscopy (SEM) of cryofractured samples was performed on a NanoSEM FEI Nova 200 microscope after platinum coating.

6.3. Results and Discussion

6.3.1. Rheological Characterization

The variation of pressure drop (DP) with the number of pairs of rings utilized in the mixer was monitored for the PP matrix, PP with 2 wt.% GnP and PP with 2 wt.% F-GnP. The results for a corrected shear rate of 500 s^{-1} are presented in **Fig. 84a**. All materials exhibit a linear increase of pressure with the increase in the number of pairs of rings. This behavior demonstrates that appending pairs of rings has an additive effect, i.e., there is no stress build-up in the mixer, nor any significant structural orientation at the shear rate tested (see for instance, Ref. [415]). Appending pairs of rings is equivalent to increasing mixing time. As such, the curves in **Fig. 84a** are reminiscent of Bagley plots used in capillary rheometry to correct pressure drop measurements from die entrance or exit effects. Thus, shear-flow curves (**Fig. 84b**) were built using the pressure data and the usual set of equations for capillary rheometry [292] (error bars would be smaller than the symbols). The shear stress is given by,

$$\sigma = \frac{\Delta P R_c}{2L} \tag{7}$$

where ΔP is the pressure drop in the mixer, R_c and L are the apparent radius and length of the mixer, respectively. Since in the prototype small-scale mixer the contribution to pressure drop should come predominantly from the flow along the smaller channel, R_c is 0.5mm and the apparent length depends on the number of stacked pairs of rings. The shear rate can be estimated using the Weissenberg– Rabinowitsch equation:

$$\dot{\gamma} = \frac{Q}{\pi R^3}\left(3 + \frac{d\,ln\,Q}{d\,ln\,\Delta P}\right) \tag{8}$$

where Q is the volumetric flow rate.

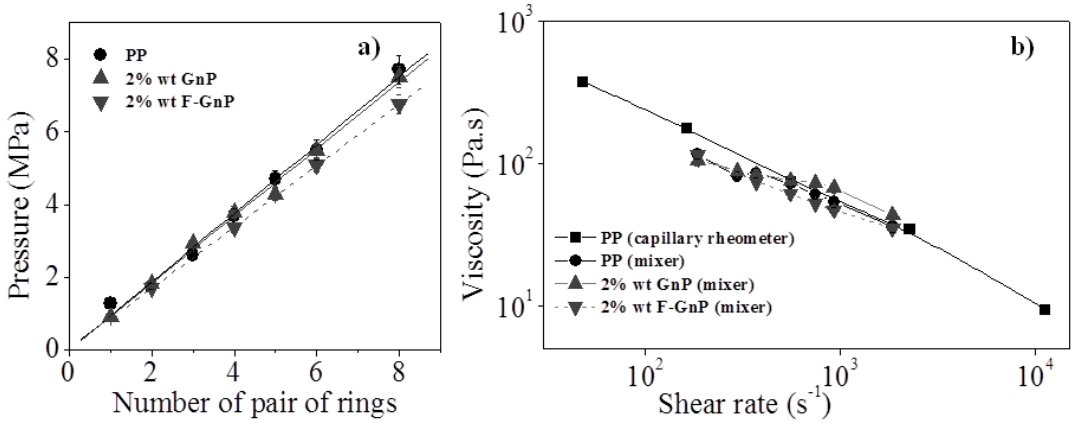

Figure 84: Shear flow behavior of PP and its composites with graphite nanoplates: (a) melt pressure axial profile; (b) shear flow curves.

Experiments using a conventional capillary rheometer were performed for PP, at the same temperature (200 ºC) and shear rate range from 50 to 11,000 s^{-1}. As shown in **Fig. 84b**, the flow curve obtained for PP in this experiment is closely matched by that obtained with the prototype mixer, thus validating the approach followed here to obtain rheological information. Additionally, the flow curves indicate that the viscosity of PP is essentially similar to that of the composites with 2 wt.% of GnP and F-GnP, which is relevant for extrusion and compounding. Small deviations are observed: a slight viscosity increase with the incorporation of GnP and a slight decrease with F-GnP. Further work is required to confirm this observation. Nonetheless, a similar relative response was observed for a polystyrene/CNT system subjected to step shear experiments and interpreted in terms of the functional groups bonded to the carbon nanotubes inducing a free volume increase that lead to a melt viscosity decrease [416]. The extrudate-swell of the filaments (computed as the ratio between their diameter and the diameter of the die orifice, which is 1 mm) is depicted in **Fig. 85a** for three distinct shear rates. At constant shear rate, the elasticity of PP varies negligibly with the number of pairs of rings stacked inside the rheometer. In the case of the composites, such stability is attained around the fourth pair. This response could be interpreted as equivalent to the progression of dispersion in the mixer, but this has to be taken cautiously, as the question remains whether there is a direct correlation between dispersion and extrudate-swell. As expected, extrudate-swell increases with increasing shear rate for all materials (**Fig. 85a and b**). It is important to note that the surface of the extrudates remained smooth and rheological defects were absent in the range of shear rates applied. As observed for other polymer composites containing different types of fillers, [417-420] addition of graphite nanoplates decreased

extrudate-swell. The nanocomposite containing F-GnP exhibits a slightly higher elasticity than that with GnP.

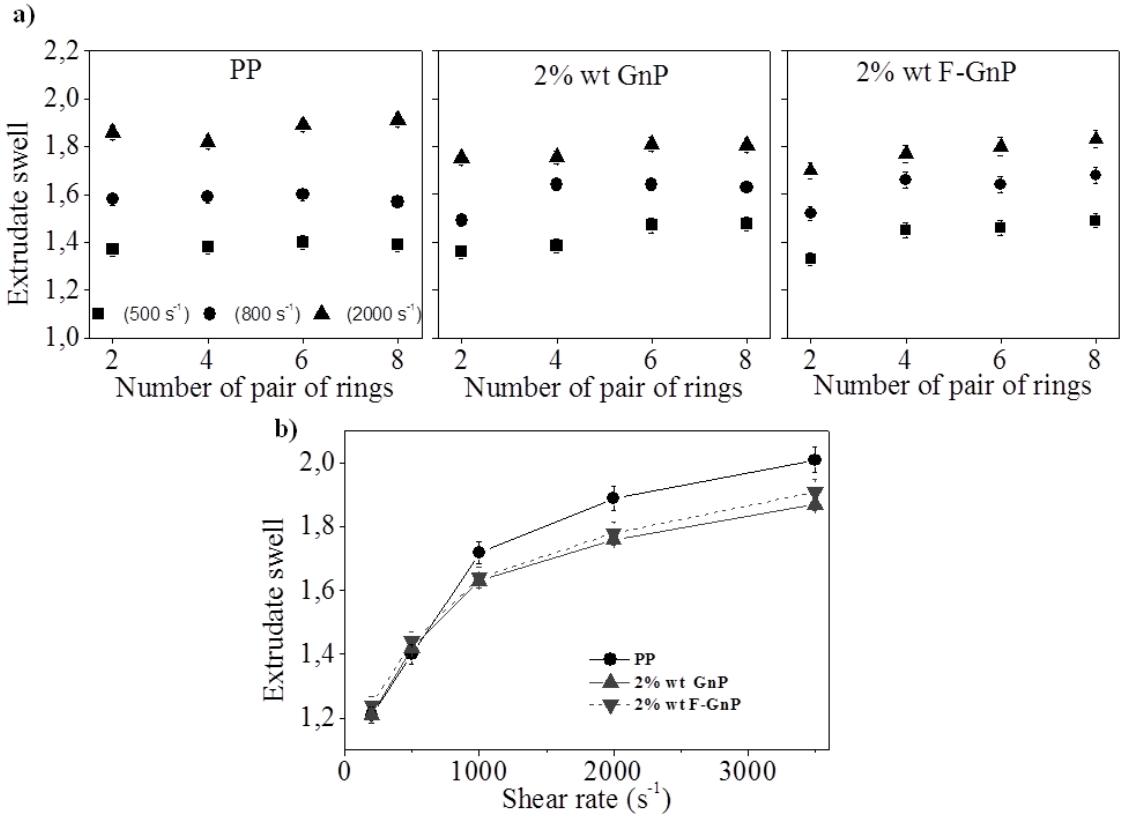

Figure 85: a) Effect of the number of pairs of rings on the extrudate-swell of PP and PP nanocomposites measured at 500 s^{-1} (squares), 800 s^{-1} (circles), and 2000 s^{-1} (upward triangles); (b) variation of the extrudate-swell of PP and PP nanocomposites with shear rate (prototype mixer equipped with 6 pairs of rings).

6.3.2. Dispersion of Graphite Nanoplates

The progression of the dispersion of GnP and F-GnP in the polymer matrix along the mixer was monitored using a setup formed by eight pairs of stacked rings. Although these graphite nanoplates (or primary nanoparticles) are characterized by the producer as having an equivalent diameter of about 5–25 μm and thickness of 15 nm, they strongly interact with each other due to Van der Waals forces, yielding large agglomerates. The aim is to disperse these large agglomerates into the primary nanoparticles, or even further exfoliate these into thinner flakes. Considering the producer's data, the primary nanoparticles may have a maximum projected area, as observed by optical microscopy, in the range of 20–500 μm^2. Increasing the angle between the particle and the observation direction, the measured projected areas will be smaller. The typical GnP powder size was experimentally measured (see the section titled "Experimental") and compared with the

dimension of the particle agglomerates observed in the nanocomposites collected along the mixer. The composites with 2 wt.% of nanoparticles were forced through the mixer at the shear rates of 500 and 2000 s^{-1}, while the composites containing 4 wt.% of nanoparticles were tested at 500 s^{-1}. **Figure 86** shows the representative optical micrographs of the samples collected along the mixer, for all the compositions and conditions tested. In general, dispersion improves along the mixer, particularly up to pair of rings no. 4, which is consistent with the behavior of extrudate-swell. No preferred orientation of the filler particles is apparent.

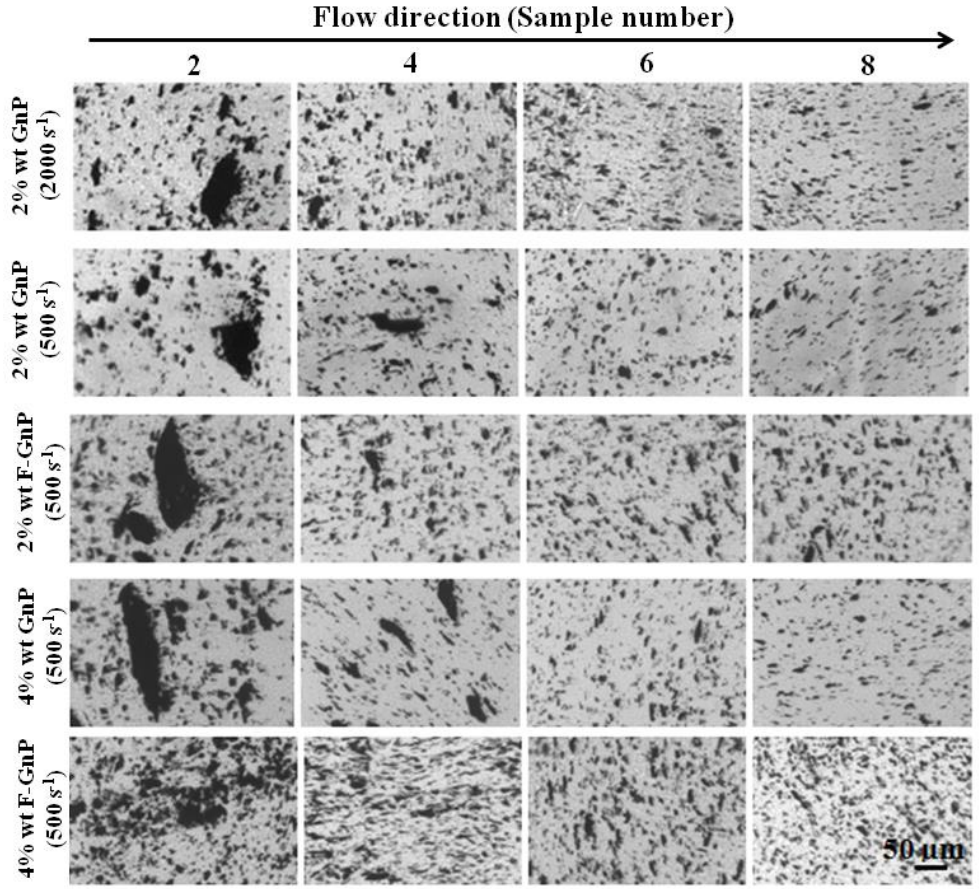

Figure 86: Optical microscopy images illustrating the progression of the dispersion of GnP and F-GnP in the PP matrix along the mixer.

Defining an agglomerate area ratio, A_R, as the ratio of the sum of the areas of all surviving agglomerates to the total area of composite analyzed, the highest dispersion level will correspond to the lowest A_R value computed. Area ratio is extensively adopted in the literature to characterize dispersion in polymer nanocomposites. [41, 43] However, its exclusive use could, in some situations, convey misleading evidence (for example, 4 smaller particles occupying the same area as a single larger one would produce the same A_R). Therefore, it seems advisable to use simultaneously various descriptors of dispersion

in order to circumvent their individual limitations. For this reason, **Fig. 87** characterizes the progression of dispersion along the mixer (samples 2, 4, 6, and 8) of the various nanocomposites manufactured in terms of A_R (**Fig. 87a and b**), average agglomerate area (A_{av}) (**Fig. 87c and d**), number of agglomerates per unit area (N_A/mm^2) (**Fig. 87e and f**), and area of the largest agglomerate **(Fig. 87b, g and h**). A decrease of A_R and A_{av} indicates higher dispersion of the GnP and F-GnP agglomerates into primary particles. As the agglomerates are subjected to shear in the polymer melt, they become progressively smaller, and this process may develop until they reach the lower possible dimensions. The dispersion limit is reached when the dimensions of the primary GnP particles are attained (or ideally, with lower flake thickness, if the shear applied is enough to further exfoliate the GnP). The nanocomposite properties are expected to improve with the extent of dispersion. As measured by A_R, A_v, and N_A/mm^2, dispersion of GnP develops gradually along the mixer, whereas that of F-GnP seems to level off between pair of rings 4 and 6. The values of A_R of the latter are systematically higher than those for the pristine counterpart. Although F-GnP presents a smaller A_{av} compared to GnP (**Fig. 87c**), a larger number of agglomerates is formed (**Fig. 87e**). These trends were observed consistently along the mixer for GnP and F-GnP at 2 and 4% wt compositions. The larger number of smaller agglomerates observed for the F-GnP may be related to lower cohesion of the polymer-functionalized primary F-GnP particles under melt processing conditions, compared to pristine GnP. Further studies are necessary to clarify this observation. It is also interesting to note that the progressive dispersion witnessed here contrasts with the progression detected for the same matrix reinforced with comparable CNT content, processed in the same device. [42, 295] In the case of CNTs, initially dispersion develops steadily, followed by a sharp increase and another gradual regimen. These stages could be associated with the onset of erosion and rupture mechanisms [43], although this is difficult to prove given the small dimension of these particles. Despite the quite distinct geometry of GnP, it could be reasoned that their dispersion seems to follow predominantly a single mechanism, although further experimental evidence is necessary to support this hypothesis. The rate of dispersion of GnP seems to be nearly independent of shear rate. Again, while A_R shows that composites subjected to higher shear rate are coarser, the remaining indices reveal that a larger number (N_A/mm^2) of smaller particles (A_{av}) are present at high shear rates.

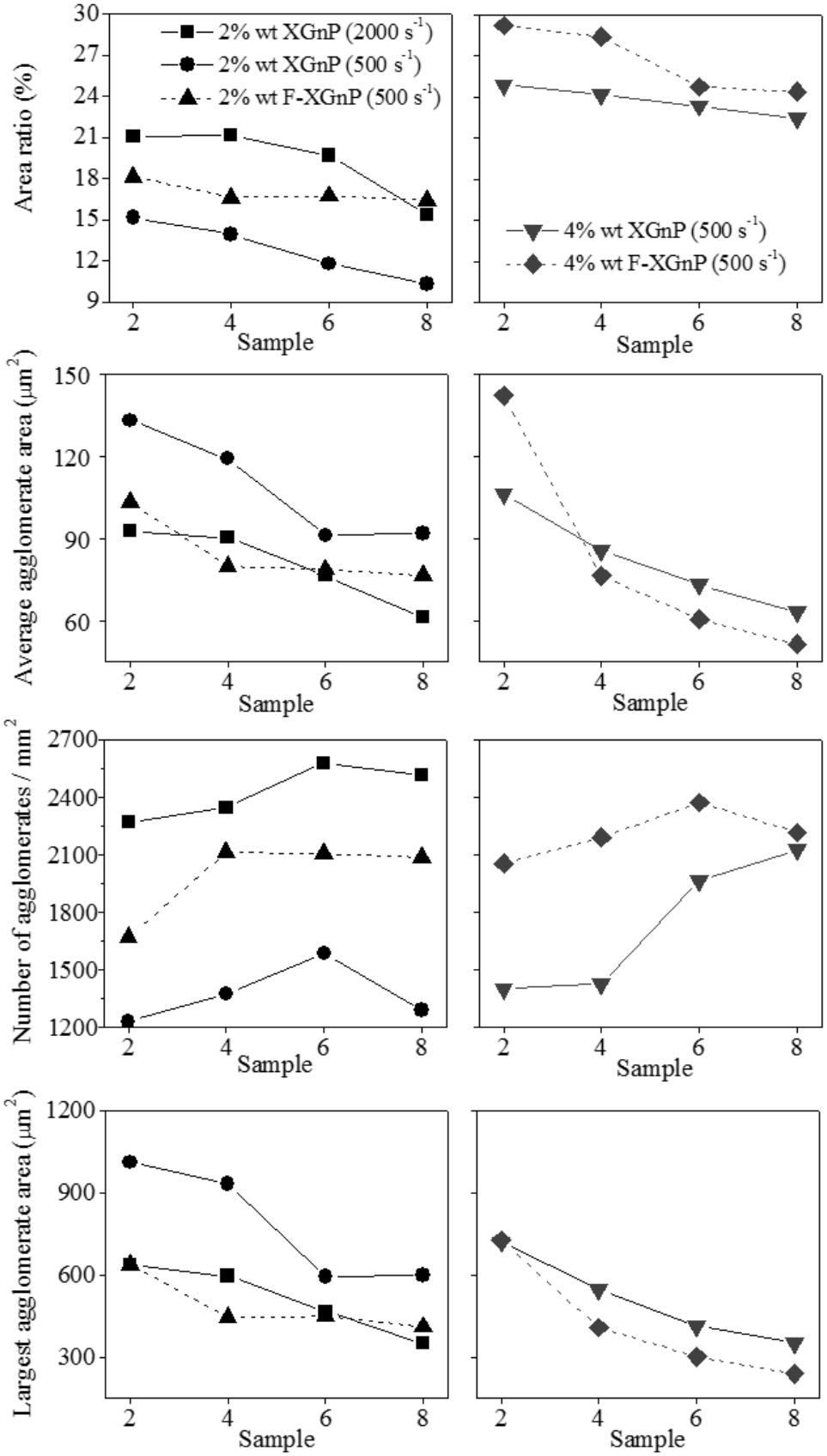

Figure 87: Characterization of the (a) progression of the dispersion of PP– graphite nanoplate composites along the mixer and (b) area ratio (A_R); (c) and (d) average agglomerate area (A_{av}); (e) and (f) number of agglomerates per unit area (N_A/mm^2); (g) and (h) largest agglomerate area. Left column: 2% wt. of GnP and F-GnP; right column: 4% wt. of GnP and F-GnP.

It is generally believed that, similar to polymer blends, dispersion in solid suspensions takes place when sufficient stress and residence time levels are attained [285]. In this case, higher shear rates promote higher stress levels at the cost of residence time (202 s for the shear rate of 500 s^{-1} and 54 s for the shear rate of 2000 s^{-1}); therefore, they seem to be the dominant factor. As expected, higher incorporation levels of graphite cause an increase in A_R, but the evolution of all dispersion indices is qualitatively, and in some cases quantitatively, similar to that of the less filled composite.

The measured average size of the GnP and F-GnP powder agglomerates was 287 ± 47 and 381 ± 93 μm^2, respectively, corresponding to an equivalent diameter of approximately 19 μm for GnP and 22 μm for F-GnP. If these numbers are compared with the sizes of the largest agglomerates present in sample 2 (**Fig. 87g**), it becomes evident that nanoparticle agglomeration occurred as the material was kept in the reservoir of the capillary rheometer in order to attain thermal stability (under quiescent conditions). Analogous agglomeration phenomena have been observed for CNT [42]. **Figure 88** presents the progression of the equivalent diameter along the mixer.

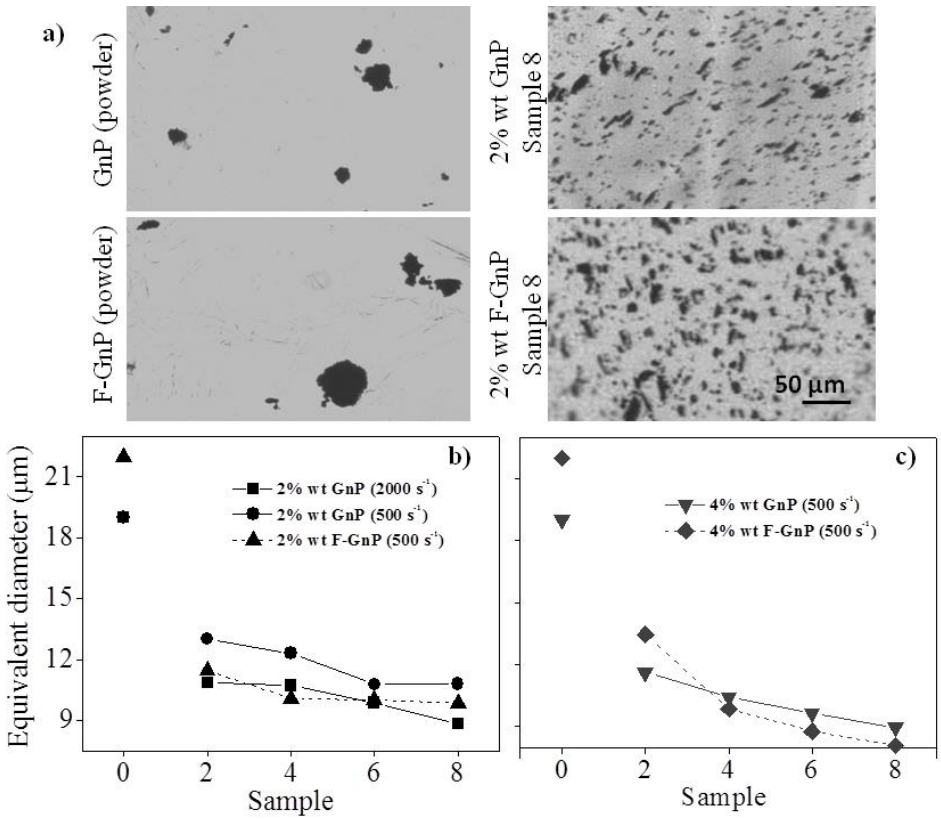

Figure 88: Progression of the equivalent diameter of GnP and F-GnP agglomerates from powder form to the final nanocomposite: (a) optical microscopy images of the GnP and F-GnP agglomerates; composites with (b) 2 wt.% nanoparticles and (c) 4 wt.% nanoparticles.

The final values obtained for the various materials and processing conditions remain within 8–11 μm (with the composites with 4 wt.% staying in the lower range). Thus, the mixer was able to prepare nanocomposites containing exfoliated graphite nanoplates within the lower range of the typical sizes of the powder form of GnP.

Figure 89 illustrates the SEM images of the pristine GnP (**Fig. 89a and** b) and the cryofractured sections of sample 8 of the nanocomposites reinforced with 2 wt.% of GnP (**Fig. 89c**) and F-GnP (**Fig. 89d**). The F-GnP showed better interfacial adhesion with the PP matrix when compared with no functionalized GnP. These results are in agreement with the higher elasticity of F-GnP nanocomposites which may have caused the decrease of the extrudate-swell of these nanocomposites, as discussed above (**Fig. 85**).

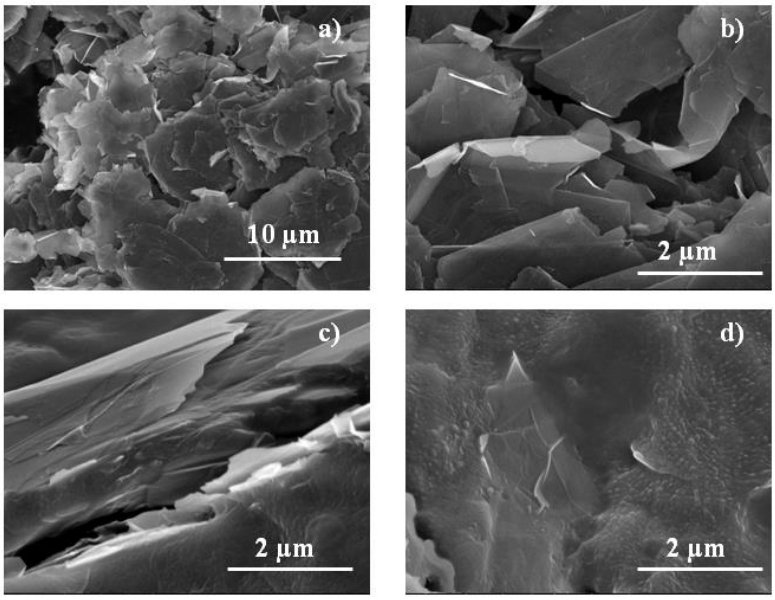

Figure 89: SEM images of (a) and (b) pristine graphite nanoplates at two magnifications; (c) cross-section of the nanocomposite reinforced with 2 wt% GnP collected from the eigth pair of rings, and (d) the same as (c) for the nanocomposite with F-GnP.

6.4. Conclusions

The dispersion of GnP and F-GnP in polypropylene was studied as well as its progression during the mixing process achieved with a small-scale prototype. The viscosity of the nanocomposites produced with 2 wt.% of nanoparticles was similar to that of the polypropylene matrix. The extrudate-swell increased with increasing shear rate and decreased with the addition of GnP and F-GnP. A slight decrease of extrudate-swell was observed for the F-GnP nanocomposites relative to GnP nanocomposites, which may result from the higher interfacial compatibility between F-GnP and the PP matrix, and

thus improved F-GnP surface wetting, also illustrated by the SEM images. The dispersion of GnP and F-GnP progressed gradually along the mixer length and for the FGnP, the dispersion seems to stabilize between pair of rings 4 and 6. Moreover, A_{av} and N_A/mm^2 are smaller for the latter, which may also be related with better interfacial adhesion. The equivalent diameter of the dispersed GnP and F-GnP also decreased along the prototype mixer and attained final values in the range of the GnP individual nanoparticle dimensions stated by the manufacturer, indicating that the GnP agglomerates were extensively dispersed along the composite formation process.

CHAPTER 7. CONCLUSIONS AND FUTURE WORK

7. CONCLUSIONS AND FUTURE WORK

7.1. General Conclusions

The focus of this thesis was the production of graphene and its applications in polymer nanocomposites.

The production of functionalized GNR (non-oxidized) and oxidized GNR by unzipping of CNT was successfully achieved. The f-GNR were produced by unzipping of functionalized CNT of different diameters. The CNT were functionalized with pyrrolidine groups, originating pyrrolidine-functionalized GNR. Raman spectroscopy evidenced the sp^2 character of the f-GNR. Self-assembled f-GNR stacks were observed and characterized by TEM and X-ray diffraction. TEM illustrated the formation of larger GNR from CNT with larger diameter, and a tendency of the deposited GNR to form regular stacks with few layers of GNR and an interlayer distance of approximately 0.5 nm. This observation was confirmed by X-ray diffraction and computer modeling. o-GNR were produced by oxidation of CNT showing a Raman spectrum with a high intensity D band, which indicates its extensive oxidation. The o-GNR formed stable aqueous suspensions of the exfoliated material, presenting a Zeta Potential large enough to allow its application on nanostructured film-forming using layer-by-layer deposition. This capacity was demonstrated by the assembly of multilayered membranes of CHI/f-GNR-ALG and CHI/o-GNR on a Quartz Crystal Microbalance. The technique showed the successful sequential deposition of the different layers, their stability and process reproducibility.

The liquid phase exfoliation of graphite was attained using two pyrene derivatives (PY2a and PY2b) which were synthetized through a simple and low cost functionalization methodology that lead to a high yield synthesis of the final compounds, and can potentially be scaled-up. These two pyrene derivatives were soluble in water and were tested for the exfoliation and stabilization of two different types of graphite nanoplates (GnPC and GnPH5) in aqueous media. The pyrene derivative 2a showed to be more effective in the exfoliation process leading to a formation of 80% of a total of bi- and few-layer graphene for GnPH5. The few layer graphene was also confirmed by STEM images. The very low concentration of pyrene derivatives used (to our knowledge, the lowest

reported in the literature) to exfoliate graphite in water opens perspectives to an efficient process to obtain few layer graphene.

The pyrene derivative 2a was used to exfoliate different graphite (Graphexel) and graphite nanoplates (Micrograf) in aqueous media. The stable aqueous suspensions obtained were constituted by more than 70 % of FLG and bi-layer graphene. They were mixed with WPU to form composite films with improved mechanical properties compared to the corresponding pristine graphite composites. The composite water vapor barrier properties increased by approximately 40 % relative to the polymer films with only 0.5 wt.% content of FLG. The electrical conductivity of the hybrid FLG/CNT/WPU composites films increased by 6 orders of magnitude relative to WPU film, and 3 orders of magnitude relative to the FLG/WPU composite, for 0.5 wt.% of reinforcement (0.25 wt.% of each reinforcement).

The dispersion of GnP and F-GnP in polypropylene was studied using a small-scale prototype mixer. The mixer was designed to generate high extensional flow and allowed the collection of samples along the mixer length, and thus to study the progression of the GnP dispersion. The dispersion of GnP and F-GnP was observed to progressed gradually along the mixer length and, for the F-GnP, the dispersion stabilized at an earlier stage compared to GnP. Moreover, the average agglomerate size and number of agglomerates are smaller for F-GnP, which may be related with better interfacial adhesion. The equivalent diameter of the dispersed GnP and F-GnP reached final values in the range of the individual nanoparticle dimensions stated by the manufacturer, indicating that the GnP agglomerates were extensively dispersed along the composite formation process.

7.2. Future work

The results obtained along the different lines of work reported here provide new perspectives and motivations for future work. The following paragraphs present suggestions that may be considered for further research.

The functionalized graphene nanoribbons (f-GNR) obtained by unzipping of functionalized carbon nanotubes (f-CNT) are an interesting material with ample potential applications. To make it possible, the optimization of the production method should be studied, in order to improve the yield of f-GNR. The parameters that could be explored are the sonication time, temperature, the CNT exfoliation in the presence of molecules

that could help to stabilize the f-CNT in water and perform the unzipping process in aqueous media. Other energy sources could be tested to induce the unzipping of the f-CNT, such as electrochemical methods. The formation of free-standing membranes with chitosan and alginate using f-GNR could be studied, considering the good results obtained in the QCM-D technique. Furthermore, due the extensive research in the application of GNR as sensors, the f-GNR could be tested, taking the advantage of the functional group (pyrrolidine or another group bonded to it) that could be used for selective interactions with specific compounds.

The liquid phase exfoliation of graphite in aqueous media could be studied using other amphiphilic molecules. Perylene derivatives have been used for the stabilization of CNT in water, and could be tested for the exfoliation and stabilization of graphene. Also, the modification of the functional groups bonded to the synthetized pyrene derivatives could be experimented. Furthermore, the exfoliated graphite materials obtained in this work, and its FLG, could be studied for sensor applications, or modification of already existing sensors to improve their selectivity and sensitivity. The non-covalent functionalization effect as well as the functional groups of the molecules adsorbed on the surface of the exfoliated graphite could be beneficial for this purpose.

In the field of nanocomposites, extensive research can still be done to achieve the maximum performance of the barrier properties of nanocomposite films. The increase of the incorporation loading of few layer graphene, the formation of hybrid structures with few layer graphene and CNT, as well as the combination of different types of few layer graphene with different equivalent diameters, other functionalization strategies (including the covalent and non-covalent functionalization) could be applied to enhance the performance of the polymer nanocomposites. This development would also benefit the electrical and mechanical properties of the composite films.

The FLG materials obtained could be tested in the melt mixing with thermoplastic polymer matrices, as well as hybrid FLG/CNT composites, to evaluate their dispersion and final composite properties.

References

[1] K. Novoselov, A. Geim, S. Morozov, D. Jiang, Y. Zhang, S. Dubonos, I. Grigorieva and A. Firsov, "Electric field effect in atomically thin carbon films," *Science,* 306, 2004, 666-669.

[2] A. Geim and, K. Novoselov, "The rise of graphene," *Nature Materials,* 6, 2007, 183-191.

[3] S. Bae, H. Kim, Y. Lee, X. Xu, J. Park, Y. Zheng, J. Balakrishnan, T. Lei, H. Kim, Y. Song, Y. Kim, K. Kim, B. Özyilmaz, J. Ahn, B. Hong and S. Ijima, "Roll-to-roll production of 30-inch graphene films for transparent electrodes," *Nature Nanotechnology,* 5, 2010, 574-578.

[4] K. Kim, Y. Zhao, H. Jang, S. Lee, J. Kim, K. Kim, J. Ahn, P. Kim, J. Choi and B. Hong, "Large-scale pattern growth of graphene films for stretchable transparent electrodes," *Nature Letters,* 457, 2009, 706-710.

[5] F. Schwierz, "Graphene transistors," *Nature Nanotechnology,* 5, 2010, 487-496.

[6] M. Stoller, S. Park, Y. Zhu, J. An and R. Ruoff, "Graphene-based ultracapacitors," *Nano Letters,* 8, 2008, 3498-3502.

[7] E. Yoo, J. Kim, E. Hosono, H. Zhou, T. Kudo and I. Honma, "Large reversible Li storage of graphene nanosheet families for use in rechargeable lithium ion batteries," *Nano Letters,* 8, 2008, 2277-2282.

[8] Y. Sun, Q. Wu and G. Shi, "Graphene based new energy materials," *Energy & Environmental Science,* 4, 2011, 1113-1132.

[9] G. Grigorenko, M. Polini and K. Novoselov, "Graphene plasmonics," *Nature Photonics,* 6, 2012, 749-758.

[10] F. Bonaccorso, Z. Sun, T. Hasan and A. Ferrari, "Graphene photonics and optoelectronics," *Nature Photonics,* 4, 2010, 611-622.

[11] H. Kim, A. Abdala and C. Macosko, "Graphene/polymer nanocomposites," *Macromolecules,* 43, 2010, 6515–6530.

[12] S. Stankovich, D. Dikin, H. Dommett, K. Kohlhaas, E. Zimney, E. Stach, R. Piner, N. Nguyen and S. Ruoff, "Graphene-based composite materials," *Nature,* 442, 2006, 282-286.

[13] X. Huang, X. Qi, F. Boey and H. Zhang, "Graphene based composites," *Chemical Society Reviews,* 41, 2012, 666-686.

[14] V. Berry, "Impermeability of graphene and its applications," *Carbon,* 62, 2013, 1-10.

[15] L. Huang, Y. Huang, J. Liang, X. Wan and Y. Chen, "Graphene based conducting inks for direct inkjet printing of flexible conductive patterns and their applications in electronic circuits and chemical sensors," *Nano Research,* 4, 2011, 675-684.

[16] Y. Su, V. Kravets, S. Wong, J. Waters, A. Geim and R. Nair, "Impermeable barrier films and protective coatings based on reduced graphene oxide," *Nature Communications,* 5, 2014, 4843 (5pp).

[17] B. Yoo, J. Shin, H. Yoon and H. Park, "Graphene and graphene oxide and their uses in barrier polymers," *Journal of Applied Polymer Science,* 131, 2014, 39628 (23pp).

[18] F. Schedin, A. Geim, S. Morozov, E. Hill, P. Blake, M. Katsnelson and S. Novoselov, "Detection of individual gas molecules adsorbed on graphene," *Nature Materials,* 6, 2007, 652-655.

[19] Y. Shao, J. Wang, H. Wu, J. Liu, I. Aksay and Y. Lin, "Graphene based electrochemical sensors and biosensors: a review," *Electroanalysis,* 22, 2010, 1027-1036.

[20] Q. He, S. Wu, Z. Yin and H. Zhang, "Graphene-based electronic sensors," *Chemical Science,* 3, 2012, 1764-1772.

[21] W. Heer, C. Berger, X. Wu, P. First, E. Conrad, X. Li, T. Li, M. Sprinkle, J. Hass, M. Sadowski, M. Potemski and G. Martinez, "Epitaxial graphene," *Solid State Communications,* 143, 2007, 92–100.

[22] C. Berger, Z. Song, X. Li, X. Wu, N. Brown, C. Naud, D. Mayou, T. Li, J. Hass, A. Marchenkov, E. Conrad, P. First and W. Heer, "Electronic confinement and coherence in patterned epitaxial graphene," *Science,* 312, 2006, 1191-1196.

[23] X. Li, W. Cai, J. An, S. Kim, J. Nah, D. Yang, R. Piner, A. Velamakanni, I. Jung, E. Tutuc, S. Banerjee, L. Colombo and R. Ruoff, "Large-area synthesis of high-quality and uniform graphene films on copper foils," *Science,* 324, 2009, 1312-1314.

[24] G. Eda, G. Fanchini and M. Chhowalla, "Large-area ultrathin films of reduced graphene oxide as a transparent and flexible electronic material," *Nature Nanotechnology,* 3, 2008, 270-274.

[25] Y. Hernandez, V. Nicolosi, M. Lotya, F. Blighe, Z. Sun, S. De, I. McGovern, B. Holland, M. Byrne, Y. GunKo, J. Boland, P. Boland, G. Duesberg, S. Krishnamurthy, R. Goodhue, J. Hutchison, V. Scardaci, A. Ferrari and J. Coleman, "High-yield production of graphene by liquid-phase exfoliation of graphite," *Nature Nanotechnology,* 3, 2008, 563 - 568.

[26] H. Yang, Y. Hernandez, A. Schlierf, A. Felten, A. Eckmann, S. Johal, P. Louette, J. Pireaux, X. Feng, K. Müellen, V. Palermo and C. Casiraghi, "A simple method for graphene production based on exfoliation of graphite in water using 1-pyrenesulfonic acid sodium salt," *Carbon,* 53, 2013, 357-365.

[27] A. Ciesielski and P. Samorì, "Graphene via sonication assisted liquid-phase exfoliation," *Chemical Society Reviews,* 43, 2014, 381--398.

[28] A. Schlierf, H. Yang, E. Gebremedhn, E. Treossi, L. Ortolani, L. Chen, A. Minoia, V. Morandi, P. Samorì, C. Casiraghi, D. Beljonne and V. Palermo, "Nanoscale insight into the exfoliation mechanism of graphene with organic dyes: effect of charge, dipole and molecular structure," *Nanoscale,* 5, 2013, 4205–4216.

[29] A. Catheline, L. Ortolani, V. Morandi, M. Melle-Franco, C. Drummond, C. Zakri and A. Pénicaud, "Solutions of fully exfoliated individual graphene flakes in low boiling point solvents," *Soft Matter,* 8, 2012, 7882-7887.

[30] L. Ma, J. Wang and F. Ding, "Recent progress and challenges in graphene nanoribbon synthesis," *Chemical Physics and Physical Chemistry,* 14, 2013, 47–54.

[31] X. Jia, J. Campos-Delgado, M. Terrones, V. Meunier and M. Dresselhaus, "Graphene edges: a review of their fabrication and characterization," *Nanoscale,* 3, 2013, 86–95.

[32] M. Terrones, "Nanotubes unzipped," *Nature,* 458, 2009, 845-846.

[33] A. Castro Neto, F. Guinea, N. Peres, K. Novoselov and A. Geim, "The electronic properties of graphene," *Reviews of Modern Physics,* 81, 2009, 109-162.

[34] K. Wakabayashi, K. Sasaki, T. Nakanishi and T. Enoki, "Electronic states of graphene nanoribbons and analytical solutions," *Science and Technology of Advanced Materials,* 11, 2010, 054504.

[35] V. Singh, D. Joung, L. Zhai, S. Das, S. Khondaker and S. Seal, "Graphene based materials: Past, present and future," *Progress in Materials Science,* 56, 2011, 1178–1271.

[36] J. Du and H. Cheng, "The fabrication, properties and uses of graphene/polymer composites," *Macromolecular Chemistry and Physics,* 213, 2012, 1060-1077.

[37] K. Noble, "Waterborne polyurethanes," *Progress in Organic Coatings,* 32, 1997, 131-136.

[38] B. Li and W. Zhong, "Review on polymer/graphite nanoplatelet nanocomposites," *Journal of Materials Science,* 46, 2011, 5595-5614.

[39] T. Das and S. Prusty, "Graphene-based polymer composites and their applications," *Polymer-Plastics Technology and Engineering,* 52, 2013, 319-331.

[40] S. Rwei, M. Zloczower and D. Feke, "Observation of carbon black agglomerate dispersion in simple shear flows," *Polymer Engineering and Science,* 30, 1990, 701-706.

[41] R. Novais, J. Covas and M. Paiva, "The effect of flow type and chemical functionalization on the dispersion of carbon nanofiber agglomerates in polypropylene," *Composites: Part A,* 43, 2012, 833-841.

[42] S. Jamali, M. Paiva and J. Covas, "Dispersion and re-agglomeration phenomena during melt mixing of polypropylene with multi-wall carbon nanotubes," *Polymer Testing,* 32, 2013, 701-707.

[43] G. Kasaliwal, S. Pegel, A. Göldel, P. Pötschke and G. Heinrich, "Analysis of agglomerate dispersion mechanisms of multiwalled carbon nanotubes during melt mixing in polycarbonate," *Polymer,* 51, 2010, 2708-2720.

[44] B. Lin, U. Sundararaj and P. Pötschke, "Melt mixing of polycarbonate with multi-walled carbon nanotubes in miniature mixers," *Macromolecular Materials and Egineering,* 291, 2006, 227-238.

[45] J. Chen, C. Jang, S. Xiao, M. Ishigami and M. Fuhrer, "Intrinsic and extrinsic performance limits of graphene devices on SiO_2," *Nature Nanotechnology,* 3, 2008, 206-209.

[46] S. Morozov, K. Novoselov, M. Katsnelson, F. Schedin, D. Elias, J. Jaszczak and A. Geim, "Giant intrinsic carrier mobilities in graphene and its bilayer," *Physical Review Letters,* 100, 2008, 016602(4 pp).

[47] A. Balandin, "Thermal properties of graphene and nanostructured carbon materials," *Nature Materials,* 10, 2011, 569-581.

[48] A. Balandin, S. Ghosh, W. Bao, I. Calizo, D. Teweldebrhan and F. Miao, "Superior thermal conductivity of single-layer graphene," *Nano Letters,* 8, 2008, 902-907.

[49] C. Lee, X. Wei, J. Kysar and J. Hone, "Measurement of the elastic properties and intrinsic strength of monolayer graphene," *Science,* 321, 2008, 385-388.

[50] R. Nair, P. Blake, A. Grigorenko, K. Novoselov, T. Booth, T. Stauber and N. Peres, "Fine structure constant defines visual transparency of graphene," *Science,* 320, 2008, 1308.

[51] A. Peigney, C. Laurent, E. Flahaut, R. Bacsa and A. Rousset, "Specific surface area of carbon nanotubes and bundles of carbon nanotubes," *Carbon,* 39, 2001, 507–514.

[52] C. Rao, A. Sood, K. Subrahmanyam and A. Govindaraj, "Graphene: the new two-dimensional nanomaterial," *Angewandte Ghemie - International Edition,* 48, 2009, 7752 – 7777.

[53] M. Pumera, "Electrochemistry of graphene: new horizons for sensing and energy storage," *The Chemical Record,* 9, 2009, 211–223.

[54] T. Durkop, S. Getty, E. Cobas and M. Fuhrer, "Extraordinary Mobility in Semiconducting Carbon Nanotubes," *Nano Letters,* 4, 2004, 35-39.

[55] T. Akasaka, F. Wudl and S. Nagase, Edits., Chemistry of nanocarbons, John Wiley & Sons Ltd, 2010, pp. 1-72; 106-128; 301-412; 433-462.

[56] K. Novoselov, D. Jiang, F. Schedin, T. Booth, V. Khotkevich, S. Morozov and A. Geim, "Two-dimensional atomic crystals," *Proceedings of the National Academy of Sciences of the United States of America,* 102, 2005, 10451-10453.

[57] H. Zhu, Y. Cao, J. Zhang, W. Zhang, Y. Xu, J. Guo, W. Yang and J. Liu, "One-step preparation of graphene nanosheets via ball milling of graphite and the application in lithium-ion batteries," *Journal of Materials Science,* 51, 2016, 3675-3683.

[58] V. Léon, M. Quintana, M. Herrero, J. Fierro, A. Hoz, M. Prato and E. Vázquez, "Few-layer graphene from ball-milling of graphite with melamine," *Chemical Communications,* 47, 2011, 10936-10938.

[59] V. Léon, A. Rodriguez, P. Prieto and E. Vázquez, "Exfoliation of graphite with triazine derivatives under ball-milling conditions: preparation of few-layer graphene via selective noncovalent interactions," *ACS Nano,* 8, 2014, 563-571.

[60] L. Liu, Z. Xiong, D. Hu, G. Wu and P. Chen, "Production of high quality single- or few-layered graphene by solid exfoliation of graphite in the presence of ammonia borane," *Chemical Communications,* 49, 2013, 7890-7892.

[61] L. Yan, M. Lin, C. Zeng, Z. Chen, S. Zhang, X. Zhao, A. Wu, Y. Wang, L. Dai, J. Qu, M. Guo and Y. Liu, "Electroactive and biocompatible hydroxyl-functionalized graphene by ball milling," *Journal of Materials Chemistry,* 22, 2012, 8367-8371.

[62] I. Jeon, Y. Shin, G. Sohn, H. Choi, S. Bae, J. Mahmood, S. Jung, J. Seo, M. Kim, D. Chang, L. Dai and J. Baek, "Edge-carboxylated graphene nanosheets via ball milling," *Proceedings of the National Academy of Science of the United States of America,* 109, 2012, 5588-5593.

[63] K. Zhu, W. Wang, A. Meng, M. Zhao, J. Wang, M. Zhao, D. Zhang, Y. Jia, C. Xu and Z. Li, "Mechanically exfoliated g-C_3N_4 thin nanosheets by ball milling as high performance photocatalysts," *RSC Advances,* 5, 2015, 56239-56243.

[64] A. Bourlinos, V. Georgakilas, R. Zboril, T. Steriotis and A. Stubos, "Liquid phase exfoliation of graphite towards solubilized graphene," *Small,* 5, 2009, 1841-1845.

[65] A. Oyer, J. Carrillo, C. Hire, H. Schniepp, A. Asandei, A. Dobrynin and D. Adamson, "Stabilization of graphene sheets by a structured benzene/ hexafluorobenzene mixed solvent," *Journal of the American Chemical Society,* 134, 2012, 5018-5021.

[66] Z. Sun, X. Huang, F. Liu, X. Yang, C. Rösler, R. Fischer, M. Muhler and W. Schuhmann, "Amine-based solvents for exfoliating graphite to graphene outperform the dispersing capacity of *N*-methyl-pyrrolidone and surfactants," *Chemical Communications,* 50, 2014, 10382-10385.

[67] A. Ciesielski and P. Samorì, "Supramolecular approaches to graphene: from self-assembly to molecule-assisted liquid-phase exfoliation," *Advanced Materials,* 28, 2016, 6030-6051.

[68] B. Brodie, "On the atomic weight of graphite," *Philosophical Transactions,* 149, 1859, 249-259.

[69] L. Staudenmaier, "verfahren zur darstellung der graphitsäure," *Berichte der Deutschen Chemischen Gesellschaft,* 31, 1898, 1481-1499.

[70] W. Hummers and R. Offeman, "Preparation of graphitic oxide," *Journal of the American Chemical Society,* 80, 1958, 1339-1339.

[71] J. Chen, B. Yao, C. Li and G. Shi, "An improved Hummers method for eco-friendly synthesis of graphene oxide," *Carbon,* 34, 2013, 225 - 229.

[72] S. Gilje, S. Han, M. Wang, K. Wang and R. Kaner, "A chemical route to graphene for device applications," *Nano Letters,* 7, 2007, 3394-3398.

[73] D. Li, M. Müller, S. Gilje, R. Kaner and G. Wallace, "Processable aqueous dispersions of graphene nanosheets," *Nature Nanotechnology,* 3, 2008, 101-105.

[74] J. Paredes, S. Rodil, A. Alonso and J. Tascón, "Graphene oxide dispersions in organic solvents," *Langmuir,* 24, 2008, 10560-10564.

[75] Y. Si and E. Samulski, "Synthesis of water soluble graphene," *Nano Letters,* 8, 2008, 1679-1682.

[76] W. Cai, R. Piner, F. Stadermann, S. Park, M. Shaibat, Y. Ishii, D. Yang, A. Velamakanni, S. An, M. Stoller, J. An, D. Chen and R. Ruoff, "Synthesis and solid-state NMR structural characterization of ^{13}C-labeled graphite oxide," *Science,* 321, 2008, 1815-1817.

[77] H. He, J. Klinowski, M. Forster and A. Lerf, "A new structural model for graphite oxide," *Chemical Physics Letters,* 287, 1998, 53–56.

[78] Y. Zhu, D. James and J. Tour, "New routes to graphene, graphene oxide and their related applications," *Advanced Materials,* 24, 2012, 4924-4955.

[79] F. Yeh, J. Syu, C. Cheng, T. Chang and H. Teng, "Graphite oxide as photocatalyst for hydrogen production from water," *Advanced Functional Materials,* 20, 2010, 2255-2262.

[80] J. Pyun, "Graphene oxide as catalyst: Application of carbon materials beyond nanotechnology," *Angewandte Chemie International Edition,* 50, 2011, 46-48.

[81] I. Lightcap and P. Kamat, "Graphitic design: Prospects of graphene based nanocomposites for solar energy conversion, storage, and sensing," *Accounts of Chemical Research,* 46, 2013, 2235-2243.

[82] C. Chung, K. Kim, D. Shin, S. Ryoo, B. Hong and D. Min, "Biomedical applications of graphene and graphene oxide," *Accounts of Chemical Research,* 46, 2013, 2211-2224.

[83] F. Bonaccorso, A. Lombardo, T. Hasan, Z. Sun, L. Colombo and A. Ferrari, "Production and processing of graphene and 2D crystals," *Materials Today,* 15, 2012, 564-589.

[84] Y. Xu, H. Bai, G. Lu, C. Li and G. Shi, "Flexible graphene films via the filtration of water-soluble noncovalent functionalized graphene sheets," *Journal of American Chemical Society,* 130, 2008, 5856-5857.

[85] B. Su, S. Pang, V. Alijani, C. Li, X. Feng and K. Müllen, "Composites of graphene with large aromatic molecules," *Advanced Materials,* 21, 2009, 3191-3195.

[86] H. Chen, M. Müller, K. Gilmore, G. Wallace and D. Li, "Mechanically strong, electrically conductive and biocompatible graphene paper," *Advanced Materials,* 20, 2008, 3557-3561.

[87] J. Liu, L. Tao, W. Yang, D. Li, C. Boyer, R. Wuhrer, F. Braet and T. Davis, "Synthesis, characterization, and multilayer assembly of pH sensitive graphene-polymer nanocomposites," *Langmuir,* 26, 2010, 10068-10075.

[88] Z. Liu, J. Liu, L. Cui, R. Wang, X. Luo, C. Barrow and W. Yang, "Preparation of graphene/polymer composites by direct exfoliation of graphite in functionalized block copolymer matrix," *Carbon,* 51, 2013, 148-155.

[89] X. Zheng, Q. Xu, J. Li, L. Li and J. Wei, "High-throughput, direct exfoliation of graphite to graphene via a cooperation of supercritical CO_2 and pyrene-polymers," *RSC Advances,* 2, 2012, 10632-10638.

[90] F. Zhang, X. Chen, R. Boulos, F. Yasin, H. Lu, C. Raston and H. Zhang, "Pyrene-conjugated hyaluronan facilitated exfoliation and stabilization of low dimensional nanomaterials in water," *Chemical Communications,* 49, 2013, 4845-4847.

[91] D. Ihiawakrim, O. Ersen, F. Melin, P. Hellwig, I. Janowska, D. Begin, W. Baaziz, S. Colin, C. Huu and R. Baati, "A single-stage functionalization and exfoliation method for the production of graphene in water: stepwise construction of 2D-nanostructured composites with iron oxide nanoparticles," *Nanoscale,* 5, 2013, 9073-9080.

[92] F. Liu, J. Choi and T. Seo, "DNA mediated water- dispersible graphene fabrication and gold nanoparticle-graphene hybrid," *Chemical Communications,* 46, 2010, 2844-2846.

[93] D. Parviz, S. Das, H. Ahmed, F. Irin, S. Bhattacharia and M. Green, "Dispersions of non-covalently functionalized graphene with minimal stabilizer," *ACS Nano,* 6, 2012, 8857–8867.

[94] X. An, T. Simmons, R. Shah, C. Wolfe, K. Lewis, M. Washington, S. Nayak, S. Talapatra and S. Kar, "Stable aqueous dispersions of noncovalently functionalized graphene from graphite and their multifunctional high-performance applications," *Nano Letters,* 10, 2010, 4295–4301.

[95] S. Ghosh, X. An, R. Shah, D. Rawat, B. Dave, S. Kar and S. Talapatra, "Effect of 1-pyrene carboxylic-acid functionalization of graphene on its capacitive energy storage," *Physical Chemistry C,* 116, 2012, 20688-20693.

[96] M. Zhang, R. Parajuli, D. Mastrogiovanni, B. Dai, P. Lo, W. Cheung, R. Brukh, P. Chiu, T. Zhou, Z. Liu, E. Garfunkel and H. He, "Production of graphene sheets by direct dispersion with aromatic healing agents," *Small Communications,* 6, 2010, 1100-1107.

[97] X. Dong, Y. Shi, Y. Zhao, D. Chen, J. Ye, Y. Yao, F. Gao, Z. Ni, T. Yu, Z. Shen, Y. Huang, P. Chen and L. Li, "Symmetry breaking of graphene monolayers by molecular decoration," *Physical Review Letters,* 102, 2009, 135501 (5pp).

[98] A. Viinikanoja, J. Kauppila, P. Damlin, E. Mäkilä, J. Leiro, T. Ääritalo and J. Lukkari, "Interactions between graphene sheets and ionic molecules used for the shear-assisted exfoliation of natural graphite," *Carbon,* 68, 2014, 195-209.

[99] H. Paloniemi, T. Äaritalo, T. Laiho, H. Liuke, N. Kocharova, K. Haapakka, F. Terzi, R. Seeber and J. Lukkari, "Water-soluble full-length single-wall carbon nanotube polyelectrolytes: preparation and characterization," *Journal of Physical Chemistry B,* 109, 2005, 8634-8642.

[100] J. Delgado, M. Herranz and N. Martín, "The nano-forms of carbon," *Journal of Materials Chemistry,* 18, 2008, 1417-1426.

[101] K. Balasubramanian and M. Burghard, "Chemically functionalized carbon nanotubes," *Small,* 2, 2005, 180-192.

[102] R. Baughman, A. Zakhidov and W. Heer, "Carbon nanotubes - the route toward applications," *Science,* 297, 2002, 787-792.

[103] D. Kosynkin, A. Higginbotham, A. Sinitskii, J. Lomeda, A. Dimiev, B. Price and J. Tour, "Longitudinal unzipping of carbon nanotubes to form graphene nanoribbons," *Nature,* 458, 2009, 872-877.

[104] A. Higginbotham, D. Kosynkin, A. Sinitskii, Z. Sun and J. Tour, "Lower-defect graphene oxide nanoribbons from multiwalled carbon nanotubes," *ACS Nano,* 4, 2010, 2059-2069.

[105] Y. Zhu, A. Higginbotham and J. Tour, "Covalent functionalization of surfactant-wrapped graphene nanoribbons," *Chemistry of Materials,* 21, 2009, 5284-5291.

[106] A. Sinitskii, A. Dimiev, D. Corley, A. Fursina, D. Kosynkin and J. Tour, "Kinetics of diazonium functionalization of chemically converted graphene nanoribbons," *ACS Nano,* 4, 2010, 1949-1954.

[107] E. Castillo-Martínez, J. Carretero-González, J. Sovich and M. Lima, "High temperature structural transformations of few layer graphene nanoribbons obtained by unzipping carbon nanotubes," *Journal of Materials Chemistry,* 2, 2014, 221-228.

[108] R. Cruz-Silva, A. Morelos-Gómez, S. Vega-Díaz, F. Tristán-López, A. Elias, N. Perea-López, H. Muramatsu, T. Hayashi, K. Fujisawa, Y. Kim, M. Endo and M. Terrones, "Formation of nitrogen-doped graphene nanoribbons via chemical unzipping," *ACS Nano,* 7, 2013, 2192-2204.

[109] A. Yazdi, K. Chizari, A. Jalilov, J. Tour and U. Sundararaj, "Helical and dendritic unzipping of carbon nanotubes: a route to nitrogen-doped graphene nanoribbons," *ACS Nano,* 9, 2015, 5833-5845.

[110] S. Shanmugam and A. Gedanken, "Generation of hydrophilic, bamboo shaped multiwalled carbon nanotubes by solid-state pyrolysis and its electrochemical studies," *Journal of Physical Chemistry B,* 110, 2006, 2037-2044.

[111] X. Wang, W. Hu, Y. Liu, C. Long, Y. Xu, S. Zhou, D. Zhu and L. Dai, "Bamboo-like carbon nanotubes produced by pyrolysis of iron(II) phthalocyanine," *Carbon,* 39, 2001, 1533-1536.

[112] O. Tiprigan, A. Koós, P. Nemes-Incze, Z. Horváth, Z. Sárközi, S. Simon and A. Darabont, "Obtaining bamboo-structured, multiwalled carbon nanotubes using the spray pyrolysis method," *Journal of Optoelectronics and Advanced Materials,* 9, 2007, 617-620.

[113] F. Cataldo, G. Compagnini, G. Patané, O. Ursini, G. Angelini, P. Ribic, G. Margaritondo, A. Cricenti, G. Palleschi and F. Valentini, "Graphene nanoribbons produced by the oxidative unzipping of single-wall carbon nanotubes," *Carbon,* 48, 2010, 2596-2602.

[114] S. Dhakate, N. Chauhan, S. Sharma and R. Mathur, "The production of multi-layer graphene nanoribbons from thermally reduced unzipped multi-walled carbon nanotubes," *Carbon,* 49, 2011, 4170-4178.

[115] A. Morelos-Gómez, S. Vega-Díaz, V. González, F. Tristán-López, R. Cruz-Silva, K. Fujisawa, H. Muramatsu, T. Hayashi, X. Mi, Y. Shi, H. Sakamoto, F. Khoerunnisa, K. Kaneto, B. Sumpter, Y. Kim, V. Meunier, M. Endo, E. Muñoz-Sandoval and M. Terrones, "Crystalline graphene nanoribbons with atomically smooth edges via a novel physico-chemical route," *World Academy of Science, Engineering and Technology*, 61, 2012, 96-100.

[116] A. Morelos-Goméz, S. Vega-Díaz, V. González, F. Tristán-López, R. Cruz-Silva, K. Fujisawa, H. Muramatsu, T. Hayashi, X. Mi, Y. Shi, H. Sakamoto, F. Khoerunnisa, K. Kaneko, B. Sumpter, Y. Kim, V. Meunier, M. Endo, E. Muñoz-Sandoval and M. Terrones, "Clean nanotube unzipping by abrupt thermal expansion of molecular nitrogen: graphene nanoribbons with atomically smooth edges," *ACS Nano,* 6, 2012, 2261-2272.

[117] C. Chang, K. Chang, H. Shen and C. Hu, "A unique two-step Hummers method for fabricating low-defect graphene oxide nanoribbons through exfoliating multiwalled carbon nanotubes," *Journal of the Taiwan Institute of Chemical Engineers,* 45, 2014, 2762-2769.

[118] C. Chua, Z. Sofer and M. Pumera, "Graphene sheet orientation of parent material exhibits dramatic influence on graphene properties," *Chemistry an Asian Journal,* 7, 2012, 2367-2372.

[119] Y. Li, J. Liao, S. Wang and W. Chiang, "Intercalation-assisted longitudinal unzipping of carbon nanotubes for green and scalable synthesis of graphene nanoribbons," *Scientific Reports,* 6, 2016, 22755 (12pp).

[120] M. Mahabadi and M. Manteghian, "Chemical oxidation of multiwalled carbon nanotube by sodium hypochlorite for production of graphene oxide nanosheets," *Fullerenes, Nanotubes and Carbon Nanostructures,* 23, 2015, 860-864.

[121] Q. Liu, T. Fujigaya and N. Nakashima, "Graphene unrolled from 'cup-stacked' carbon nanotubes," *Carbon,* 50, 2012, 5421-5428.

[122] C. Wong and M. Pumera, "Highly conductive graphene nanoribbons from the reduction of graphene oxide nanoribbons with lithium aluminium hydride," *Journal of Materials Chemistry,* 2, 2014, 856-863.

[123] L. Jiao, X. Wang, G. Diankov, H. Wang and H. Dai, "Facile synthesis of high-quality graphene nanoribbons," *Nature Nanotechnology,* 5, 2010, 321-325.

[124] C. Chen, J. Wu, K. Lam, G. Hong, M. Gong, B. Zhang, Y. Lu, A. Antaris, S. Diao, J. Guo and H. Dai, "Graphene nanoribbons under mechanical strain," *Advanced Materials,* 27, 2015, 303-309.

[125] M. Kabbani, C. Tiwary, P. Autreto, G. Brunetto, A. Som, K. Krishnadas, S. Ozden, K. Hackenberg, Y. Gong, D. Galvao, R. Vajtai, A. Kabbani, T. Pradeep and P. Ajayan, "Ambient solid-state mechano-chemical reactions between functionalized carbon nanotubes," *Nature Communications,* 6, 2015, 7291 (8pp).

[126] M. Kabbani, C. Tiwary, A. Som, K. Krishnadas, P. Autreto, S. Ozden, K. Keyshar, K. Hackenberg, A. Chipara, D. Galvao, R. Vajtai, A. Kabbani, T. Pradeep and P. Ajayan, "A generic approach for mechano-chemical reactions between carbon nanotubes of different functionalities," *Carbon,* 104, 2016, 196-202.

[127] J. Liu, A. Rinzler, H. Dai, J. Hafner, R. Bradley, P. Boul, A. Lu, T. Iverson, K. Shelimov, C. Huffman, F. Rodriguez-Macias, Y. Shon, T. Lee, D. Colber and R. Smalley, "Fullerene pipes," *Science,* 280, 1998, 1253-1256.

[128] D. Yang, G. Guo, J. Hu, C. Wang and D. Jiang, "Hydrothermal treatment to prepare hydroxyl group modified multi-walled carbon nanotubes," *Journal of Materials Chemistry,* 18, 2008, 350-354.

[129] W. Mahmoud, F. Al-Hazmi and T. Al-Harbi, "Wall by wall controllable unzipping of MWCNTs via intercalation with oxalic acid to produce multilayers graphene oxide ribbon," *Chemical Engineering Journal,* 281, 2015, 192-198.

[130] A. Cano-Márquez, F. Rodríguez-Macías, J. Campos-Delgado, C. Espinosa-González, F. Tristán-López, D. Ramírez-González, D. Cullen, D. Smith, M. Terrones and Y. Vega-Cantú, "Ex-MWNTs: graphene sheets and ribbons produced by lithium intercalation and exfoliation of carbon nanotubes," *Nano Letters,* 9, 2009, 1527-1533.

[131] D. Kosynkin, W. Lu, A. Sinitskii, G. Pera, Z. Sun and J. Tour, "Highly conductive graphene nanoribbons by longitudinal splitting of carbon nanotubes using potassium vapor," *ACS Nano,* 5, 2011, 969-974.

[132] B. Genorio, W. Lu, A. Dimiev, Y. Zhu, A. Raji, B. Novosel, L. Alemany and J. Tour, "In situ intercalation replacement and selective functionalization of graphene nanoribbons stacks," *ACS Nano,* 6, 2012, 4231-4240.

[133] D. Shinde, M. Majumder and V. Pillai, "Counter-ion dependent, longitudinal unzipping of multiwalled carbon nanotubes to highly conductive and transparent graphene nanoribbons," *Scientific Reports,* 4, 2014, 4363 (6pp).

[134] A. Elías, A. Botello-Méndez, D. Meneses-Rodrı´guez, V. González, D. Ramirez-González, L. Ci, E. Miñhoz-Sandoval, P. Ajayan, H. Terrones and M. Terrones, "Longitudinal cutting of pure and doped carbon nanotubes to form graphitic nanoribbons using metal clusters as nanoscalpels," *Nano Letters,* 10, 2010, 366-372.

[135] U. Parashar, S. Bhandari, R. Srivastava, D. Jariwala and A. Srivastava, "Single step synthesis of graphene nanoribbons by catalyst particle size dependent cutting of multiwalled carbon nanotubes," *Nanoscale,* 3, 2011, 3876-3882.

[136] I. Janowska, O. Ersen, T. Jacob, P. Vennégues, D. Bégin, M. Ledoux and C. Huu, "Catalytic unzipping of carbon nanotubes to few-layer graphene sheets under microwaves irradiation," *Applied Catalysis,* 371, 2009, 22-30.

[137] L. Jiao, L. Zhang, X. Wang, G. Diankov and H. Dai, "Narrow graphene nanoribbons from carbon nanotubes," *Nature,* 458, 2009, 877-880.

[138] L. Valentini, "Formation of unzipped carbon nanotubes by CF_4 plasma treatment," *Diamond and Related Materials,* 20, 2011, 445-448.

[139] S. Mohammadi, Z. Kolahdouz, S. Darbari, S. Mohajerzadeh and N. Masoumi, "Graphene formation by unzipping carbon nanotubes using a sequential plasma assisted processing," *Carbon,* 52, 2013, 451-463.

[140] S. Mohammadi, Z. Kolahdouz and S. Mohajerzadeh, "Hydrogenation-assisted unzipping of carbon nanotubes to realize graphene nano-sheets," *Journal of Materials Chemistry C,* 1, 2013, 1309-1316.

[141] D. Shinde, J. Debgupta, A. Kushwaha, M. Aslam and V. Pillai, "Electrochemical unzipping of multiwalled carbon nanotubes for facile synthesis of high-quality graphene nanoribbons," *Journal of the American Chemical Society,* 133, 2011, 4168-4171.

[142] M. Jaison, K. Vikram, T. Narayanan and V. Pillai, "Electric field induced transformation of carbon nanotube to graphene nanoribbons using Nafion as a solid polymer electrolyte," *Applied Physics Letters,* 104, 2014, 153111 (6pp).

[143] R. John, D. Shinde, L. Liu, F. Ding, Z. Xu, C. Vijayan, V. Pillai and T. Pradeep, "Sequential electrochemical unzipping of single-walled carbon nanotubes to graphene ribbons revealed by in situ Raman spectroscopy and imaging," *ACS Nano,* 8, 2014, 234-242.

[144] W. Kim, S. Moon, S. Bang, B. Choi, H. Ham, T. Sekino and K. Shim, "Fabrication of graphene layers from multiwalled carbon nanotubes using high dc pulse," *Applied Physics Letters,* 95, 2009, 083103 (4pp).

[145] W. Kim, S. Moon, N. Park, H. Huh, K. Shim and H. Ham, "Electrical and structural feature of monolayer graphene produced by pulse current unzipping and microwave exfoliation of carbon nanotubes," *Chemistry of Materials,* 23, 2011, 940-944.

[146] K. Kim, A. Sussman and A. Zettl, "Graphene nanoribbons obtained by electrically unwrapping carbon nanotubes," *ACS Nano,* 4, 2010, 1362-1366.

[147] N. Wan, L. Sun, S. Ding, T. Xu, X. Hu, J. Sun and H. Bi, "Synthesis of graphene–CNT hybrids via joule heating: structural characterization and electrical transport," *Carbon,* 53, 2013, 260-268.

[148] D. Wei, L. Xie, K. Lee, Z. Hu, S. Tan, W. Chen, C. Sow, K. Chen, Y. Liu and T. Wee, "Controllable unzipping for intramolecular junctions of graphene nanoribbons and single-walled carbon nanotubes," *Nature Communications,* 4, 2013, 1374 (9pp).

[149] A. Talyzin, S. Luzan, I. Anoshkin, A. Nasibulin, H. Jiang, E. Kauppinen, V. Mikoushikin, V. Shnitov, D. Marchenko and D. Noréus, "Hydrogenation, purification and unzipping of carbon nanotubes by reaction with molecular hydrogen: road to graphene nanoribbons," *ACS Nano,* 5, 2011, 5132-5140.

[150] S. Vadahanambi, J. Jung, R. Kumar, H. Kim and I. Oh, "An ionic liquid-assisted method for splitting carbon nanotubes to produce graphene nanoribbons by microwave radiation," *Carbon,* 53, 2013, 391-398.

[151] S. Ozden, P. Autreto, C. Tiwary, S. Khatiwada, L. Machado, D. Galvao, R. Vajtai, E. Barrera and P. Ajayan, "Unzipping carbon nanotubes at high impact," *Nano Letters,* 14, 2014, 4131−4137.

[152] C. Tiwary, B. Javvaji, C. Kumar, D. Mahapatra, S. Ozden, P. Ajayan and K. Chattopadhyay, "Chemical-free graphene by unzipping carbon nanotubes using cryo-milling," *Carbon,* 89, 2015, 217-224.

[153] Y. Fan, J. Li, X. Liu, L. Wang, X. Chen, S. Sun, A. Kawasaki and W. Jiang, "A microexplosion method for the synthesis of graphene nanoribbons," *Carbon,* 49, 2011, 1439-1445.

[154] S. Huang, H. Lin, L. Qiu, L. Zhang, Z. Cai, T. Chen, Z. Yang, S. Yang and H. Peng, "Perpendicularly aligned carbon nanotube/olefin composite films for the preparation of graphene nanomaterials," *Journal of Materials Chemistry,* 22, 2012, 16209-16213.

[155] Y. Kang, Y. Li and M. Deng, "Precise unzipping of flattened carbon nanotubes to regular graphene nanoribbons by acid cutting along the folded edges," *Journal of Materials Chemistry,* 22, 2012, 16283-16287.

[156] H. Kohno, T. Komine, T. Hasegawa, H. Niioka and S. Ichikawa, "Formation of a carbon nanoribbon by spontaneous collapse of a carbon nanotube grown from a y-Fe nanoparticle via an origami mechanism," *Nanoscale*, 5, 2013, 570-573.

[157] P. Kumar, L. Panchakarla and C. Rao, "Laser-induced unzipping of carbon nanotubes to yield graphene nanoribbons," *Nanoscale,* 3, 2011, 2127-2129.

[158] S. Bang, J. Ryu, B. Choi e K. Shim, "A simple route for fabrication of graphene nanoribbons by pulsed laser irradiation in ethanol," *Journal of Alloys and Compounds*, 618, 2015, 33-36.

[159] M. Paiva, W. Xu, M. Proença, R. Novais, E. Lægsgaard and F. Besenbacher, "Unzipping of functionalized multiwall carbon nanotubes induced by STM," *Nano Letters,* 10, 2010, 1764–1768.

[160] M. Paiva, F. Simon, R. Novais, T. Ferreira, M. Proença, W. Xu and F. Besenbacher, "Controlled functionalization of carbon nanotubes by a solvent-free multicomponent approach," *ACS Nano,* 4, 2010, 7379–7386.

[161] S. Lee, J. Kim, H. Kim, D. Kim, W. Silva, F. Schneider, A. Yusoff and J. Jang, "An organic photovoltaic featuring graphene nanoribbons," *Chemical Communications,* 51, 2015, 9185-9188.

[162] M. Liu, Y. Song, S. He, W. Tjiu, J. Pan, Y. Xia and T. Liu, "Nitrogen-doped graphene nanoribbons as efficient metal-free electrocatalysis for oxygen reduction," *ACS Applied Materials and Interfaces,* 6, 2014, 4214-4222.

[163] A. Yazdi, H. Fei, R. Ye, G. Wang, J. Tour and U. Sundararaj, "Boron/nitrogen co-doped helically unzipped multiwalled carbon nanotubes as efficient electrocatalysis for oxygen reduction," *ACS Applied Materials and Interfaces*, 7, 2015, 7786-7794.

[164] A. Yazdi, E. Roberts and U. Sundararaj, "Nitrogen/sulfur co-doped helical graphene nanoribbons for efficient oxygen reduction in alkaline and acidic electrolytes," *Carbon*, 100, 2016, 99-108.

[165] X. Hu, C. Lin, L. Wei, C. Hong, Y. Zhang and N. Zhuang, "High electrocatalytic performance of graphene nanoribbon supported PtAu nanoalloy for direct ethanol fuel cell and theoretical analysis of anti-CO poisoning," *Electrochimica Acta*, 187, 2016, 560-566.

[166] Q. Liu, K. Jiang, J. Fan, Y. Lin, Y. Min, Q. Xu and W. Cai, "Manganese dioxide coated graphene nanoribbons supported palladium nanoparticles as an efficient catalyst for ethanol electrooxidation in alkaline media," *Electrochimica Acta*, 203, 2016, 91-98.

[167] C. Wang, H. Li, J. Zhao, Y. Zhu, W. Yuan and Y. Zhang, "Graphene nanoribbons as a novel support material for high performance fuel cell electrocatalysts," *International Journal of Hydrogen Energy,* 38, 2013, 13230-13237.

[168] C. Zhao, P. Gai, C. Liu, X. Wang, H. Xu, J. Zhang e J. Zhu, "Polyaniline networks grown on graphene nanoribbons-coated carbon paper with a synergistic effect for

high-performance microbial fuel cells," *Journal of Materials Chemistry A,* 1, 2013, 12587-12594.

[169] H. Huang, G. Ye, S. Yang, H. Fei, C. Tiwary, Y. Gong, R. Vajatai, J. Tour, X. Wang and P. Ajayan, "Nanosized Pt anchored onto 3D nitrogen-doped graphene nanoribbons towards efficient methanol electrooxidation," *Journal of Materials Chemistry A,* 3, 2015, 19696-19701.

[170] L. Chen, R. Du, J. Zhu, Y. Mao, C. Xue, N. Zhang, Y. Hou, J. Zhang and T. Yi, "Three-dimensional nitrogen-doped graphene nanoribbons aerogel as highly efficient catalyst for the oxygen reduction reaction," *Small,* 11, 2015, 1423-1429.

[171] M. Fathi, M. saghafi, F. Mahboubi and S. Mohajerzadeh, "Synthesis and electrochemical investigation of polyaniline/unzipped carbon nanotube composites as electrode material in supercapacitors," *Synthetic Metals,* 198, 2014, 345-356.

[172] M. Saghafi, F. Mahboubi, S. Mohajerzadeh, M. Fathi and R. Holze, "Longitudinal unzipping of carbon nanotubes and their electrochemical performance in supercapacitors," *Current Applied Physics,* 14, 2014, 1335-1343.

[173] H. Wang, Y. Wang, Z. Hu and X. Wang, "Cutting and unzipping multiwalled carbon nanotubes into curved graphene sheets and their enhanced supercapacitor performance," *ACS Applied Materials and Interfaces,* 4, 2012, 6827-6834.

[174] C. Zhang, Z. Peng, J. Lin, Y. Zhu, G. Ruan, C. Hwang, W. Lu, R. Hauge and J. Tour, "Splitting of a vertical multiwalled carbon nanotube carpet to graphene nanoribbon carpet and its use in supercapacitors," *ACS Nano,* 7, 2013, 5151-5159.

[175] Y. Ding, J. Zhu, C. Wang, B. Dai, Y. Li, Y. Qin, F. Xu, Q. Peng, Z. Yang, J. Bai, W. Cao, Y. Yuan and Y. Li, "Multifunctional three-dimensional graphene nanoribbons composite sponge," *Carbon,* 104, 2016, 133-140.

[176] C. Zheng, X. Zhou, H. Cao, H. Wang and P. Liu, "Edge-enriched porous graphene nanoribbons for high energy density supercapacitors," *Journal of Materials Chemistry A,* 2, 2014, 7484-7490.

[177] S. Ujjain, P. Ahuja and K. Sharma, "Graphene nanoribbon wrapped cobalt manganite nanocubes for high performance all-solid-state flexible supercapacitors," *Journal of Materials Chemistry A,* 3, 2015, 9925-9931.

[178] P. Ahuja, R. Sharma e G. Singh, "Solid-state, high-performance supercapacitor using graphene nanoribbons embedded with zinc manganite," *Journal of Materials Chemistry A,* 3, 2015, 4931-4937.

[179] P. Ahuja, V. Sahu, K. Ujjain and R. Sharma, "Performance evaluation of Asymmetric Supercapacitor based on Cobalt manganite modified graphene nanoribbons," *Electrochimica Acta,* 146, 2014, 429-436.

[180] M. Liu, W. Tjiu, J. Pan, C. Zhang, W. Gao and T. Liu, "One-step synthesis of graphene nanoribbon–MnO_2 hybrids and their all-solid-state asymmetric supercapacitors," *Nanoscale,* 6, 2014, 4233-4242.

[181] V. Sahu, S. Goel, R. Sharma and G. Singh, "Zinc oxide nanoring embedded lacey graphene nanoribbons in symmetric/asymmetric electrochemical capacitive energy storage," *Nanoscale,* 7, 2015, 20642-20651.

[182] J. Lim, U. Maiti, N. Kim, R. Narayan, W. Lee, D. Choi, Y. Oh, J. Lee, S. Kang, H. Kim, Y. Kim and S. Kim, "Dopant-specific unzipping of carbon nanotubes for intact crystalline graphene nanostructures," *Nature Communications,* 7, 2015, 10364 (9pp).

[183] A. Raji, S. Salters, E. Samuel, Y. Zhu, V. Volman and J. Tour, "Functionalized graphene nanoribbon films as radiofrequency and optically transparent material," *ACS Applied Materials and Interfaces,* 6, 2014, 16661-16668.

[184] X. Zheng, M. Feng and H. Zhan, "Giant optical limiting effect in ormosil gel glasses doped with graphene oxide materials," *Journal of Materials Chemistry C,* 1, 2013, 6759-6766.

[185] Y. Zhang, Y. Song, Y. Gan, M. Feng and H. Zhan, "Broadband nonlinear optical and optical limiting effects of partially unzipped carbon nanotubes," *Journal of Materials Chemistry C,* 3, 2015, 9948-9954.

[186] C. Gao, L. Li, A. Raji, A. Kovalchuk, Z. Peng, H. Fei, Y. He, N. Kim, Q. Zhong, E. Xie and J. Tour, "Tin disulfide nanoplates on graphene nanoribbons for full lithium ion batteries," *ACS Applied Materials and Interfaces,* 7, 2015, 26549-26556.

[187] P. Ilango, K. Prasanna, T. Subburaj, Y. Jo e C. Lee, "Facile longitudinal unzipping of carbon nanotubes to graphene nanoribbons and their effects on $LiMn_2O_4$ cathodes in rechargeable lithium-ion batteries," *Acta Materialia,* 100, 2015, 11-18.

[188] J. Lin, A. Raji, K. Nan, Z. Peng, Z. Yan, E. Samuel, D. Natelson and J. Tour, "Iron oxide nanoparticles and graphene nanoribbon composite as anode material for high-performance Li-ion batteries," *Advanced Functional Materials,* 24, 2014, 2044-2048.

[189] L. Chen, X. Jin, Y. Wen, H. Lan, X. Yu, D. Sun e T. Yi, "Intrinsically coupled 3D nGs@CNTs frameworks as anode materials for lithium-ion batteries," *Chemistry of Materials,* 27, 2015, 7289-7295.

[190] K. Pirnat, J. Bitenc, I. Jerman, R. Dominko and B. Genorio, "Redox-active functionalized graphene nanoribbons as electrode material for Li-ion batteries," *ChemElectroChem,* 1, 2014, 2131-2137.

[191] X. Li, T. Li, Q. Zhong, K. Du, H. Li and J. Huang, "Chemical unzipping of multiwalled carbon nanotubes for high-capacity lithium storage," *Electrochimica Acta,* 125, 2014, 170-175.

[192] X. Huang, Z. Fan, C. Lin, L. Jia, B. Lin, J. Wang, X. Hu and N. Zhuang, "High electrochemical properties of graphene nanoribbons-hybridized manganese dioxide as cathode material for lithium battery," *Journal of Nanoparticle Research,* 17, 2015, 97 (6pp).

[193] T. Bhardwaj, A. Antic, B. Pavan, V. Barone and B. Fahlman, "Enhanced electrochemical lithium storage by graphene nanoribbons," *Journal of American Chemical Society,* 132, 2010, 12556-12558.

[194] Y. Liu, X. Wang, Y. Dong, Z. Wang, Z. Zhao and J. Qiu, "Nitrogen-doped graphene nanoribbons for high-performance lithium ion batteries," *Journal of Materials Chemistry A,* 2, 2014, 16832-16835.

[195] B. Xiao, X. Li, X. Li, B. Wang, C. Langford, R. Li and X. Sun, "Graphene nanoribbons derived from the unzipping of carbon nanotubes: controlled synthesis and superior lithium storage performance," *Journal of Physical Chemistry C,* 118, 2014, 881-890.

[196] Y. Kim, G. Shoorideh, Y. Zhmayev, J. Lee, Z. Li, B. Patel, S. Chakrapani, J. Park, S. Lee and Y. Joo, "The critical contribution of unzipped graphene nanoribbons to scale silicon-carbon fiber anodes in rechargeable Li-ion batteries," *Nano Energy,* 16, 2015, 446-457.

[197] L. Li, A. Kovalchuk and J. Tour, "SnO_2–reduced graphene oxide nanoribbons as anodes for lithium ion batteries with enhanced cycling stability," *Nano Research,* 7, 2014, 1319-1326.

[198] M. Sahoo and S. Ramaprabhu, "Enhanced electrochemical performance by unfolding a few wings of graphene nanoribbons of multiwalled carbon nanotubes as an anode material for Li ion battery applications," *Nanoscale,* 7, 2015, 13379-13386.

[199] Y. Liu, X. Wang, W. Wan, L. Li, Y. Dong, Z. Zhao and J. Qiu, "Multifunctional nitrogen-doped graphene nanoribbon aerogels for superior lithium storage and cell culture," *Nanoscale,* 8, 2016, 2159-2167.

[200] A. Sinitskii, A. Dimiev, D. Kosynkin and J. Tour, "Graphene nanoribbon devices produced by oxidative unzipping of carbon nanotubes," *ACS Nano,* 4, 2010, 5405-5413.

[201] Y. Yu, H. Wada, J. Inoue, S. Imaizumi, Y. Kounosu, K. Tsuboi, H. Matsumoto, M. Ashizawa, T. Mori, M. Minagawa and A. Tanioka, "Inkjet printing of graphene nanoribbons for organic field-effect transistors," *Applied Physics Express,* 4, 2011, 115101 (4pp).

[202] R. Khare, D. Shinde, S. Bansode, M. More, M. Majumder, V. Pillai and D. Late, "Graphene nanoribbons as prospective field emitter," *Applied Physics Letters,* 106, 2015, 023111 (6pp).

[203] Y. Zhu, W. Lu, Z. Sun, D. Kosynkin, J. Yao and J. Tour, "High throughput preparation of large area transparent electrodes using non-functionalized graphene nanoribbons," *Chemistry of Materials,* 23, 2011, 935-939.

[204] X. Wang, Y. Guo and Z. Zhang, "Field-effect transistors based on single graphene oxide nanoribbon from longitude-unzipped carbon nanotubes," *Journal of Nanoparticle Research,* 15, 2013, 2147 (6pp).

[205] S. Salimian, M. Araghi and A. Golikand, "Preparation and characterization of semiconductor GNR-CNT nanocomposite and its application in FET," *Journal of Physics and Chemistry of Solids,* 91, 2016, 170-181.

[206] Y. Zhu and J. Tour, "Graphene nanoribbon thin films using layer-by-layer assembly," *Nano Letters,* 10, 2010, 4356-4362.

[207] M. Lin, C. Ling, Y. Zhang, H. Yoo, M. Cheng, L. Agapito, N. Kioussis, N. Widjaja and Z. Zhou, "Room-temperature high on/off ratio in suspended graphene nanoribbon field-effect transistors," *Nanotechnology,* 22, 2011, 265201 (7pp).

[208] J. Liu, G. Kim, Y. Xue, J. Kim, J. Baek, M. Durstock and L. Dai, "Graphene oxide nanoribbon as hole extraction layer to enhance efficiency and stability of polymer solar cells," *Advanced Materials,* 26, 2014, 786-790.

[209] Z. Yang, M. Liu, C. Zhang, W. Tjiu, T. Liu and H. Peng, "Carbon nanotubes bridged with graphene nanoribbons and their use in high efficiency dye-sensitized solar cells," *Angewandte Chemie International Edition,* 52, 2013, 3996-3999.

[210] J. Velten, J. Carretero-González, E. Castillo-Martínez, J. Bykova, A. Cook, R. Baughman and A. Zakhidov, "Photoinduced optical transparency in dye-sensitized solar cells containing graphene nanoribbons," *Journal of Physical Chemistry C,* 115, 2011, 25125-25131.

[211] S. Pan, Z. Yang, P. Chen, X. Fang, G. Guan, Z. Zhang, J. Deng and H. Peng, "Carbon nanostructured fibers as counter electrodes in wire-shaped dye-sensitized solar cells," *Journal of Physical Chemistry C,* 118, 2014, 16419-16425.

[212] G. Lalwani, A. Henslee, B. Farshid, L. Lin, F. Kasper, Y. Qin, A. Mikos and B. Sitharaman, "Two-dimensional nanostructure reinforced biodegradable polymeric nanocomposites for bone tissue engineering," *Biomacromolecules,* 14, 2013, 900-909.

[213] O. Akhavan, E. Ghaderi and H. Emamy, "Nontoxic concentrations of PEGylated graphene nanoribbons for selective cancer cell imaging and photothermal therapy," *Journal of Materials Chemistry,* 22, 2012, 20626-20633.

[214] A. Gizzatov, V. Keshishian, A. Guven, A. Dimiev, F. Qu, R. Muthupillai, P. Decuzzi, R. Bryant and J. Tour, "Enhanced MRI relaxivity of aquated Gd^{3+} ions by carboxyphenylated water-dispersed graphene nanoribbons," *Nanoscale,* 6, 2014, 3059-3063.

[215] Y. Lu, C. Lin, H. Yang, K. Lin, S. Wey, C. Sun, K. Wei, T. Yen, C. Lin, C. Ma and J. Chen, "Biodistribution of PEGylated graphene oxide nanoribbons and their application in cancer chemo-photothermal therapy," *Carbon,* 74, 2014, 83-95.

[216] C. Xiang, W. Lu, Y. Zhu, Z. Sun, Z. Yan, C. Hwang and J. Tour, "Carbon nanotube and graphene nanoribbon-coated conductive kevlar fibers," *ACS Applied Materials and Interfaces,* 4, 2012, 131-136.

[217] L. Gan, S. Shang, C. Yuen and S. Jiang, "Graphene nanoribbon coated flexible and conductive cotton fabric," *Composites Science and Technology,* 117, 2015, 208-214.

[218] M. Lian, J. Fan, Z. Shi, H. Li and J. Yin, "Kevlar functionalized graphene nanoribbon for polymer reinforcement," *Polymer,* 55, 2014, 2578-2587.

[219] Y. Wang, Z. Shi and J. Yin, "Unzipped multiwalled carbon nanotubes for mechanical reinforcement of polymer composites," *Journal of Physical Chemistry C,* 114, 2010, 19621-19628.

[220] J. Fan, Z. Shi, M. Tian, J. Wang and J. Yin, "Unzipped multiwalled carbon nanotube oxide/multiwalled carbon nanotube hybrids for polymer reinforcement," *ACS Applied Materials and Interfaces,* 4, 2012, 5956-5965.

[221] R. Nadiv, M. Shtein, M. Buzaglo, S. Peretz-Damari, A. Kovalchuk, T. Wang, J. Tour and O. Regev, "Graphene nanoribbon e Polymer composites: the critical role of edge functionalization," *Carbon,* 99, 2016, 444-450.

[222] C. Xiang, P. Cox, A. Kukovecz, B. Genorio, D. Hashim, Z. Yan, Z. Peng, C. Hwang, G. Ruan, E. Samuel, P. Sudeep, Z. Konya, R. Vajtai, P. Ajayan and J. Tour, "Functionalized low defect graphene nanoribbons and polyurethane composite film for improved gas barrier and mechanical performances," *ACS Nano,* 7, 2013, 10380-10386.

[223] M. Liu, C. Zhang, W. Tjiu, Z. Yang, W. Wang and T. Liu, "One-step hybridization of graphene nanoribbons with carbon nanotubes and its strong-yet-ductile thermoplastic polyurethane composites," *Polymer,* 54, 2013, 3124-3130.

[224] Q. Peng, Y. Li, X. He, X. Gui, Y. Shang, C. Wang, C. Wang, W. Zhao, S. Du, E. Shi, P. Li, D. Wu and A. Cao, "Graphene nanoribbon aerogels unzipped from carbon nanotubes sponges," *Advanced Materials,* 26, 2014, 3241-3247.

[225] P. Ding, N. Zhuang, X. Cui, L. Shi, N. Song and S. Tang, "Enhanced thermal conductive property of polyamide composites by low mass fraction of covalently grafted graphene nanoribbons," *Journal of Materials Chemistry,* 3, 2015, 10990-10997.

[226] S. Sadeghi, Z. Yazdi and U. Sundararaj, "Controlling short-range interactions by tuning surface chemistry in HDPE/graphene nanoribbon nanocomposites," *Journal of Physical Chemistry B,* 119, 2015, 11867-11878.

[227] J. Wang, Z. Shi, Y. Ge, Y. Wang, J. Fan and J. Yin, "Functionalization of unzipped carbon nanotube via in situ polymerization for mechanical reinforcement of polymer," *Journal of Materials Chemistry,* 22, 2012, 17663-17670.

[228] Y. Shang, T. Li, X. Zhu, Y. Zhang, X. Chen and T. Zhao, "Effect of the graphene sheets derived from multistep oxidized carbon nanotubes on the performance of graphene sheets/poly(methyl methacrylate) composites," *Journal of Analytical and Applied Pyrolysis,* 114, 2015, 243-249.

[229] L. He, G. Xia, J. Sun, Q. Zhao, R. Song and Z. Ma, "Unzipped multiwalled carbon nanotubes-incorporated poly(vinylidene fluoride) nanocomposites with enhanced

interface and piezoelectric B phase," *Journal of Colloid and Interface Science,* 393, 2013, 97-103.

[230] L. He, J. Sun, X. Wang, X. Fan, Q. Zhao, L. Cai, R. Song, Z. Ma and W. Huang, "Unzipped multiwalled carbon nanotubes-incorporated poly(L-lactide) nanocomposites with enhanced interface and hydrolytic degradation," *Materials Chemistry and Physics,* 134, 2012, 1059-1066.

[231] M. Liu, Y. Du, Y. Miao, Q. Ding, S. He, W. Tjiu, J. Pan and T. Liu, "Anisotropic conductive films based on highly aligned polyimide fibers containing hybrid materials of graphene nanoribbons and carbon nanotubes," *Nanoscale,* 7, 2015, 1037-1046.

[232] M. Khajehpour, S. Sadeghi, Z. Yazdi and U. Sundararaj, "Tuning the curing behavior of fluoroelastomer (FKM) by incorporation of nitrogen doped graphene nanoribbons (CNx-GNRs)," *Polymer,* 55, 2014, 6293-6302.

[233] A. Dimiev, D. Zakhidov, B. Genorio, K. Oladimeji, B. Crowgey, L. Kempel, E. Rothwell and J. Tour, "Permitivity of dielectric composite materials comprising graphene nanoribbons. The effect of nanostructure," *ACS Applied Materials and Interfaces,* 5, 2013, 7567-7573.

[234] W. Chen, Y. Zhu, S. Wang, W. Pei and Y. Jiang, "Effects of carbon nanofillers on enhancement of polymer composites," *Journal of Applied physics,* 112, 2012, 074302 (7pp).

[235] M. Rafiee, W. Lu, A. Thomas, A. Zandiatashbar, J. Rafiee, J. Tour and A. Koratkar, "Graphene nanoribbons composites," *ACS Nano,* 4, 2010, 7415-7420.

[236] A. Raji, T. Varadhachary, K. Nan, T. Wang, J. Lin, Y. Ji, B. Genorio, Y. Zhu, C. Kittrell and J. Tour, "Composites of graphene nanoribbon stacks and epoxy for joule and deicing of surfaces," *ACS Applied Materials and Interfaces,* 8, 2016, 3551-3556.

[237] P. Li, Y. Zheng, T. Shi, Y. Wang, M. Li, C. Chen and J. Zhang, "A solvent-free graphene oxide nanoribbon colloid as filler phase for epoxy-matrix composites with enhanced mechanical, thermal and tribological performance," *Carbon,* 96, 2016, 40-48.

[238] N. Kim, A. Metzger, V. Hejazi, Y. Li, A. Kovalchuk, S. Lee, R. Ye, J. Mann, C. Kittrell, R. Shahsavari and J. Tour, "Microwave heating of functionalized graphene nanoribbons in thermoset polymers for wellbore reinforcement," *ACS Applied Materials and Interfaces,* 8, 2016, 12985-12991.

[239] C. Sun, C. Chang, H. Lee, J. Zhou, J. Wang, T. Sham and W. Pong, "Microwave-assisted synthesis of a core-shell MWCNT/GONR heterostruture for the electrochemical detection of ascorbic acid, dopamine, and uric acid," *ACS Nano,*5, 2011, 7788-7795.

[240] C. Lim, C. Chua and M. Pumera, "Detection of biomarkers with graphene nanoplatelets and nanoribbons," *Analyst,* 139, 2014, 1072-1080.

[241] C. Sun, C. Su and J. Wu, "Synthesis of short graphene oxide nanoribbons for improved biomarker detection of Parkinson's disease," *Biosensors and Bioelectronics,* 67, 2015, 327-333.

[242] F. Valentini, D. Romanazzo, M. Carbone and G. Palleschi, "Modified screen-printed electrodes based on oxidized graphene nanoribbons for selective electrochemical detection of several molecules," *Electroanalysis,* 24, 2012, 872-881.

[243] A. Martín, J. Hernández-Ferrer, M. Martínez and A. Escarpa, "Graphene nanoribbon-based electrochemical sensors on screen-printed platforms," *Electrochimica Acta,* 172, 2015, 2-6.

[244] H. Hu, Y. Song, M. Feng e H. Zhan, "Carbon nanomaterials for simultaneous determination of dopamine and uric acid in the presence of ascorbic acid: from one-dimensional to the quasi one-dimensional," *Electrochimica Acta,* 190, 2016, 40-48.

[245] J. Lavanya and N. Gomathi, "High-sensitivity ascorbic acid sensor using graphene sheet/graphene nanoribbon hybrid material as an enhanced electrochemical sensing platform," *Talanta,* 144, 2015, 655-661.

[246] R. Srivastava, S. Srivastava, T. Narayanan, B. Mahlotra, R. Vajtai, P. Ajayan and A. Srivastava, "Functionalized multilayered graphene platform for urea sensor," *ACS Nano,* 6, 2012, 168-175.

[247] N. Ismail, Q. Le, H. Yoshikawa, M. Saito and E. Tamiya, "Development of non-enzymatic electrochemical glucose sensor based on graphene oxide nanoribbon-gold nanoparticle hybrid," *Electrochimica Acta,* 146, 2014, 98-105.

[248] H. Hu, M. Feng and H. Zhan, "A glucose biosensor based on partially unzipped carbon nanotubes," *Talanta,* 41, 2015, 66-72.

[249] J. Huan, Q. Liu, A. Fei, J. Qian, X. Dong, B. Qiu, H. Mao and K. Wang, "Amplified solid-state electrochemiluminescence detection of cholesterol in near-infrared range based on CdTe quantum dots decorated multiwalled carbon nanotubes@reduced graphene oxide nanoribbons," *Biosensors and Bioelectronics,* 73, 2015, 221-227.

[250] Y. Pan, L. Shang, F. Zhao and B. Zeng, "A novel electrochemical 4-nonyl-phenol sensor based on molecularly imprinted poly (o-phenylenediamine-co-o-toluidine)-nitrogen-doped graphene nanoribbons -ionic liquid composite film," *Electrochimica Acta,* 151, 2015, 423-428.

[251] G. Zhu, Y. Yi, Z. Liu, H. Lee and J. Chen, "Highly sensitive electrochemical sensing based on 2-hydroxypropyl-β-cyclodextrin-functionalized graphene nanoribbons," *Electrochemistry Communications,* 66, 2016, 10-15.

[252] G. Zhu, Y. Yi, Z. Han, K. Wang e X. Wu, "Sensitive electrochemical sensing for polycyclic aromatic amines based on a novel core–shell multiwalled carbon nanotubes@ graphene oxide nanoribbons heterostructure," *Analytica Chimica Acta,* 845, 2014, 30-37.

[253] Y. Yi, G. Zhu, X. Wu and K. Wang, "Highly sensitive and simultaneous electrochemical determination of 2-aminophenol and 4-aminophenol based on poly (L-arginine)-B-cyclodextrin/ carbon nanotubes@graphene nanoribbons modified electrode," *Biosensors and Bioelectronics,* 77, 2016, 353-358.

[254] J. Tang, L. Hou, D. Tang, J. Zhou, Z. Wang, J. Li and G. Chen, "Magneto-controlled electrochemical immunoassay of brevetoxin B in seafood based on guanine-functionalized graphene nanoribbons," *Biosensors and Bioelectronics,* 38, 2012, 86-93.

[255] Q. Liu, A. Fei, J. Huan, H. Mao and K. Wang, "Effective amperometric biosensor for carbaryl detection based on covalent immobilization acetylcholinesterase on multiwall carbon nanotubes/graphene oxide nanoribbons nanostructure," *Journal of Electroanalytical Chemistry,* 740, 2015, 8-13.

[256] R. Zhang, C. Sun, Y. Lu and W. Chen, "Graphene nanoribbon-supported PtPt concave nanotubes for electrochemical detection of TNT with high sensitivity and selectivity," *Analytical Chemistry,* 87, 2015, 12262-12269.

[257] S. Tan, C. Chua e M. Pumera, "Graphene prepared from multi-walled carbon nanotubes and stacked graphene nanofibers for detection of 2,4,6-trinitrotoluene (TNT) in seawater," *Analyst,* 138, 2013, 1700-1704.

[258] S. Chowdhury, S. Zafar, V. Tellez e B. Sitharaman, "Graphene nanoribbon-based platform for highly efficacious nuclear gene delivery," *ACS Biomaterials Science and Engineering,* 2, 2016, 798-808.

[259] H. Dong, L. Ding, F. Yan, H. Ji and H. Ju, "The use of polyethylenimine-grafted graphene nanoribbon for cellular delivery of locked nucleic acid modified molecular beacon for recognition of microRNA," *Biomaterials,* 32, 2011, 3875-3882.

[260] S. Chowdhury, P. Manepalli and B. Sitharaman, "Graphene nanoribbons elicit cell specific uptake and delivery via activation of epidermal growth factor receptor enhanced by human papillomavirus E5 protein," *Acta Biomaterialia,* 10, 2014, 4494-4504.

[261] S. Chowdhury, C. Surhland, Z. Sanchez, P. Chaudhary, S. Kumar, S. Lee, L. Peña, M. Waring, B. Sitharaman e M. Naidu, "Graphene nanoribbons as a drug delivery agent for lucanthone mediated therapy of glioblastoma multiforme," *Nanomedicine: Nanotechnology, Biology, and Medicine,* 11, 2015, 109-118.

[262] S. Chowdhury, G. Lalwani, K. Zhang, J. Yang, K. Neville and B. Sitharaman, "Cell specific cytotoxicity and uptake of graphene nanoribbons," *Biomaterials,* 34, 2013, 283-293.

[263] Y. Talukdar, J. Rashkow, G. Lalwani, S. Kanakia and B. Sitharaman, "The effects of graphene nanostructures on mesenchymal stem cells," *Biomaterials,* 35, 2014, 4863-4877.

[264] B. Farshid, G. Lalwani and B. Sitharaman, "In vitro cytocompatibility of one-dimensional and two-dimensional nanostructure-reinforced biodegradable

polymeric nanocomposites," *Journal of Biomadical Materials Research: Part A,* 103, 2015, 2309-2321.

[265] D. Mbeh, O. Akhavan, T. Javanbakht, M. Mahmoudi and L. Yahia, "Cytotoxicity of protein corona-graphene oxide nanoribbons on human epithelial cells," *Applied Surface Science,* 320, 2014, 596-601.

[266] S. Chowdhury, S. Dasgupta, A. McElroy and B. Sitharaman, "Structural disruption increases toxicity of graphene nanoribbons," *Journal of Applied Toxicology,* 34, 2014, 1235-1246.

[267] O. Akhavan, E. Ghaderi, H. Emamy and F. Akhavan, "Genotoxicity of graphene nanoribbons in human mesenchymal stem cells," *Carbon,* 54, 2013, 419-431.

[268] E. Chng, C. Chua e M. Pumera, "Graphene oxide nanoribbons exhibit significantly greater toxicity than graphene oxide nanoplatelets," *Nanoscale,* 6, 2014, 10792-10797.

[269] P. Blake, E. Hill, A. Castro Neto, K. Novoselov, J. Jiang, R. Yang, T. Booth and A. Geim, "Making graphene visible," *Applied Physics Letters,* 91, 2007, 063124.

[270] T. Kuila, S. Bose, A. Mishra, P. Khanra, N. Kim and J. Lee, "Chemical functionalization of graphene and its applications," *Progress in Materials Science,* 57, 2012, 1061-1105.

[271] E. Andrei, G. Li and X. Du, "Electronic properties of graphene: a perspective from scanning tunneling microscopy and magnetotransport," *Reports on Progress in Physiscs,* 75, 2012, 056501 (47pp).

[272] A. Deshpande and B. LeRoy, "Scanning probe microscopy of graphene," *Physica E: Low-dimensional Systems and Nanostructures,* 44, 2012, 743-759.

[273] R. Young, I. Young, L. Gong e K. Novoselov, "The mechanics of graphene nanocomposites: A review," *Composites Science and Technology,* 72, 2012, 1459-1476.

[274] Z. Lee, J. Meyer, H. Rose and U. Kaiser, "Optimum HRTEM image contrast at 20kV and 80kV - exemplified by graphene," *Ultramicroscopy,* 112, 2012, 39-46.

[275] J. Meyer, A. Geim, M. Katsnelson, K. Novoselov, D. Obergfell, S. Roth, C. Girit and A. Zettl, "On the roughness of single- and bi-layer graphene membranes," *Solid State Communications,* 143, 2007, 101–109.

[276] C. Papp and H. Steinrück, "In situ high-resolution X-ray photo electron spectroscopy - fundamental insights in surface reactions," *Surface Scientific Reports,* 68, 2013, 446-487.

[277] K. Wepasnick, B. Smith, J. Bitter and D. Fairbrother, "Chemical and structural characterization of carbon nanotube surfaces," *Analytical and Bioanalytical Chemistry,* 396, 2010, 1003-1014.

[278] G. Wang, B. Wang, J. Park, J. Yang, X. Shen and J. Yao, "Synthesis of enhanced hydrophilic and hydrophobic graphene oxide nanosheets by a solvothermal method," *Carbon,* 47, 2009, 68 -72.

[279] Z. Sun, Z. Yan, J. Yao, E. Beitler, Y. Zhu and J. Tour, "Growth of graphene from solid carbon sources," *Nature,* 468, 2010, 549-552.

[280] U. Khan, A. O'Neill, M. Lotya, S. De and J. Coleman, "High-concentration solvent exfoliation of graphene," *Small,* 6, 2010, 864–871.

[281] A. Ferrari and D. Basko, "Raman spectroscopy as a versatile tool for studying the properties of graphene," *Nature Nanotechnology,* 8, 2013, 235-246.

[282] L. Malard, M. Pimenta and G. Dresselhaus, "Raman spectroscopy in graphene," *Physics Reports,* 473, 2009, 51-87.

[283] A. Ferrari, J. Meyer, V. Scardaci, C. Casiraghi, M. Lazzeri, F. Mauri, S. Piscanec, D. Jiang, K. Novoselov, S. Roth and A. Geim, "Raman Spectrum of Graphene and Graphene Layers," *Physical Review Letters,* 97, 2006, 187401(4).

[284] K. Kalaitzidou, H. Fukushima and L. Drzal, "A new compounding method for exfoliated graphite–polypropylene nanocomposites with enhanced flexural properties and lower percolation threshold," *Composites Science and Technology,* 67, 2007, 2045–205.

[285] G. Kasaliwal, T. Villmow, S. Pegel and P. Pötschke, "Chapter 4: Influence of material and processing parameters on carbon nanotube dispersion in polymer melts," *Polymer - carbon nanotube composites: Preparation, properties and applications,* T. McNally e P. Pötschke, Edits., Cambridge, Woodhead Publishing Limited, 2011, pp. 92-132.

[286] M. Wang, "Developing bioactive composite materials for tissue replacement," *Biomaterials,* 24, 2003, 2133-2151.

[287] G. Taylor, "The viscosity of a fluid containing small drops of another fluid," *Proceedings of the Royal Society A,* 138, 1932, 41-48.

[288] H. Grace, "Dispersion phenomena in high viscosity immiscible fluid systems and application of static mixers as dispersion devices in such systems," *Chemical Engineering Communications,* 14, 1982, 225-277.

[289] R. Powell and S. Mason, "Dispersion by laminar flow," *AlChE Journal,* 28, 1982, 286-293.

[290] K. Min, J. White and J. Fellers, "High density polyethylene/polystyrene blends: phase distribution morphology, rheological measurements, extrusion, and melt spinning behavior," *Journal of Applied Polymer Science,* 29, 1984, 2117-2142.

[291] I. Manas-Zloczower and D. Feke, "Analysis of agglomerate rupture in linear flow fields," *International Polymer Processing,* 4, 1989, 3-8.

[292] C. Macosco, Rheology: principles, measurements and applications, United States of America: Wiley, 1994.

[293] G. Tadmor and G. Gogos, Principles of polymer processing, New York: Willey-Interscience, 1979.

[294] X. Nguyen and L. Utracki, "Extensional flow mixer". Nacional Research Council Canada Patent US 5,451,106, 19 September 1995.

[295] R. Novais, F. Simon, M. Paiva and J. Covas, "The influence of carbon nanotube functionalization route on the efficiency of dispersion in polypropylene by twin-screw extrusion," *Composites: Part A,* 43, 2012, 2189-2198.

[296] R. Sengupta, M. Bhattacharya, S. Bandyopadhyay and Bhowmick, "A review on the mechanical and electrical properties of graphite and modified graphite reinforced polymer composites," *Progress in Polymer Science,* 36, 2011, 638-670.

[297] A. Sham and M. Notley, "A review of fundamental properties and applications of polymer–graphene hybrid materials," *Soft Matter,* 9, 2013, 6645-6653.

[298] A. Duguay, J. Nader, A. Kisiltas, D. Gradner and H. Dagher, "Exfoliated graphite nanoplatelet-filled impact modified polypropylene nanocomposites: influence of particle diameter, filler loading, and coupling agent on the mechanical properties," *Applied Nanoscience,* 4, 2014, 279-291.

[299] J. An, G. Jeon and Y. Jeong, "Preparation and properties of polypropylene nanocomposites reinforced with exfoliated graphene," *Fibers and Polymers,* 13, 2012, 507-514.

[300] E. Kuvardina, L. Novokshonova, S. Lomakin, S. Timan and I. Tchmutin, "Effect of the graphite nanoplatelet size on the mechanical, thermal, and electrical properties of polypropylene / exfoliated graphite nanocomposites," *Journal of Applied Polymer Science,* 128, 2013, 1417-1424.

[301] P. Song, Z. Cao, Y. Cai, L. Zhao, Z. Fang and S. Fu, "Fabrication of exfoliated graphene-based polypropylene nanocomposites with enhanced mechanical and thermal properties," *Polymer,* 52, 2011, 4001-4010.

[302] C. Garzón and H. Palza, "Electrical behavior of polypropylene composites melt mixed with carbon-based particles: Effect of the kind of particle and annealing process," *Composites Science and Technology,* 99, 2014, 117-123.

[303] M. Achaby, F. Arrakhiz, S. Vaudreuil, A. Qaiss, M. Bousmina and O. Fassi-Fehri, "Mechanical, thermal and rheological properties of graphene-based polypropylene nanocomposites prepared by melt mixing," *Polymer Composites,* 33, 2012, 733-744.

[304] P. Hubert, K. Kathiresan and K. Wakabayashi, "Filler exfoliation and dispersion in polypropylene/as received graphite nanocomposites via cryogenic milling," *Polymer and Engineering Science,* 51, 2011, 2273-2281.

[305] K. Kalaitzidou, H. Fukushima and T. Drzal, "A route for polymer nanocomposites with engineered electrical conductivity and percolation threshold," *Materials,* 3, 2010, 1089-1103.

[306] Y. Li, J. Zhu, S. Wei, J. Ryu, L. Sun and Z. Guo, "Poly(propylene)/graphene nanoplatelet nanocomposites: Melt rheological behavior and thermal, electrical and electronic properties," *Macromolecular Chemistry and Physics,* 212, 2011, 1951-1959.

[307] J. Zhong, I. Isayev and X. Zhang, "Ultrasonic twin screw compounding of polypropylene with carbon nanotubes, graphene nanoplates and carbon black," *European Polymer Journal,* 80, 2016, 16-39.

[308] J. Liang, Q. Du, G. Tsui and C. Tang, "Tensile properties of graphene nanoplatelets reinforced polypropylene composites," *Composites Part B,* 95, 2016, 166-171.

[309] C. Huang, C. Lou, C. Liu, C. Huang, X. Song and J. Lin, "Polypropylene/graphene and polypropylene/carbon fiber conductive composites: mechanical, crystallization and electromagnetic properties," *Applied Sciences,* 5, 2015, 1196-1210.

[310] C. Vallés, A. Abdelkader, R. Young and I. Kinloch, "Few layer graphene–polypropylene nanocomposites: the role of flake diameter," *Faraday Discussions,* 173, 2014, 379-390.

[311] B. Dittrich, K. Wartig, D. Hofmann, R. Mlhüaupt and B. Schartel, "The influence of layered, spherical, and tubular carbon materials' concentration on the flame retardancy of polypropylene," *Polymer composites,* 36, 2015, 1230-1241.

[312] P. Chammingkwan, K. Matsushita, T. Taniike and M. Terano, "Enhancement in mechanical and electrical properties of polypropylene using graphene oxide grafted with end-functionalized polypropylene," *Materials,* 240, 2016, 1-14.

[313] J. Pionteck, E. Valdez, F. Piana, M. Omastová, A. Luyt and B. Voit, "Reduced percolation concentration in polypropylene/expanded graphite composites: effect of viscosity and polypyrrole," *Journal of Applied Poymer Science,* 132, 2015, 41994 (12pp).

[314] R. Ramasamy, K. Yang e H. Rafailovich, "Polypropylene–graphene – a nanocomposite that can be converted into a meta-material at desired frequencies," *RSC Advances,* 4, 2014, 44888-44895.

[315] Editorial, "All in the graphene family - A recommended nomenclature for two-dimensional carbon materials," *Carbon,* 65, 2013, 1-6.

[316] R. Greinke, "Expandable graphite and method". United States Patent US 6,406,612 B1, 18 June 2002.

[317] D. Chattopadhyay and K. Raju, "Structural engineering of polyurethane coatings for high performance applications," *Progress in Polymer Science,* 32, 2007, 352-418.

[318] G. Lomax, "Breathable polyurethane membranes for textile and related industries," *Journal of Materials Chemistry,* 17, 2007, 2775-2784.

[319] J. Hu, H. Meng, G. Li and S. Ibekwe, "A review of stimuli-responsive polymers for smart textile applications," *Smart Materials and Structures,* 21, 2012, 053001 (23pp).

[320] W. Zhao, M. Li and H. Peng, "Functionalized MWNT-doped thermoplastic polyurethane nanocomposites for aerospace coating applications," *Macromolecular Materials and Engineering,* 295, 2010, 838-845.

[321] D. Crawford and J. Escarsega, "Dynamic mechanical analysis of novel polyurethane coating for military applications," *Thermochimica Acta,* 357, 2000, 161-168.

[322] A. Nasar, G. Srinivasan, R. Mohan and G. Radhakrishnan, "Polyurethane solvent-based adhesives for footwear applications," *Journal of Adhesion,* 68, 1998, 21-29.

[323] M. Kathalewar, P. Joshi, A. Sabnis and V. Malshe, "Non-isocyanate polyurethanes: from chemistry to applications," *RSC Advances,* 3, 2013, 4110-4129.

[324] X. Zhou, Y. Li, C. Fang, S. Li, Y. Cheng, W. Lei and X. Meng, "Recent advances in synthesis of waterborne polyurethane and their application in water-based ink: a review," *Journal of Materials Science & Technology,* 31, 2015, 708-722.

[325] B. Ren, H. Wang, Z. Ren, W. Liu, L. Jiang and S. He, "Synthesis of MDI-50 and tung oil based non-ionic waterborne polyurethanes," *Materials Science Forum,* 848, 2016, 160-166.

[326] K. Nagao, K. Tanaka, M. Inoue and M. Matsuo, "Cationic polyurethane resin aqueous dispersion, ink-jet receiving agent including the same, and ink-jet recording medium using the same". Boston, MA, USA Patent 2008/0090949 A1, 17 April 2008.

[327] F. Coutinho, M. Delpech and L. Alves, "Anionic waterborne polyurethane dispersions based on hydroxyl-termined polybutadiene and poly(propylene glycol): Synthesis and characterization," *Journal of Applied Polymer Science,* 80, 2001, 566-572.

[328] Y. Xiao, X. Fu, Y. Zhang, Z. Liu, L. Jiang and J. Lei, "Preparation of waterborne polyurethanes based on the organic solvent-free process," *Green Chemistry,* 18, 2016, 412-416.

[329] W. Du, J. Liu, Y. Wang, Y. Li and Z. Li, "Polyurethane encapsulated carbon black particles and enhanced properties of water polyurethane composite films," *Progress in Organic Coatings,* 97, 2016, 146-152.

[330] M. Michálek and M. Bredol, "Incorporation of functionalized multiwall carbon nanotubes into a polyurethane matrix," *Advances in Materials Science and Engineering,* 2013, 2013, 929865 (6pp).

[331] A. Rahmatpour, B. Kaffashi and S. Maghami, "Preparation and rheological properties of functionalized multiwalled carbon nanotube/waterborne

polyurethane nanocomposites," *Journal of Macromolecular Science, Part B: Physics,* 50, 2011, 1834-1846.

[332] J. Kwon and H. Kim, "Preparation and properties of acid-treated multiwalled carbon nanotube/waterborne polyurethane nanocomposites," *Journal of Applied Polymer Science,* 96, 2005, 595-604.

[333] D. Molina, G. Griffini, M. Levi and S. Turri, "Novel conductive nanocomposites from perfluoropolyether waterborne polyurethanes perfluoropolyether waterborne polyurethanes," *Polymers Advanced Technology,* 25, 2014, 1082-1088.

[334] C. Zhao, W. Zhang and D. Sun, "Preparation and mechanical properties of waterborne polyurethane/ carbon nanotube composites," *Polymer Composites,* 30, 2009, 649-654.

[335] h. Kuan, C. Ma, W. Chang, S. Yuen, H. Wu and T. Lee, "Synthesis, thermal, mechanical and rheological properties of multiwall carbon nanotube/waterborne polyurethane nanocomposite," *Composites Science and Technology,* 65, 2005, 1703-1710.

[336] Z. Wu, H. Wang, M. Xue, X. Tian, H. Zhou, X. Ye and K. Zheng, "Preparation of carbon nanotubes/waterborne polyurethane composites with the emulsion particles assisted dispersion of carbon nanotubes," *Composites Science and Technology,* 114, 2015, 50-56.

[337] Z. Zeng, H. Jin, L. Zhang, H. Zhang, Z. Chen, F. Gao and Z. Zhang, "Low-voltage and high-performance electrothermal actuator based on multi-walled carbon nanotube/ polymer composites," *Carbon,* 84, 2015, 327-334.

[338] H. He, X. Xu and D. Zhang, "An aligned macro-porous carbon nanotube/waterborne polyurethane sensor for the detection of flowing organic vapors," *Sensors and Actuators B,* 176, 2013, 940-944.

[339] Z. Zheng, M. Chen, H. Jin, W. Li, X. Xue, L. Zhou, Y. Pei, H. Zhang and Z. Zhang, "Thin and flexible multi-walled carbon nanotube/waterborne polyurethane composites with high-performance electromagnetic interference shielding," *Carbon,* 96, 2016, 768-777.

[340] H. Chang, Y. Yeh and K. Huang, "Electromagnetic shielding by composite films prepared with carbon fiber, Ni nanoparticles and multiwalled carbon nanotubes in polyurethane," *Materials Transactions,* 51, 2010, 1145-1149.

[341] M. Rahman, E. Kim, K. Lim and W. Lee, "Morphology and properties of waterborne polyurethane/CNT nanocomposite adhesives with various carboxyl acid salt groups," *Journal of Adhesion Science and Technology,* 23, 2009, 839-850.

[342] M. Rahman, A. Hasneen, W. Lee, H. Kim, H. Chun, H. Shin, J. Yoon and H. Park, "Properties of waterborne polyurethane/CNT nanocomposites adhesives: effect of countercations," J*ournal of Adhesion Science and Technology,* 25, 2011, 1073-1086.

[343] J. Kwon and H. Kim, "Comparison of the properties of waterborne polyurethane/ multiwalled carbon nanotube and acid-treated multiwalled carbon nanotube composites prepared by in situ polymerization," *Journal of Polymer Science: Part A: Polymer Chemistry,* 43, 2005, 3973-3685.

[344] J. Ding, Y. Fan, C. Zhao, Y. Liu, C. Yu and N. Yuan, "Electrical conductivity of waterborne polyurethane/graphene composites prepared by solution mixing," *Journal of Composite Materials,* 46, 2011, 747-752.

[345] N. Yousefi, M. Gudarzi, Q. Zheng, S. Aboutalebi, F. Sharif and J. Kim, "Self-alignment and high electrical conductivity of ultralarge graphene oxide–polyurethane nanocomposites," *Journal of Materials Chemistry,* 22, 2012, 12709–12717.

[346] N. Yousefi, M. Gudarzi, Q. Zheng, X. Lin, X. Shen, J. Jia, F. Sharif and J. Kim, "Highly aligned, ultralarge-size reduced graphene oxide/polyurethane nanocomposites: mechanical properties and moisture permeability," *Composites: Part A,* 49, 2013, 42-50.

[347] S. Wu, T. Shi and L. Zhang, "Latex co-coagulation approach to fabrication of polyurethane/graphene nanocomposites with improved electrical conductivity, thermal conductivity, and barrier property," *Journal of Applied Polymer Science,* 133, 2016, 43117 (13pp).

[348] V. Anjanapura, A. Raghu, Y. Lee, H. Jeong and C. Shin, "Preparation and physical properties of waterborne polyurethane/functionalized graphene sheet nanocomposites," *Macromolecular Chemistry and Physics,* 209, 2008, 2487-2493.

[349] Y. Lee, V. Anjanapura, A. Raghu, H. Jeong and B. Kim, "Properties of waterborne polyurethane/functionalized graphene sheet nanocomposites prepared by in situ method," *Macromolecular Chemistry and Physics,* 210, 2009, 1247-1254.

[350] P. Król, B. Król, K. Pielichowska and M. Špírková, "Composites prepared from the waterborne polyurethane cationomers—modified graphene. Part I. Synthesis, structure, and physicochemical properties," *Colloid and Polymer Science,* 293, 2015, 421-431.

[351] P. Król, B. Król, M. Zenker and J. Subocz, "Composites prepared from the waterborne polyurethane cationomers-modified graphene. Part II. Electrical properties of the polyurethane films," *Colloid and Polymer Science,* 293, 2015 2941-2947.

[352] Y. Kim and B. Kim, "Synthesis and properties of silanized waterborne polyurethane/graphene nanocomposites," *Colloid and polymer Science,* 292, 2014, 51-58.

[353] M. Quintana, E. Vazquez and M. Prato, "Organic functionalization of graphene in dispersions," *Accounts of Chemical Research,* 46, 2013, 138–148.

[354] P. Li, H. Ren, F. Qiu, J. Xu, Z. Yu, P. Yang, B. Xu, Y. Jiang and D. Yang, "Preparation and properties of graphene oxide modified waterborne polyurethane

-acrylate hybrids," *Polymer- Plastics Technology and Engineering,* 53, 2014, 1408-1416.

[355] X. Luo, P. Zhang, R. Liu, W. Li, B. Ge and M. Cao, "Preparation and physical properties of functionalized graphene/waterborne polyurethane UV-curing composites by click chemistry," *Polymer International,* 65, 2016, 415-422.

[356] X. Luo, P. Zhang, J. Ren, R. Liu, J. Feng and B. Ge, "Preparation and properties of functionalized graphene/waterborne polyurethane composites with highly hydrophobic," *Journal of Applied Polymer Science,* 132, 2015, 42005 (8pp).

[357] Y. Li, Z. Yang, H. Qiu, Y. Dai, Q. Zheng, J. Li and J. Yang, "Self-aligned graphene as anticorrosive barrier in waterborne polyurethane composite coatings," *Journal of Materials Chemistry A,* 2, 2014, 14139–14145.

[358] X. Wang, W. Xing, L. Song, H. Yang, Y. Hu and G. Yeoh, "Fabrication and characterization of graphene-reinforced waterborne polyurethane nanocomposite coatings by the sol–gel method," *Surface and Coatings Technology,* 206, 2012, 4778-4784.

[359] L. Lei, Z. Xia, L. Zhang, Y. Zhang and L. Zhong, "Preparation and properties of amino-functional reduced graphene oxide/waterborne polyurethane hybrid emulsions," *Progress in Organic Coatings,* 97, 2016, 19-27.

[360] H. Pan, X. Wang, Y. Zhang, L. Yu and Z. Zhang, "Graphene oxides reduced and modified by hydramines – Potentials as electrode materials of supercapacitors and reinforcing agents of waterborne polyurethane," *Materials Research Bulletin,* 59, 2014, 117-124.

[361] Y. Zhuo, J. Liu, Q. Li, B. Qiu and G. Xing, "Preparation and characterization of WPU/CNT/GO nanocomposites," *Integrated Ferroelectronics,* 171, 2016, 52-58.

[362] S. Hsiao, C. Ma, H. Tien, W. Liao, S. Wang, S. Li, C. Yang, S. Lin and R. Yang, "The effect of covalent modification of graphene nanosheets on the electrical property and electromagnetic interference shielding performance of water-borne polyurethane composite," *ACS Applied Materials and Interfaces,* 7, 2015, 2817-2826.

[363] S. Hsiao, C. Ma, H. Tien, W. Liao, Y. Wang, S. Li and Y. Huang, "Using a non-covalent modification to prepare a high electromagnetic interference shielding performance graphene nanosheet/water-borne polyurethane composite," *Carbon,* 60, 2013, 57-66.

[364] X. Hu, M. Tian, L. Qu, S. Zhu and G. Han, "Multifunctional cotton fabrics with graphene/polyurethane coatings with far-infrared emission, electrical conductivity, and ultraviolet blocking properties," *Carbon,* 95, 2015, 625-633.

[365] J. Li, J. Cui, J. Yang, Y. Li, H. Qiu and J. Yang, "Reinforcement of graphene and its derivatives on the anticorrosive properties of waterborne polyurethane coatings," *Composites Science and Technology,* 129, 2016, 30-37.

[366] G. Christopher, M. Kulandainathan and G. Harichandran, "Comparative study of effect of corrosion on mild steel with waterborne polyurethane dispersion

containing graphene oxide versus carbon black nanocomposites," *Progress in Organic Coatings,* 89, 2015, 199-211.

[367] J. Hu and F. Zhang, "Self-assembled fabrication and flame-retardant properties of reduced graphene oxide/waterborne polyurethane nanocomposites," *Journal of Thermal Analysis and Calorimetry,* 118, 2014, 1561-1568.

[368] S. Choi, D. Kim, A. Raghu, K. Reddy, H. Lee, K. Yoon, H. Jeong and B. Kim, "Properties of graphene/waterborne polyurethane nanocomposites cast from colloidal dispersion mixtures," *Journal of Macromolecular Science , Part B: Physics,* 51, 2012, 197-207.

[369] L. Zhang and J. Webster, "Nanotechnology and nanomaterials: promises for improved tissue regeneration," *Nano Today,* 4, 2009, 66-80.

[370] B. Ulery, L. Nair and C. Laurencin, "Biomedical applications of biodegradable polymers," *Journal of polymer Science Part B - Polymer Physics,* 49, 2011, 832-864.

[371] P. Gentile, V. Chiono, C. Tonda-Turo, A. Ferreira and G. Ciardelli, "Polymeric membranes for guided bone regeneration," *Biotechnology Journal,* 6, 2011, 1187-1197.

[372] T. Garg, O. Singh, S. Arora and R. Murthy, "Scaffold: a novel carrier for cell and drug delivery," *Critical Reviews in Therapeutic Drug Carrier Systems,* 29, 2012, 1-63.

[373] S. Venkatraman, F. Boey and L. Lao, "Implanted cardiovascular polymers: Natural, synthetic and bio-inspired," *Progress in Polymer Science,* 33, 2008, 853-874.

[374] A. Asti and L. Gioglio, "Natural and synthetic biodegradable polymers: different scaffolds for cell expansion and tissue formation," *International Journal of Aetificial Organs,* 37, 2014, 187-205.

[375] R. LogithKumar, A. KeshavNarayan, S. Dhivya, A. Chawla and S. Saravanan, "A review of chitosan and its derivatives in bone tissue engineering," *Carbohydrate Polymers,* 151, 2016, 172-188.

[376] N. Alves and J. Mano, "Chitosan derivatives obtained by chemical modifications for biomedical and environmental applications," *International Journal of Biological Macromolecules,* 43, 2008, 401-414.

[377] A. Hoffman, "Hydrogels for biomedical applications," *Advanced Drug Delivery Reviews,* 54, 2002, 3-12.

[378] K. Lee and D. Mooney, "Alginate: properties and biomedical applications," *Progress in Polymer Science,* 37, 2012, 106-126.

[379] J. Borges and J. Mano, "Molecular interactions driving the layer-by-layer assembly of multilayers," *Chemical Reviews,* 114, 2014, 8883-8942.

[380] K. Ariga, J. Hill and Q. Ji, "Layer-by-layer assembly as a versatile bottom-up nanofabrication technique for exploratory research and realistic application," *Physical Chemistry Chemical Physics,* 9, 2007, 2319-2340.

[381] P. Wagner, V. Ivanovskaya, M. Melle-Franco, B. Humbert, J. Adjizian, P. Briddon and C. Ewels, "Stable hydrogenated graphene edge types: normal and reconstructed Klein edges," *Physical Review B,* 88, 2013, 094106(6).

[382] K. Strutyński, A. Gomes and M. Melle-Franco, "Accuracy of dispersion interactions in semi empirical and molecular mechanics models: the benzene dimer case," *Journal of Physical Chemistry A,* 118, 2014, 9561-9567.

[383] M. Dudek and J. Ponder, "Accurate modeling of the intramolecular electrostatic energy of proteins," *Journal of Computational Chemistry,* 16, 1995, 791-816.

[384] M. Melle-Franco, M. Prato and F. Zerbetto, "Permanent chiral twisting of nonchiral carbon nanotubes," *Journal of Physical Chemistry A,* 106, 2002, 4795-4797.

[385] N. Alves, C. Picart and F. Mano, "Self-assembly and crosslinking of polyelectrolyte multilayer films of chitosan and alginate studied by QCM and IR spectroscopy," *Macromolecular Bioscience,* 9, 2009, 776-785.

[386] A. Neto, A. Cibrão, C. Correia, R. Carvalho, G. Luz, G. Ferrer, G. Botelho, C. Picart, N. Alves and J. Mano, "Nanostructured polymeric coatings based on chitosan and dopamine-modified hyaluronic acid for biomedical applications," *Small,* 10, 2014, 2459-2469.

[387] F. Tuinstra and J. Koenig, "Raman spectra of graphite," *Journal of Chemical Physics,* 53, 1970, 1126-1130.

[388] H. Chen, C. Chen, Q. Chen, F. Cheng, G. Zhang and Z. Chen, "Non-destructive purification of multiwalled carbon nanotubes produced by catalyzed CVD," *Materials Letters,* 57, 2002, 734-738.

[389] Y. Liu, M. Park, K. Shin, B. Pant, J. Choi, W. Park, Y. Lee, J. Park and Y. Kim, "Facile preparation and characterization of poly(vinyl alcohol)/chitosan/graphene oxide biocomposite nanofibers," *Journal of Industrial and Engineering Chemistry,* 20, 2014, 4415-4420.

[390] A. Ferrari and J. Robertson, "Interpretation of Raman spectra of disordered and amorphous carbon," *Physical Review B,* 61, 2000, 14095-14107.

[391] W. Zhu, S. Murali, W. Cai, S. Li, W. Suk, R. Potts and S. Ruoff, "Graphene and graphene oxide: synthesis, properties and applications," *Advanced Materials,* 22, 2010, 3906-3924.

[392] L. Guo, F. Wang, Y. Qian, B. Wang and H. Xia, "A green approach to the synthesis of graphene nanosheets," *ACS Nano,* 3, 2009, 2653-2659.

[393] M. Acik, G. Lee, C. Mattevi, A. Pirkle, M. Wallace, M. Chowalla, K. Cho and Y. Chabal, "The role of oxygen during thermal reduction of graphene oxide studied

by infrared absorption spectroscopy," *Journal of Physical Chemistry C,* 115, 2011, 19761-19781.

[394] F. Navarro-Pardo, G. Martinez-Barrera, L. Martinez-Hernadez, M. Castano, L. Rivera-Armenta, F. Medellin-Rodriguez and C. Velasco-Santos, "Effects on the thermo-mechanical and crystallinity properties of nylon 6,6 electrospun fibers reinforced with one dimensional (1D) and two dimensional (2D) carbon," *Materials,* 6, 2013, 3494-3513.

[395] R. Gao, T. Hu, Z. Yang, R. Zhu, J. Chai, J. Su, Y. Zhang and F. Zhang, "Paper-like graphene-Ag composite films with enhanced mechanical and electrical properties," *Nanoscale Research Letters,* 8, 2013, 32 (8pp).

[396] B. Konkena and S. Vasudevan, "Understanding aqueous dispersibility of graphene oxide and reduced graphene oxide through pK(a) measurements," *Journal of Physical Chemistry Letters,* 3, 2012, 867-872.

[397] R. Costa, C. Custódio, A. Testera, F. Arias, J. Rodriguez-Cabello, N. Alves and J. Mano, "Stimuli-responsive thin coatings using elastin-like polymers for biomedical applications," *Advanced Functional Materials,* 19, 2009, 3210-3218.

[398] K. Marx, "Quartz crystal microbalance: a useful tool for studying thin polymer films and complex biomolecular systems at the solution-surface interface," *Biomacromolecules,* 4, 2003, 1099-1120.

[399] L. Han, F. Yan, F. Chen and W. Li, "Preparation of chitosan/graphene oxide composite film with enhanced mechanical strength in the wet state," *Carbohydrate Polymers,* 83, 2011, 653-658.

[400] E. Guzmán, F. Ortega, N. Baghdadli, G. Luengo and R. Rubio, "Effect of the molecular structure on the adsorption of conditioning polyelectrolytes on solid substrates," *Colloids and Surfaces A: Physicochemical and Engineering Aspects,* 375, 2011, 209-218.

[401] X. Huang, Z. Yin, S. Wu, X. Qi, Q. He, Q. Zhang, Q. Yan, F. Boey and H. Zhang, "Graphene-based materials: Synthesis, characterization, properties and applications," *Small,* 7, 2011, 1876-1902.

[402] K. Novoselov, V. Fal'ko, L. Colombo, P. Gellert, M. Schwab and K. Kim, "A roadmap for graphene," *Nature,* 490, 2012, 192-200.

[403] J. MacLeod and F. Rosei, "Molecular self-assembly on graphene," *Small,* 10, 2014, 1038-1049.

[404] Y. Kung and S. Hsiao, "Fluorescent and electrochromic polyamides with pyrenylamine chromophore," *Journal of Materials Chemistry,* 20, 2010, 5481-5492.

[405] R. Silverstein, F. Webster and D. Kiemle, Spectrometric identification of organic compounds, 7th edition ed., New York: John Wiley & Sons, Inc., 2005.

[406] C. Ehli, G. Rahman, N. Jux, D. Balbinot, D. Guldi, F. Paolucci, M. Marcaccio, D. Paolucci, M. Melle-Franco, F. Zerbetto, S. Campidelli and M. Prato, "Interactions

in Single Wall Carbon Nanotubes/Pyrene/Porphyrin Nanohybrids," *Journal of the American Chemical Society,* 128, 2006, 11222-11231.

[407] Y. Zhang, H. Ma, Q. Zhang, J. Peng, J. Li, M. Zhai and Z. Yu, "Facile synthesis of well-dispersed graphene by Y-ray induced reduction of graphene oxide," *Journal of Materials Chemistry,* 22, 2012, 13064-13069.

[408] J. Jang, D. Rangappa, Y. Kwon and I. Honma, "Direct preparation of 1-PSA modified graphene nanosheets by supercritical fluidic exfoliation and its electrochemical properties," *Journal of Materials Chemistry,* 21, 2011, 3462–3466.

[409] X. Wang, W. Xing, X. Feng, B. Yu, L. Song, G. Yeoh and Y. Hu, "Enhanced mechanical and barrier properties of polyurethane nanocomposite films with randomly distributed molybdenum disulfide nanosheets," *Composites Science and Technology,* 127, 2016, 142-148.

[410] H. Bai, C. Li and G. Shi, "Functional composite materials based on chemically converted graphene," *Advanced Materials,* 23, 2011, 1089-1115.

[411] J. Ma, Q. Meng, I. Zaman, S. Zhu, A. Michelmore, N. Kawashima, C. Wang and H. Kuan, "Development of polymer composites using modified, high-structural integrity graphene platelets," *Composites Science and Technology,* 91, 2014, 82-90.

[412] M. Naebe, J. Wang, A. Amini, H. Khayyam, N. Hameed, L. Li, Y. Chen and B. Fox, "Covalent functionalized graphene/epoxy nanocomposites," *Scientific Reports,* 4, 2014, 4375 (7pp).

[413] H. Oxfall, J. Rondin, M. Bouquey, R. Muller, M. Rigdahl and R. Rychwalski, "Elongational flow mixing for manufacturing of graphite nanoplatelet/polystyrene composites," *Journal of Applied Polymer Science,* 128, 2013, 2679-2686.

[414] L. Hilliou, D. Dusschoten, M. Wilheim, H. Burhin and Rodger R., "Increasing the force torque transducer sensitivity of an RPA 2000 by a factor 5 - 10 via advanced data acquisition," *Rubber Chemistry and Technology,* 77, 2004, 192-200.

[415] P. Moldenaers, J. Vermant, J. Mewis and I. Heynderickx, "Origin of nonlinearities in the Bagley plots of thermotropic copolyesters," *Journal of Rheology,* 40, 1996, 203-219.

[416] J. Martins, V. Cruz and M. Paiva, "Flow activation volume in composites of polystyrene and multiwall carbon nanotubes with and without functionalization," *Macromolecules,* 44, 2011, 9804-9813.

[417] K. Wang, "Description of extrudate swell for polymer nanocomposites," *Materials,* 3, 2010, 386-400.

[418] S. Sadhu and A. Bhowmick, "Unique rheological behavior of rubber based nanocomposites," *Journal of Polymer Science: Part B: Polymer Physics,* 43, 2005, 1854-1864.

[419] H. Uematsu, N. Horisawa, T. Horikida, S. Tanoue and Y. Iemoto, “Effect of carbon fiber on the capillary extrusion behaviors of high-density polyethylene,” *Polymer*, 45, 2013, 449-456.

[420] J. Gao, H. Bai, X. Zhou, G. Yang, C. Xu, Q. Zhang, F. Chen and Q. Fu, “Observation of strong nanoeffect via tuning distributed architecture of graphene oxide in poly(propylene carbonate),” *Nanotechnology*, 25, 2014, 025702 (11pp).